Propagation channel modeling at centimeter–and–millimeter–wave frequencies in 5G urban micro–cellular context

Cheikh Diakhate

NNT : 2019SACLT017

Propagation Channel Modeling at Centimeter–and–Millimeter–Wave Frequencies in 5G Urban Micro–cell Context.

Thèse de doctorat de l'Université Paris-Saclay
préparée à Télécom ParisTech

École doctorale n°580 Sciences et Technologies de l'Information et de la Communication (STIC)
Spécialité de doctorat: Réseaux, Information et Communications

Thèse présentée et soutenue à Paris, le 28 Mars 2019, par

Cheikh A. L. DIAKHATE

Composition du Jury :

Hélène ROUSSEL Professeur, Université Sorbonne	Présidente
Bernard UGUEN Professeur, IETR	Rapporteur
Davy GAILLOT Maître de conférences, TELICE	Rapporteur
Alain SIBILLE Professeur, Télécom ParisTech	Directeur de thèse
Jean–Christophe COUSIN Maître de conférences, Télécom ParisTech	Co–Directeur de thèse
Jean–Marc CONRAT Ingénieur R&D, Orange Labs	Co–Encadrant

Thèse de doctorat

"We should consider every day lost on which we have not danced at least once."

Friedrich Nietzsche, "Thus Spoke Zarathustra".

xo

Acknowledgements

Most definitely my favorite part of this dissertation because I get to momentarily part ways with the impartial professional narration… but I will try not to be too flippant about it ☺

To the Orange Labs entity in Belfort, especially the Wireless Engineering and Propagation (WEP) team which hosted this Ph.D. thesis, a profound acknowledgement to every individual for their contribution to my integration and well–being and to all the accomplishments along the way.

A special thank you to our team manager Daniel Milli, for his understanding and his availability, and, especially, to my supervisor Jean–Marc Conrat for his continued support and his highly relevant feedbacks on this work throughout these three years. The same goes for my thesis supervisors at Telecom ParisTech, Jean–Christophe Cousin and Alain Sibille, whose contributions to this work have also been of significant importance.

A sincere acknowledgment to the committee members—the referees Bernard Uguen at IETR and Davy Gaillot at TELICE, and the examiner Hélène Roussel at Paris VI, UPMC—for their acceptance to review this work in detail.

To my latest friends, Cyrille (quiet force, Hahahaa), Hajer, Nada (music connoisseur, Jajajaa!), Yosra, Adoni, Ayoub, Maroua, Marc, Brieuc, Salima, ..., the darts amateurs i.e. Philippe, Christel, Patrick, Imed, …, the coffee regulars i.e. Mounir, Patrice, Philippe, …, my office mates i.e. Stefan, Yohann and Lionel, I am thankful for the wonderful moments we have shared together, *and the show must go on*!

To my childhood friends of "Central Side" i.e. Papis Diaboula (twin brother), Karim Ndour, Papa Niane, Khadim Cissé, ..., to my friends of "Kaaatteusss FC" i.e. Jean–Baptiste (those were the days), Fodé, Chérif (mancunian bro), Eugène, Seydina, ..., to my "Thuillier & Enseirb co–pilots" i.e. Abou, Abass, Eddy Jaures—this attempt to make a list is probably my worst idea in the last three years—thank you all for the memorable laughs and our unterminable debates, *and long may it last*!

Finally, to my parents and role models i.e. Diarra Diakhate and Moussa Diakhate, to my sister Bousso (my number one fan) and my brothers i.e. Modou (stay gassing me up!), Maleye (the happy one) and Mouhammed (the main man), I am extremely grateful to have you in my life. Although you did not necessarily grasp the details of what it has been all about, every single one of you actively listened to me rambling over and over about my activities… literally at any time of day or night because, of course, I do not fare well with multiple time zones ☺ *I owe it all to you, many thanks*! At last, a big thank you to my other two mothers, Mame Sissokho and Leila Mbengue, my second father Ady Ndiaye and to Baye O. Ndiaye and Ndeye S. Mbengue, *I have extremely appreciated your support*.

Title: Propagation Channel Modeling at Centimeter–and–Millimeter–Wave Frequencies in 5G Urban Micro–cellular Context.

Keywords: Propagation, Millimeter–Wave, Measurements, 5G, Urban micro–cellular.

Abstract—The advent of bandwidth–demanding mobile applications and services has led to a massive explosion of the network data traffic. In order to alleviate this issue, millimeter–Wave communications systems are a promising technology for future 5G systems thanks to the large amount of bandwidth available in this frequency range. However, in order to take full advantage of this technology, knowledge of the radio propagation channel characteristics in these frequency bands is paramount. Therefore, in this thesis, the objective is to study the frequency–dependence of the propagation channel large scale parameters (LSPs), which describe the main channel characteristics. These LSPs include the building penetration losses, the channel delay spread, the channel azimuth spread and the propagation path–loss. The studies are performed thanks to measurement campaigns conducted in Belfort, in typical 5G deployment scenarios such as outdoor–to–indoor and urban outdoor environments, between 3 and 60 GHz.

Titre : Modélisation du canal de propagation en contexte urbain, petite cellule, dans les fréquences centimétriques et millimétriques pour la 5G.

Mots clés : Propagation, Millimétrique, Mesures, 5G, Urbain petite cellule.

Résumé—L'émergence des nouvelles applications et services mobiles, nécessitant de plus en plus de débits de communications, contribue à une explosion massive du trafic de données au sein du réseau. Pour faire face à ce challenge, les systèmes millimétriques sont une des technologies identifiées pour les futurs réseaux 5G en raison de la bande passante accrue disponible dans cette plage du spectre. Toutefois, pour tirer pleinement profit de tels systèmes, la connaissance des caractéristiques liées à la propagation des ondes radio dans ces bandes de fréquence est primordiale. Ainsi, dans cette thèse, l'attention est portée sur l'évaluation de la dépendance en fréquence des caractéristiques principales du canal de propagation, généralement décrites par les paramètres dits « large scale parameters (LSPs) ». Ceux–ci incluent les pertes de pénétration, l'étalement temporel ou angulaire du canal et l'affaiblissement moyen du canal. Les études sont basées sur des campagnes de mesures réalisées à Belfort, dans des scénarios de déploiement 5G typiques comme la pénétration à l'intérieur des bâtiments et la propagation en milieu urbain extérieur, entre 3 et 60 GHz.

Table of Contents

Acronyms

Introduction

Mobile and wireless communications systems have witnessed a remarkable success over the years, further improving the connectivity experience of the end–users. Approximately every decade, a set of new specifications and requirements are proposed in order to redefine new communications standards destined to upgrade the performances of the existing ones.

The 1st generation (1G) wireless communications systems were introduced in the 1980s. These early systems, designed for voice communications, were based on telecommunications standards such as AMPS (Advanced Mobile Phone System), NTM (Nordic Mobile Telephone) or TACS (Total Access Communications Systems). They used analog technology and operated mainly in the 800 MHz frequency band, allowing for communication data rates of 2.4 kbps. However, in addition to their lack of support for data services, such systems presented quite a few disadvantages including poor battery life, poor voice quality, limited capacity and poor security. Therefore, in the 1990s, the first digital communications systems, the 2nd generation (2G) cellular networks, were launched. The most successful 2G systems are based on GSM (Global System for Mobile Communications) standard. Not only have 2G systems marked the transition from the analog era to the digital era of cellular phones, they have also introduced data services like text and picture messages. GSM most widely used frequency bands include 900 and 1800 MHz. These systems operate over a 200 kHz channel bandwidth with communication data rates up to 9.6 kbps. Despite still being used worldwide, 2G systems have been gradually superseded by newer technologies that are able to handle more complex data such as video and streaming contents for instance. In this sense, the 3rd generation (3G) systems, based on UMTS (Universal Mobile Telecommunications System) technology, appeared in the 2000s. These systems target high speed data. They operate around the 2 GHz frequency band, with a channel bandwidth of about 5 MHz, allowing for communication data rates up to 2 Mbps. 3G systems have introduced the era of smartphones with the availability of services like mobile internet access and video calls. However, they have quickly found themselves overwhelmed with the emergence of bandwidth–intensive applications such as DVB (Digital Video Broadcasting),

HDTV (High Definition TeleVision), streaming, etc. Therefore, the 4th generation (4G) cellular networks, based on LTE (Long Term Evolution) standard, emerged in 2010. These LTE–based 4G networks offer a significant improvement in communication data rates, up to 300 Mbps. They operate in a relatively wide range of frequencies, from 450 MHz to 3.8 GHz, with channel bandwidths between 1.4 and 20 MHz. In LTE–Advanced (LTE–A) standard, the use of carrier aggregation (CA) enables bandwidths up to 100 MHz.

In the past few years, there has been an incredible ascension of smartphones and tablets and a proliferation of mobile applications and services, which have caused a massive explosion of the network mobile data traffic. Current figures suggest that existing cellular networks will no longer be able to sustain such a growth in the horizon of 2020, hence the race to build the 5th generation (5G) mobile and wireless communications systems.

One of the major challenges faced by the wireless industry is the impending spectrum shortage accentuated by the increase of the network mobile data traffic. To alleviate this growing problem, millimeter–Wave (mm–Wave) technology is considered as a key enabler for 5G systems, thanks to the large amount of bandwidth available in this frequency range. However, in order to take full advantage of mm–Wave benefits, it is crucial to get a better knowledge of the propagation channel characteristics in these frequency bands than the status quo. In this sense, the characterization of the mm–Wave radio propagation channel is our main motive in this Ph.D. project.

This subject is, however, too broad to be covered completely over a three–year Ph.D. program. Therefore, the focus is particularly on the frequency–dependence of the main propagation channel characteristics, commonly described by the so–called channel large–scale parameters (LSPs). Additionally, typically envisioned 5G deployment scenarios including outdoor–to–indoor (O2I) and urban outdoor environments are investigated herein. The studies also cover a wide frequency range, from the sub–6 GHz bands up to the mm–Wave frequency bands.

The studies performed in this project can thus be divided in mainly four distinctive parts.

In the first part, the journey to fulfilling the ambition of 5G is discussed. Specifically, the vision for upcoming 5G systems is laid out and some key enabling technologies for such systems, including mm–Wave technology, are described. This is the topic of **Chapter I**.

The second part of the studies is centered on the literature regarding mm–Wave channel modeling and characterization for future 5G systems. Numerous collaborative projects have tackled this issue and several other studies on the matter have been published in recent years. These efforts are discussed in **Chapter II**.

In the third part of this project, we provide a detailed analysis of the frequency–dependence of the propagation channel from a theoretical stand point. The main radio propagation phenomena are modeled and their behavior with regards to the frequency, discussed. This topic is addressed in **Chapter III**.

The fourth part of the studies is dedicated to experimental characterizations of the radio propagation channel, especially in the mm–Wave bands. In this sense, two measurement campaigns were conducted in Belfort, from 3 to 60 GHz. The first channel measurement studies, conducted in an O2I scenario, are described in **Chapter IV**. In **Chapter V**, the second measurement studies conducted in an urban outdoor environment are presented.

The added value of these studies is mainly an incremental input on channel modeling activities for the development of future 5G systems, with a focus on areas that are insufficiently investigated. Besides this scientific contribution, a better knowledge of the propagation channel characteristics is critical for adequate spectrum resource management from telecommunications operators. Therefore, they can optimize their radio resources and provide better services to the end–users.

This Ph.D. project has been conducted under the supervision of Jean–Marc Conrat at Orange Labs in Belfort. Jean–Christophe Cousin and Alain Sibille, from Telecom ParisTech, have ensured the academic follow–up. The studies took place within the Orange Labs research team in Belfort which is focused on developing propagation models for radio simulation tools. Telecom ParisTech brought its expertise and support in terms of development of high frequency equipments and electromagnetic wave propagation.

The studies performed in this Ph.D. project have also fueled the European project 5G PPP mmMAGIC, which kicked off on July 2015 and was completed on June 2017. One of the objectives of mmMAGIC was to propose a propagation model for frequencies between 6 and 100 GHz. Therefore, the studies performed herein have benefited from the highly collaborative environment within mmMAGIC.

Chapter I

I. On the Next Generation (5G) Mobile and Wireless Systems

In this chapter, the vision for future 5G communications systems is discussed. **Section 1** first gives a brief description of 5G technology with its targeted use cases and applications. Then, some of 5G main requirements such as support of massive capacity and connectivity, increased communication data rates, reduced latency, low power consumption and low cost devices are discussed. **Section 2** details key enabling technologies identified to fulfill such requirements. They include, but are not limited to, new radio access technologies (RATs) solutions such as the use of massive multiple–input multiple–output (MIMO) systems or the disruptive move to the millimeter–Wave (mm–Wave) frequency bands and novel network architecture concepts such as small–cells network densification, cloud–based radio access network (C–RAN) or network function virtualization (NFV). Finally, in **Section 3**, our objective to delve into the topic of mm–Wave communications is laid out.

1. Vision and Requirements for 5G

1.1. Overview on 5G technology

True, the main driving force behind 5G is mobile broadband as improving user data rates has always been a priority in the development of mobile communications systems. However future 5G systems are expected to have a much larger impact on a societal level than their predecessors. In this sense, they will target very diverse use cases as laid out in the 5G roadmap by the ITU (International Telecommunications Union) for 2020 and beyond [1]. These use cases include enhanced mobile broadband (eMBB), massive machine–type communications (mMTCs) and ultra–reliable low latency communications (URLLCs), as illustrated in **Fig. I.1.1**.

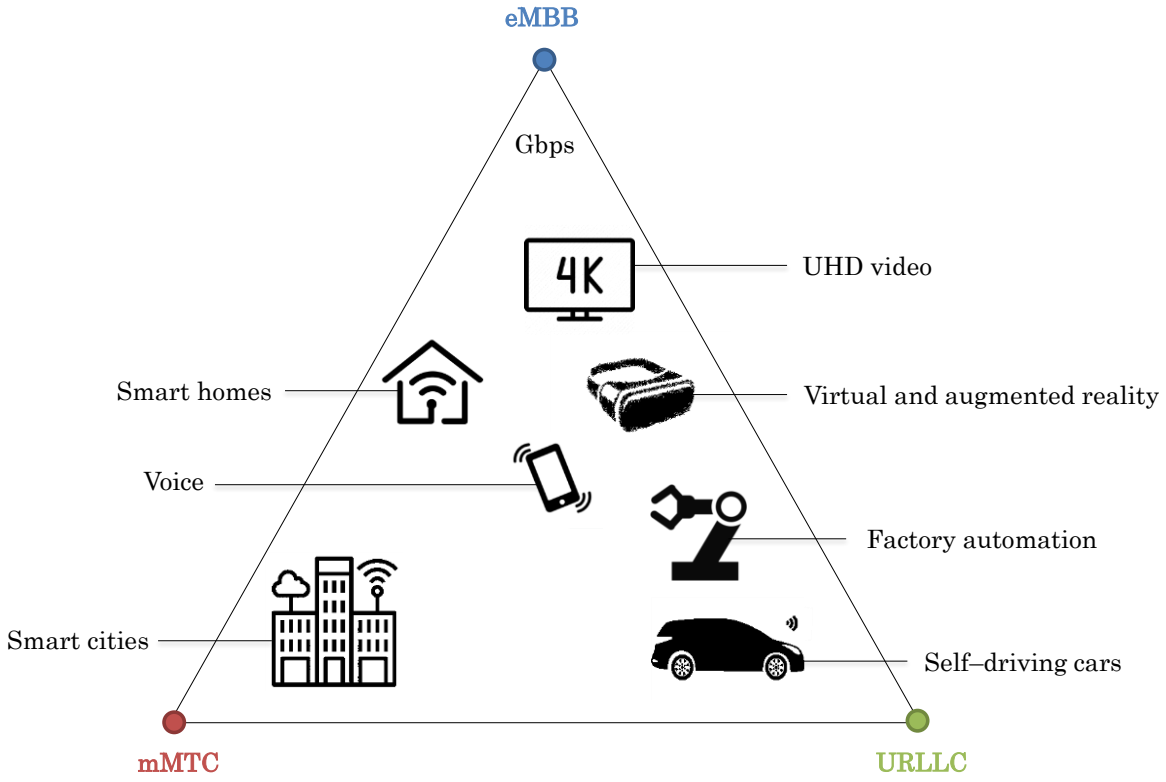

Fig. I.1.1 – 5G usage scenarios identified in IMT for 2020 and beyond

In the eMBB category, a significant improvement over 4G mobile broadband is expected, with high bandwidth applications such as ultra–high definition (UHD) video streaming targeted. Additionally, it is expected that broadband services be available everywhere, from sparsely populated areas in rural environments to dense areas such as indoor hotspots, stadiums, venues, etc., in order to ensure a seamless user experience. Furthermore, high mobility scenarios such as high–speed trains are also targeted in this use case. Finally, it is also believed that eMBB will open up an avenue for immersive multimedia applications such as virtual reality (VR) and augmented reality (AR).

With mMTC services, the aim is to basically connect everything to the network. This massive connectivity will enhance automation and monitoring of infrastructures so that they can operate with little to no human intervention. Thus, mMTC services will enable Internet of Things (IoT) applications such as smart homes or cities and smart agriculture among others. Besides this high–density connectivity, mMTC attributes should also include extended coverage and, mainly, low power consumption and low cost devices which are paramount to achieve such a vision.

Finally, the URLLC segment targets applications that have extremely stringent latency requirements such as remote healthcare, autonomous or self–driving cars and factory automation. Since these applications usually involve individual or public safety, extreme reliability, constant availability and very high security are also expected attributes of URLLCs.

1.2. Main 5G requirements

The multiplicity of 5G use cases leads to very diverse requirements that need to be met in order to achieve efficient 5G networks. Such requirements, ranging from high capacity and throughput needs to stringent latency, reliability, power consumption and cost constrains, are discussed below in more detail.

1.2.1. Massive capacity and connectivity

Over the past few years, the advent of mobile and wireless communications technologies has resulted in an unprecedented growth rate of the number of devices connected to the network, especially smartphones. Ericsson mobility report [2] predicts that, from 7.8 billion in 2017, worldwide mobile subscriptions will reach about 8.9 billion in 2023, of which 7.2 billion smartphone subscriptions. This is shown in **Fig. I.1.2** obtained from Ericsson's traffic exploration tool (TET) [3].

This increase is due to the apparition of new applications and services, destined to meet the user ever–increasing need for more and more connectivity. For instance, subscriptions to mobile broadband services have increased from 4.5 to 5.3 billion between 2016 and 2017, and they are expected to reach 8.3 billion in 2023, as underlined in [2]. As a result, a massive explosion of the network mobile data traffic is expected. In [2], it is reported that the total mobile data traffic will increase from the 15 Exabytes (EBs) per month in 2017 to an astonishing 107 EBs per month in 2023, with video contents accounting for about 73% of this number and future 5G networks expected to carry around 20% of this load. These predictions are illustrated in **Fig. I.1.3**, also extracted from Ericsson's TET [3].

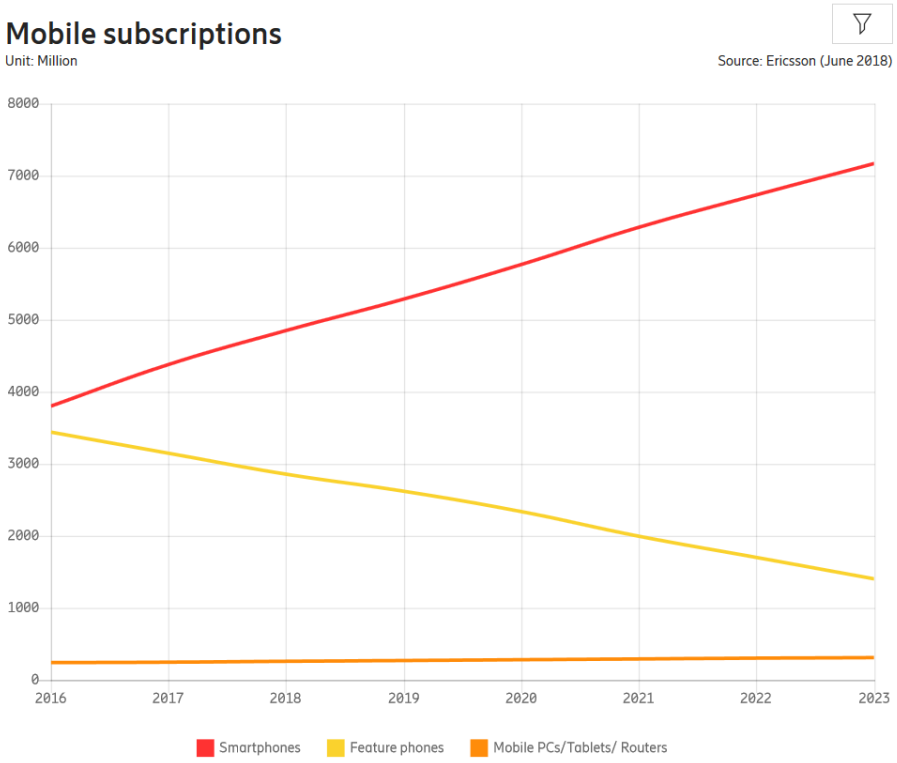

Fig. I.1.2 – Worldwide mobile subscriptions forecasts in the horizon of 5G

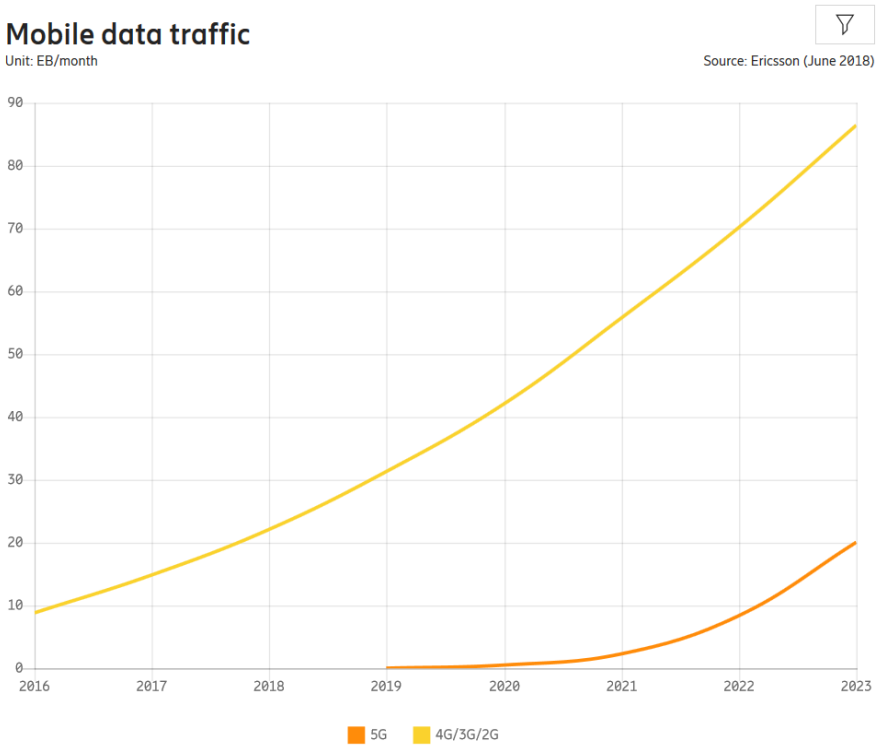

Fig. I.1.3 – Mobile data traffic predictions in the horizon of 5G

Additionally, CISCO visual networking index [4] predicts up to 49 EBs of monthly mobile data traffic as soon as 2021, a seven–fold increase over 2016 figures of 7.2 EBs per month. It is also reported in [4] that 5G networks will have to support billions of other connected devices, dedicated for applications beyond mobile broadband such as cellular IoT connections for e.g. which are expected to reach 3.5 billion in 2023.

At this rate, a sheer incremental approach based on current technologies will not be sufficient to support the impending data traffic in the horizon of 2020. This is a challenge that 5G networks will have to tackle by providing extremely high system capacity. Overall, it is commonly agreed that, at least, a 1,000–fold improvement over the current network capacity is required for future 5G systems as underlined in [5], [6], [7] and [8].

1.2.2. Very high data rates

In the course of the evolution of mobile networks, improving communication data rates has always been the main incentive. 5G mobile systems will make no exception to this rule. They are expected to deliver peak data rates greater than 10 Gbps, up to 100–fold increase over current figures.

In [5], Huawei argues that 5G will need to deliver a fiber–like 10 Gbps experience which will enable unprecedented immersive multimedia experiences such as UHD video streaming, VR/AR and the support for cloud services. In [8], Ericsson emphasizes the importance of the iniquitousness of these services in real world scenarios. They claim that while more than 10 Gbps peak data rates are expected in specific indoor and dense urban scenarios, end–user data rates greater than 100 Mbps should be achievable in urban and suburban environments. In all rural areas around the world, a minimum of 10 Mbps should be targeted. Nokia shares similar visions with expectations of peak data rates that exceed 10 Gbps and at least 100 Mbps end–user data rates, even under severe conditions such as cell–edge, as noted in [9]. In this regard, authors in [6] argue that edge rate between 100 Mbps and 1 Gbps should be achievable. Such figures are also in line with Orange's vision of 10 Gbps peak data rate and a minimum of 50 Mbps throughput everywhere, as underlined in [10]. Finally, NTT Docomo sets similar targets in [7] as they evoke a 1 Gbps experienced user throughput everywhere.

In summary, there is a common agreement that 5G mobile systems should be capable of providing at least 100 times more user data rates than existing cellular systems.

1.2.3. Ultra–low latency and high reliability

It is critical that 5G systems be capable of fulfilling certain latency requirements to enable the expected services. For instance, Orange key performance objectives, addressed in [10], include 8 milliseconds latency for eMBB services and 1 millisecond for URLLC. Authors in [6] argue that a 1 millisecond roundtrip latency, an order of magnitude faster than 4G systems for e.g., is required in 5G for applications such as online gaming, VR/AR and the tactile Internet. Similarly, in [9], Nokia claims that latency times as low as 1 millisecond will be necessary for new immersive multimedia applications such as VR/AR, the tactile Internet, machine control and remote healthcare. In [7], NTT Docomo reports that less than 1 millisecond user–plane latency over the radio access network (RAN) should be achievable for such applications. This would represent a remarkable upgrade over current figures, approximately a 10–fold improvement. Additionally, in [5] and [8] respectively, Huawei and Ericsson argue that less than 1 millisecond latency times will be required for mission–critical applications such as autonomous or self–driving cars, control of industry processes and health monitoring services. Overall, latency times of 1 millisecond or less are expected in future 5G networks.

Furthermore, it is highly important that 5G mission–critical applications, which often involve individual and/or public safety, be ultra–reliable and constantly available. In this sense, Orange sets a 99.999 % reliability goal in [10].

1.2.4. Low energy consumption and low cost devices

Over the last few years, the environmental impact of wireless technological advances has become a growing concern. Although previous generations of cellular systems have more or less addressed this issue, 5G systems will need to make significant improvements in this area in order to support the impending data traffic in a sustainable way.

According to Huawei's vision reported in [5], a 1,000–fold reduction on the energy per bit usage should be targeted in order to considerably improve device battery life. In addition, 5G's ambition of connecting everything will require very low cost devices with battery life of

several years according to Nokia and Ericsson reports in [9] and [8] respectively. In [8], energy performance on the network side, important for optimizing resources and operational costs, is also emphasized.

2. Key enabling technologies for 5G

In order to accommodate this very diverse set of requirements, disruptive breakthrough technologies are required for future 5G systems. In addition, contrary to its predecessors, 5G technology is expected to be inclusive with legacy technologies such as Wi–Fi, UMTS and LTE expected to be an integrant part of its ecosystem. This will require a profound shift in the way wireless communication systems are designed.

This need for innovative technologies has gathered strong interest among academic and industrial researchers in the wireless community, telecommunications operators, service providers and equipment vendors among others. Since 2010, extensive works have been conducted through various European collaborative projects such as METIS, mmMAGIC 5GNOW, Fantastic–5G, MCN, One5G, etc., and beyond, toward the development of 5G wireless and mobile communications systems. Multiple research studies addressing this topic have also been published in the literature. From these investigations, several technology drivers have been identified. In this section, we discuss some of the most recurring ones.

2.1. Massive multiple–input multiple–output (MIMO) systems

Multiple–input multiple–output (MIMO) technology consists of the use of multiple transmit (TX) and receive (RX) antennas for wireless communications. With such technology, additional degrees of freedom become available in the spatial dimension thanks to the antenna arrays. Through exploitation of spatial diversity [11] or spatial multiplexing [12], it is possible to significantly improve signal–to–noise ratio (SNR) and/or achieve better overall spectral efficiency [13].

Initially used in Wi–Fi systems, MIMO technology has gained a lot of attention in recent years. There were initially two modes in which MIMO technology were envisioned: single–user MIMO (SU–MIMO) and multi–user MIMO (MU–MIMO).

In conventional SU–MIMO a base station (BS), equipped with multiple antennas, transmits all its data streams to a single user mobile station (MS) in a given time slot. Besides only serving one user at a time, another downside of this approach is that it requires that the MS support MIMO technology and have multiple antennas as well. This leads to increased device cost and size and also demands more processing resources.

MU–MIMO, however, enables the BS to transmit its data streams to different users at the same time. The main advantage of this approach is that many users can be served simultaneously, thereby contributing to a better overall network efficiency. Additionally, although support of MIMO technology is required at the MS, the latter does not necessarily have to be equipped with multiple antennas. This technique is thus more flexible with regards to device cost and size.

Nevertheless, in its original form where roughly as many BS antennas as user MSs were targeted, MU–MIMO is not scalable because of the requirements regarding the knowledge of the channel state information (CSI) at both ends.

To alleviate this issue, the concept of massive MIMO, which consists of equipping the BS with a very large number of antennas, say 100, serving a fairly smaller number of user MSs simultaneously, began to gather significant interest as discussed in [14], [15] and [16]. This technology leverages time division duplexing (TDD), where only the uplink CSI is estimated. Therefore, the benefits of conventional MIMO can be scaled up with respect to the number of BS antennas and, thereby, help achieve the mobile broadband experience envisioned with 5G systems.

In fact, with knowledge of the downlink channels via uplink training, massive MIMO enables beamforming i.e. the ability to focus the radio signal in desired directions thanks to precoding techniques. This concept is illustrated in **Fig. I.2.1**.

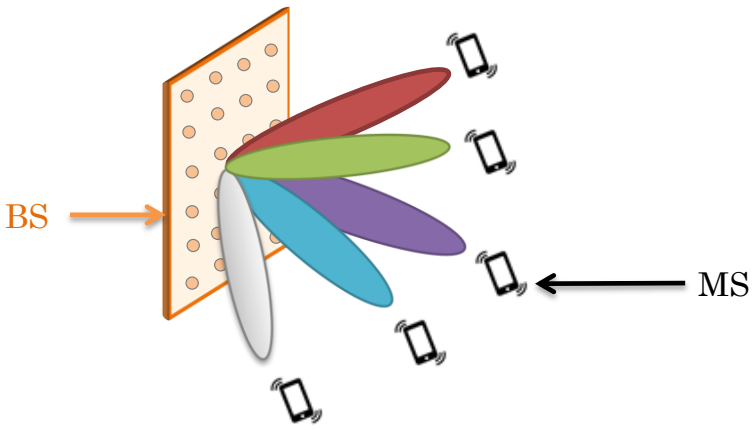

Fig. I.2.1 – Illustration of massive MIMO beamforming

Therefore, throughput can be increased and energy efficiency improved. In this regard, authors in [15] have suggested that massive MIMO systems should be capable of delivering 10 times more capacity while improving energy efficiency by a factor of 100, in comparison to the performances of conventional MIMO systems. They also claim that massive MIMO systems shall be built with low power, in the order of milliwatts, and low cost components since the required transmit power level per antenna decreases with increasing number of antennas. Furthermore, the use of massive MIMO precoding techniques in order to combat interferences has also been underlined in [15]. Finally, it is also claimed that beamforming will limit fading effects and thereby contribute to reduced latency times.

These benefits, among others, have made massive MIMO technology a promising candidate for 5G systems. However, there are numerous challenges that need to be addressed in order to design such systems.

To achieve the expected beamforming gains for instance, it is required that the CSI of each served terminal be available at the BS. Therefore, all terminals need to send out pilots to the BS for channel estimation. For a good CSI estimation, these pilots need to be orthogonal. However, due to limited channel coherence time, it is possible for a pilot sequence to be shared by multiple terminals across different cells. This re–using of pilot sequences by different terminals may cause a phenomenon known as pilot contamination [17]. This phenomenon, whose negative effects are amplified in massive MIMO systems, represents a major problem. Studies in [18] have investigated ways of mitigating such a phenomenon.

Additionally, massive MIMO can also suffer from hardware impairments, as discussed in [19]. In fact, the technology relies on a large number of low cost radio frequency (RF) components or chains with limited performances. This results into greater signal distortion and increased phase noise for instance. Furthermore, massive MIMO systems are expected to operate in TDD mode under the assumption that the channel is reciprocal. Although the radio propagation channel can be considered as such, it is not necessarily the case with the RF chains. Therefore, calibration of these chains may be required [15].

2.2. Millimeter–Wave (mm–Wave) communications systems

Spectrum allocation for cellular networks has not kept pace with the tremendous technological advances in mobile and wireless communications systems over the years. Almost all mobile and wireless systems operate in the frequency bands below 6 GHz. These frequency bands are becoming saturated due to the exponential growth of the network data traffic. Studies in [20] have shown that the frequency bandwidth available in the sub–6 GHz spectrum will not be sufficient to provide the capacity required for upcoming systems. Therefore, a disruptive move toward the millimeter–Wave (mm–Wave) frequency bands, where larger frequency bandwidths are available, is inevitable.

Theoretically, mm–Wave frequencies range from 30 to 300 GHz which corresponds to wavelengths in the range between 1 and 10 mm. However, researchers in the wireless community frequently refer to the frequency bands above 6 GHz as the mm–Wave bands. The simplified frequency spectrum chart represented in **Fig. I.2.2** highlights the frequency bands proposed by the ITU at WRC–2015 [20]. These frequency bands include 24.25 – 27.5 GHz, 31.8 – 33.4 GHz, 37 – 43.5 GHz, 45.5 – 50.2 GHz, 50.4 – 52.6 GHz, 66 – 76 GHz and 81 – 86 GHz.

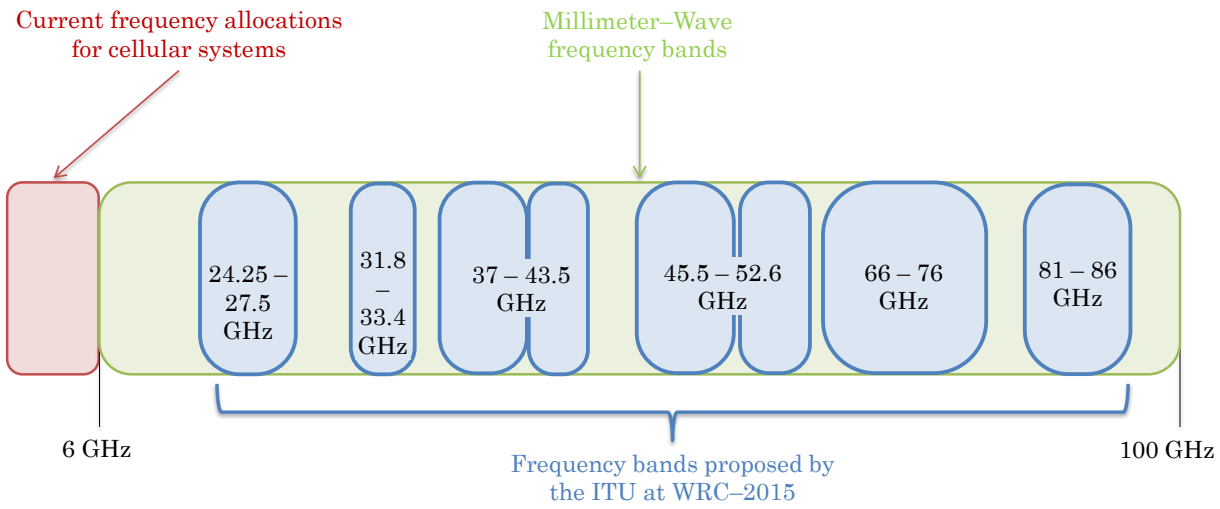

Fig. I.2.2 – Frequency bands proposed by the ITU at WRC–2015

Mm–Wave technology has been used in the past in applications such as radar remote sensing [21]. Satellite communications and security systems have also been using mm–Wave frequencies [22] in order to improve their performances in terms of precision and resolution. However, this technology is relatively unused for terrestrial mobile applications due to the severe propagation conditions associated with very high frequency communications, particularly for non–line–of–sight (NLoS) channels.

In comparison to the lower frequency bands, the hurdles faced in the mm–Wave range include greater free–space path–loss (PL) due to the increase in frequency as predicted by Friis' law, greater rain and atmospheric attenuation [23], [24], more foliage losses [25] and more sensitivity to blockage effects [6]. For these reasons among others, the use of mm–Wave in wireless communications has been restricted to specific applications such as short range communications or indoor services. In this regard, the Local Multipoint Distribution Service (LMDS) technology, destined for provision of broadband services to fixed networks, was deployed in the 28 GHz frequency band in the late 1990s [26]. Originally intended for distribution of TV services, this technology has not necessarily reached its envisioned commercial success. The unlicensed 60 GHz band has also attracted considerable interest. The IEEE 802.11.ad standard, also known as WiGig (Wireless Gigabit), was defined in this band [27] in 2012. This technology, intended for Wi–Fi services, enables data rates in the order of Gbps for short range indoor communications.

Recently, researchers in the wireless community have been reconsidering the feasibility of mm–Wave for terrestrial mobile communications [28], [29], [30], [6]. Several ways to overcome some of the aforementioned challenges, related with propagation conditions in this frequency range, have been proposed.

Studies in [6] have claimed that the increased free–space PL experienced in higher frequency bands due to the decrease of antenna size can be compensated for. They argue that so long as the antenna effective aperture is kept constant, mm–Wave frequencies will not result in higher free–space PL in comparison to legacy frequencies. This is achievable with the use of directional antennas and/or antenna arrays for more gain.

Authors in [28] and [6] have downplayed the impact of rain and atmospheric attenuation. In [6], it is argued that atmospheric attenuation, essentially noticeable at specific frequencies such as 60 GHz, results in about 15 dB/km attenuation in this frequency band. Such losses are thought to be insignificant in the targeted communications ranges for 5G mm–Wave systems, which are typically less than 200 m. The studies in [28] have also found out that atmospheric absorption and rain attenuation, even at heavy rates, are negligible at frequencies such as 28 and 38 GHz, with only 7 dB/km signal attenuation, which equates to 1.4 dB at 200 m.

It is true that mm–Wave signals are more sensitive to blockage effects than lower frequency signals. In fact, due to the short wavelengths, contributions from diffraction phenomenon for example are relatively insignificant at mm–Wave frequencies in comparison to the lower frequency bands. Therefore, the presence of obstacles may create abrupt changes with signal attenuation up to 40 dB at mm–Wave frequencies according to [6]. The use of adaptive antenna arrays and beam steering solutions can be considered in order to overcome this issue [31].

2.3. Small–cells network densification

Traditionally, macro–cell BSs are mounted on high towers. They are geared to serve a number of terminals within their coverage areas. These macro–cell BSs have been at the center of the evolution of cellular networks. With the looming capacity challenge in the horizon of 5G, further BS deployment is necessary in order to improve the connectivity experience of the end–users. However, this is not a workable solution for macro–cells for

numerous reasons including high operational and maintenance costs, lack of available sites and high output power. To circumvent this bottleneck, the concept of network densification by means of small–cells, illustrated in **Fig. I.2.3**, have gained huge momentum in recent years [32].

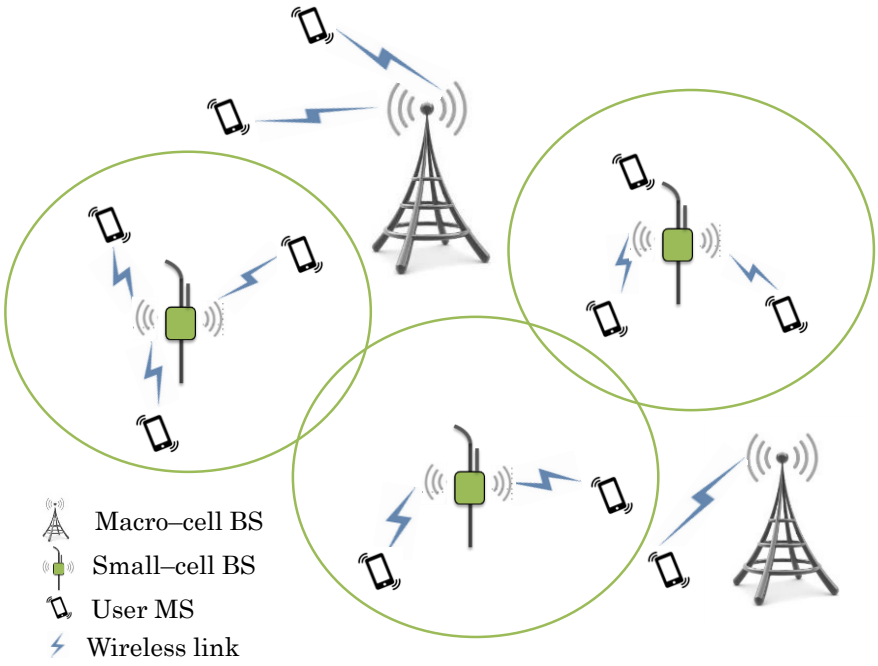

Fig. I.2.3 – Illustration of small–cells network densification concept

The idea is to offload parts of the traffic, currently being handled by the macro–cells, through the deployment of a large number of small–cells in a heterogeneous networks (HetNets) configuration. This densification approach is practical for enhancing network capacity in a cost efficient manner as argued in [33]. Furthermore, since small–cells are set to be located much nearer to the terminals compared to conventional macro–cells, better coverage will be achieved [34]. The deployment of small–cells, ranging from micro–cells to femto–cells, will increase the spectrum reuse ratio as the cell sizes become smaller. Thus, it is expected that HetNets will enable significant improvements on key metrics such as spectral efficiency [35].

In addition to these small–cells, HetNets may also include other components such as remote radio heads (RRHs), relays and multi–hop relays which will contribute to further improvements of the network performances.

However, with such extremely dense networks, there are several critical challenges that need to be addressed in order to reap the aforementioned benefits.

The sheer number of BSs within HetNets is a source of interferences [32], especially with spectrum reuse being a key aspect for improving spectral efficiency. Solutions to mitigate these inferences include CoMP (Coordinated Multipoint) techniques found in LTE standard as discussed in [36] and enhanced Inter–Cell Interference Coordination (eICIC) [37] adopted in LTE–A standard.

Moreover, mobility is a major concern in HetNets as demonstrated in [38]. The high density of small–cells increases the frequency of handovers for mobile terminals, which was already an issue in macro–cell–based networks. Studies in [39] and [40] have investigated mobility–aware solutions to solve this problem.

Finally, reliable wireless backhauling is mandatory for these HetNets since the high density of small–cells limits the availability of wired backhaul connections. In [41], non–orthogonal multiple access–based solutions have been investigated for this purpose.

2.4. Cloud–based radio access network (C–RAN)

Traditionally, the RAN is made of many standalone BSs. There are, up to now, mainly two network architectures: the single–cell site architecture and the distributed BS architecture, as illustrated in **Fig. I.2.4**.

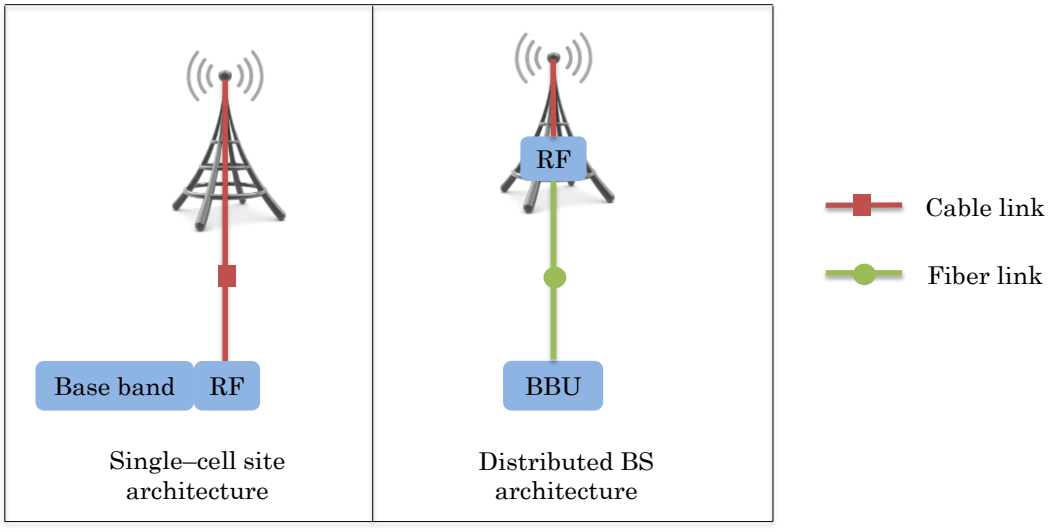

Fig. I.2.4 – Traditional network architectures

In the single cell site architecture, both the digital unit and the radio unit are housed together within the same structure, linked to the BS antenna by a long cable. However, in the distributed BS architecture, the radio function unit, referred to as RRH, is separated from the digital baseband unit (BBU) by fiber and placed closer to the BS antenna in order to minimize cable losses.

Nevertheless, in both cases, each BS requires its own power supply, conditioning and monitoring system. As massive deployment of additional BSs in the form of small–cells is considered as a promising solution to satisfy the capacity demand of 5G systems, these RAN architectures are not optimal for many reasons including increased susceptibility to interferences and expensive costs.

To circumvent these challenges, the concept of cloud–based radio access network (C–RAN) has received considerable attention in the context of 5G [42]. C–RAN is a novel network architecture that can be viewed as an evolution from the distributed BS architecture. As illustrated in **Fig. I.2.5**, it is based on this same decoupled architecture but on a much larger scale. Multiple BBUs decoupled from the RRHs are pooled into a cloud–like centralized unit, the BBU pool. Therefore, the BBU pool is tasked with baseband signal processing and signal transmission to the RRHs.

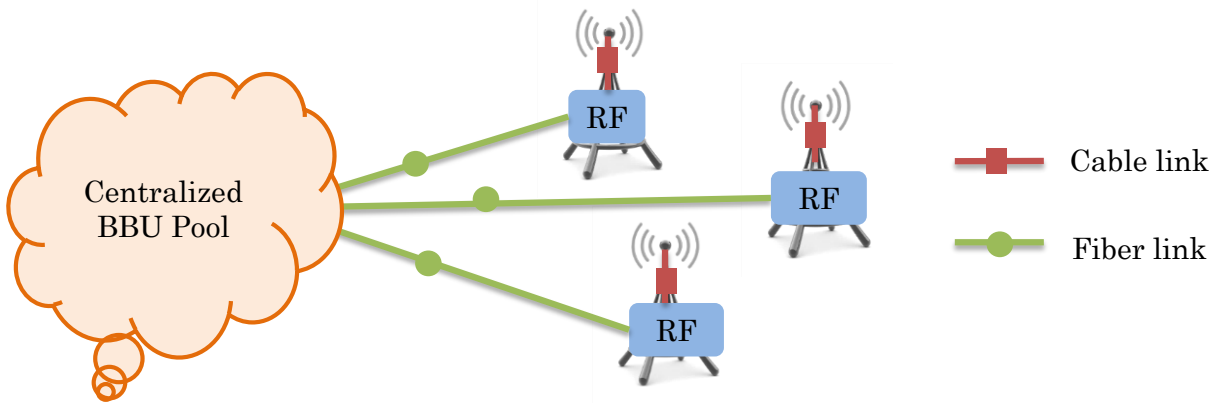

Fig. I.2.5 – Cloud–RAN (C–RAN) architecture for 5G

With such network architecture, it is possible to enhance capacity by massively deploying RRHs connected to a centralized cloud with high processing capabilities [43]. C–RAN architecture also enables support of multiple standards, reduced energy consumption and reduced capital expenditure (CAPEX) and operational expenditure (OPEX) for operators [43].

However, one of the main challenges related with C–RAN is the design of the communication layer between the BBU pool and the RRHs, known as the fronthaul network. Generally, optical links are preferred thanks to the available bandwidth but their high cost remains a limitation [43].

2.5. Network function virtualization (NFV)

Future 5G networks are expected to provide multiple services with different requirements. However, hardware–based functions of today's network are unfavorable for a continuous deployment of additional network services.

To solve this problem, seven of the world's leading telecom operators, including AT&T, BT, Deutsche Telekom, Orange, Telecom Italia, Telefonica and Verizon, came together through the European Telecommunications Standards Institute (ETSI) to introduce the concept of network functions virtualization (NFV) in 2012.

The idea is to decouple network functions from the dedicated physical infrastructure to a virtual instance. The NFV reference architecture defined by ETSI [44] and illustrated in **Fig. I.2.6** can be subdivided in mainly three parts:

- The NFV infrastructure (NFVI), which consists of the hardware resources, a virtualization layer and a virtual interface
- The Virtual Network Function (VNF), grouping together the virtual functions that can be run on the NFVI hardware resources
- The NFV Management and Orchestration (NFV MANO) module, charged with management of the infrastructure through the Virtualized Infrastructure Manager (VIM), management of lifecycle of VNF instances through the VNF manager and control of the network services through the Orchestrator.

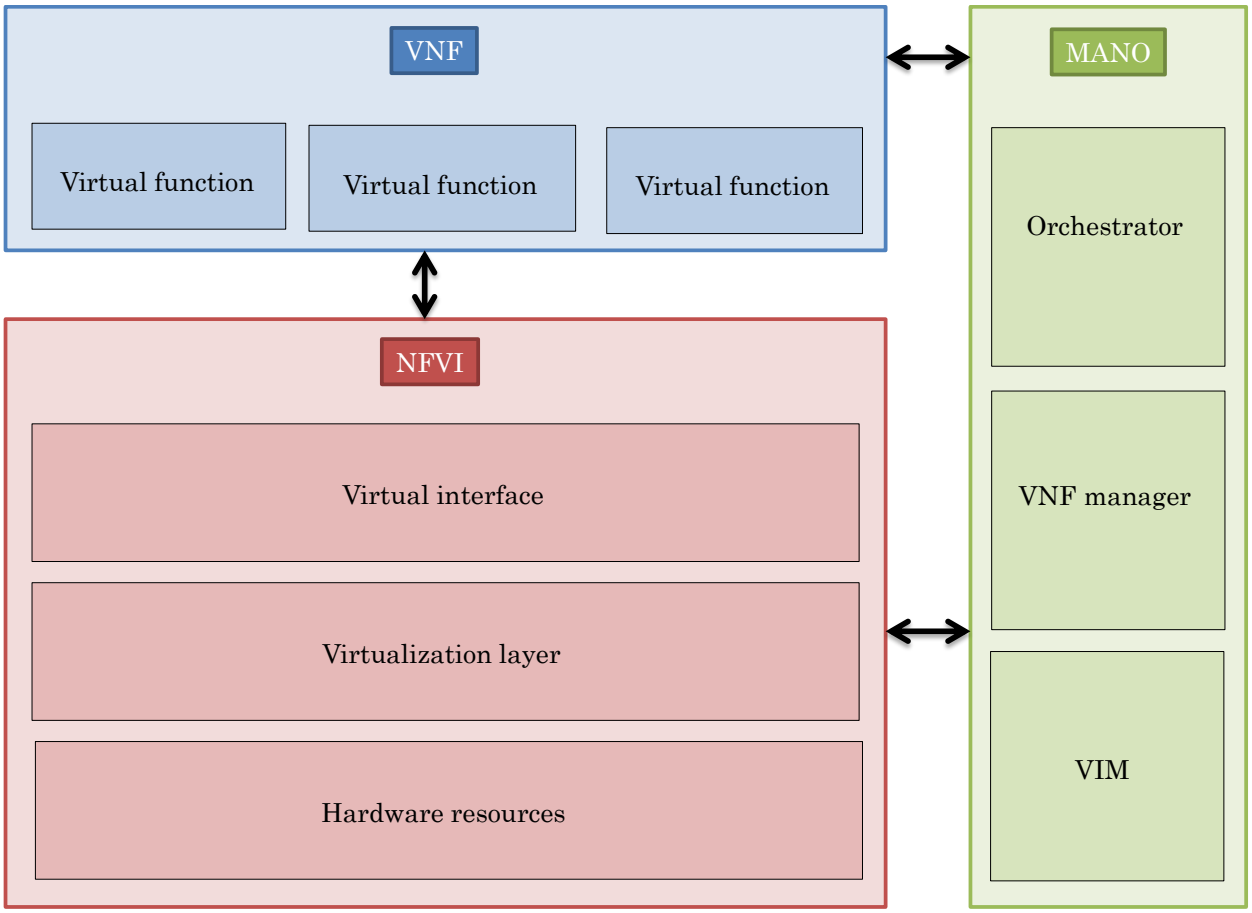

Fig. I.2.6 – Network function virtualization (NFV) architecture

This virtualization mechanism enables the coexistence of heterogeneous virtual network functions on the same physical infrastructure. It offers great flexibility to service providers in terms of resource management and rapid migration to new technologies. The benefits of NFV also include CAPEX and OPEX reduction and energy saving since the same physical infrastructure can be shared by multiple service providers [45]. However, NFV will face a number of challenges including the design of a simple NFV MANO that accommodates legacy management systems, optimal and flexible VNF instances, robustness against VNFI hardware failures, security and scalability [44], [46].

In addition, NFV will enable network slicing [47], a recurring concept in 5G discussions [48]. First introduced in [45], network slicing consists of creating multiple virtual networks from a single physical infrastructure. These virtual networks are designed to meet specific requirements from users and/or service providers. Network slicing's target

implementations include both the core network (CN) and the RAN as illustrated in **Fig. I.2.7**.

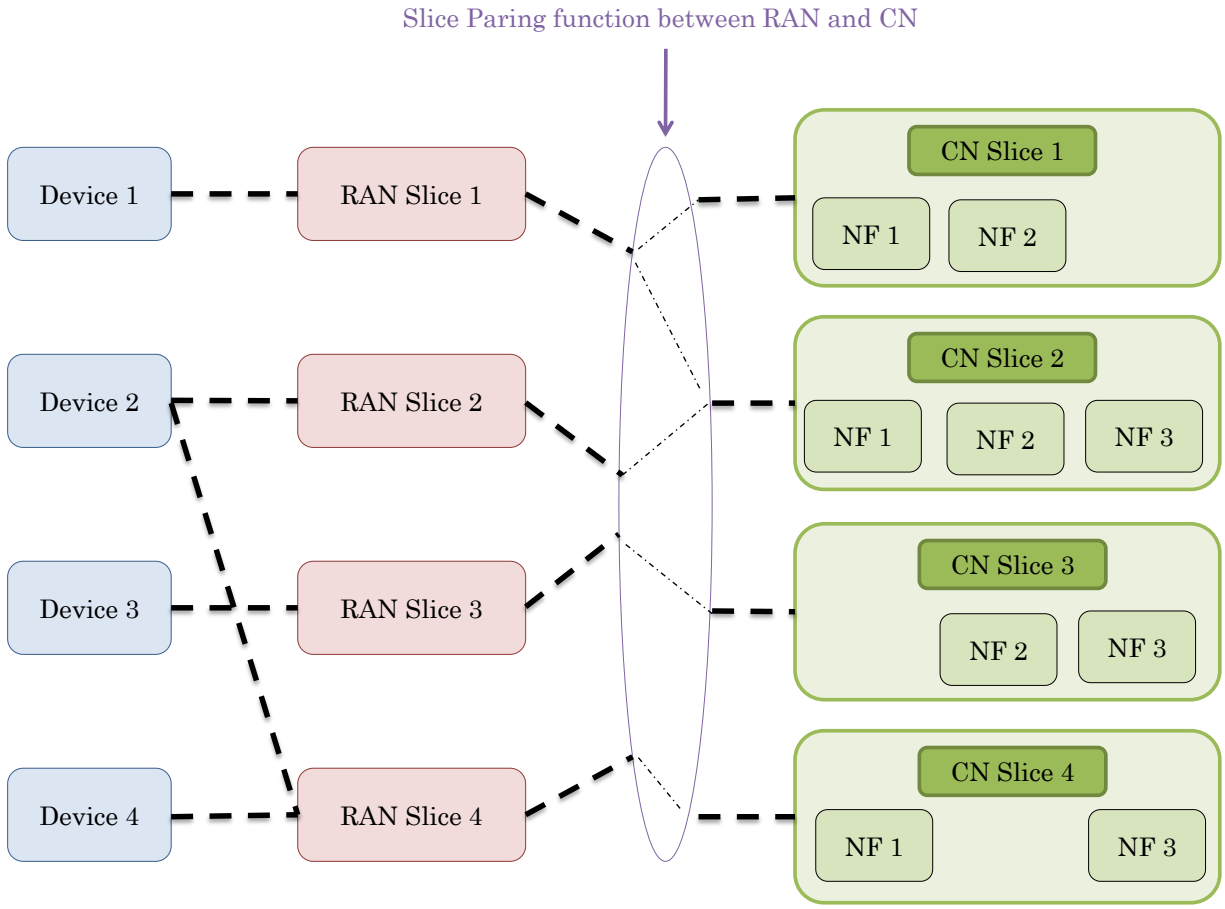

Fig. I.2.7 – Illustration of network slicing concept

2.6. Full–duplex communications

Traditionally, it has been assumed that radio units cannot receive and transmit on the same frequency resource at the same time due to self–interference. Transmission and reception are either alternated via time division, or they occur in different frequency resources. This is referred to as half–duplex (HD) communications.

However, recent research studies have started to invalidate this belief. Studies in [49], [50], and [51] have claimed the feasibility of simultaneous two–way communications, termed as full–duplex (FD) communications, by means of interference cancelation techniques such as antenna cancellation.

The self–interference antenna cancellation consists of deploying two transmit antennas, say TX_1 and TX_2, and one receive antenna, say RX_1, on the same radio unit, as shown in **Fig. I.2.8**. TX_1 and TX_2 are placed at distances d and $d + \lambda/2$ respectively away from RX_1, where λ denotes the radio signal wavelength.

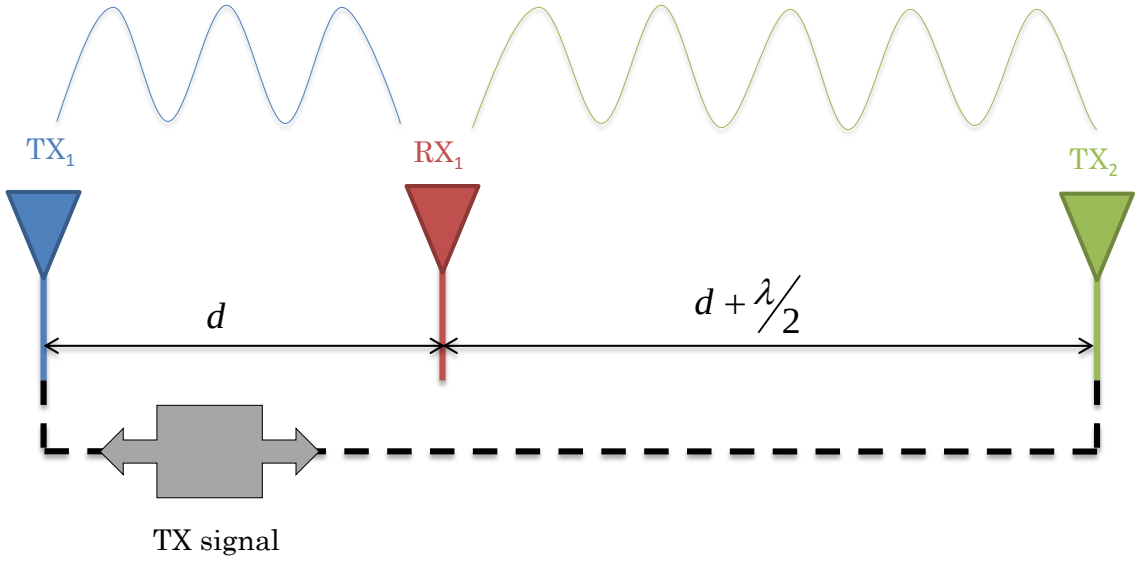

Fig. I.2.8 – Full–duplex (FD) topology for self–interference cancellation

Because of this phase offset of half a wavelength, the signals from TX_1 and TX_2 cancel out at RX_1, thereby significantly reducing self–interference [49]. Further digital and hardware interference cancellation techniques can also be applied to improve FD performances.

The reason FD is considered a key enabling technology for 5G is because it could potentially double spectral efficiency as there is no need for time slot allocation or frequency resource division between uplink and downlink.

However, FD presents some limitations including increased interference effects between users as tackled in [52] and [53], restriction to low power and narrowband communications, and adaptability to real–world scenarios.

2.7. Device–to–device communications

In traditional cellular technologies, devices do not directly communicate with each other without involvement of the network infrastructure. This inherently induces some latency.

Regarding 5G mission–critical applications where ultra–low latency is required, device–to–device (D2D) communications, with very little to no involvement of the network infrastructure, must be enabled.

Besides reduced latency, D2D communications are beneficial for improving throughput and fairness [54]. However, such communications may require that user equipments be able to function as relays. This paradigm shift will face strong challenges ranging from security and privacy to interference management and resource allocation [55], [56]. Additionally, since relaying devices lend their own resources including battery, storage and bandwidth, incentivizing users for their cooperation may be required [55].

3. Focus on millimeter–Wave (mm–Wave) technology

The overview presented in this chapter shows that significant efforts have been put into the development of future 5G communications systems. Innovative technologies are proposed to fulfill the challenging requirements posed by the envisioned 5G applications. With regards to the remaining studies in this Ph.D. project, the focus is on mm–Wave technology.

Although the prospect of mm–Wave technology for mobile communications systems is a very enticing one, there is still a lot of work to be done in order to bring this technology to fruition. Precise knowledge of the mm–Wave propagation channel, yet to be achieved, is paramount to fully assess the feasibility of mobile communications in such frequency bands.

Extensive research studies have been conducted worldwide in this regard but some areas still remain insufficiently investigated. Thus, it is our objective in this Ph.D. project, especially in the remaining chapters, to contribute to a better knowledge of the propagation channel properties in these frequency bands than the status quo.

Chapter II

II. Millimeter–Wave Channel Modeling and Characterization for 5G

In this chapter, the literature on mm–Wave channel modeling and characterization for future 5G systems is examined. In **Section 1**, a review of earlier channel models, developed for frequencies below 6 GHz and intended for 3G and/or 4G systems, is first performed. Then, the shortcomings of these models with regards to 5G requirements are highlighted. In response to the challenges, intensive investigations have been conducted under various European collaborative projects such as METIS, MiWEBA and mmMAGIC. The studies carried out in such projects are discussed in **Section 2**. The channel modeling studies undertaken in these collaborative projects are mainly fueled by measurement campaigns conducted all over the world by various research groups. These measurement campaigns are critical in channel modeling and characterization as they provide valuable knowledge and the data basis necessary to develop and validate models. Indeed, there are numerous issues related with 5G channel modeling. The support of frequency bands from below 6 GHz up to 100 GHz is an important consideration which many studies have focused on. In this regard, the frequency–dependence of channel large scale parameters (LSPs), which describe the main characteristics of the environment, has been the main interest in these investigations. Therefore, in **Section 3**, literature results, relevant to this topic, are reported. Finally, our motivations to perform further investigations on this subject are explained in **Section 4**.

1. Review of earlier channel models

In this section, the most popular channel modeling approaches, adopted in early system simulation and design, are discussed. More specifically, 3GPP, WINNER, COST and IEEE 802.11 efforts on the matter are documented. Following a brief description of these

entities, the main characteristics of the proposed channel models are highlighted. Additionally, the shortcomings of these models with regards to 5G requirements are emphasized.

1.1. 3GPP channel models

The 3rd generation partnership project (3GPP) is a cooperation of seven telecommunications standardization bodies, charged with the production of technical specifications meant to be transposed into deliverables by its very organizational partners. These partners include ARIB (Japan), ATIS (North America), CCSA (China), ETSI (Europe), TSDSI (India), TTA (South Korea) and TTC (Japan).

The 3GPP consortium have initially played a big part in the success of geometric channel models (see **Chapter III**, **Section 1** for more details) during the early stages of the work toward 4G networks. Moreover, as MIMO technology began to gain momentum, the need for standardized channel models to evaluate the performances of such a technology was raised. The 3GPP Spatial Channel Model (SCM) [57], introduced earlier in 2003, was then first considered to address this issue. Based on the geometrical principle, the proposed two–dimensional (2–D) model was developed for the 2 GHz frequency band with channel bandwidths up to 5 MHz. The model covers propagation scenarios such as suburban macro–cellular (SMa), urban macro–cellular (UMa) and urban micro–cellular (UMi).

In 2005, its wideband extension referred to as SCM–extended (SCM–E) [58] was developed to support larger bandwidths, up to 100 MHz. This latter model also supports the 5 GHz frequency band as well.

1.2. WINNER channel models

The Wireless World Initiative New Radio (WINNER) was a project initiated under the European FP6 research program, with over forty partners including operators, vendors and academics. Its objective was to develop a unique system concept adaptable to a wide range of communications scenarios.

In WINNER I [59], channel modeling for wideband MIMO was addressed. The proposed model, released in 2005, used very similar approaches as those adopted in the SCM–E [58]. The model was developed, based on measurements performed at 2 and 5 GHz. Multiple

propagation scenarios and environments including indoor, UMi, UMa, SMa and rural macro–cell (RMa) are covered in WINNER I and additional features such stationary feeder links are supported.

In WINNER II [60], the studies initiated in WINNER I [59] have continued. The frequency range was extended to the bands between 2 and 6 GHz in WINNER II models, released in 2007. More propagation scenarios and environments, including indoor–to–outdoor (I2O), outdoor–to–indoor (O2I), bad UMi and bad UMa are covered and additional features such as moving networks are supported.

The WINNER family models are geometry–based stochastic channel models (GSCMs). The channel parameters are determined stochastically based on statistical distributions extracted from measurements. Furthermore, in WINNER models, the entire modeling process, i.e. the stochastic definition of the LSPs and the generation of the multi–path components (MPCs), must be specified for each channel instance between the BS and the MS. These models are referred to as "system–level models" [61].

WINNER models have been widely used and, thereby, served as a framework for many studies. For instance, IMT–Advanced channel models [62] released in 2009, are based on WINNER models and also cover the frequency range between 2 and 6 GHz. Later on, WINNER channel models were extended to the three–dimensional (3–D) case in WINNER+ [63] in 2010, with support of the frequency range from 1 to 6 GHz. Similar modeling approaches were also adopted for the 3GPP 3–D channel model [64], released in 2015. This model, however, was developed for the 2 GHz frequency band with channel bandwidth of only 10 MHz.

1.3. COST channel models

The Cooperation in Science and Technology (COST) is a European funded program that brings together researchers from Europe and beyond to ensure a strong position for Europe in scientific and technical research fields. There are about thirty–six member states in COST. The ICT COST Action 2100 addresses the specific topic of mobile and wireless communications. Its objective is to propose solutions enabling the development of next generation communications systems.

In COST 2100 [61], a GSCM for MIMO communications was proposed as an extension of earlier models developed in COST 259 and COST 273 [65]. However, unlike WINNER "system–level models", COST 2100 channel modeling process is based on clusters, i.e. scattering elements, present in the environment and not specific to an individual channel instance. Therefore, once clusters are consistently stochastically defined for a given propagation environment with respect to the BS location, those visible at each channel instance between the BS and the MS are used to synthesize the channel LSPs. These models are referred to as "cluster–level models" [61].

1.4. IEEE 802.11ad channel model

The Institute of Electrical and Electronics Engineers (IEEE) 802.11 committee is a working group, "responsible for writing Wireless Local Area Network (WLAN) standards". Typically, ranges up to 100 m are targeted and unlicensed spectrum is used.

Therefore, the committee has been interested in channel modeling in the unlicensed 60 GHz frequency band for WLAN standards such as IEEE 802.11ad also known as WiGig. The covered propagation scenarios are indoor environments, typically a conference room. Thus, based on specific measurements and ray–tracing simulations in these specific scenarios, a deterministic cluster–based channel model [66] was proposed in 2010. The modeled paths are the line–of–sight (LoS) path and low order reflections as it was argued that diffracted paths are negligible at 60 GHz. The model is also supportive of antenna arrays and beamforming techniques and takes into account human blockage effects.

1.5. Shortcomings of early channel models with regards to 5G

COST 2100, IEEE 802.11ad and especially WINNER channel modeling approaches found their way into standardized models developed by the 3GPP and/or the ITU. These models have played a key role in the performance evaluation of current cellular systems such as 4G. However, there are some limitations with regards to their use for 5G development.

Both WINNER and COST–based channel models were designed for the evaluation cellular systems, like 3G and 4G, which operated in the frequency bands below 6 GHz. Thus, it is not straightforward to extend their applicability to the frequencies in the mm–Wave bands, targeted for future 5G networks. This is mainly due to the differences regarding the

propagation channel characteristics between the mm–Wave bands and the lower frequency bands as underlined in **Chapter I**, **Section 2.2**.

Although the frequency extension to the mm–Wave bands is our main interest in these studies, there are many other areas of improvement identified in 5G channel modeling tasks. Firstly, the WINNER and COST models were developed for communications systems where one end of the link is fixed, e.g. a fixed BS and a moving MS. Therefore, they do not support the dual–mobility required in D2D links for e.g. or even the concept of small–cells densification where BSs are located close to each other.

Additionally, WINNER models do not support the modeling of spherical waves, important for massive MIMO and beamforming performance evaluation. They also lack spatial consistency i.e. smooth evolution of the channel between closely located users due to their "system level approach". Although COST models do not have these limitations, the "cluster level approach" considered in their development is very complex and there is still no open source implementation available for such models.

Finally, due to its deterministic characteristics, the IEEE 802.11ad model is ill–suited to accommodate the large panel of propagation scenarios envisioned for 5G.

2. Channel modeling for 5G systems

In the horizon of 5G, a set of key requirements including, but not limited to, support of a very wide range of frequencies up to the mm–Wave bands, support of massive MIMO technology, spatial consistency, support of dual–mobility for D2D communications and support for a very wide range of propagation scenarios, have been identified in order to provide flexible channel models for 5G system simulation and design.

Therefore, studies have been conducted in various international projects such as METIS, MiWEBA and mmMAGIC in order to develop channel models that are suitable for 5G scenarios and use cases. Following a brief presentation of these groups, the channel modeling works conducted in these projects are discussed in this section.

2.1. METIS channel models

METIS (Mobile and wireless communications Enablers for the Twenty-twenty Information Society) was a European–lead project, kicked off in 2012, whose aim was "to lay the foundation for and to generate a European consensus on the future global mobile and wireless communications system". Twenty–nine entities ranging from telecommunications manufacturers and network operators to academic organizations and automotive industrials collaborated in this project. It was structured in eight work packages (WPs) among which WP1, charged with propagation channel measurement and modelling tasks among others.

METIS final channel models are described in [67]. The main 5G requirements targeted in METIS included support of a very wide range of frequency up to the mm–Wave bands, support of massive MIMO technology, spatial consistency and support of dual–mobility for D2D communications. Based on measurements and simulations, channel models accounting for different environment types such as dense urban, urban and rural, different link types including access, backhaul and D2D and propagation scenarios such as outdoor, indoor and O2I, were developed. The three proposed channel models were: a map–based model, a stochastic model and a hybrid model.

The map–based model is based on a simplified 3–D geometrical description of the environment and on ray–tracing simulations. The propagation paths are calculated deterministically thanks to the knowledge of the characteristics of the environment (building structures, scene models, etc.). The model takes into account main propagation mechanisms such as specular and diffuse reflection, refraction and diffraction. Such a model, set to be applicable up to 100 GHz, is intended for use cases such as massive MIMO where accuracy is paramount for effective beamforming implementations.

The stochastic model is an extension of the GSCM developed in WINNER II [60]. The propagation paths are determined fully stochastically from statistical distributions extracted from measurements. They must be generated for each user link depending on the user location. The model is applicable up to 70 GHz despite limited measurements at higher frequencies, especially above 6 GHz.

Finally, the hybrid model, a combination of the previous two, is obtained by utilizing deterministic environment features in the stochastic model and is applicable up to 70 GHz.

Specifically, the path–loss and shadowing parameters, obtained from the map–based model, are fed into the stochastic model in order to derive the hybrid one.

In comparison, the map–based model is thought to be more complete than the stochastic model, especially due to lack of sufficient measurement data with the latter. However, the complexity of the map–based model remains a concern. The hybrid model is, thus, viewed as a viable alternative.

2.2. MiWEBA channel model

MiWEBA (Millimeter–Wave Evolution for Backhaul and Access) was a project co–funded by the European Commission within the FP7, launched in June 2013. Its partners included Intel, Fraunhofer HHI, Orange, POLII, CEA–LETI, Osaka University, Tokyo Tech and KDDI R&D Laboratories. The project focused on the use of mm–Wave technology in order to overcome the spectrum shortfall and the system capacity shortage that are pending with the increase of the network mobile data traffic. There were seven WPs in MiWEBA. The channel modeling and characterization tasks were undertaken in WP5, interested in 60 GHz communications links.

The key 5G requirements identified in MiWEBA and laid out in [68] include spatial consistency, environment dynamics, support of dual–mobility and support of very large antenna arrays. Three different link types are studied in MiWEBA: access, backhaul/fronthaul and D2D. The considered propagation environments include open area, street canyon and hotel lobby. Based on experimental measurement results along with ray–tracing simulations, a quasi–deterministic 3–D channel model was developed at 60 GHz.

The quasi–deterministic approach consists of modeling the propagation channel with both quasi–deterministic strong rays and relatively weak random rays. The quasi–deterministic rays are specific to a given scenario and environment. In an open area, they consist of the LoS and ground–reflected paths. In a street canyon scenario, the reflected paths from the nearest walls shall be added. In indoor hotel lobby, all paths up to second order reflections are considered, similarly to the deterministic models developed in [66]. The random rays, stochastically generated, usually consist of second and/or higher order reflections. They model far–away reflections and are, thus, considered as secondary.

2.3. MmMAGIC channel model

Millimeter–Wave Based Mobile Radio Access Network for Fifth Generation Integrated Communications (mmMAGIC) was a project co–funded by the European Commission's 5G Public Private Partnership (PPP) program, launched in July 2015. The project participants included major infrastructure vendors (Samsung, Ericsson, Alcatel–Lucent, Huawei, Intel, and Nokia), major European operators (Orange, Telefonica), leading research institutes and universities (Fraunhofer HHI, CEA LETI, IMDEA Networks, Universities Aalto, Bristol, Chalmers and Dresden), measurement equipment vendors (Keysight Technologies, Rohde & Schwarz) and one SME (Qamcom). The project aimed at developing new concepts for mobile RAT at the mm–Wave frequency bands (6–100 GHz) for 5G. It was structured in six WPs. In WP2 led by Fraunhofer HHI, the focus was on channel measurement and modeling in the 6–100 GHz range. It should be noted that the studies carried out in this Ph.D. thesis have significantly contributed to the channel modeling work performed in the mmMAGIC project.

Similarly to METIS and MiWEBA, additional channel model requirements with regards to 5G were specified. Among these requirements, there are: support of massive MIMO, support of wider frequency range, spatial consistency, continuous variation over time, etc. In mmMAGIC final deliverable [69], envisioned propagation environments and scenarios for mmMAGIC channel models are discussed. They include UMi street canyon and open area, indoor office, shopping mall, airport, O2I, stadium and metro station. In this variety of scenarios, more than twenty measurements campaigns were carried out across eight frequency bands between 6 and 100 GHz. Based on the acquired measurement data and some input from ray–tracing simulations also validated by measurements, a GSCM was proposed.

The model is fully stochastic and the channel parameters are generated for each user link depending on the user location, similarly to WINNER GSCMs [60]. Novelties of the mmMAGIC channel model include incorporation of blockage effect, ground reflection, and extended O2I penetration losses (PELs) modeling. Such features have been adopted in the latest standardization activities led by 3GPP and ITU.

2.4. 3GPP channel models

The 3GPP technical specification group RAN (TSG RAN) has had a study item titled "Study on channel model for frequency spectrum above 6 GHz" covering channel modeling for frequencies up to 100 GHz. Based on measurement results mostly provided by partners of the aforementioned collaborative projects and some dedicated measurements as well, a stochastic 3GPP 3–D mm–Wave model [70], similar to WINNER models, was proposed in 2016. The model covers various scenarios such as UMi street canyon, UMa, RMa and indoor office. The features of the model include support of large bandwidth up to 10% of the center frequency but no larger than 2 GHz, mobility of one end of the link, spatial consistency, large antenna arrays and modeling of blockage and oxygen attenuation phenomena. In addition, similarly to METIS, a hybrid model based on the inclusion of deterministic environmental characteristics in the stochastic model was proposed as an alternative for more precision.

However, in [70], backwards compatibility with former 3GPP models specified in [64] and [62] was broken. Therefore, later on in 2017, a new 3GPP 3–D mm–Wave model [71], covers the frequency range between 0.5 and 100 GHz, was released.

2.5. Parallel channel modeling works

In 2014, the Fraunhofer HHI research institute also proposed a QUAsi Deterministic RadIo channel GenerAtor (QuaDRiGa) model, for MIMO modeling. The proposed 3–D GSCM [72] mainly included a collection of features from the SCM–E and from WINNER models as well. In the latest QuaDRIGa version, additional 5G features such as spatial consistency and support of mm–Wave frequencies, up to 100 GHz are added. The latter is essentially enabled by measurements performed in the mmMAGIC project. Furthermore, the model is compatible with the 3GPP 3–D mm–Wave model [71] and with the mmMAGIC channel model [69].

The New York University (NYU) Wireless research center has also been in interested in mm–Wave channel modeling. Based on extensive measurements conducted at 28, 38, 60 and 73 GHz in both outdoor and indoor scenarios, they have proposed a 3–D statistical spatial channel model (SSCM) [73] similar to the 3GPP 3–D model [64] but with some modifications. Their model extends the 3GPP model to mm–Wave frequencies and includes

features such as blockage modeling, standard definition of the propagation PL exponent (PLE) with a 1 m close–in reference distance, support of both omnidirectional and directional antennas and propagation channel representation with time clusters and spatial lobes.

3. Channel measurements for 5G mm–Wave

The channel modeling efforts performed in the collaborative projects discussed above have mainly been enabled by multiple measurement campaigns conducted by various research groups. In this section, the main findings from these measurement campaigns are discussed. More specifically, the frequency–dependence of the channel LSPs, in envisioned 5G propagation scenarios such as O2I and urban outdoor, is investigated.

First, a definition of the LSPs of interest is provided. Then, literature measurement results on the matter are presented. In O2I environments, building PELs caused by standard old buildings and energy–efficient (EE) modern buildings are mainly provided. Some results about the channel DS are also given. In urban outdoor environments, channel delay spread (DS) values and propagation PL modeling results are essentially documented. The channel azimuth spread (AS) parameter is also briefly discussed.

3.1. Channel large–scale parameters (LSPs) definition

Channel LSPs are derived from the channel complex impulse response (CIR). They are usually considered to describe the main characteristics of the radio propagation channel. In this section, we define some of these LSPs. They include the propagation PL, the channel DS and the channel AS.

Let us denote by $h(t,\tau,\varphi)$ the directional channel CIR, where t accounts for the temporal variability of the radio propagation environment, τ is a measure of the multi–path propagation delays and φ accounts for the angular properties of the propagation channel at the TX and/or RX end.

Let PDP denote the channel power delay profile (PDP) derived from the channel CIR as written in (**Eq. II.3.1**). Similarly, the power angular profile (PAP), denoted by PAP, is defined as shown in (**Eq. II.3.2**). The variable T is chosen such that the wide–sense

stationary uncorrelated scattering (WSSUS) properties [74] are fulfilled in this time interval.

$$PDP(\tau) = \int_{\varphi} \left(\frac{1}{T} \int_{(T)} \left| h(t, \tau, \varphi) \right|^2 \cdot dt \right) \cdot d\varphi \qquad \textbf{(Eq. II.3.1)}$$

$$PAP(\varphi) = \int_{\tau} \left(\frac{1}{T} \int_{(T)} \left| h(t, \tau, \varphi) \right|^2 \cdot dt \right) \cdot d\tau \qquad \textbf{(Eq. II.3.2)}$$

The propagation PL, denoted by $PL_{[dB]}$, accounts for the average signal attenuation between the TX antenna and the RX antenna. Its expression is given in (**Eq. II.3.3**).

$$PL_{[dB]} = -10 \cdot \log_{10} \left(\int_{\tau} PDP(\tau) \cdot d\tau \right) \qquad \textbf{(Eq. II.3.3)}$$

The channel DS, denoted by DS, is a measure of the signal dispersion in the temporal domain. It is defined as the standard deviation of the propagation delays τ, weighted by PDP. Its expression is given in (**Eq. II.3.4**).

$$DS = \sqrt{\frac{\int_{\tau} (\tau - \tau_m)^2 \cdot PDP(\tau) \cdot d\tau}{\int_{\tau} PDP(\tau) \cdot d\tau}}, \quad \tau_m = \frac{\int_{\tau} \tau \cdot PDP(\tau) \cdot d\tau}{\int_{\tau} PDP(\tau) \cdot d\tau} \qquad \textbf{(Eq. II.3.4)}$$

Similarly, the channel AS, denoted by AS, is a measure of the angular dispersion at the TX and/or RX. Its expression can be derived thanks to the relations given in (**Eq. II.3.5–II.3.6**) according to [57].

$$AS = \min_{\Delta} \left(\sqrt{\frac{\int_{\varphi} \varphi_{\mu,\Delta}^2 \cdot PAP(\varphi) \cdot d\varphi}{\int_{\varphi} PAP(\varphi) \cdot d\varphi}} \right) \qquad \textbf{(Eq. II.3.5)}$$

$$\varphi_{\mu,\Delta} = \begin{cases} 2\pi + \left(\varphi_\Delta - \mu_\varphi\right) & \text{if } \left(\varphi_\Delta - \mu_\varphi\right) < -\pi \\ \varphi_\Delta - \mu_\varphi & \text{if } \left|\varphi_\Delta - \mu_\varphi\right| \le \pi \\ 2\pi - \left(\varphi_\Delta - \mu_\varphi\right) & \text{if } \left(\varphi_\Delta - \mu_\varphi\right) > \pi \end{cases}, \quad \mu_\varphi = \frac{\int_\varphi \varphi \cdot PAP(\varphi) \cdot d\varphi}{\int_\varphi PAP(\varphi) \cdot d\varphi}, \quad \varphi_\Delta = \varphi + \Delta$$

(Eq. II.3.6)

For the channel DS or AS computation, a noise threshold, relative to the main path, must be applied on the PDP or PAP beforehand. Indeed, the channel DS or AS will increase as the threshold is larger. In fact, a low threshold value may downplay the significance of certain MPCs whereas a high threshold value takes into account more MPCs. However, this threshold remains upper–bounded by the PDP or PAP dynamic range. It is thus important to carefully set this value in order to avoid biases in the study of the channel DS and/or AS parameter. In the literature, the value of 20 dB is usually chosen.

3.2. Outdoor–to–indoor (O2I) propagation scenarios

In–building wireless communications account for a significant amount of mobile data traffic. Thus, radio propagation into buildings needs to be thoroughly investigated for 5G systems. Moreover, over the last few years, there has also been a growing interest in modern buildings. The window and wall material composition of these modern buildings is different from that of standard buildings or old buildings. Therefore, the frequency–dependence of the PELs caused by these types of buildings in O2I propagation scenarios is the main topic of discussion in this section. The channel DS is also evoked.

3.2.1. Penetration losses (PELs)

The PELs are usually computed as the difference between the propagation PL measured in the presence of obstacles and the measured (or theoretical) free–space PL. In **Annex A**, **Table A.1** describes multiple measurement campaigns conducted by different research groups with regards to the study of this parameter. For each of these campaigns, detailed measurement settings and parameters are provided in order to allow for a reasonable comparison across the different measurement campaigns. **Table II.3.1** below represents a summarized version of **Table A.1**, with the main measurement results and findings provided. Additionally, unless otherwise specified, the attenuation caused by the tested

material, rather than an average attenuation measured in a building room for e.g., is referred to as the PELs.

Table II.3.1 – Literature results on PELs in O2I scenarios

References	Frequency bands	Main measurement results
[75]	Frequency : **28 GHz**	↓ Clear glass (< 1.3 cm thick) : PELs = 3.6 – 3.9 dB ↓ Tinted glass (1.3 – 3.8 cm thick) : PELs = 24.5 – 40.1 dB
[76]	Frequency : **15 GHz** Bandwidth : 200 MHz	↓ 3–layered standard glass : PELs = 6 dB ↓ 3–layered IRR coated glass : PELs = 24 dB
[77]	Frequencies : **0.8 to 18 GHz** (Continuous sweep at 800 MHz and, from 2 to 18 GHz per 1 GHz step)	↓ 1–layered standard glass : PELs = 5.16 dB (on average) ↓ 2–layered EE glass : PELs = 24.86 – 28.43 dB (on average) ↓ 3–layered EE glass : PELs = 31.98 dB (on average)
[78]	Frequency : **28 GHz** Bandwidth : 50 MHz	↓ Standard glass : PELs = 3 – 5 dB ↓ Coated glass : PELs = 30 dB
[79]	Frequency : **10.1 GHz** Bandwidth : 500 MHz	↓ 2–layered standard glass PELs = 5 dB at 90° grazing angle PELs = 28 dB at 0° grazing angle
[80]	Frequencies : **0.8, 2.2, 4.7, 8.4, 26.3 and 37.0 GHz**	↓ Material composition not specified PELs = 6.8 dB at 0° incidence angle PELs = 21.9 dB at 90° incidence angle
[81]	Frequency **38 GHz** Bandwidth : 28 MHz	↓ 2–layered EE glass : PELs = 22 – 25 dB ↓ 3–layered EE glass : PELs = 35 – 40 dB
[82]	Frequencies : **9.6, 28.8 and 57.6 GHz** Sequence rate : 500 Mb/s	↓ Clear glass : PELs small at all frequencies ↓ Coated glass : PELs increase by 25 – 50 dB per layer of metal coating
[83]	Frequency : **73.5 GHz** Bandwidth : 1 GHz	↓ 1 cm thick clear glass windows and glass doors PELs = 7.1 and 5.1 dB resp.
[69]	Frequencies : **2, 6, 15 and 60 GHz** Bandwidth (in processing) : 80 MHz	↓ 3–layered pure glass (without metallization) PELs = 2, 0, 10 and 6 dB at 2, 6, 15 and 60 GHz resp.

References	Frequency bands	Main measurement results
[70]	Frequencies **from 6 to 100 GHz**	▪ Standard glass : PELs = 4 – 14 dB at 10 – 60 GHz ▪ Modern glass : PELs = 26 – 41 dB at 10 – 60 GHz

- **Material–dependence of the PELs**

The investigated literature summarized **Table II.3.1** for the frequency range from 0.8 to 73.5 GHz is unanimous about the material–dependence of the PELs. For instance, among all studies, there is a common agreement that modern buildings, often made of multi–layered glass materials with metal coating in order to allow for thermal insulation for e.g., result in higher PELs than standard buildings, mostly composed with single–layered glass materials. Specifically, it was found that infrared (IRR) coated or EE modern glass windows cause over 30 dB of PELs whereas standard old glass windows result in PELs of only around 5 dB [75], [76], [77], [78], [79], [81], [82], [83] and [69]. Furthermore, as shown in **Table A.1**, materials such as concrete and brick, which are usually found on building walls and facades, were shown to result in higher PELs (about 10 dB) compared to glass materials found in windows [75], [76] and [83] while wood materials were found to result in relatively low PELs, similar to those of glass materials [84]. In the cases where thick reinforced–concrete or brick walls were tested, significantly higher PELs (mostly above 30 dB) were recorded [77], [81], [82] and [83]. Thus, it is reasonable to assume that radio propagation into buildings mainly occurs through windows. Finally, studies in [84] and [76] reported human body PELs between 10 and 40 dB, depending on the distance between the obstacle and the RX unit (from 30 cm to 1 cm).

- **Frequency–dependence of the PELs**

Regarding the frequency–dependence, **Table II.3.1** shows that there is overall no trend that clearly characterizes the evolution of the PELs with regards to the frequency from the individual measurement campaigns, much less across these different campaigns reported herein, between 0.8 and 73.5 GHz. For window materials, the most dominant trend observed among the reported multi–frequency campaigns is the frequency–independence or irregular frequency–dependence of the PELs [77], [80], [82] and [69] although the 3GPP model [70] suggests an increasing tendency with increasing frequency, especially for coated

windows. However, as shown in **Table A.1**, the PELs caused by reinforced–concrete and/or brick walls, usually characterized by large thicknesses (at least an order of magnitude greater than that of glass materials), tend to rapidly increase with the frequency [77], [70]. Additionally, studies of the human body PELs conducted in [84] showed an increasing trend of the PELs with increasing frequency.

- **Incidence angle dependence of the PELs**

Moreover, studies in [79], [80] have shown that these PELs are also dependent on the incidence angle, as shown in **Table II.3.1**. It was observed that larger incidence angles, i.e. smaller grazing angles, result in greater building PELs.

3.2.2. Channel delay spread (DS)

The O2I channel DS in the mm–Wave frequency bands is hardly investigated in the literature. Studies in [85] have provided a summary of literature results on the matter as well as some specific measurement results but only in the lower frequency bands i.e. below 6 GHz. From their measurements performed at 3.6 GHz with a channel bandwidth of 250 MHz, the mean channel DS was found to be between 75 and 160 ns. In these measurements, the TX and RX antennas are placed at 21 and 1.5 m high respectively, with separation distances ranging from 200 to 300 m. Authors argued that such high values, in comparison to those observed in the literature, were due to the fact that other buildings were obstructing the LoS conditions between the TX and the building where the RX was located. In literature studies where the TX directly illuminates the building in most cases, the DS was often found to be below 40 ns in the frequency bands between 2.5 and 5.7 GHz with channel bandwidths ranging from 60 to 250 MHz.

High channel DS values are also observed in [86] where an O2I scenario is investigated at 6 GHz over a 100 MHz channel bandwidth. In these measurements, the TX antenna was set at 13.5 m high and the RX antenna was placed on a trolley located at different floors, with horizontal TX–RX separation distance of 28 m. In LoS conditions, DS values between 97.7 and 123.0 ns were measured while the NLoS conditions resulted in DS values between 380.2 and 549.5 ns. Additionally, higher DS values were recorded for lower RX heights in LoS while an opposite trend was observed in NLoS.

In the mm–Wave bands, studies in [69] at 2, 6, 15 and 60 GHz investigated the O2I channel DS parameter. Details about these measurements are given in **Table A.1** in **Annex A**. It was concluded that the channel DS increases with frequency from 50 to 100 ns with a channel bandwidth of 80 MHz. However, only a 10 dB threshold was used to compute the channel DS, which may explains such low values in comparison to those reported in [85] and [86].

3.3. Urban outdoor propagation scenarios

Urban outdoor environments, including UMi and UMa environments are also typical 5G deployment scenarios. In this section, the focus is mainly on the characterization of the access link in UMi environments i.e. the BS is placed on roof levels while the MS is kept at mobile user level. Nevertheless, some backhaul measurements as well as some measurements performed in UMa environments are included in the analysis. The frequency–dependence of essential channel LSPs such as DS, propagation PL and AS is discussed.

Additionally, on one hand, directional channel DS or PL will refer to channel parameters computed directly from directional measurements. These directional measurements are obtained by using directional antennas, especially on the RX side. On the other hand, omnidirectional channel DS or PL will refer to channel parameters computed from omnidirectional measurements. These omnidirectional measurements are either directly obtained thanks to omnidirectional antennas or synthesized from directional measurements through post–processing.

In omnidirectional measurements, the main reason for the use of directional antennas is to compensate for the increased attenuation observed at higher frequencies thanks to the antenna gain. Additionally, as directional antennas are expected to be used in future 5G mm–Wave systems, directional measurements are also important for a good understanding of the propagation channel directional characteristics.

3.3.1. Channel delay spread (DS)

Urban outdoor channel DS evaluations from different measurement campaigns are summarized in **Table II.3.2**. **Table A.2** given in **Annex A** provides more specific details on the measurement campaigns reported in **Table II.3.2**.

Table II.3.2 – Literature on channel DS in urban outdoor environments

References	Frequency bands	Main measurement results
[73]	Frequencies : **28, 38 and 73 GHz** Bandwidth : 800 MHz	**Directional DS** - LoS : virtually no DS (28 and 73 GHz) - NLoS : 90% DS < 50 ns (28 GHz), DS < 25 ns (in general at 73 GHz), 90% DS < 40 ns (38 GHz)
[87]	Frequencies : **71–76 and 81–86 GHz** Bandwidth : 5 GHz	**Directional DS** (LoS) - Street canyon : DS = 0.10 ns (on average) - Long street canyon : DS = 0.125 ns (on average)
[69]	Frequencies : **10, 28, 41 and 82 GHz** Bandwidth : 500 MHz	**Omnidirectional DS** (LoS) - 20 dB threshold : 90% DS < 40 ns at 10, 28 and 41 GHz - 15 dB threshold : lower DS at 82 GHz - 25 dB threshold : higher DS at 10 GHz
[88]	Frequency : **59 GHz** Bandwidth : 200 MHz	**Omnidirectional DS** - Empty street (no major reflectors) : 90 % DS < 20 ns - Parked bus in the street : 90% DS < 50 ns
[89]	Frequency : **59 GHz** Bandwidth : 200 MHz	**Omnidirectional DS** - City streets/ Road tunnel **[NTR.-94]** : 90% DS < 20 ns - City squares and parking garage : increased DS
[90]	Frequencies : **10 and 60 GHz** Bandwidth : 250 MHz	**Omnidirectional DS** - LoS : 90% DS < 35 ns (10 GHz), 90% DS < 25 ns (60 GHz) - NLoS : 90% DS < 65 ns (10 GHz), 90% DS < 45 ns (60 GHz)
[91]	Frequencies : **28 and 38 GHz** Bandwidth : 500 MHz	**Directional DS** - LoS : 90% DS < 30 ns - NLoS : 90% DS < 90 ns
[92]	Frequencies : **15, 28 and 60 GHz** Bandwidth : 0.5, 0.9 and 4 GHz at 15, 28 and 60 GHz resp.	**Omnidirectional DS** - LoS links : DS < 30 ns - Presence of major obstacles (15 and 60 GHz) : more DS than at 28 GHz than at 15 and 60 GHz

References	Frequency bands	Main measurement results
[69]	Frequencies : **15, 28 60 and 86 GHz** Bandwidth : 0.5, 0.9, 4 and 4 GHz at 15, 28, 60 and 86 GHz resp.	**Omnidirectional DS** Street canyon, LoS links, (on average): 15 GHz : DS = 15.1 ns, 28 GHz : DS = 14.3 ns 60 GHz : DS = 14.2 ns, 86 GHz : DS = 10.8 ns Open square (on average) 28 GHz : DS = 45.9 ns, 86 GHz : DS = 36.8 ns
[93]	Frequency : **60 GHz** Bandwidth : 1 GHz	**Directional DS** Strongest path : DS < 12 ns (LoS), DS < 22 ns (NLoS) Secondary paths : 90% DS < 12 ns (LoS), 90% DS < 20 ns (NLoS)
[94]	Frequency : **28 GHz** Bandwidth : 250 MHz	**Omnidirectional DS** NLoS (only 11 valid locations) DS < 100 ns (in general), DS = 22.29 ns (on average)
[95]	Frequency : **11 GHz** Bandwidth : 400 MHz	**Directional DS** UMa, UMi, street–cell : DS < 20 ns (on average) Smaller DS in street–cell than in UMi and UMa
[96]	Frequency **: 3–18 GHz** (per step of 500 MHz) Bandwidth : 1 GHz	**Omnidirectional DS** LoS : DS < 50 ns (UMa), DS < 30 ns (UMi) DS decreases from 3 to 18 GHz NLoS : DS < 300 ns (UMa), DS < 125 ns (UMi) DS ≈ the same from 3 to 18 GHz
[97]	Frequency : **28 GHz** Sequence rate : 250 Mcps	**Omnidirectional DS** NLoS (38 valid locations) DS < 200 ns (in general), 55.43 ns (on average)
[69]	Frequency : **2, 15 and 60 GHz** Bandwidth : 80 MHz	**Omnidirectional DS** LoS (2, 15 and 60 GHz) : DS = 20 – 50 ns NLoS (2, 15 and 60 GHz) : DS = 75 – 200 ns
[98]	Frequency : **28 GHz** Bandwidth : 400 MHz	**Directional DS** LoS : DS = 29.51 ns (on average) NLoS : DS = 37.15 ns (on average)

References	Frequency bands	Main measurement results
[99]	Frequency : **60 GHz** Bandwidth : 2.2 GHz	**Directional DS** (LoS) - 50% percentile DS ≈ 20 ns - 90% percentile DS > 50 ns

Rather than comparing the specific DS values from the different measurement campaigns given in **Table II.3.2**, it is preferable to discuss the different trends that are observed because the channel DS is extremely sensitive to specific parameters such as the measurement bandwidth and threshold value among others. Nevertheless, it can be noted that the NLoS DS values are greater than the LoS DS values and that directional DS values reported in [73], [87], [91], [93], [95], [98], [99] are, in general, smaller than omnidirectional DS values reported in [69], [88], [89], [90], [92], [94], [96], [97]. Additionally, almost all reported DS values, in the frequency range between 2 and 86 GHz with channel bandwidth ranging from 80 MHz to 5 GHz, are below 150 ns in UMi environments, with ranges up to about 300 m.

- **Frequency–dependence of the channel DS**

From the investigated literature, there is no definite consensus on the frequency–dependence of the channel DS in the frequency range from 2 to 86 GHz, as shown in **Table II.3.2**. The vast majority of the encountered (multi–frequency) studies have either claimed that the channel DS is frequency–independent [87], [91], [69] or argued in favor of a decreasing behavior of the channel DS with increasing frequency [73], [90], [69]. In the latter case, the decrease was usually found to be relatively small. For instance, studies in [69] reported a decrease of the channel DS at 82 GHz (with a relatively low threshold value of 15 dB) compared to lower frequency bands such as 10, 28 and 42 GHz where a frequency–independence of the channel DS is claimed. In [96], it was found out the LoS channel DS decreases with increasing frequency while the NLoS channel DS is frequency–independent.

This frequency–dependence of the channel DS is an issue that has also been subject of intense discussions within the mmMAGIC project to which studies conducted herein have contributed. In a landmark paper [100], the frequency–dependence of the channel DS was

analyzed, based on measurement campaigns conducted within the project. It was mainly concluded that the frequency–dependence of the channel DS is, if at all, very small.

- **Environment–dependence of the channel DS**

The studies reported in **Table II.3.2** have also shown that the channel DS is strongly dependent on the environment, specifically on the nature and density of scattering elements that are present in the environment. For instance, the DS values measured in environments like street canyons are smaller than those measured in open square environments, as underlined in [89]. The large dimensions of typical open square areas in comparison to the narrow width street canyons are thought to be the main reason for this observation. Furthermore, studies in [73] concluded that highly dense environments such as downtown Manhattan result in greater channel DS than less urban environments like UTA campus in Austin since the formers tend to be more reflective. However, in [92] and [88], larger channel DS values are observed with fewer number of blocking elements in street canyon–like environments. The authors conjecture that, perhaps, less multi–path blockage occurred in such cases. Finally, authors in [96] concluded that the DS values increase with BS heights (in the UMi scenarios) and that they are also greater in UMa environments compared to UMi environments since far–away obstacles are more likely to be illuminated with higher BSs.

- **Distance–dependence of the channel DS**

On the distance–dependence, some studies reported in **Table II.3.2** have found some correlation between the channel DS and TX–RX distance. In street canyon scenarios for e.g., the channel DS is observed to increase with the link distance in [87], [69], and [90] whereas results in [92] and [93] pointed out an opposite trend. In [73], it was concluded that channel DS slightly decreases with increasing distance, more rapidly in less reflective environments like Austin than in downtown Manhattan.

3.3.2. Propagation path–loss (PL)

The propagation PL, denoted by $PL_{[dB]}$, has been evaluated in numerous mm–Wave channel measurement campaigns. The major tendencies observed in such studies are discussed.

The most commonly used propagation PL models are the alpha–beta–gamma (ABG) model and the close–in (CI) free–space reference distance model.

The ABG model, shown in (**Eq. II.3.7**), is essentially characterized by three parameters, α, β and γ. The parameters α and β respectively denote the slope and the intercept of a least–square linear regression best line fit to the measurements. The additional parameter γ accounts for the different offsets estimated in different frequency bands.

$$PL_{[dB]} = \beta_{[dB]} + 10 \cdot \gamma \cdot \log_{10}\left(f / 1\,Hz\right) + 10 \cdot \alpha \cdot \log_{10}\left(d / 1\,m\right) + \chi_\sigma \qquad \textbf{(Eq. II.3.7)}$$

In the CI model shown in (**Eq. II.3.8**), an arbitrary free–space reference distance, denoted by d_0, is first chosen to compute the free–space reference PL. Then, the PLE, denoted by n, is derived using minimum mean square error estimate to best fit the measurements.

$$PL_{[dB]} = 20 \cdot \log_{10}\left(4\pi f d_0 / c\right) + 10 \cdot n \cdot \log_{10}\left(d / d_0\right) + \chi_\sigma \qquad \textbf{(Eq. II.3.8)}$$

f and d resectively denote the frequency and the distance while c is the speed of light.

χ_σ is a zero mean Gaussian random variable with a standard deviation of σ, also called the shadow factor.

It is important to note that the ABG slope α does not automatically equate to the PLE n in the CI model. It simply serves as the best fit for the measurement data in order to minimize the shadow factor σ. Thus, it would be ill–advised to directly compare these two parameters.

Note that most of the measurements campaigns discussed herein are reported in **Table II.3.2** and described in detail in **Table A.2**.

- **Path–loss in LoS conditions**

In LoS conditions, for both omnidirectional and directional PL models, the PLE n estimated in [73], [101], [84], [91], [90], [92], [102], [96] and the slope α estimated [91], [103], [104] are often found to be very close to 2 (between 1.8 and 2.2) in the frequency range from 3 to 73 GHz. In [84] and [92], it is argued that constructive and/or destructive

interferences between the main LoS path and other incoming MPCs are the reason for observing these slight differences. UMi access scenarios were mainly investigated in these studies. Studies in [73] and [92] are the ones that investigated backhaul scenarios and measurements in UMa environments were performed in [104] and [96].

Nevertheless, studies in [95] reported, for the PLE n, values between 1.2 (BS near MS) and 2.7 (BS far from MS) in UMi environments and about 2.7 in UMa environments. These results were observed from 11 GHz measurements where dual polarized 12–element uniform circular arrays were used. The PL was calculated with polarimetric beamforming at both the BS and the MS. It was argued that the direct and ground reflected waves were dominant. Their constructive or destructive reconstructions may, therefore, explain such differences.

Furthermore, studies in [93] also found the slope α to be equal to 3.7 at 60 GHz in measurements where directional steering antennas were used. Similarly, authors in [73] indicated, for the slope α, values between 1.5 and 2.9 at 28 and 38 GHz, and even negative values (around –1.2) at 73 GHz. They argued that such inconsistent values of α can be explained with the lack of physical basis of the ABG model.

- **Path–loss in NLoS conditions**

In NLoS conditions, for both directional and omnidirectional PL models, the PLE n estimated in [73], [91], [90], [94], [102], [97], [96] and the slope α given in [91], [103], [104] and [97] are usually greater than 2, up to almost 5, in the frequency range between 3 and 73 GHz. However, directional PL models resulted in slightly higher values of n or α than omnidirectional PL models as noted in [73].

As it was the case in the LoS conditions, studies in [93] reported significantly higher value of α, reaching 7.5 at 60 GHz with the use of directional steering antennas whereas studies in [73] also found very volatile values of α, between 0.1 and 4.7, for both directional and omnidirectional PL models. The lack of physical basis of the ABG model was, once more, thought to be the reason for these observations.

- **Frequency–dependence of the PL**

In general, in both LoS and NLoS conditions, no frequency–dependence of the PLE n derived from the CI model or the slope α derived from the ABG model is observed in the studies reported herein. However, in [96], PL model parameters extracted by dividing the 3–18 GHz wideband channel response into 15 non–overlapping 1 GHz–bandwidth subbands displayed some frequency–dependence. Important variations of the PLE n, between 1 and 3 in LoS and between 2 and 5 in NLoS, were observed over the subbands in both the UMi and UMa environments. Since these measurements were performed using isotropic antennas in azimuth but with the elevation half–power beam–width (HPBW) varying from 65 to 45° in the frequency range from 3 to 18 GHz, it was conjectured that such differences in the elevation pattern of the antennas could partly explain these variations in the PLE n.

- **Impact of antenna height and environment on the PL**

Among all studies where different BS antenna heights are considered, no significant variations of the PL depending on the BS antenna height, is noted in LoS conditions [73], [103], [104], and [96]. In NLoS conditions, the PL decreases with increasing BS height according to results in [73], [103], and [104]. However, the UMi NLoS studies in [96] show an increasing tendency of the PLE with increasing BS height. They also conclude the values of the PLE values in UMa environments are larger than those in UMi environments. Additionally, the environment–dependence has been emphasized in studies reported in [73]. In less cluttered environments, it is observed that the PLE tends to be smaller in comparison to the values recorded in ultra–dense environments. As a result, the PLE values from the 28 GHz measurements performed in downtown Manhattan were greater than those from the 38 GHz measurements conducted at the UTA campus in Austin.

3.3.3. Channel azimuth spread (AS)

The channel AS (at the RX unit) in urban environments has been discussed in [94], [97], [92], [91], [105] and [106] and the derived results are summarized in **Table II.3.3**.

Table II.3.3 – Literature results on channel AS in urban outdoor environments

References	Frequency bands	RX antenna	RX Azimuth Spread (AS)
[94]	Frequency : **28 GHz** Bandwidth : 250 MHz	24.5 dBi gain 10° HPBW	NLoS (only 11 valid locations) AS < 70°, mean AS = 25.16°
[97]	Frequency : **28 GHz** Sequence rate : 250 Mcps	24.5 dBi gain 10° HPBW	NLoS (38 valid locations) AS < 70°, mean AS = 31.39°
[92]	Frequencies : **15, 28 and 60 GHz** Bandwidth : 0.5, 0.9 and 4 GHz at 15, 28 and 60 GHz resp.	19 dBi gain 10° azimuth HPBW 40° elevation HPBW	LoS links AS < 25° (mostly) AS decreases with increasing distance
[91]	Frequencies : **28 and 38 GHz** Bandwidth : 500 MHz	15.4–16.4 dBi gain 30° HPBW	LoS : 90% AS < 45° NLoS : 90% AS < 75°
[105]	Frequency : **28 GHz** Bandwidth : 400 MHz	25 dBi gain 11° azimuth HPBW 10° elevation HPBW	LoS : mean AS = 14.13° NLoS : mean AS = 29.51°
[106]	Frequency : **28 GHz** Bandwidth : 800 MHz	Directional horn antenna	LoS : AS = 30.2° NLoS : AS = 51.2°

In the frequency bands between 15 and 60 GHz, with ranges up to 200 m, the reported AS values are all below 75°. The antenna azimuth HPBW used in these studies are mostly 10°, except for studies in [91] where a 30° azimuth HPBW RX antenna was used. The NLoS conditions resulted in greater AS than the LoS conditions [91], [105], and [106]. However, no frequency–dependence was noted in the multi–frequency results provided reported in [92].

4. Motivations for further studies

Literature studies discussed above show the tremendous efforts put into mm–Wave channel characterization for upcoming 5G systems. Specifically, it is shown that channel LSPs have been investigated at different frequency bands, from below 6 GHz up to 100 GHz, in scenarios such as O2I and urban outdoor environments.

However, the lack of sufficient measurement data to allow for full comparisons of these LSPs across the entire frequency range targeted in 5G channel modeling is identified as a major limitation with regards to these studies. Most measurement campaigns are performed in specific frequency bands between 6 and 100 GHz and comparisons of propagation channel parameters derived from different measurement campaigns is inconvenient for many reasons including differences with regards to: the hardware equipments (antennas, sounding system, etc.) used to perform measurements, the measurement parameters such as channel bandwidth, the data processing and the sounded environments in the different measurement campaigns.

It has therefore been our objective, in our studies presented in **Chapter IV–V**, to revisit these channel LSPs through multi–frequency measurement campaigns between 3 and 60 GHz. We thus intend to ensure full comparability of the derived channel parameters across multiple frequency bands, from below 6 GHz up to the mm–Wave frequencies.

Prior to our experimental studies in **Chapter IV–V**, a theoretical analysis of main radio propagation phenomena is first provided in **Chapter III** in order to get a better understanding of the multi–path radio propagation channel and its frequency–dependence.

Chapter III

III. Theoretical Characterization of the Wireless Propagation Channel

In this chapter, the frequency–dependence of the radio propagation channel characteristics is discussed, from a theoretical stand point. The channel modeling framework used by standard bodies such as the 3GPP and ITU is considered as a baseline for these theoretical studies. This framework utilizes a geometrical approach in order to characterize the multi–path radio propagation channel. It is presented in **Section 1**. In **Section 2**, a deeper analysis of the geometric model components is performed. The main radio propagation phenomena accounted for in the geometrical modeling approach are characterized and their frequency–dependence, investigated. They include free–space phenomenon tackled in **Section 2.1**, reflection and transmission phenomena discussed in **Section 2.2** and diffraction phenomenon investigated in **Section 2.3**. Finally, in **Section 3**, the limitations regarding this theoretical approach are discussed and the necessity for experimental studies is highlighted.

1. Geometrical modeling approach

The multi–path radio propagation channel is first described in this section. Then, the geometrical modeling approach is discussed.

1.1. Multi–path radio propagation channel

In wireless communications systems, the radio propagation channel is described as the physical link between the TX antenna and the RX antenna i.e. the surrounding environment. The signal recorded at the RX antenna is usually a combination of multiple replicas of the signal transmitted from the TX antenna, as a result of interactions between the radio signal and the propagation environment. These interactions are generally modeled

with propagation phenomena such as reflection, transmission, diffraction or scattering, as illustrated in **Fig. III.1.1**. The radio propagation channel is thus referred to as a multi–path propagation channel.

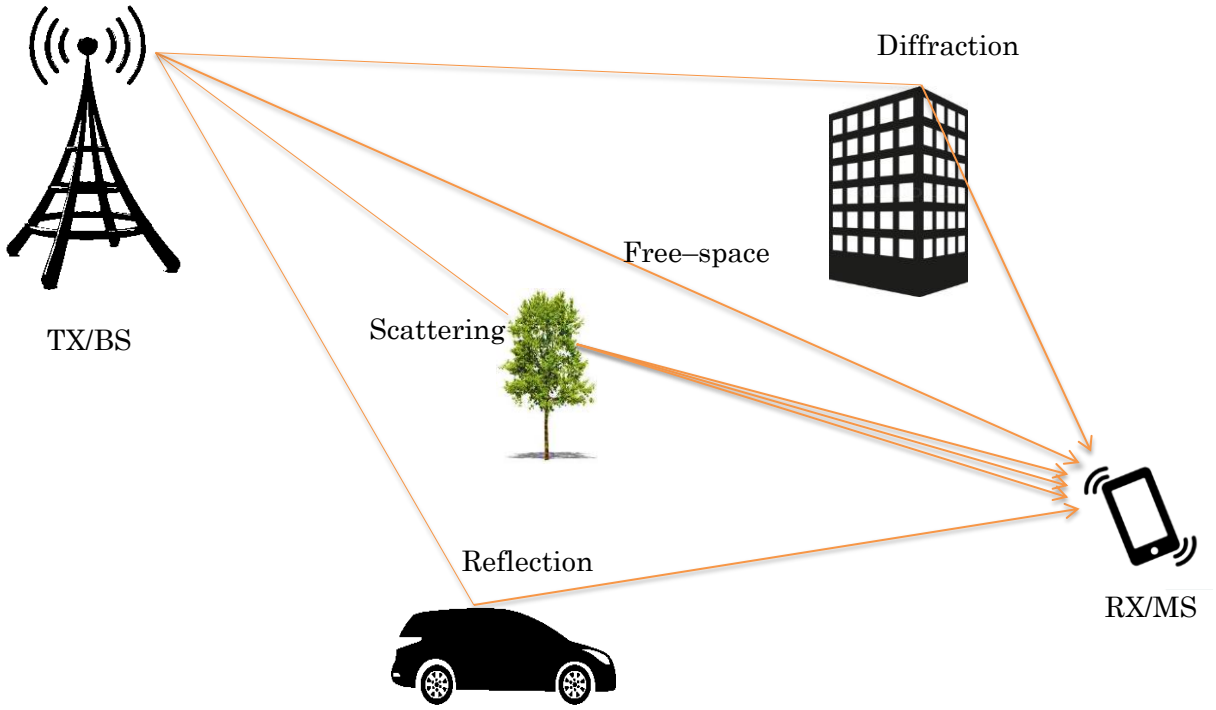

Fig. III.1.1 – Multi–path radio propagation channel

1.2. Geometric channel model

The multi–path radio propagation channel can be represented in the delay domain by its CIR, denoted by $h(t,\tau)$, which accounts for the physical effects of the environment. The parameter t accounts for the temporal variability of the radio propagation environment while the parameter τ is a measure of the multi–path propagation delays. Let $x(t)$ and $y(t)$ denote the electric signals at the TX antenna input and RX antenna output respectively. The impact of the propagation channel is often modeled with a time–variant linear system, under the WSSUS assumptions [74], as shown in (**Eq. III.1.1**).

$$y(t) = \int_{-\infty}^{\infty} h(t,\tau) \cdot x(t-\tau) \cdot d\tau \qquad \textbf{(Eq. III.1.1)}$$

The channel CIR $h(t,\tau)$ not only depends on the radio propagation environment but also on other parameters such as the TX and RX antenna field patterns or the channel bandwidth. The geometrical modeling approach enables separation between radio propagation characteristics and such parameters. In this approach, the MPCs of the radio propagation channel are modeled with a finite number, say N, of rays considered as plane waves under the far–field assumptions. Thus, each ray n is essentially described by its specific attenuation coefficient H_n, its propagation delay τ_n and its angular characteristics $(\theta_{n,ZOD}, \phi_{n,AOD}, \theta_{n,ZOA}, \phi_{n,AOA})$. $\theta_{n,ZOD}$, $\phi_{n,AOD}$, $\theta_{n,ZOA}$ and $\phi_{n,AOA}$ respectively denote the elevation departure, azimuth departure, elevation arrival and azimuth arrival angles of ray n, expressed in the spherical coordinate system (θ,ϕ) shown in **Fig. III.1.2**.

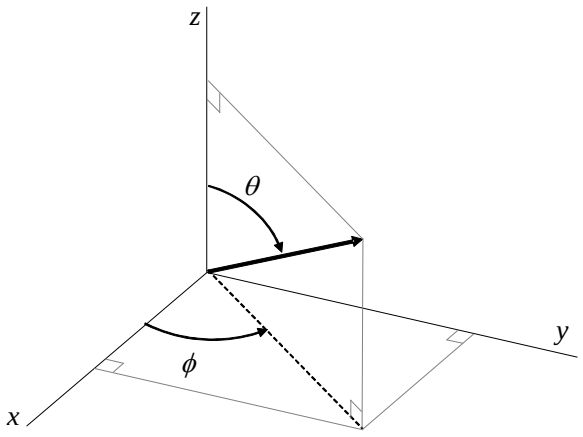

Fig. III.1.2 – Spherical coordinate system

The antenna field patterns in the direction of these angular coordinates (θ,ϕ), denoted by $(F_{TX}^{\theta}, F_{TX}^{\phi})$ on the TX side and $(F_{RX}^{\theta}, F_{RX}^{\phi})$ on the RX side, are subsequently inserted in the model description. The contributions of the rays are then summed in order to derive the geometric CIR, as shown in (**Eq. III.1.2**). v_n is the Doppler frequency component of ray n.

$$h(t,\tau)=\sum_{n=1}^{N}\begin{pmatrix} F_{RX}^{\theta}\left(\theta_{n,ZOA},\phi_{n\,AOA}\right) \\ F_{RX}^{\phi}\left(\theta_{n,AOD},\phi_{n\,AOA}\right)\end{pmatrix}^{T}\cdot H_n\cdot\begin{pmatrix} F_{TX}^{\theta}\left(\theta_{n,ZOD},\phi_{n,AOD}\right) \\ F_{TX}^{\phi}\left(\theta_{n,ZOD},\phi_{n\,AOD}\right)\end{pmatrix}\cdot\delta(\tau-\tau_n)\cdot\exp(j2\pi v_n\cdot t)$$

(Eq. III.1.2)

When polarization is considered, the attenuation coefficient H_n is a 2x2 matrix composed with four complex coefficients $\alpha_n^{\theta\theta}$, $\alpha_n^{\theta\phi}$, $\alpha_n^{\phi\theta}$ and $\alpha_n^{\phi\phi}$ for the polarization combinations $\theta\theta$, $\theta\phi$, $\phi\theta$ and $\phi\phi$ respectively, as written in (**Eq. III.1.3**).

$$H_n = \begin{pmatrix} \alpha_n^{\theta\theta} & \alpha_n^{\theta\phi} \\ \alpha_n^{\phi\theta} & \alpha_n^{\phi\phi} \end{pmatrix} \qquad \text{(Eq. III.1.3)}$$

2. Frequency–dependence of the propagation channel

In the geometric channel model, the polarimetric matrix H_n defined in (**Eq. III.1.3**) accounts for the radio propagation channel effects i.e. the overall attenuation and phase shift, undergone by ray n. In this sense, it encompasses propagation phenomena such as free–space, reflection, transmission, diffraction and scattering among others. Therefore, this matrix can be modeled thanks to the expression written in (**Eq. III.2.1**).

$$H_n = \begin{pmatrix} \alpha_n^{\theta\theta} & \alpha_n^{\theta\phi} \\ \alpha_n^{\phi\theta} & \alpha_n^{\phi\phi} \end{pmatrix} = \frac{1}{\sqrt{PL_{FS,n}}} \cdot \prod_q \left(\beta_q^A\right) \cdot A_{n,q} \cdot \left(\beta_q^D\right) \qquad \text{(Eq. III.2.1)}$$

where the scalar $PL_{FS,n}$ accounts for the free–space phenomenon experienced by ray n and the coefficient $A_{n,q}$ is a 2x2 matrix associated with the q^{th} propagation phenomenon undergone by ray n, besides free–space. $\left(\beta_q^D\right)$ and $\left(\beta_q^A\right)$ are transformation matrices that allow transfers from the spherical basis (θ, ϕ) to a local basis (V, H) specific to each interaction and from that local basis to the spherical basis respectively.

The study of the radio propagation channel frequency–dependence can therefore be reduced to the investigation of $PL_{FS,n}$ and $A_{n,q}$, associated with each ray n. Regarding $A_{n,q}$, only the reflection, transmission and diffraction phenomena are addressed in herein.

2.1. Free–space phenomenon

2.1.1. Friis formula

As radio signals travel through a wireless channel, in free–space conditions, they experience a power decay that is inversely proportional to the square of the travelled distance. This behavior is modeled thanks to Friis' free–space law, independently of polarization, as written in (**Eq. III.2.2**).

$$P_{RX} = P_{TX} \cdot G_{TX} \cdot G_{RX} \cdot \left(\frac{c}{4\pi fd} \right)^2 \qquad \textbf{(Eq. III.2.2)}$$

Where P_{TX} and P_{RX} are the TX and RX power respectively. G_{TX} and G_{RX} are the TX and RX antenna gains respectively. c is the speed of light, f is the frequency and d, the TX–RX separation distance. The free–space attenuation coefficient also known as free–space PL, denoted by PL_{FS}, is defined as the ratio between the TX and RX power assuming isotropic antennas at both the TX and RX ends (**Eq. III.2.3**).

$$PL_{FS}(d) = \left(\frac{4\pi fd}{c} \right)^2 \qquad \textbf{(Eq. III.2.3)}$$

It is important to note that this relation is only valid under the far–field conditions where the propagating ray acts as a plane wave, as hypothesized in the geometric model.

Therefore, denoting by d_n the total distance travelled by ray n between TX and RX, $PL_{FS,n}$ is given as shown in (**Eq. III.2.4**).

$$PL_{FS,n} = PL_{FS}(d_n) \qquad \textbf{(Eq. III.2.4)}$$

2.1.2. Frequency–dependence

The frequency–dependence of PL_{FS} is straigthforward. It can be analitycally shown from its definition in (**Eq. III.2.3**) that $PL_{FS[dB]}$ is proportional to $\left(20 \cdot \log_{10}(f)\right)$. **Fig. III.2.1** provides a visual representation of this behavior with the distance d set to 50 m.

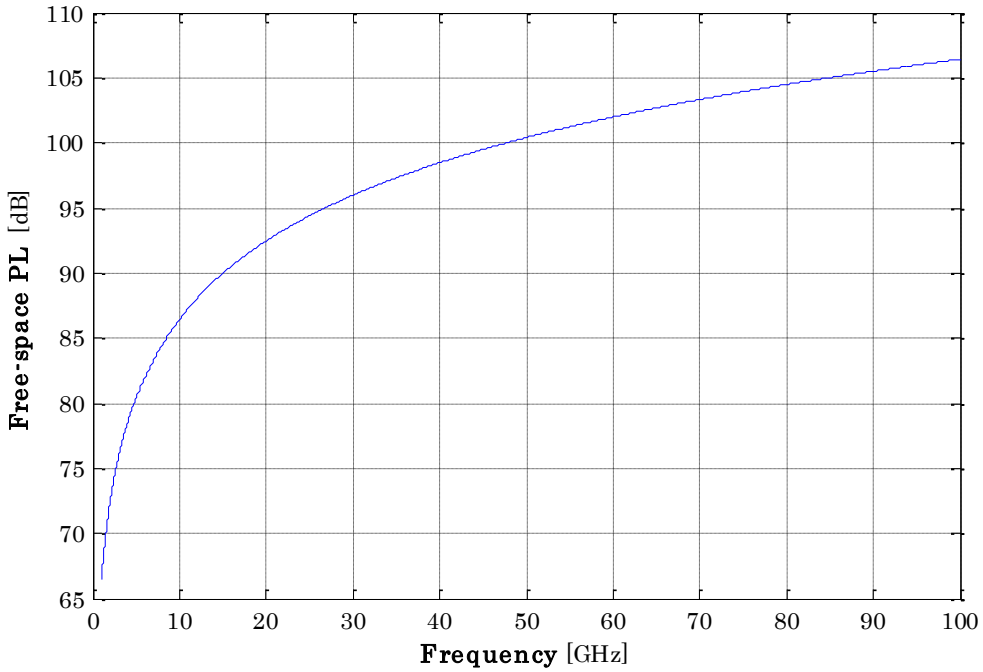

Fig. III.2.1 – Free–space PL vs frequency

2.2. Reflection and transmission phenomena

Reflection occurs when an incident ray impinges on surfaces whose dimensions are greater than the wavelength of the propagating ray. The reflected ray propagates in the same medium as the incident ray. In the case of perfectly plane and homogenous surfaces such as ground, building facades, etc., the characteristics of the reflected ray can be determined as function of those of the incident ray thanks to Fresnel coefficients, assuming plane wave propagation.

Transmission is the phenomenon by which a portion of an incident ray passes through an obstacle instead of being reflected back in the same medium. Thus, the transmitted ray propagates in a medium different from that of the incident and reflected rays. Its characteristics can be determined, as function of those of the incident ray, thanks to Fresnel coefficients, assuming plane wave propagation.

The expressions of the reflected and transmitted rays as functions of the incident ray by means of Fresnel coefficients fall into the field of Geometrical Optics (GO). Below, we first describe these coefficients for the simple case of the interaction between a ray and a single

interface. Then, the case of interactions with more complex structures such as multi–layered glass materials is characterized.

2.2.1. Fresnel coefficients for a single interface: Definition

Let us consider two media, say M_1 and M_2, separated by an interface and an incoming ray, propagating in M_1, arriving on the interface as illustrated in **Fig. III.2.2**. At the interface, the GO theory predicts that a portion of the ray is sent back into the medium M_1 in accordance with the reflection phenomenon whereas another portion of the incident ray passes through the interface, into the medium M_2, by virtue of the transmission phenomenon.

Let $\left(E_i^V, E_i^H\right)^T$ be the electric field vector which characterizes the incident ray, expressed in the local basis (V, H). In this same local basis, we denote by $\left(E_r^V, E_r^H\right)^T$ and $\left(E_t^V, E_t^H\right)^T$ the electric field vectors which characterize the reflected and transmitted rays respectively. $\vec{k}_i$, $\vec{k}_r$ and $\vec{k}_t$ denote the propagation vectors of the incident, reflected and transmitted rays respectively.

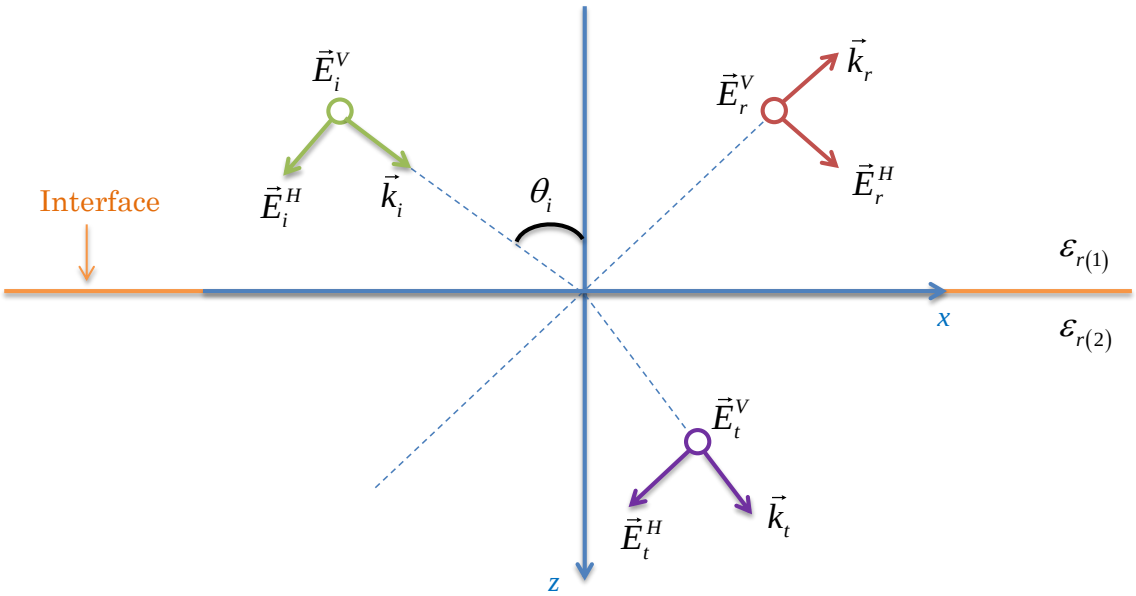

Fig. III.2.2 – Interaction between a ray and an interface

Since the GO theory describes reflection and transmission as local phenomena [107], the reflection and transmission coefficients, respectively denoted by R and T, are defined as written in (**Eq. III.2.5–III.2.6**). R and T are dyadic matrices (**Eq. III.2.7–III.2.8**) the expressions of which are given thanks to the Fresnel relations (**Eq. III.2.9–III.2.10**).

$$\begin{pmatrix} E_r^V \\ E_r^H \end{pmatrix} = R \cdot \begin{pmatrix} E_i^V \\ E_i^H \end{pmatrix} \quad \textbf{(Eq. III.2.5)}; \qquad \begin{pmatrix} E_t^V \\ E_t^H \end{pmatrix} = T \cdot \begin{pmatrix} E_i^V \\ E_i^H \end{pmatrix} \quad \textbf{(Eq. III.2.6)}$$

$$R = \begin{pmatrix} r^V & 0 \\ 0 & r^H \end{pmatrix} \quad \textbf{(Eq. III.2.7)}; \qquad T = \begin{pmatrix} t^V & 0 \\ 0 & t^H \end{pmatrix} \quad \textbf{(Eq. III.2.8)}$$

$$r^V = \frac{\sqrt{\varepsilon_{r(1)}}\cos(\theta_i) - \sqrt{\varepsilon_{r(2)} - \varepsilon_{r(1)}\sin^2(\theta_i)}}{\sqrt{\varepsilon_{r(1)}}\cos(\theta_i) + \sqrt{\varepsilon_{r(2)} - \varepsilon_{r(1)}\sin^2(\theta_i)}}; \quad r^H = \frac{\varepsilon_{r(2)}\cos(\theta_i) - \sqrt{\varepsilon_{r(1)}}\sqrt{\varepsilon_{r(2)} - \varepsilon_{r(1)}\sin^2(\theta_i)}}{\varepsilon_{r(2)}\cos(\theta_i) + \sqrt{\varepsilon_{r(1)}}\sqrt{\varepsilon_{r(2)} - \varepsilon_{r(1)}\sin^2(\theta_i)}}$$

(Eq. III.2.9)

$$t^V = \frac{2 \cdot \sqrt{\varepsilon_{r(1)}}\cos(\theta_i)}{\sqrt{\varepsilon_{r(1)}}\cos(\theta_i) + \sqrt{\varepsilon_{r(2)} - \varepsilon_{r(1)}\sin^2(\theta_i)}}; \quad t^H = \frac{2 \cdot \sqrt{\varepsilon_{r(1)}}\sqrt{\varepsilon_{r(2)}}\cos(\theta_i)}{\varepsilon_{r(2)}\cos(\theta_i) + \sqrt{\varepsilon_{r(1)}}\sqrt{\varepsilon_{r(2)} - \varepsilon_{r(1)}\sin^2(\theta_i)}}$$

(Eq. III.2.10)

θ_i is the incident angle i.e. is the angle formed by the incident ray and the vector that is normal to the reflecting surface. $\varepsilon_{r(1)}$ and $\varepsilon_{r(2)}$ denote the complex relative permittivities of media M_1 and M_2 respectively.

The coefficient $A_{n,q}$ is thus given by the relations written in (**Eq. III.2.11**).

$$A_{n,q} = \begin{cases} R, \text{ if the } q^{th} \text{ propagation phenomenon undergone by ray } n \text{ is a reflection} \\ T, \text{ if the } q^{th} \text{ propagation phenomenon undergone by ray } n \text{ is a transmission} \end{cases} \quad \textbf{(Eq. III.2.11)}$$

In **Fig. III.2.3** and **Fig. III.2.4**, plotted are the Fresnel reflection and transmission coefficients as function of the incidence angle for the example of a single "air/glass" interface. The relative permittivity of medium M_1 is that of air, i.e. $\varepsilon_{r(1)} = 1$, while the

relative permittivity of medium M_2, composed with glass, is set to $\varepsilon_{r(2)} = 2$ at 10 GHz according to [108].

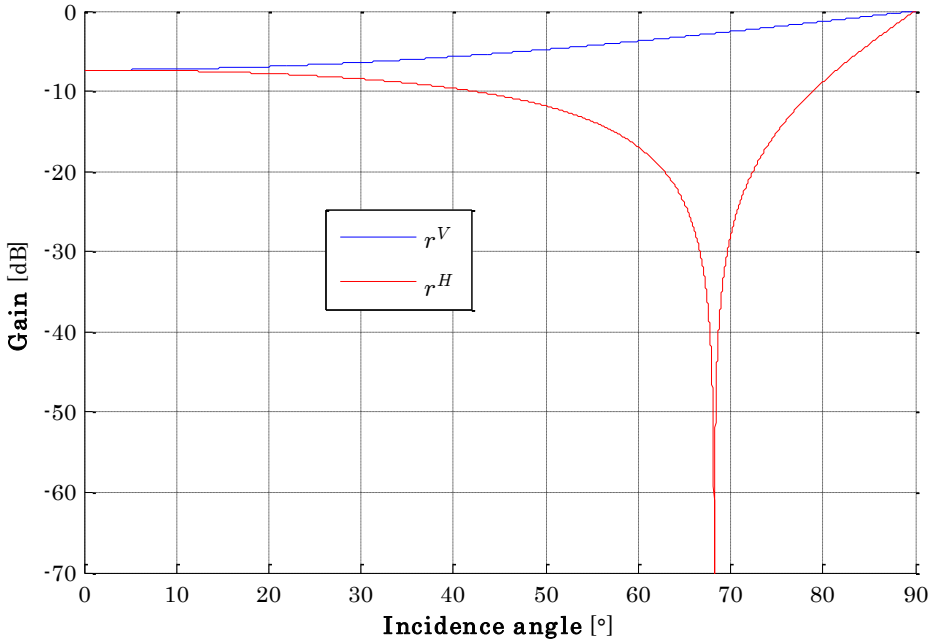

Fig. III.2.3 – Fresnel reflection coefficients vs incidence angle

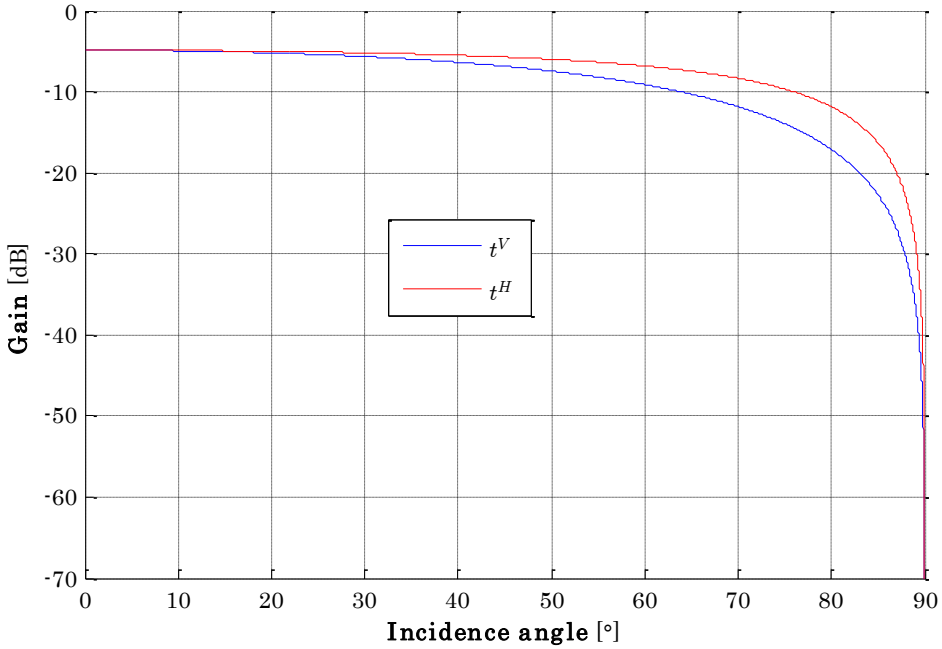

Fig. III.2.4 – Fresnel transmission coefficients vs incidence angle

2.2.2. Fresnel coefficients for a single interface: Frequency–dependence

At first glance, the Fresnel coefficients for a single interface separating two media M_1 and M_2, as written in (**Eq. III.2.9–III.2.10**), do not directly depend on the frequency. However, the complex relative permittivities $\varepsilon_{r(1)}$ and $\varepsilon_{r(2)}$ of the two media M_1 and M_2 respectively may display a frequency–dependence as suggested in [108]. The authors in [108] proposed the approach written in (**Eq. III.2.12**) for modeling the frequency–dependent relative permittivities. This model was developped based on literature data sets in the frequency range between 1 and 100 GHz. The model parameters, for the materials of interest in our studies, are summarized in **Table III.2.1**. These materials include glass, concrete and metal.

$$\varepsilon_{r(1,2)} = a \cdot f^{\,b} + j \cdot 17.98 \frac{c \cdot f^{\,d}}{f}, \quad \left(f_{[GHz]} \in [1,100] \right) \quad \textbf{(Eq. III.2.12)}$$

Table III.2.1 – ITU model parameters for relative permittivities

ITU–R parameters	a	b	c	d
Air	1	0	0	0
Glass	6.27	0	0.0043	1.1925
Concrete	5.31	0	0.0326	0.8095
Metal	1	0	10^7	0

Therefore, taking into account these frequency–dependent material properties, the Fresnel reflection and transmission coefficients, for "air/glass", "air/concrete" and "air/metal" interfaces, are plotted in **Fig. III.2.5**, assuming normal incidence i.e. $\left(\theta_i = 0^\circ\right)$ so that the following relations are satisfied $\left(r^V = -r^H = r \text{ and } t^{V,H} = t\right)$.

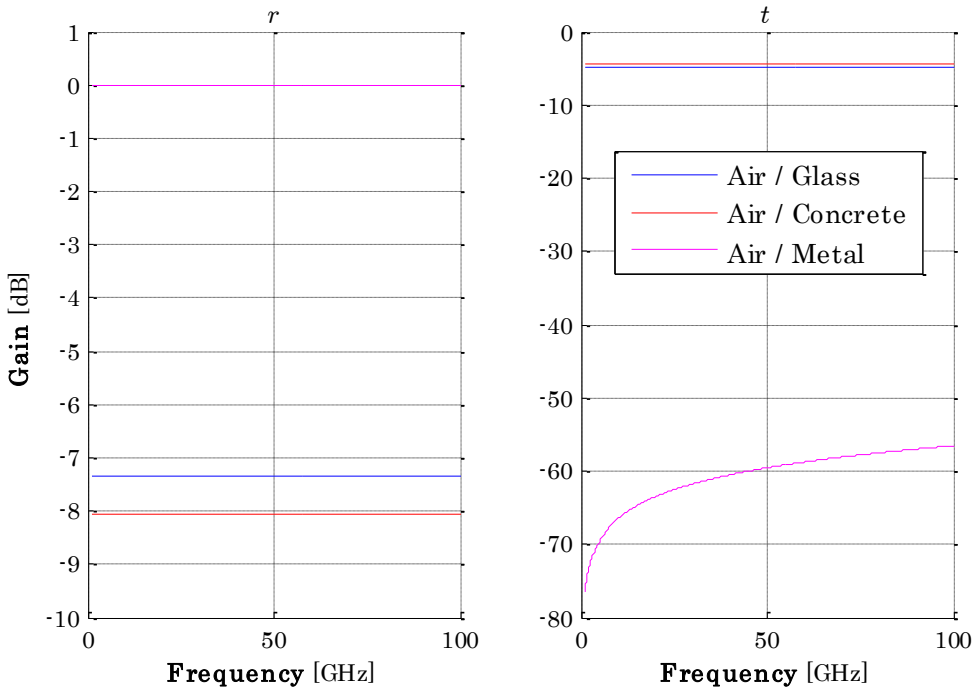

Fig. III.2.5 – Fresnel coefficients vs frequency in the case of a single interface

The Fresnel coefficients for "air/glass" and "air/concrete" interfaces, comprised between –10 and 0 dB, are very similar. However, as expected, there is total reflection for the "air/metal" interface. For these single interfaces, no frequency–dependence of the Fresnel coefficients is observed except for the extremely low transmission coefficient of "air/metal" interface which is, therefore, insignificant.

2.2.3. Fresnel coefficients for layered structures: Definition

- **Multiple reflection phenomena**

The relations given in (**Eq. III.2.9–III.2.10**) are determined for an interaction between a ray and a single interface. However, in real–word environments, the materials encountered are much more complex. They often consist of multiple layers delimited by multiple interfaces. Such a configuration causes multiple reflection phenomena inside the material. Therefore, the reflected and/or transmitted ray is a combination of different rays resulting from multiple bounces. This is illustrated in **Fig. III.2.6** where a structure consisting of Q interfaces, i.e. $(Q-1)$ layers, is represented.

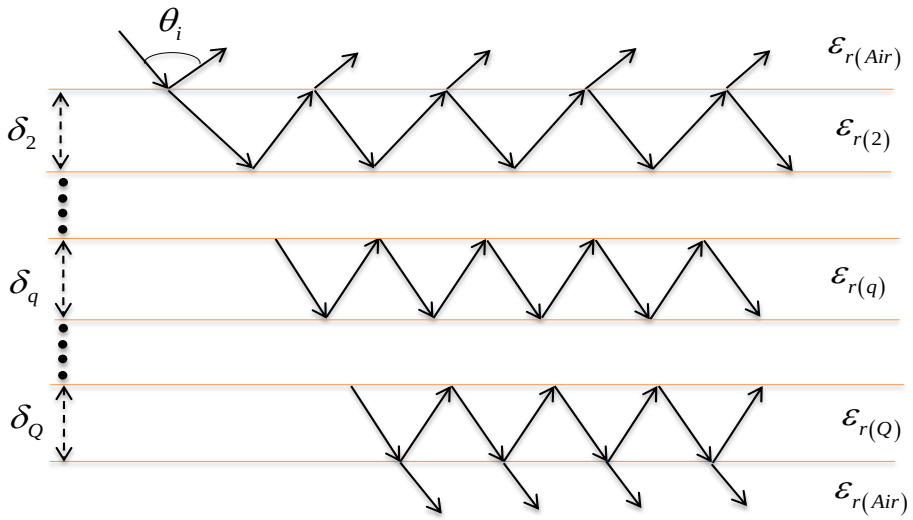

Fig. III.2.6 – Complex multi–layered structure

For such a structure, it is demonstrated in [107] that the reflection and transmission coefficients can be approximated by the expressions given in (**Eq. III.2.13–III.2.14**).

$$r^{V,H} = U_1 \begin{cases} U_Q = r^{V,H}_{Q,Q+1} \\ U_{q-1} = \dfrac{r^{V,H}_{q-1,q} + U_q \cdot e^{-j2k_0\sqrt{\varepsilon_{r(q)}}\delta_q}}{1 + r^{V,H}_{q-1,q} \cdot U_q \cdot e^{-j2k_0\sqrt{\varepsilon_{r(q)}}\delta_q}}, \quad q \text{ ranges from } Q \text{ to } 2 \end{cases}$$

(Eq. III.2.13)

$$t^{V,H} = V_1 \begin{cases} U_Q = r^{V,H}_{Q,Q+1}, \quad V_Q = t^{V,H}_{Q,Q+1} \\ U_{q-1} = \dfrac{r^{V,H}_{q-1,q} + U_q \cdot e^{-j2k_0\sqrt{\varepsilon_{r(q)}}\delta_q}}{1 + r^{V,H}_{q-1,q} \cdot U_q \cdot e^{-j2k_0\sqrt{\varepsilon_{r(q)}}\delta_q}}, \quad V_{q-1} = \dfrac{t^{V,H}_{q-1,q} \cdot V_q \cdot e^{-jk_0\sqrt{\varepsilon_{r(p)}}\delta_p}}{1 + r^{V,H}_{q-1,q} \cdot U_q \cdot e^{-j2k_0\sqrt{\varepsilon_{r(q)}}\delta_q}}, \quad q \text{ ranges from } Q \text{ to } 2 \end{cases}$$

(Eq. III.2.14)

$r^{V,H}_{q-1,q}$ and $t^{V,H}_{q-1,q}$ $\left(q \in [2, Q+1]\right)$ are the individual Fresnel reflection and transmission coefficients respectively at interface $(q-1)$ while $\varepsilon_{r(q)}$ and δ_q $\left(q \in [2, Q]\right)$ denote the relative permittivity and thickness of layer $(q-1)$ respectively.

- **Material attenuation rate**

Regarding layered structures, for each given layer, a coefficient denoted by $L_{[dB]}$, accounting for the attenuation caused by the dielectric, should be taken into account in the computation of the reflection and transmission coefficients. This is the case in the results presented herein. $L_{[dB]}$ is a function of the frequency f, the relative permittivity ε_r and the thickness δ of the considered layer, as shown in (**Eq. III.2.15**). k_0 is the wavenumber in free–space.

$$L_{[dB]} = 20 \cdot \log_{10}(e) \cdot \frac{\delta}{\Delta}; \Delta = \frac{1}{k_0 \sqrt{\mathrm{Re}(\varepsilon_r)}} \sqrt{\frac{2\cos(\gamma)}{1-\cos(\gamma)}}; \tan(\gamma) = \frac{\mathrm{Im}(\varepsilon_r)}{\mathrm{Re}(\varepsilon_r)} \qquad \textbf{(Eq. III.2.15)}$$

2.2.4. Fresnel coefficients for layered structures: Frequency–dependence

- **Material attenuation rate**

We first investigate the frequency–dependence of the attenuation rate $L_{[dB]}$, defined in (**Eq. III.2.15**), for single–layered materials composed with glass, concrete and metal, the properties of which are given in **Table III.2.1**. In **Fig. III.2.7**, $L_{[dB]}$ is evaluated as function of the frequency for these different materials, with different thickness values considered.

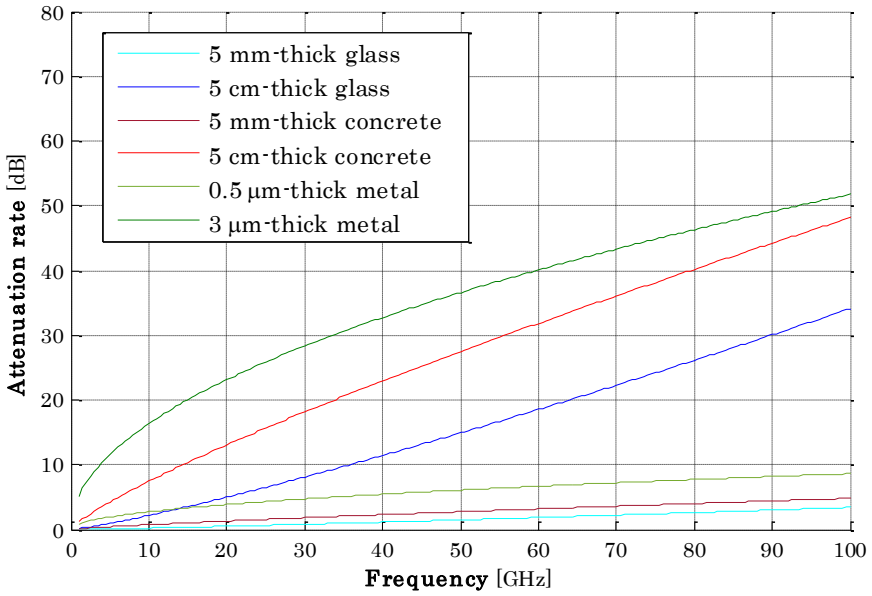

Fig. III.2.7 – Material attenuation rate vs frequency for single–layered structures

It can be seen that $L_{[dB]}$ linearly increases with the frequency for all studied materials. This behavior can be deduced from its analytical expression given in (**Eq. III.2.15**). In this expression, $L_{[dB]}$ is directly proportional to (f) if the frequency–dependence of ε_r is considered to be insignificant.

The increase of $L_{[dB]}$ with increasing frequency is more important with larger thickness values. Futhemore, for the same thickness value, concrete materials result in more attenuation than glass materials while the attenuation caused by metal remains the highest, even with much thinner layers.

However, in practical scenarios, these different materials do not usually have the same thicknesses. The thickness of glass materials, often found on building windows, is in the order of a few millimeters while that of concrete materials found on walls is in the order of a few tens of centimeters. The metal coated layer found on EE windows for example is however much thinner, only a few nanometers.

- **Multiple reflection phenomena**

Let us now evaluate the frequency–dependence the reflection and transmission coefficients for two specific strucures: a 2–layered standard glass window and a 2–layered modern glass window with additional metal coating, as illustated in **Fig. III.2.8**.

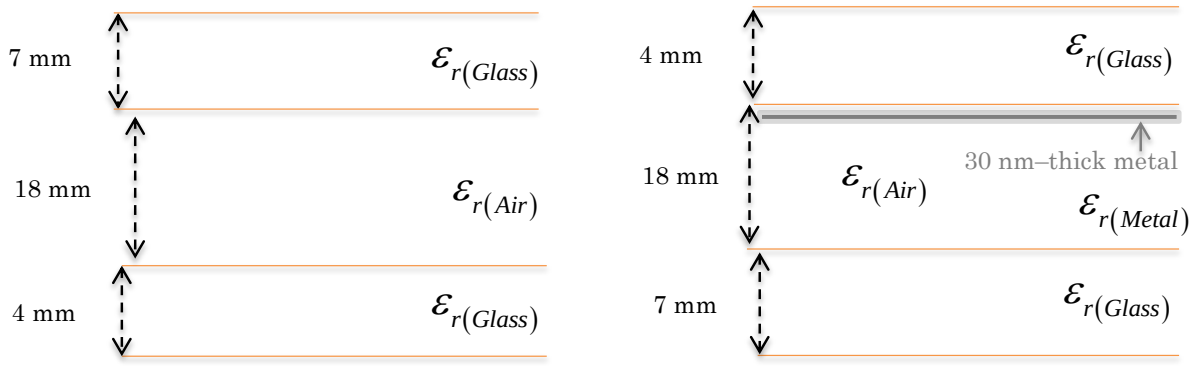

Fig. III.2.8 – Standard and coated glass window structures

These structures are found in Orange Labs premises in Belfort. They are provided by "Saint–Gobain", French glass manufacturer for windows in private homes and professional buildings. More details on their characteristics can be found in [109].

It is important to note that, while the thicknesses of the glass layers as well as the separation distance between such layers are usually well–known, the exact value of metalized layer thickness is not reported by manufcturers.

In [110], it is argued that values between 5 and 50 nm are a resonable estimation. In the results presented herein, this value is set to 30 nm.

Fig. III.2.9 and **Fig. III.2.10** show the reflection and transmission coefficients respectively, as function of the frequency, for both structures with the assomption of normal incidence.

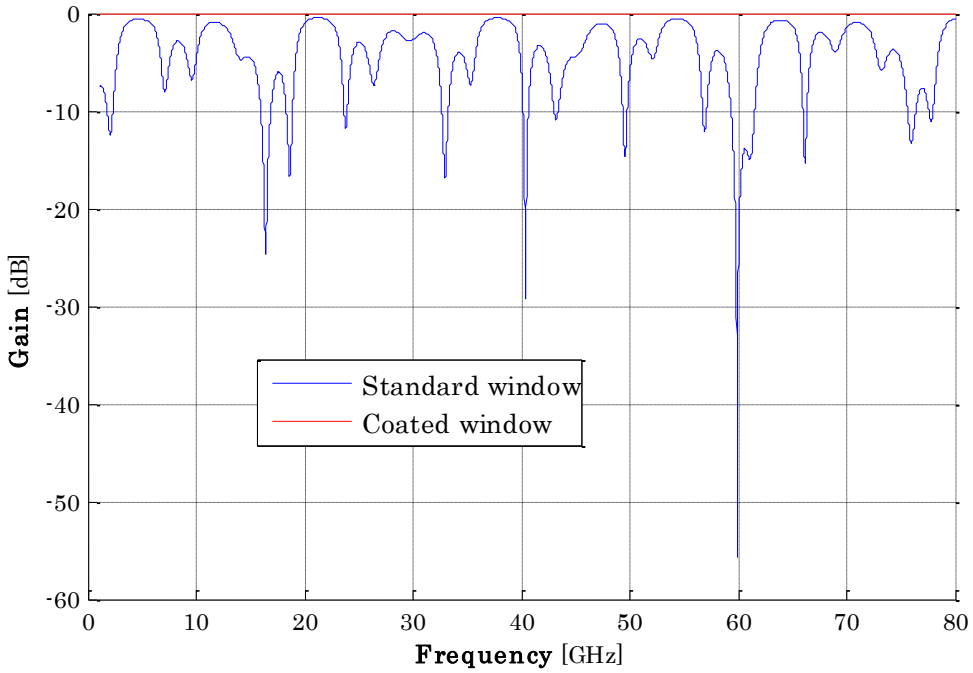

Fig. III.2.9 – Fresnel reflection coefficients vs frequency for multi–layered stuctures

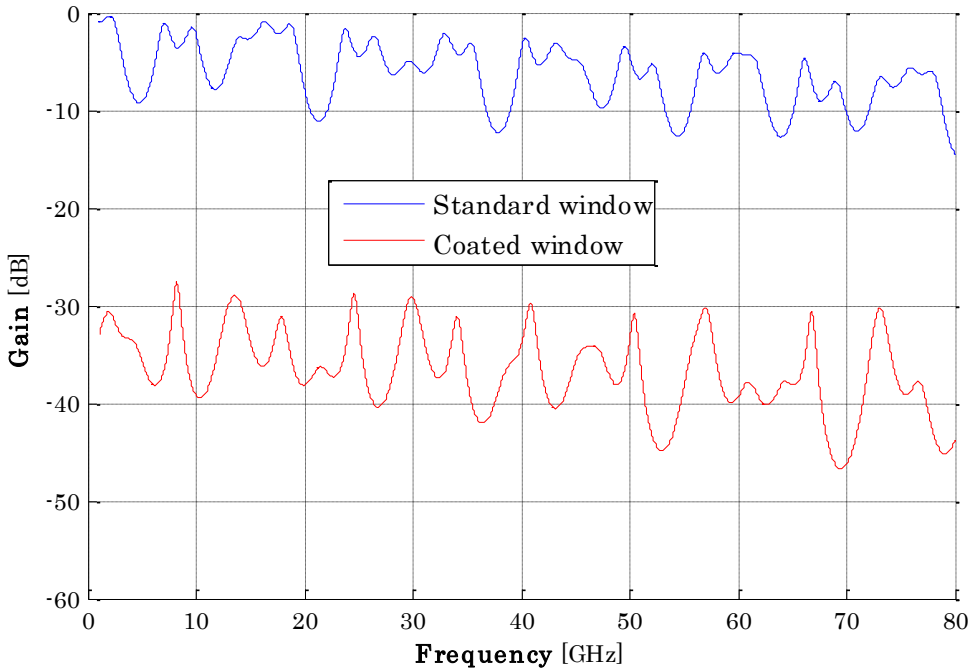

Fig. III.2.10 – Fresnel transmission coefficients vs frequency for multi–layered stuctures

The ripples observed in the evolution of these coefficients can be associated with the multiple reflection phenomena inside the layered structures. The reflection coefficient of the metal–coated window is, expectedly, extremely close to 0 dB. There is, however, a slight decreasing trend of the transmission coefficients with increasing frequency. This is essentially due to the attenuation rate inside the different materials. These transmission coefficients also reveal that the attenuation caused by the coated window (more than 30 dB on average) is significanlty higher than that of the standard window (around 7 dB on average). These findings are in line with the studies reported in **Chapter II**.

2.3. Diffraction phenomenon

Diffraction is the propagation phenomenon that allows bending of rays around edges of obstacles. This phenomenon explains the presence of electromagnetic field in the shadow areas, which is not accounted for in the GO theory. Diffraction can be modeled thanks to either the geometrical theory of diffraction (GTD) or the uniform theory of diffraction (UTD), with polarization accounted for. Fresnel knife–edge diffraction (KED) approximation also provides a simple modeling of this phenomenon. However, this approximation does not

account for polarization. Therefore, in order to remain consistent with the previously defined Fresnel coefficients, only the GTD and UTD are described herein.

2.3.1. Geometrical theory of diffraction (GTD)

The GTD [111], developed by Keller, quantifies the amount of diffracted field in the shadow region where the GO theory fails to predict correct fields. Let us consider a ray incident on a perfectly conducting wedge, at point Q, as shown in **Fig. III.2.11**.

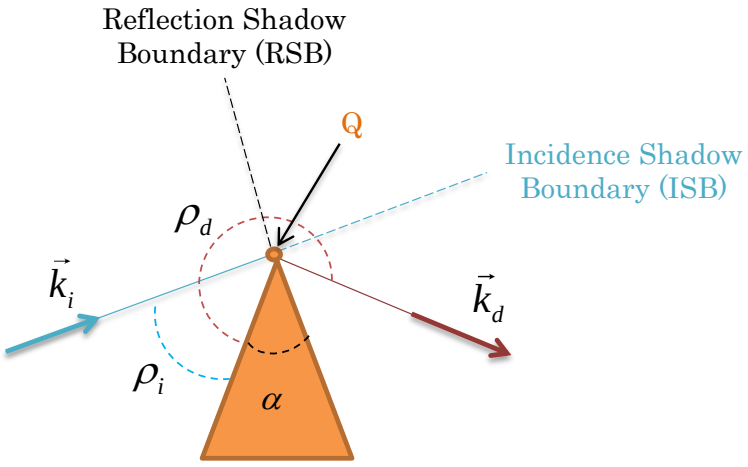

Fig. III.2.11 – Diffraction on a perfectly conducting wedge

Let $\left(E_i^V, E_i^H\right)^T$ and $\left(E_d^V, E_d^H\right)^T$ be the electric field vectors that characterize the incident and diffracted rays at point Q respectively, in the same local basis (V, H). $\vec{k}_i$ and $\vec{k}_d$ denote the propagation vectors of the incident and diffracted rays respectively.

Since the GTD describes diffraction as a local phenomenon [111], in an analogous manner to how the reflection and transmission phenomena are described within the GO field, the diffracted ray can thus be determined from the incident ray by means of a dyadic diffraction matrix D as shown in (**Eq. III.2.16–III.2.17**).

$$\begin{pmatrix} E_d^V \\ E_d^H \end{pmatrix} = D \cdot \begin{pmatrix} E_i^V \\ E_i^H \end{pmatrix} \quad \textbf{(Eq. III.2.16)}; \qquad D = \begin{pmatrix} d^V & 0 \\ 0 & d^H \end{pmatrix} \quad \textbf{(Eq. III.2.17)}$$

The detailed expression of D is shown in (**Eq. III.2.18**) in the case of a perfectly conducting wedge, with **Fig. III.2.11** providing an illustration of the parameters involved in the

definition of such coefficients. Note that the definition is restricted to the 2–D case for simplicity, without loss of generality with regards to the frequency–dependence characterization.

$$d^{V,H} = -\frac{e^{-j\frac{\pi}{4}} \cdot \sin\left(\frac{\pi}{\eta}\right)}{\eta\sqrt{2k_0\pi}} \left[\frac{1}{\cos\left(\frac{\pi}{\eta}\right) - \cos\left(\frac{\rho_d - \rho_i}{\eta}\right)} \mp \frac{1}{\cos\left(\frac{\pi}{\eta}\right) - \cos\left(\frac{\rho_d + \rho_i}{\eta}\right)} \right] \qquad \textbf{(Eq. III.2.18)}$$

ρ_i and ρ_d are the incident and diffraction (or observation) angles respectively. $\eta = {(2\pi - \alpha)}/{\pi}$ with α the interior wedge angle and k_0 is the wavenumber in free–space.

The coefficient $A_{n,q}$, in the case of diffraction, is thus given in **(Eq. III.2.19)**.

$$A_{n,q} = D \qquad \textbf{(Eq. III.2.19)}$$

The GTD coefficients are plotted in **Fig. III.2.12**, as function of the observation angle ρ_d, with the following parametrization: $\rho_i = 55^\circ$, $\alpha = 40^\circ$ and $f = 15$ GHz.

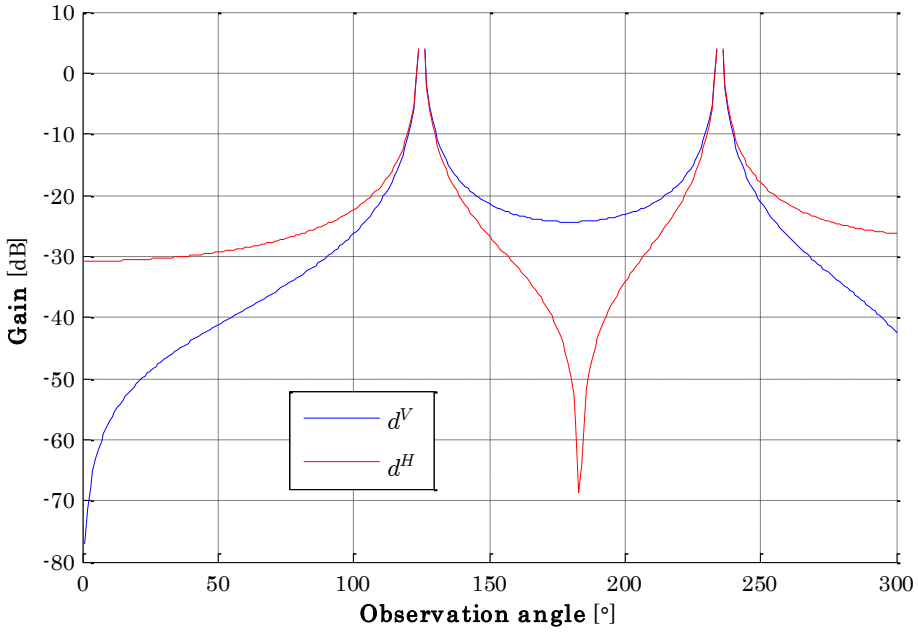

Fig. III.2.12 – GTD coefficients vs observation angle

2.3.2. Uniform theory of diffraction

In **Fig. III.2.12**, it can be noticed that the GTD coefficients are undefined at certain values of ρ_d. These discontinuities in the GTD happen at the transition regions surrounding the shadow boundaries known as the reflection shadow boundary (RSB) where $\rho_d = \pi - \rho_i$ and the incidence shadow boundary (ISB) where $\rho_d = \pi + \rho_i$.

The UTD [111] set out by Kouyoumjian and Pathak resolve this issue of discontinuity by introducing a transition function, denoted by F, in the expression of the diffraction coefficients. The UTD coefficients are thus given in (**Eq. III.2.20**) below, for the same case of the perfectly conduting wedge described in **Fig. III.2.11**.

$$d^{V,H} = \left(d_1 + d_2\right) \mp \left(d_3 + d_4\right)$$

$$d_1 = -\frac{e^{-j\frac{\pi}{4}}}{2\eta\sqrt{2k_0\pi}} \cdot \cot\left[\frac{\pi + \left(\rho_d - \rho_i\right)}{2\eta}\right] \cdot F\left[kLa^{+}\left(\rho_d - \rho_i\right)\right]$$

$$d_2 = -\frac{e^{-j\frac{\pi}{4}}}{2\eta\sqrt{2k_0\pi}} \cdot \cot\left[\frac{\pi - \left(\rho_d - \rho_i\right)}{2\eta}\right] \cdot F\left[kLa^{-}\left(\rho_d - \rho_i\right)\right]$$

$$d_3 = -\frac{e^{-j\frac{\pi}{4}}}{2\eta\sqrt{2k_0\pi}} \cdot \cot\left[\frac{\pi + \left(\rho_d + \rho_i\right)}{2\eta}\right] \cdot F\left[kLa^{+}\left(\rho_d + \rho_i\right)\right]$$

$$d_4 = -\frac{e^{-j\frac{\pi}{4}}}{2\eta\sqrt{2k_0\pi}} \cdot \cot\left[\frac{\pi - \left(\rho_d + \rho_i\right)}{2\eta}\right] \cdot F\left[kLa^{-}\left(\rho_d + \rho_i\right)\right]$$

$$a^{\pm}\left(\beta^{\pm}\right) = 2\cos^2\left(\frac{2\eta\pi N^{\pm}\left(\beta^{\pm}\right) - \beta^{\pm}}{2}\right)$$

$$N^{\pm}\left(\beta^{\pm}\right) = \frac{\pm\pi + \beta^{\pm}}{2\eta\pi}, \quad \beta^{\pm} = \rho_d \pm \rho_i$$

$$F\left(x\right) = 2j\sqrt{x} \cdot e^{jx} \int_{\sqrt{x}}^{+\infty} e^{-jt^2} \cdot dt$$

(**Eq. III.2.20**)

The function F is an appropriately modified Fresnel integral. This function converges towards unit function as the observation point is moved further away from the shadow boundaries, so that the UTD coefficients coincide with the GTD coefficients. The UTD coefficients plotted in **Fig. III.2.13**, with the same parametrization as in the GTD case, show uniform continuity, particulary around the transition regions surrounding the shadow boundaries where the GTD is deficient.

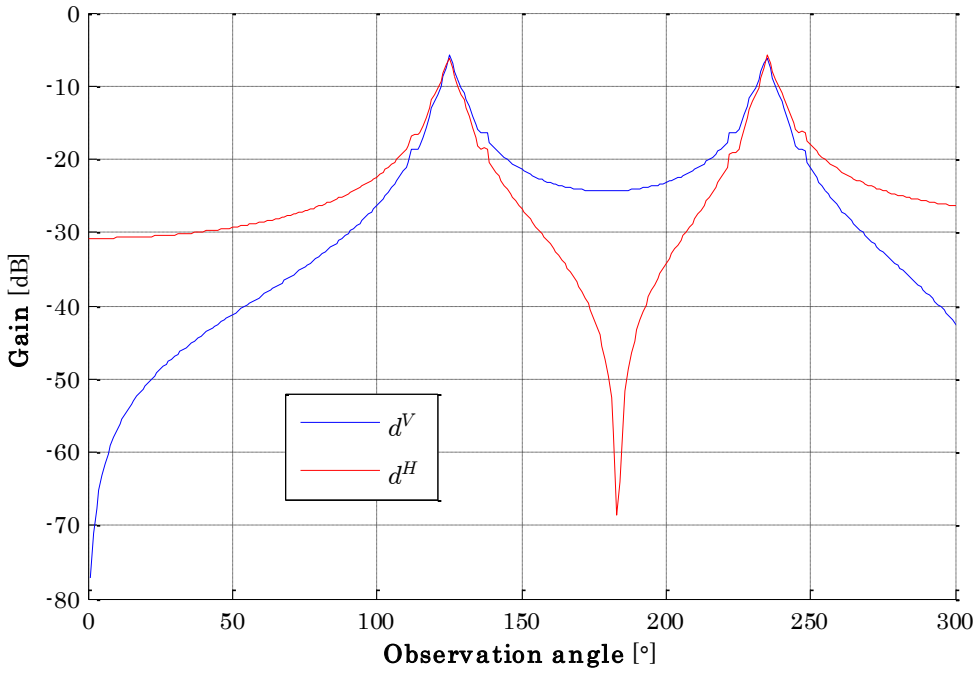

Fig. III.2.13 – UTD coefficnents vs observation angle

2.3.3. Frequency–dependence

From the analytical expressions given in (**Eq. III.2.18**) and (**Eq. III.2.20**), the diffraction coefficients provided by the GTD/UTD, expressed in dB, are proportional to $\left(-10\cdot\log_{10}(f)\right)$. **Fig. III.2.14** is an illustration of this behavior, with the following parametrization considered: $\rho_i = 55^\circ$, $\rho_i = 55^\circ$ and $\alpha = 40^\circ$. It is important to note that this parametrization corresponds with a point of continuity in the GTD coefficients which, therefore, coincide with the UTD coefficients.

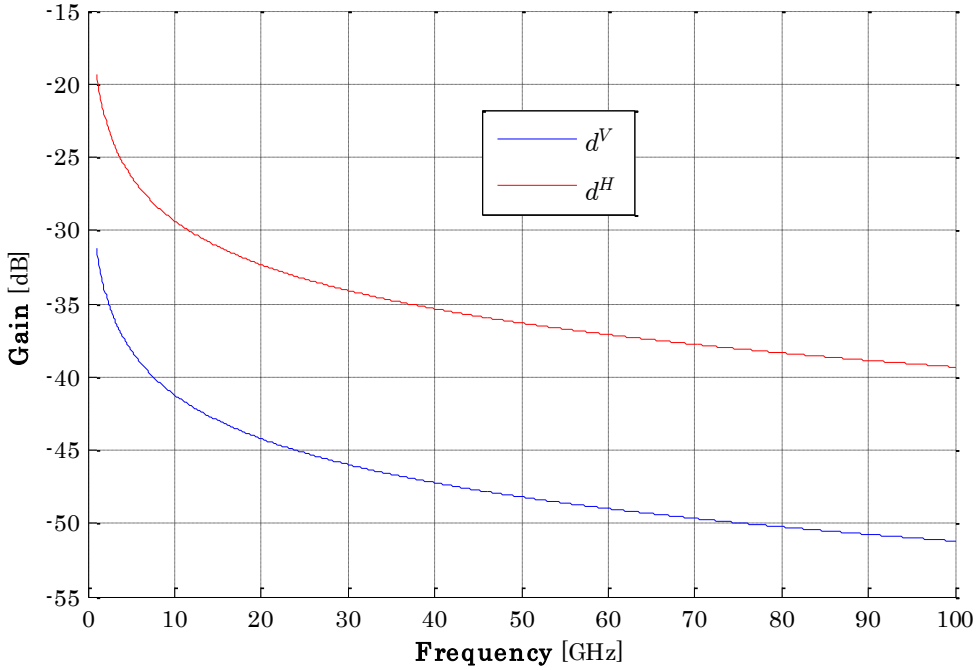

Fig. III.2.14 – GTD/UTD coefficients vs frequency

3. Limitations of the theoretical approach

In these theoretical studies, the geometric model adopted by standard bodies such as 3GPP and ITU has been considered a baseline. The main propagation phenomena including free–space, reflection, transmission and diffraction, accounted for in this model, have been characterized and their frequency–dependence, investigated.

The findings regarding the frequency–dependence of these canonical phenomena provide valuable insights on the behavior of the radio propagation channel with regards to the frequency.

However, a full description of the propagation channel needs to incorporate complex interactions between the radio signal and the environment, which may be caused by diffuse scatterers, vegetation, rain and atmospheric gases among others. Therefore, a complete modeling based on this geometrical approach requires that these complex interactions be decomposed by means of the canonical phenomena. This is, however, not necessarily convenient.

These limitations of the theoretical approach can be circumvented thanks to experimental characterization of the radio propagation channel. In this sense, measurement campaigns are considered as a fundamental component in wireless propagation channel studies. Therefore, in our objective to investigate the frequency–dependence of the radio propagation channel, two measurement campaigns, presented in **Chapter IV–V**, have been conducted during this Ph.D. project. The emphasis remains on the investigation of the channel LSPs in O2I and urban outdoor environments, as addressed in **Chapter II**.

Chapter IV

IV. Outdoor–to–Indoor (O2I) Propagation Channel Measurements

In this chapter, the O2I measurement campaign, conducted in the 3, 10, 17 and 60 GHz frequency bands in Orange Labs premises in Belfort, is presented. The main objective of this measurement campaign is to give an estimation of the building PELs in the selected frequency bands, for both standard and coated glass windows, in order to assess the frequency–dependence of this parameter. The channel DS is also discussed in the same way. The measurement campaign is first described in **Section 1** where the measurement scenario, setup and procedure are presented. Then, details of the measurement data processing are provided in **Section 2**. In **Section 3**, the measurement results analysis is performed. Finally, a summary is provided in **Section 4**.

1. Outdoor–to–Indoor (O2I) measurement campaign

1.1. Measurement scenario description

The radio propagation channel was investigated at 3, 10, 17 and 60 GHz in the O2I scenario described in **Fig. IV.1.1**. The TX antenna was located outside and mounted on the roof of the white van, at 4 m above ground level. The RX antenna was placed at different positions inside the building Orange Labs premises. It was kept at mobile user level i.e. 1.5 m high above ground level. The distance between the TX antenna and the building exterior walls was about 10 m.

Fig. IV.1.1 – O2I measurement scenario in Belfort

The indoor building layout is shown in **Fig. IV.1.2** where the RX positions are depicted. Each number comprised between 1 and 38 corresponds with an RX position. Inside the building, different locations were considered during the measurements. They include large offices (LO1 and LO2), a corridor (Co), a break–room (BR) and a residential flat (Fl).

Fl consists of a living room and small offices, separated by partition walls. BR, adjacent to Fl, is separated with the latter by a bearing wall. LO1, LO2 and the Co are located on the same side of the bearing wall as BR. They are separated with each other by partition walls. The building exterior walls are made of concrete and the windows of standard double–layered glass (for BR and LO1) or coated double–layered glass (for Fl and LO2). The distances between the TX and the different RX positions ranged between 10 and 25 m.

In the remainder of this chapter, the TX and RX will be also referred to as the BS and MS respectively.

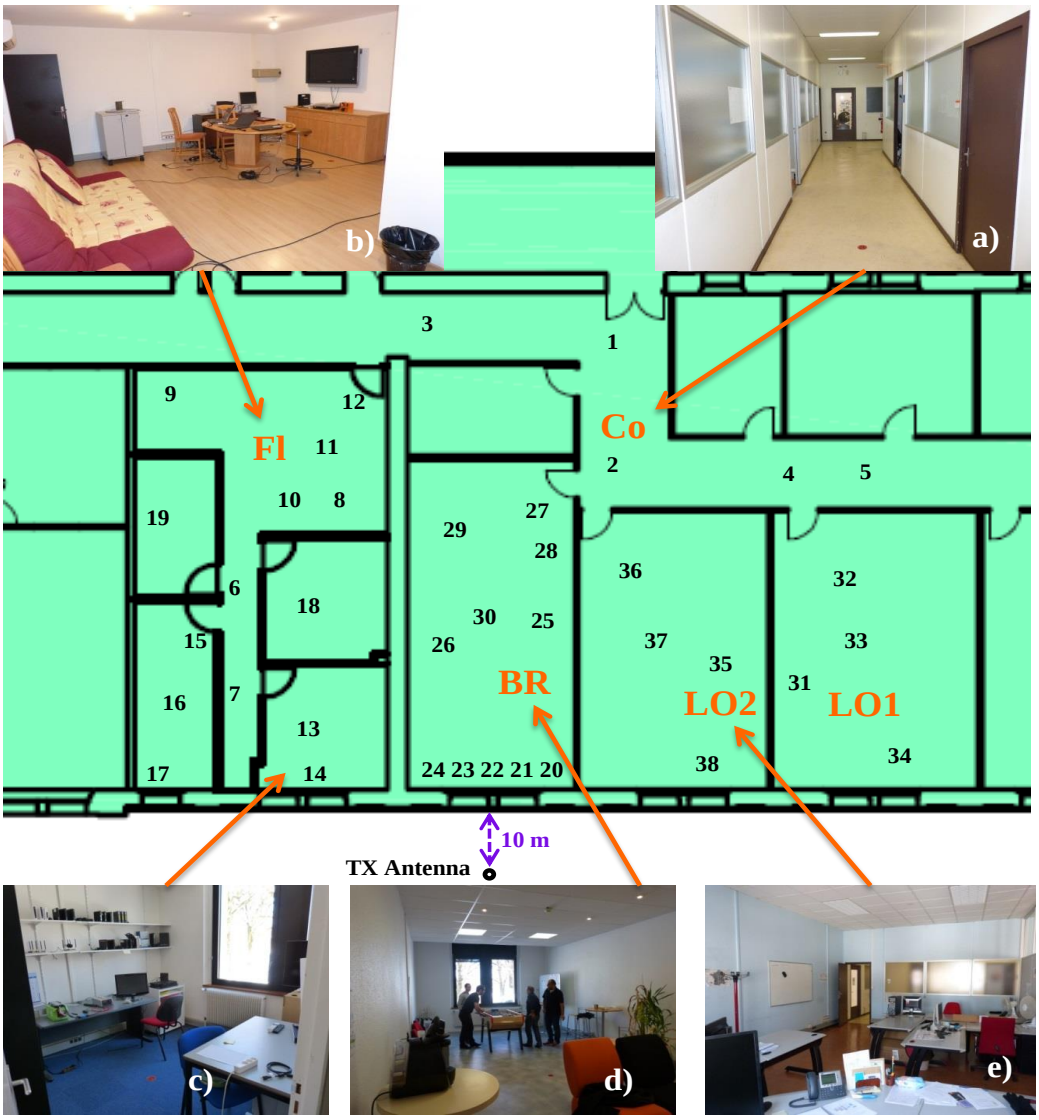

Fig. IV.1.2 – Indoor building layout for the O2I scenario in Belfort:
a) Co; b) and c) Fl; d) BR; e) LO1or LO2.

1.2. Measurement setups

The measurements were performed using a wideband channel sounding system developed by Orange [112]. An arbitrary waveform generator (AWG) produced successive 8192–length wideband sequences at 1 Gbps–rate.

The measurement channel bandwidth was 125 MHz at 3, 10 and 17 GHz and 250 MHz at 60 GHz while the TX/BS power ranged from 20 dBm at 60 GHz to 30 dBm at 3 GHz. At both the BS and MS ends, vertical antenna polarization was considered.

As path loss increases with frequency, directional MS antennas with narrower beams but larger gains were used at higher frequencies in order to have sufficient dynamic range. In this sense, three main setups were considered depending on the MS antenna radiation pattern, as indicated in **Table IV.1.1**. First, setup S1 used omnidirectional MS antennas at 3, 10 and 17 GHz. Then, for setup S2, directional MS antennas with 90° HPBW were used at 17 and 60 GHz. Finally, setup S3 used highly directional MS antennas, with 20/30° HPBW, at 60 GHz. The antenna gains are provided in **Table IV.1.1**.

On the BS side, irrespective of the setup, omnidirectional antennas were used at 3 and 10 GHz while directional antennas with 90° and 50° HPBW were used at 17 and 60 GHz respectively. The antenna gains are provided in **Table IV.1.1** as well.

Table IV.1.1 – O2I measurement setup parameters

Parameters	Measurement Setups					
	S1		S2		S3	
	3 GHz	10 GHz	17 GHz		60 GHz	
Frequency [GHz]	3.6 – 3.725	10.5 – 10.625	17.3 – 17.425		59.875 – 60.125	
RX/MS antenna	Omni. 1 dBi	Omni. 0 dBi	Omni. 0 dBi	90° HPBW 7 dBi	90° HPBW 6 dBi	20/30° HPBW 20/15 dBi
TX/BS antenna	Omni. 1 dBi	Omni. 0 dBi	90° HPBW 7 dBi		50° HPBW 10 dBi	
Antenna polarization	Vertical					
Bandwidth [MHz]	125				250	
TX power	From 20 dBm (60 GHz) to 30 dBm at 3 GHz					

Omni. : Omnidirectional

Some of the TX/BS and RX/MS measurement equipments used to perform these measurements are presented in **Fig. IV.1.3** and **Fig. IV.1.4–IV.1.5** respectively.

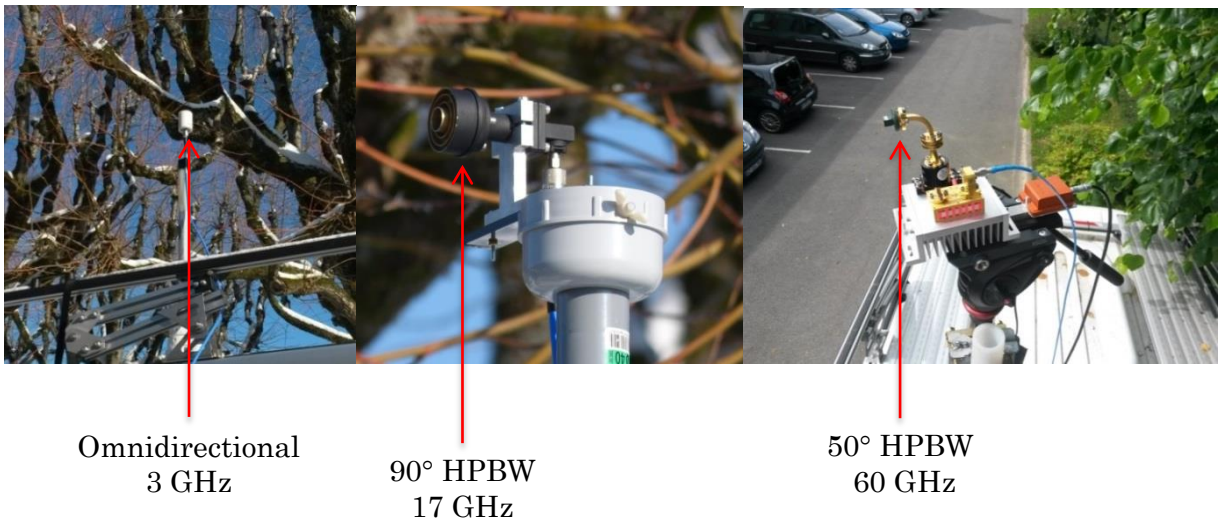

Fig. IV.1.3 – TX/BS measurement equipment

Fig. IV.1.4 – RX/MS measurement equipment (1)

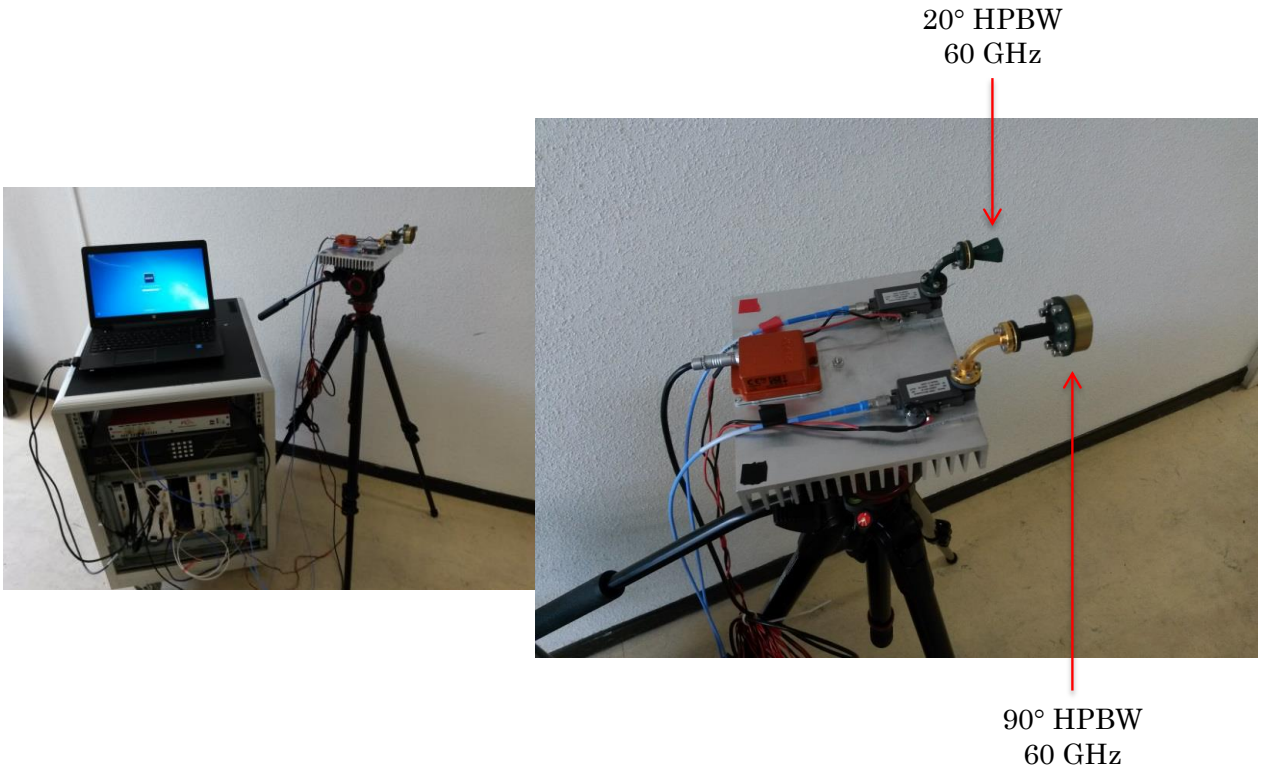

Fig. IV.1.5 – RX/MS measurement equipment (2)

1.3. Measurement procedures

In all four frequency bands including 3, 10, 17 and 60 GHz, the BS antenna was fixed and set up to illuminate the indoor building. At the MS end, however, the measurement procedures differed depending on the three different setups i.e. on the MS antenna radiation patterns.

For setup S1, the omnidirectional MS antenna was mounted on a rotating arm describing a circular trajectory while the measurement data were being collected. This is shown in **Fig. IV.1.6**. The radius of the trajectory was 2λ, 4λ and 6λ at 3, 10 and 17 GHz respectively, where λ is the radio signal wavelength.

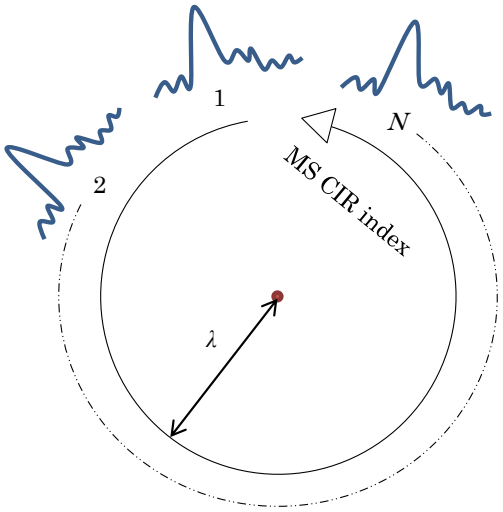

Fig. IV.1.6 – Measurement procedure for setup S1

For setup S2, the 90° HPBW MS antenna was pointed towards four different directions, with a 90° (antenna HPBW) angular step, partitioning the space into four sectors. In each sector, the antenna remained static while the data were being collected. This configuration is illustrated in **Fig. IV.1.7**.

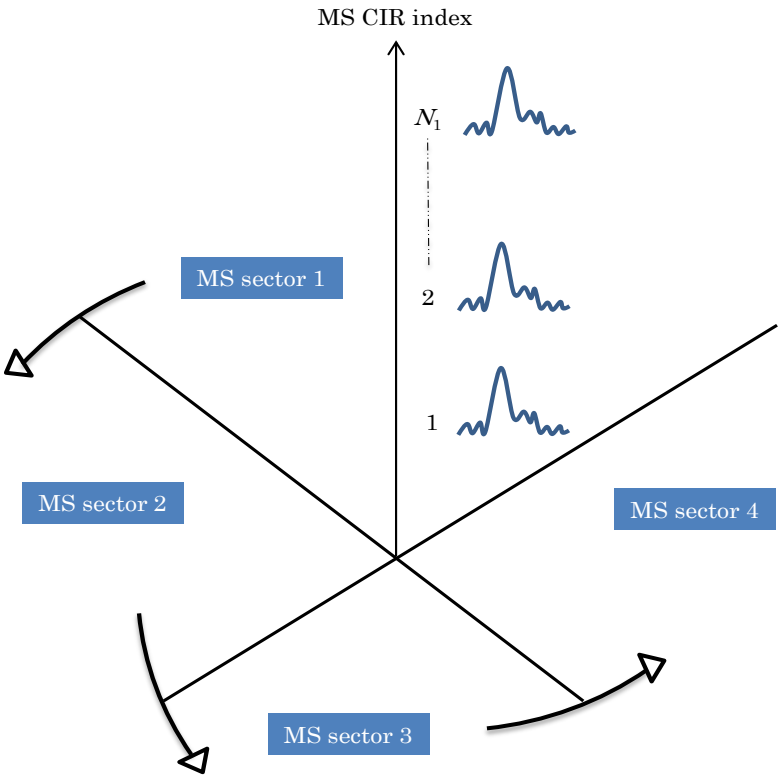

Fig. IV.1.7 – Measurement procedure for setup S2

For S3, the 20/30° HPBW MS antenna was mounted on a panoramic tripod head and manually moved by the operator to describe a 3–D trajectory during the measurement. The azimuth and elevation angles, ranging from –180 to 180° and –40 to 40° respectively, were recorded by an inertial unit. Therefore, a "cloud" of CIRs was collected at irregular angular in azimuth/elevation pointing angles, as shown in **Fig. IV.1.8**. The interval between two consecutive azimuth/elevation points was about 2 to 3°.

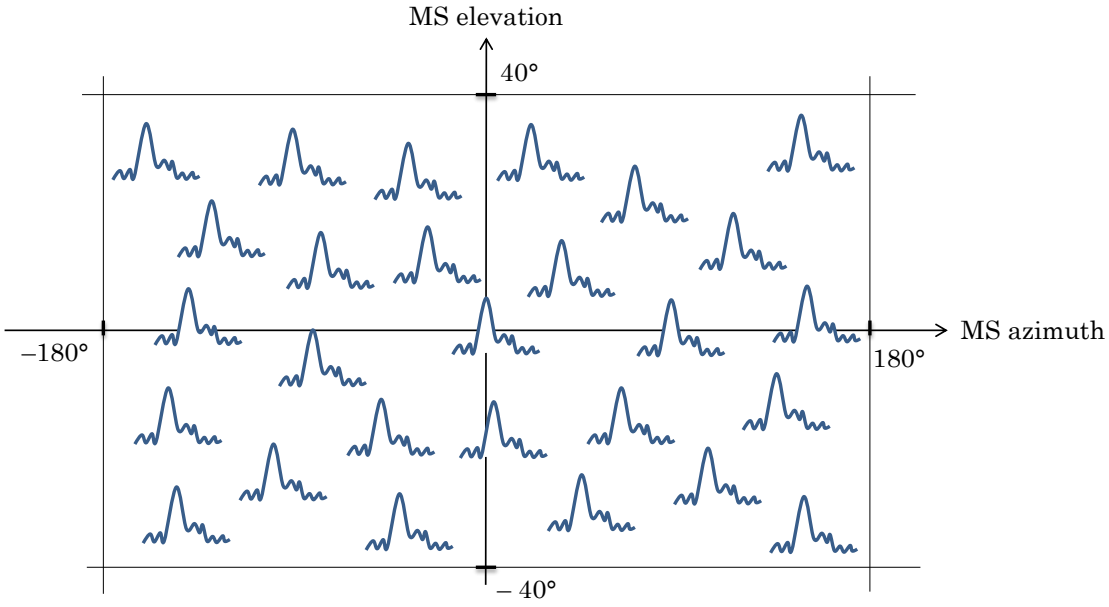

Fig. IV.1.8 – Measurement procedure for setup S3

2. Measurement data processing

The measurement data processing was performed accordingly to the different setups, with the aim of determining the omnidirectional characteristics of the propagation channel at all frequencies. This makes for a fairer comparison between the different frequency bands.

Therefore, omnidirectional PDPs were computed at the MS end for each setup. Note that, in all three setups, the BS antenna was set up to illuminate the indoor building homogeneously. The different processing methods are described in this section.

2.1. Data processing for setup S1

For setup S1, let $h_n^{Omni}(\tau)$ be the n^{th} channel CIR recorded during the arm rotation at the MS end with τ denoting the propagation delay. Let N, equal to a few hundred, denote the total number of CIRs distributed along the circular trajectory. The omnidirectional PDP denoted by $PDP^{Omni}(\tau)$ is the average gain, associated with each propagation path, between the N measured CIRs, as written in (**Eq. IV.2.1**).

$$PDP^{Omni}(\tau) = \frac{1}{N}\sum_{n=1}^{N}\left|h_n^{Omni}(\tau)\right|^2 \qquad \textbf{(Eq. IV.2.1)}$$

The averaging procedure in (**Eq. IV.2.1**) contributes to the filtering of the small–scale fading effects caused by multiple propagation paths. To illustrate such effects, the evolution of different MPCs during the MS arm rotation, i.e. as function of the CIR index n, is shown in the typical examples given in **Fig. IV.2.1–IV.2.2**, at 3 GHz. MPC_1 is the main MPC and MPC_2 is a secondary MPC. Significant variations of the RX signal power can be observed, even for the main MPCs. The averaging performed in (**Eq. IV.2.1**) is thus an appropriate method to filter these fading phenomena, as indicated by the PDPs on the right side of these plots. Similar observations are made at 10 and 17 GHz.

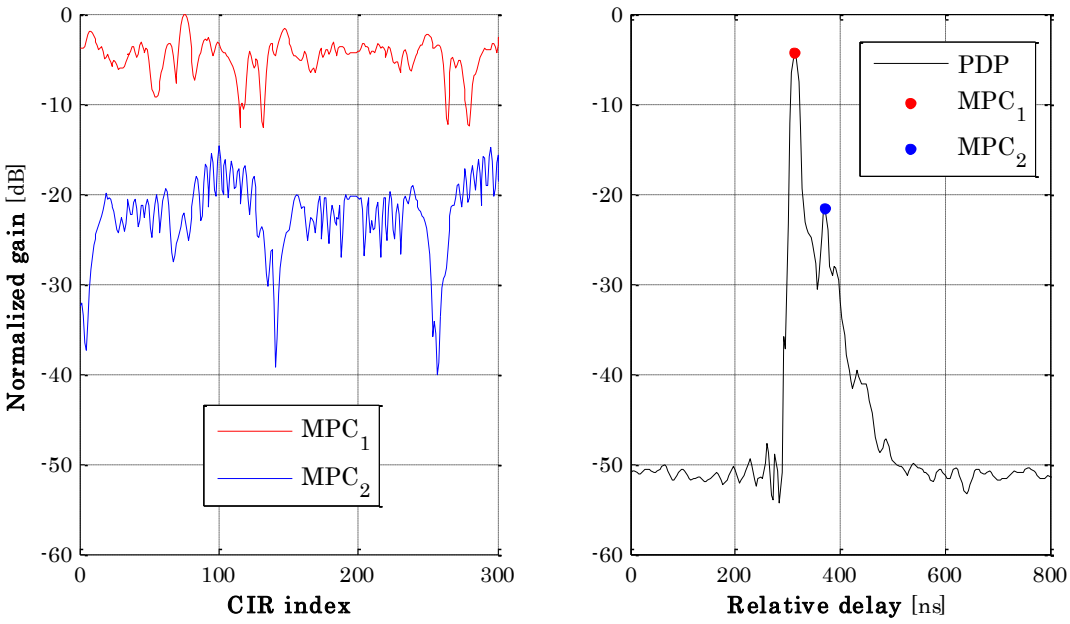

Fig. IV.2.1 – Illustration of small–scale fading filtering in S1 for MS position R21 in LoS

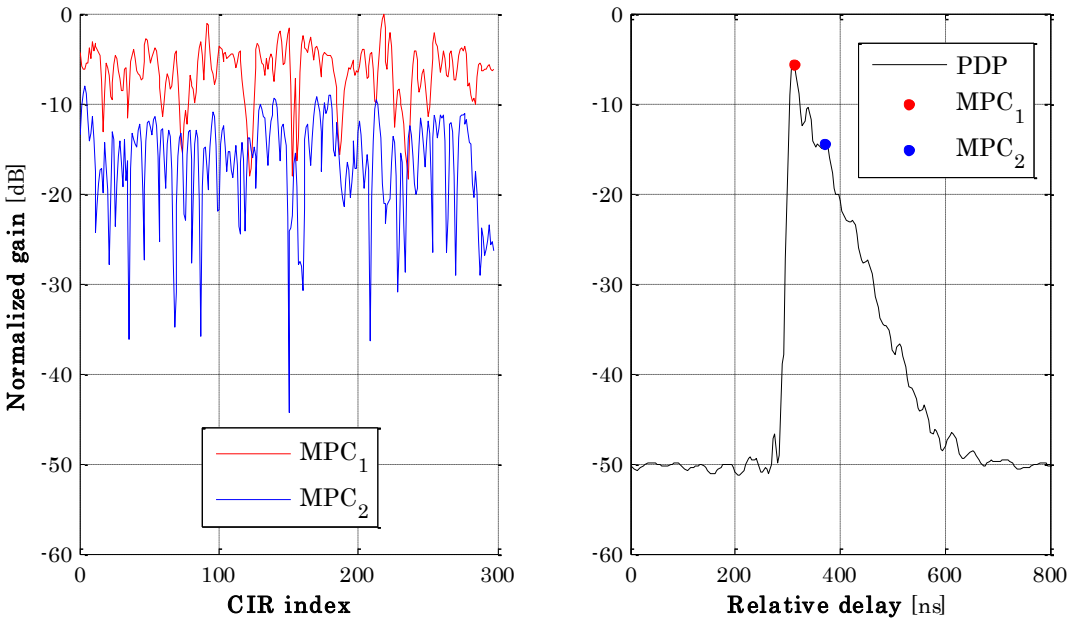

Fig. IV.2.2 – Illustration of small–scale fading filtering in S1 for MS position R37 in NLoS

2.2. Data processing for setup S2 and setup S3

For setups S2 and S3, the omnidirectional PDP needs to be synthesized from the measurements that were performed using directional MS antennas. The synthesizing procedure adopted herein is similar to the approach described in [113].

In this approach, channel CIRs are first computed at different pointing angles with a step that is equal to the MS antenna HPBW. Then, the omnidirectional PDP is obtained by summing the contributions from all MS pointing angles. Since the angular step is equal to the antenna HPBW, the synthesized omnidirectional antenna pattern has a gain that is approximately equal to the directional antenna maximum gain.

It is important to note the antenna maximum gains are subtracted beforehand from all measured CIRs in order to effectively synthesize omnidirectional antennas with a 0 dBi gain across all frequency bands and/or setups.

Fig. IV.2.3 illustrates this synthesizing process for a 90° HPBW antenna. In **Fig. IV.2.4**, synthesized omnidirectional antenna patterns from 20, 30 45 and 90° HPBW antennas are also represented.

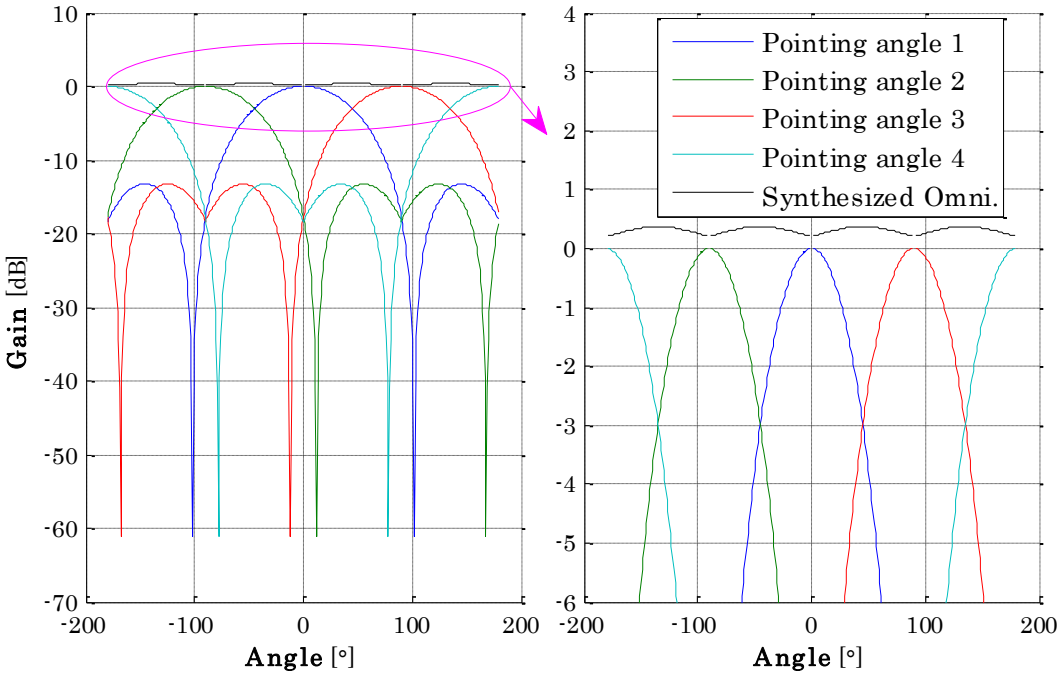

Fig. IV.2.3 – Omnidirectional pattern synthesis from a 90° HPBW antenna

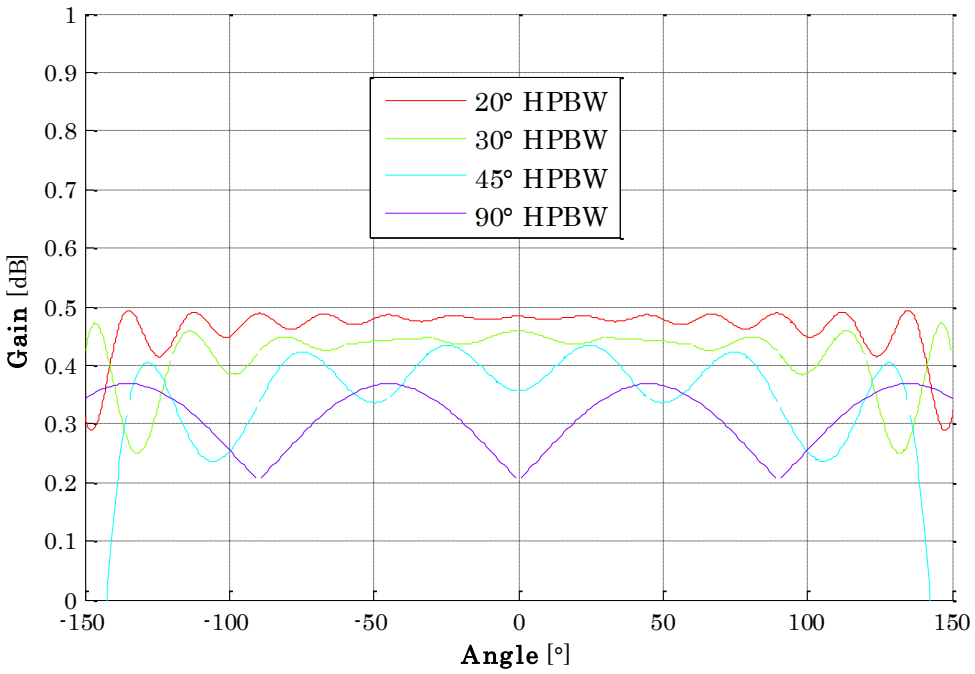

Fig. IV.2.4 – Synthesized omnidirectional patterns from directional antennas

2.2.1. S2 processing

For setup S2, let $h_n^{Dir}(\phi_{MS}(k),\tau)$ denote the n^{th} CIR measured at the k^{th} MS pointing angle $\phi_{MS}(k)$. Let N_k, equal to a few hundred, denote the total number of CIRs measured at MS pointing angle $\phi_{MS}(k)$ and K, equal to 4 with a 90° HPBW antenna, denote the total number of MS pointing angles. The omnidirectional PDP denoted by $PDP^{Omni}(\tau)$ is thus obtained by summing the contributions from all MS pointing angles as written in (**Eq. IV.2.2**).

$$PDP^{Omni}(\tau)=\sum_{k=1}^{K}\left|\frac{1}{N_k}\sum_{n=1}^{N_k}h_n^{Dir}(\phi_{MS}(k),\tau)\right|^2 \qquad \textbf{(Eq. IV.2.2)}$$

The contribution from each MS pointing angle is derived after a complexing averaging between the N_k CIRs measured in this orientation. This averaging procedure contributes to the cancelling out of the noise effects since the MS antenna remained static at each pointing angle. These effects are illustrated in the typical PDP examples given in **Fig. IV.2.5–IV.2.6**.

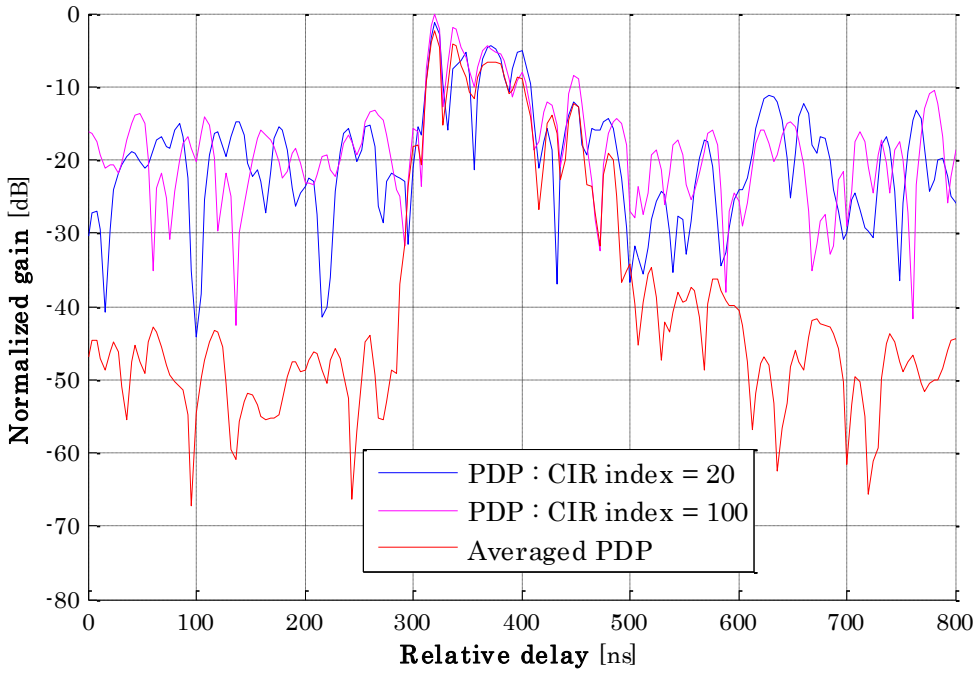

Fig. IV.2.5 – Illustration of complex averaging for noise cancellation in S2 for MS position R3

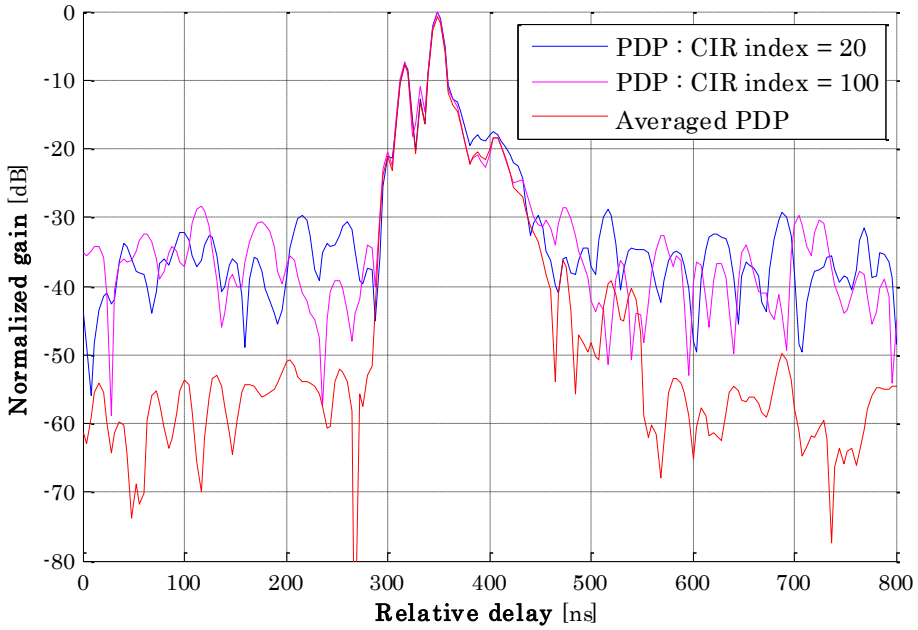

Fig. IV.2.6 – Illustration of complex averaging for noise cancellation in S2 for MS position R5

In **Fig. IV.2.7** and **Fig. IV.2.8**, typical examples of synthesized omnidirectional PDPs are given, along with the PDPs measured in the different MS pointing angles, in LoS and NLoS conditions respectively, at 17 GHz.

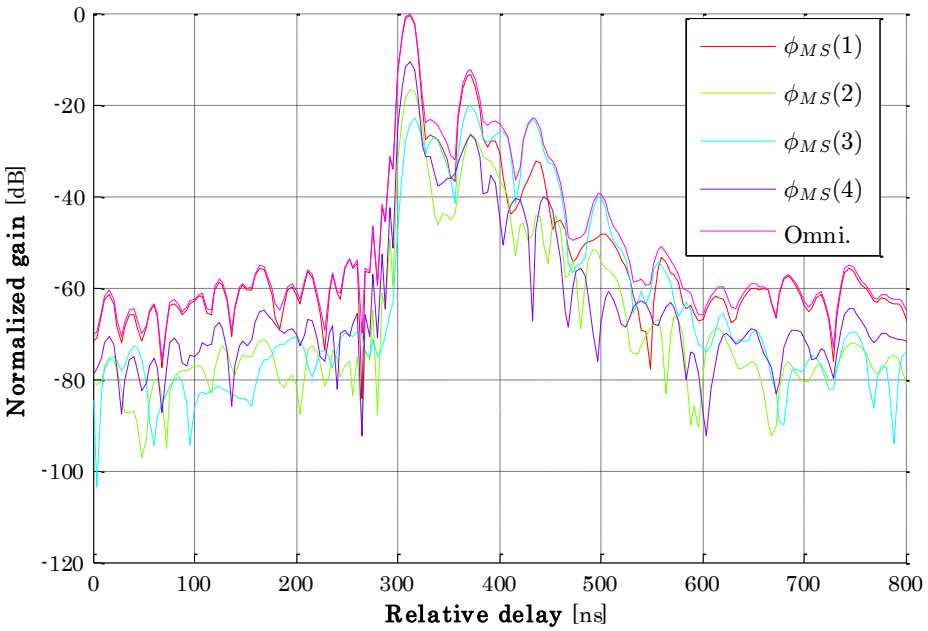

Fig. IV.2.7 Synthesized omnidirectional PDPs from S2 for MS position R23 in LoS

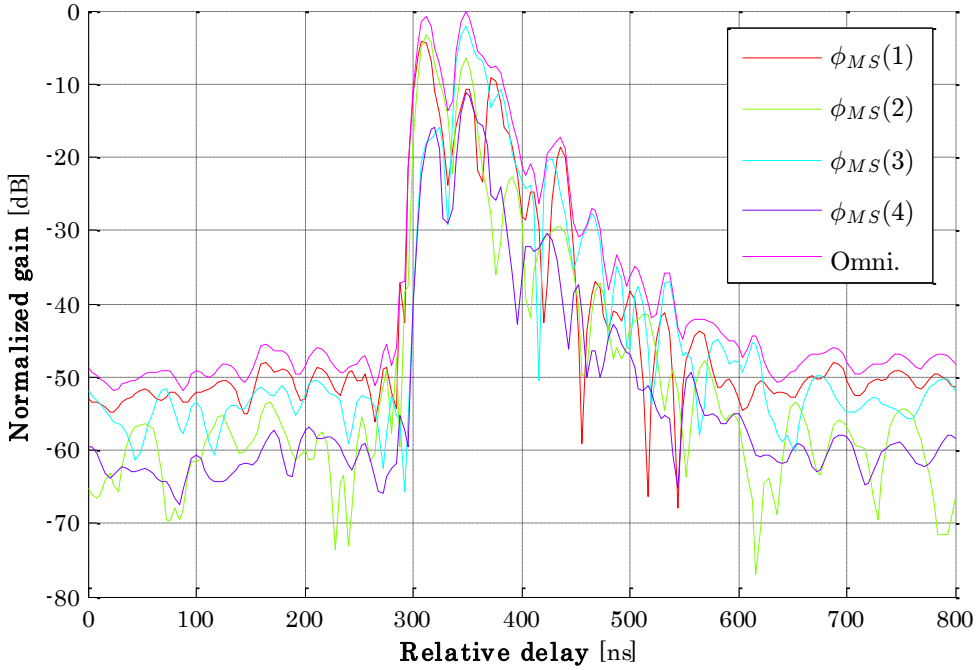

Fig. IV.2.8 Synthesized omnidirectional PDPs from S2 for MS position R26 in NLoS

It can be seen that most of the received power at a given delay only comes from a single sector, especially in LoS conditions. Similar observations are made at 60 GHz.

2.2.2. S3 processing

For setup S3, a regularly spaced $(P \times Q)$ MS–grid, with a 20/30° step (MS antenna HPBW) in the azimuth and elevation domain, is first synthesized from the measurement "cloud" shown in **Fig. IV.1.8.** P and Q are the number of azimuth and elevation pointing angles respectively.

For the p^{th} and q^{th} azimuth and elevation pointing angles $\phi_{MS}(p)$ and $\theta_{MS}(q)$ respectively, $h_{p,q}^{Dir}(\phi_{MS}(p), \theta_{MS}(q), \tau)$ is defined. The CIR in the "cloud" the angular orientation of which is the closest to $(\phi_{MS}(p), \theta_{MS}(q))$ is assigned to $h_{p,q}^{Dir}(\phi_{MS}(p), \theta_{MS}(q), \tau)$. Then, the omnidirectional PDP denoted by $PDP^{Omni}(\tau)$ is obtained by summing the contributions from all MS pointing angles in the azimuth dimension as shown in **Eq. IV.2.3**. In the elevation dimension, the maximum contribution from the different pointing angles is considered.

$$PDP^{Omni}(\tau) = \sum_{p=1}^{P} \max_{q} \left(\left| h_{p,q}^{Dir}\left(\phi_{MS}(p), \theta_{MS}(q), \tau\right) \right|^2 \right) \qquad \textbf{(Eq. IV.2.3)}$$

2.2.3. Validation of S2 and S3 processing

The omnidirectional PDP resulting from the synthesizing procedure applied in both S2 and S3 setups is expected to be identical to the PDP that would be directly derived from measurements performed using omnidirectional MS antennas i.e. with setup S1.

Fig. IV.2.9 and **Fig. IV.2.10** show typical examples illustrating this agreement at 17 GHz between S1 and S2 and at 60 GHz between S2 and S3 respectively.

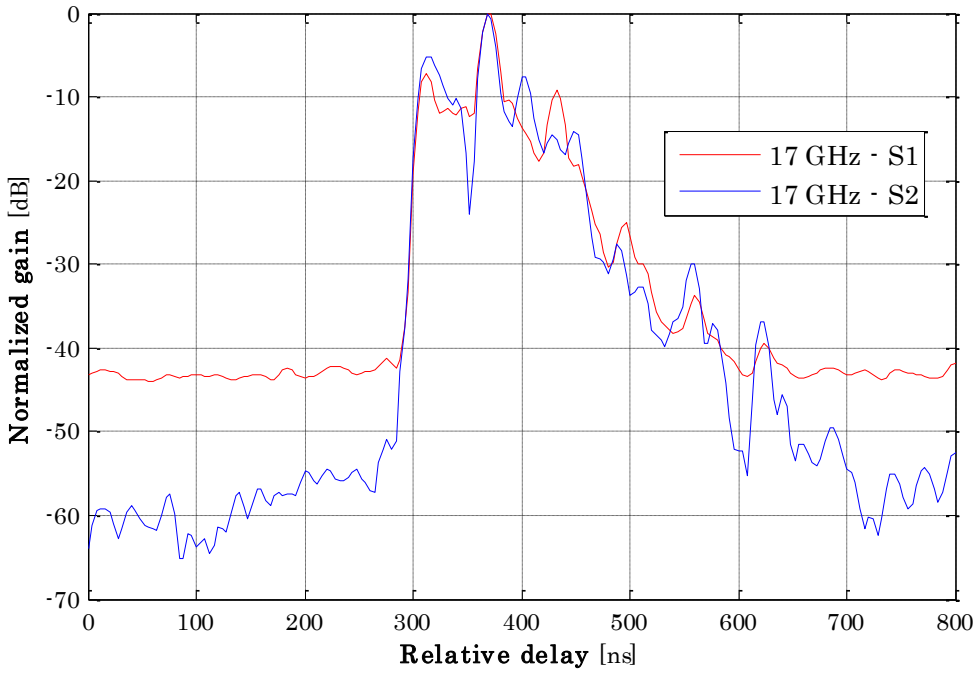

Fig. IV.2.9 – Omnidirectional PDPs from S1 and S2 at 17 GHz for MS position R24

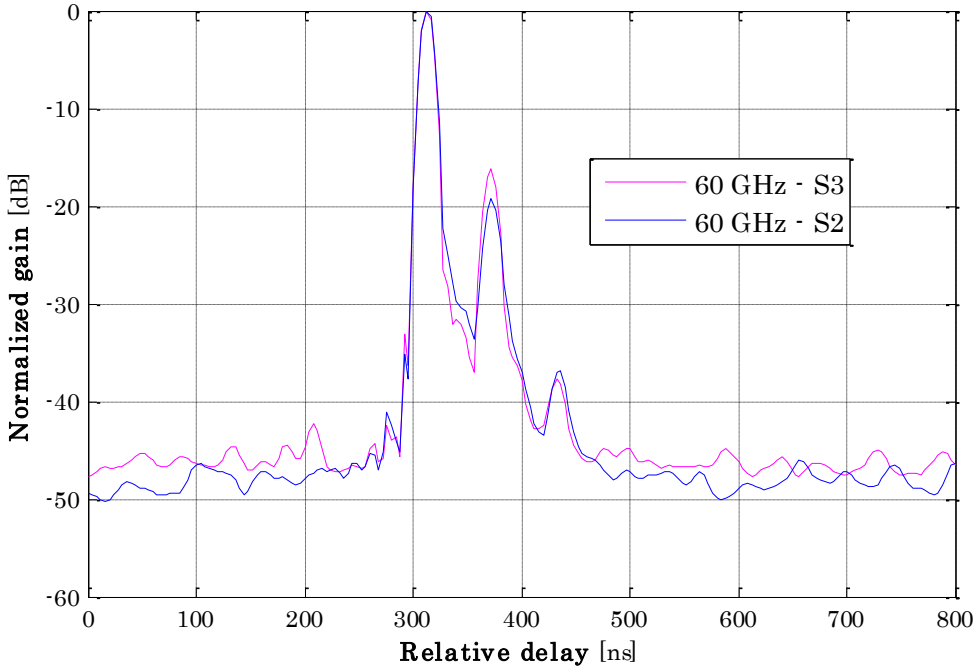

Fig. IV.2.10 – Omnidirectional PDPs from S1 and S2 at 60 GHz for MS position R23

3. Result analysis

In this section, the validity of the measurements is first addressed. Then, the discussion is centered on the estimation of the PELs caused by different window materials and the investigation of their frequency–dependence. The channel DS parameter is also investigated.

The building PELs, denoted by $PEL_{[dB]}$, are defined as the difference between the measured PL, denoted by $PL_{[dB]}$, and the theoretical free–space PL, denoted by $PL_{FS\,[dB]}$, as written in (**Eq. IV.3.1**).

$$PEL_{[dB]} = PL_{[dB]} - PL_{FS\,[dB]} \qquad \textbf{(Eq. IV.3.1)}$$

$PL_{[dB]}$ is defined in (**Eq. II.3.3**) and $PL_{FS\,[dB]} = 10 \cdot \log_{10}\left(PL_{FS}\right)$ with PL_{FS} defined in (**Eq. III.2.3**).

The expression of the channel DS, denoted by DS^{Omni}, is also given in given in (**Eq. II.3.4**).

3.1. Measurement validation

The idea herein is to verify, how close $PEL_{[dB]}$ is to zero in free–space conditions. In **Table IV.3.1**, the computed values of $PEL_{[dB]}$ for different MS positions located just behind the building, in free–space conditions i.e. "open window", are given at 3, 10, 17 and 60 GHz.

Table IV.3.1 – O2I PELs values in LoS conditions

RX positions LoS conditions	PELs [dB]					
	S1			S2		S3
	3 GHz	10 GHz	17 GHz		60 GHz	
R21	0	0	2	2	1	0
R23	0	0	1	–1	0	0
R14	1	–1	–2	–1	N/A	–1
R38	N/A	N/A	N/A	N/A	0	0

N/A: not performed

Table IV.3.1 shows that $PEL_{[dB]}$ values are comprised between –2 and 2 dB in these free–space conditions. These variations can be attributed to various factors including, but not limited to, :

- the impact of the multi–path fading phenomena which causes secondary paths to interfere with the signal LoS component,
- and the drift of the amplifier gain with temperature throughout the measurements, which may lead to some bias in the estimations.

These observations suggest that a difference up to 4 dB between measured attenuation values may not necessarily have a physical meaning. A straightaway comparison between two different MS positions and/or carrier frequencies should, therefore, be done with cautiousness.

3.2. Building penetration losses (PELs)

The building PELs $PEL_{[dB]}$ were evaluated at the 38 NLoS RX/MS positions shown in the building layout given in **Fig. IV.1.2**. The estimated values are summarized in **Table B.1** given in **Annex B**.

3.2.1. Material and frequency–dependence

In **Table IV.3.2** below, the average values of $PEL_{[dB]}$ measured in the different MS locations, including Co, Fl, BR, LO1 and LO2, are provided. Additionally, **Fig. IV.3.1** shows $PEL_{[dB]}$ values for RX positions just behind the building.

Table IV.3.2 – O2I average PELs in different MS locations

RX positions	PELs [dB]					
	S1			S2		S3
	3 GHz	10 GHz	17 GHz		60 GHz	
Co	20	20	21	21	N/A	N/A
Fl	27	30	34	34	N/A	N/A
BR	11	9	8	6	12	11
LO1	14	17	17	19	20	16
LO2	20	22	20	21	30	22

N/A: not performed or lack of sufficient dynamic range

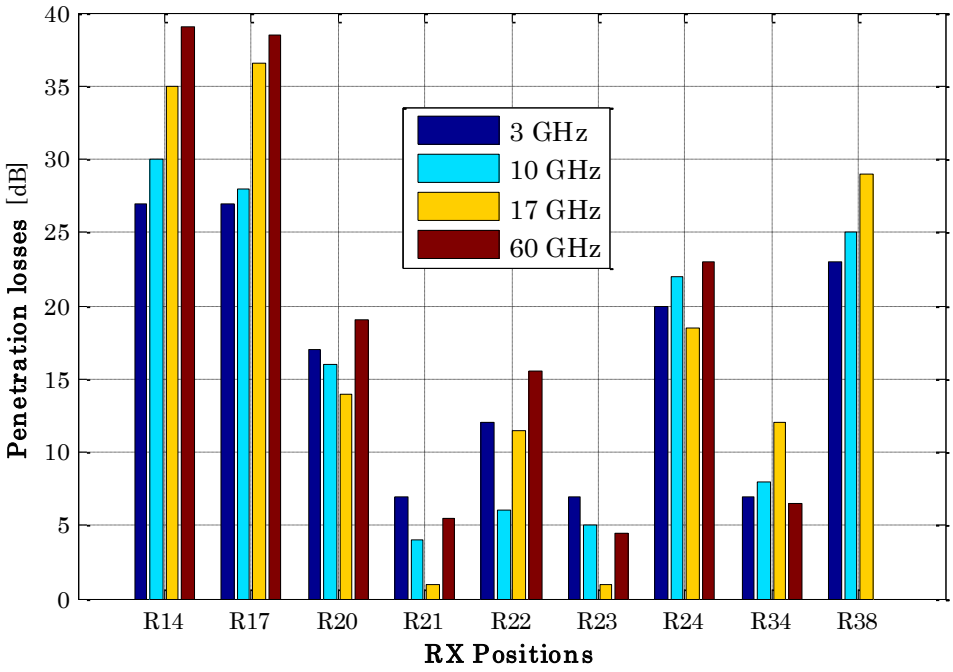

Fig. IV.3.1 – O2I PELs for MS positions just behind the indoor building

The most significant results are those from Fl and BR, separated by a bearing wall. These two locations also have the same incidence angle from the BS.

In BR, $PEL_{[dB]}$ is about 10 dB on average as shown in **Table IV.3.2**. Furthermore, **Fig. IV.3.1** shows that MS positions behind the windows (R21, R23) result in lower $PEL_{[dB]}$ values than MS positions behind the walls (R20, R22 and R24). This is expected because concrete materials usually result in greater attenuation than glass materials, as supported by the literature results provided in **Chapter II** and also demonstrated in **Chapter III**. Additionally, as shown in **Table B.1**, for the MS positions which are located deeper inside the room (R25 to R30), $PEL_{[dB]}$ is lower than the values observed just behind the walls. It is thus likely that the radio channel viewed by MS positions from R25 to R30 is dominated by the direct path and/or single–bounce reflections, while at R20, R22 and R24 the propagation may occur through multiple bounces.

In Fl, however, $PEL_{[dB]}$ is around 30 dB on average as shown in **Table IV.3.2**. In this location, MS positions facing the windows exhibit $PEL_{[dB]}$ values similar to those of other

MS positions located deeper inside the rooms, as illustrated in **Table B.1**. However at 60 GHz, for the most part, the measured CIRs do not have enough dynamic range despite the use of high gain MS antennas. Therefore, the attenuation was not quantifiable for MS positions deeper inside Fl.

These significant differences between BR and Fl is due to the different material composition of their windows since coated glass windows (Fl) result in more signal attenuation than standard glass windows (BR). There is a unanimous agreement on this matter in the literature reports provided in **Chapter II**. The theoretical analyses performed in **Chapter III** are also supportive of such a claim.

In LO1 where standard windows are found, $PEL_{[dB]}$ values for MS positions behind the windows (R34) are relatively low, around 10 dB, although higher than in BR (R21 and R23), around 5 dB, as shown in **Fig. IV.3.1**. This increase could be associated with the different incidence angles between these two rooms. This claim is also supported by literature results discussed in **Chapter II**. However, $PEL_{[dB]}$ values recorded in LO2 where coated windows are found are relatively high, around 20 dB. They are similar to those recorded in Co, but overall lower than the values in Fl. This is shown in **Table IV.3.2**. We conjecture that the electromagnetic waves propagating into BR may pass through the partition walls that separate the latter from LO2 and Co. The transmission through these walls causes additional attenuation which could also explain the scarcity of $PEL_{[dB]}$ values at 60 GHz in these locations (mainly Co), as in Fl.

There is hardly any frequency–dependence of $PEL_{[dB]}$ caused by the windows in BR whereas this parameter seems to increase slightly with the frequency with regards to the windows in Fl, especially from 3 to 17 GHz. Similar trends have been observed in the vast majority of the literature studies provided in **Chapter II** as well as in the theoretical studies presented in **Chapter III**.

3.2.2. Comparison to the 3GPP model

In [70], the building PELs for frequencies above 6 GHz are modeled as shown in (**Eq. IV.3.2**). The parameters of this model are given in **Table IV.3.3**.

$$PEL_{[dB]} = \begin{cases} A_{[dB]} - 10 \cdot \log_{10}\left(0.3 \cdot 10^{\frac{-L_{glass}}{10}} + 0.7 \cdot 10^{\frac{-L_{concrete}}{10}} \right), \text{for low loss model} \\ A_{[dB]} - 10 \cdot \log_{10}\left(0.7 \cdot 10^{\frac{-L_{IRRglass}}{10}} + 0.3 \cdot 10^{\frac{-L_{concrete}}{10}} \right), \text{for high loss model} \end{cases} \quad \textbf{(Eq. IV.3.2)}$$

Table IV.3.3 – 3GPP PELs model parameters

Materials	**Attenuation** [dB]
Standard multi–pane glass	$L_{glass} = 2 + 0.2 f_{[GHz]}$
IRR coated glass	$L_{glass} = 23 + 0.3 f_{[GHz]}$
Concrete	$L_{glass} = 5 + 4 f_{[GHz]}$

In the 3GPP modeling approach, low loss buildings are considered to be composed with 30% standard glass windows and 70% concrete while high loss buildings are supposed to be made of 70% IRR coated glass windows and 30% concrete. The variable $A_{[dB]}$ accounts for the losses caused by oblique incidence angles. These considerations are, however, not in agreement with the actual composition of the building "Orange Labs premises", where our measurements were performed. Thus, it would be ill–advised to directly compare our measurements to this model.

Therefore, $PEL_{[dB]}$ values recorded at MS positions behind the windows, where the attenuation is strictly due to the window glass materials, are compared to the material loss model given in **Table IV.3.3**. R21 and R23, located in BR, and R34 located in LO1 are the MS positions chosen to estimate the attenuation caused by the standard glass windows while R14 and R17, located in Fl, are the ones used to evaluate the losses through the IRR coated glass windows. **Fig. IV.3.2** shows the measurement results and the values provided by the 3GPP model in this regard.

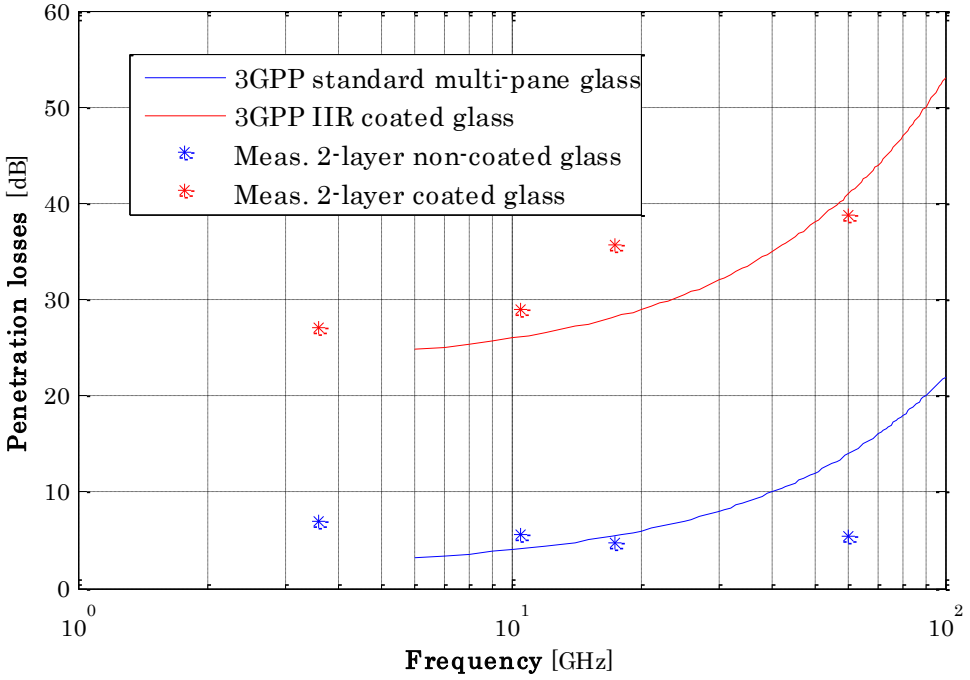

Fig. IV.3.2 – PELs comparison between measurements and the 3GPP model

Firstly, there is a good agreement between the measurements and the 3GPP model with regards to the material–dependence of $PEL_{[dB]}$. However, regarding the frequency–dependence, some disparities are observed. The measurement results support a low and almost frequency–independent $PEL_{[dB]}$ when standard windows are tested whereas the 3GPP model suggests an increasing tendency of $PEL_{[dB]}$ with increasing frequency. When coated windows are tested, an increasing behavior of $PEL_{[dB]}$ with increasing frequency is observed in both our measurements and the 3GPP model, especially between 3 and 17 GHz. However, this increasing trend is much less emphasized in our measurements between 17 and 60 GHz.

3.3. Channel delay spread (DS)

Similarly, DS^{Omni} was estimated for the 38 NLoS RX/MS positions. The derived values are summarized in **Table B.2** given in **Annex B**. The average values in the different MS locations, including Co, Fl, BR, LO1 and LO2 are given in **Table IV.3.4**. It should be noted

that a 20 dB threshold is applied on the omnidirectional PDPs in order to compute DS^{Omni}. This is a common practice in the literature, as argued in **Chapter II**, **Section 3.1**.

Table IV.3.4 – O2I average channel DS in different MS locations

RX positions	DS [ns]					
	S1			S2		S3
	3 GHz	10 GHz	17 GHz		60 GHz	
Co	19	19	19	19	N/A	N/A
Fl	22	20	19	20	N/A	N/A
BR	18	17	20	18	13	14
LO1	14	15	15	18	13	15
LO2	29	26	22	23	18	13

N/A: not performed or lack of sufficient dynamic range

In general, DS^{Omni} (less than 30 ns on average) is relatively low. This can be explained by the fact that the BS antenna was directly illuminating the indoor building so that the direct path from the BS to the building was completely cleared. Similar observations have been reported in literature studies presented in **Chapter II**, but mainly in the frequency bands below 6 GHz.

Furthermore, DS^{Omni} values measured LO2 are, on average, higher the values measured in the other locations. LO2, comprised between BR and LO1 which are made of standard glass windows, is composed with coated glass windows. Thus, it can be argued that, as $PEL_{[dB]}$ is higher in LO2, the main LoS component becomes increasingly attenuated and secondary MPCs that come from BR/LO1 contribute to higher DS^{Omni} in LO2.

Finally, DS^{Omni} seems to be weakly correlated with this frequency, especially between 3 and 17 GHz, as illustrated by the typical PDPs example given in **Fig. IV.3.3** and **Fig. IV.3.4** for the LoS and NLoS conditions respectively. However, the DS values recorded at 60 GHz are slightly lower than their counterparts in the lower frequency bands.

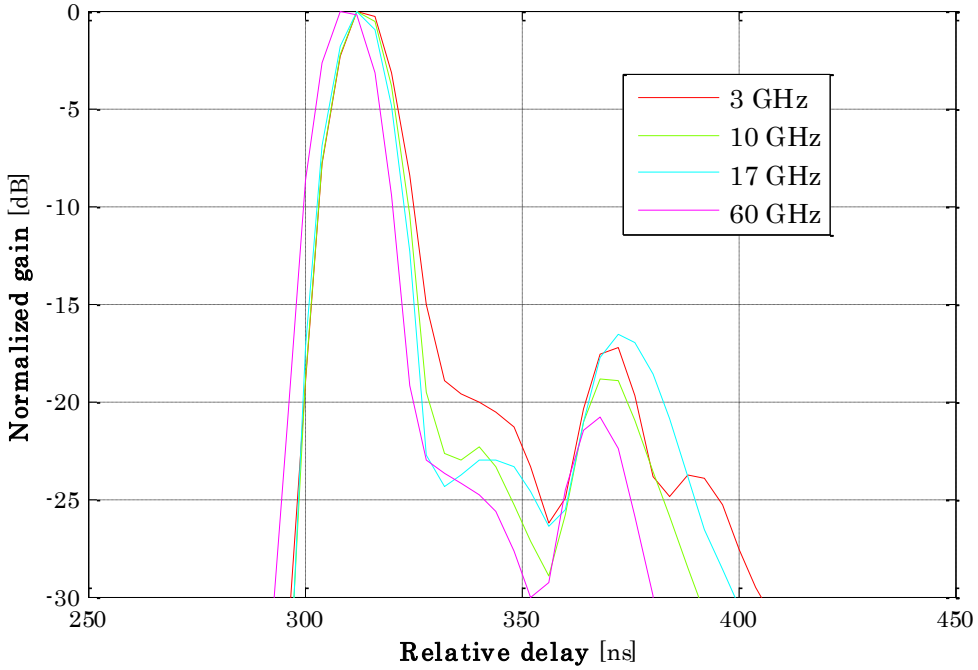

Fig. IV.3.3 – PDPs at 3, 10, 17 and 60 GHz for MS positions R21 in LoS

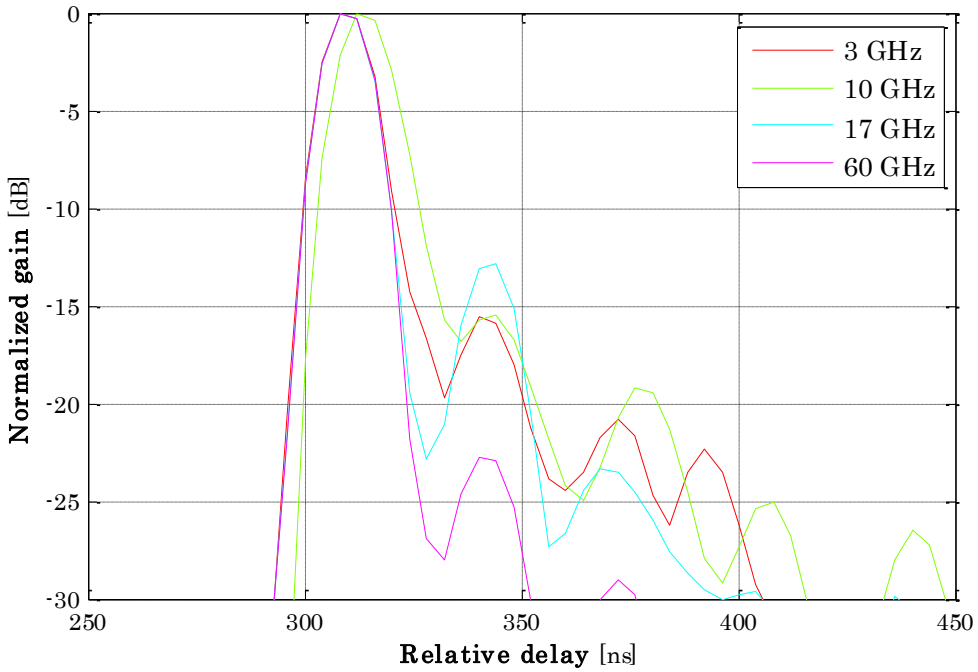

Fig. IV.3.4 – PDPs at 3, 10, 17 and 60 GHz for MS positions R30 in NLoS

4. Summary

The radio propagation channel has been investigated at 3, 10, 17 and 60. The measurement environment is an O2I scenario, with Orange Labs premises in Belfort representing the indoor building. The different rooms in this building are mainly made of concrete walls and standard or coated glass windows. Channel LSPs such as building PELs and DS have been determined at different locations inside the building.

The results reveal a strong variation in signal attenuation, between 5 and 40 dB, mainly depending on the window material composition. Two major tendencies have emerged. A relatively low and frequency–independent attenuation (around 5 dB) is observed for standard glass windows while a high attenuation (30 dB or more), slightly increasing with the frequency, is recorded for coated glass windows. The estimated channel DS values are relatively low (below 30 ns) for all the measurements and more or less uniformly distributed across the different frequency bands.

These findings suggest that radio propagation into buildings is not specifically unfavorable at mm–Wave frequencies. Rather, the building material composition has a significant impact on signal attenuation. In particular, modern buildings, usually composed with coated glass windows in order to allow for thermal insulation, may represent a limiting factor for O2I communications.

Chapter V

V. Urban Outdoor Propagation Channel Measurements

In continuity with the O2I channel measurement studies described in **Chapter IV**, the radio propagation channel has also been investigated in an urban outdoor environment. The measurement campaign conducted in this regard is described in this chapter.

In this measurement campaign, the main objective is to evaluate the frequency–dependence of the channel DS in urban outdoor scenarios in the frequency bands including 3, 17 and 60 GHz. Furthermore, since directional antennas are foreseen to be used in future 5G systems, their impact on the channel DS parameter is discussed. Additionally, other important channel characteristics such as the azimuth–delay power profile (ADPP), the channel AS and the propagation PL are investigated, especially at 17 and 60 GHz, in order to allow for a deeper comparison between different mm–Wave frequency bands.

Similarly to the outline of **Chapter IV**, the measurement scenario and setups and procedures are first presented in **Section 1.** Then, **Section 2** describes the measurement data processing. In **Section 3**, the measurement results analysis is provided. Finally, a summary is provided in **Section 4**.

1. Urban Outdoor measurement campaign

1.1. Measurement scenario description

The measurement campaign was conducted in the industrial area "Techn'hom" in Belfort, where Orange Labs premises are located. The aerial map view of the measurement environment is depicted in **Fig. V.1.1**.

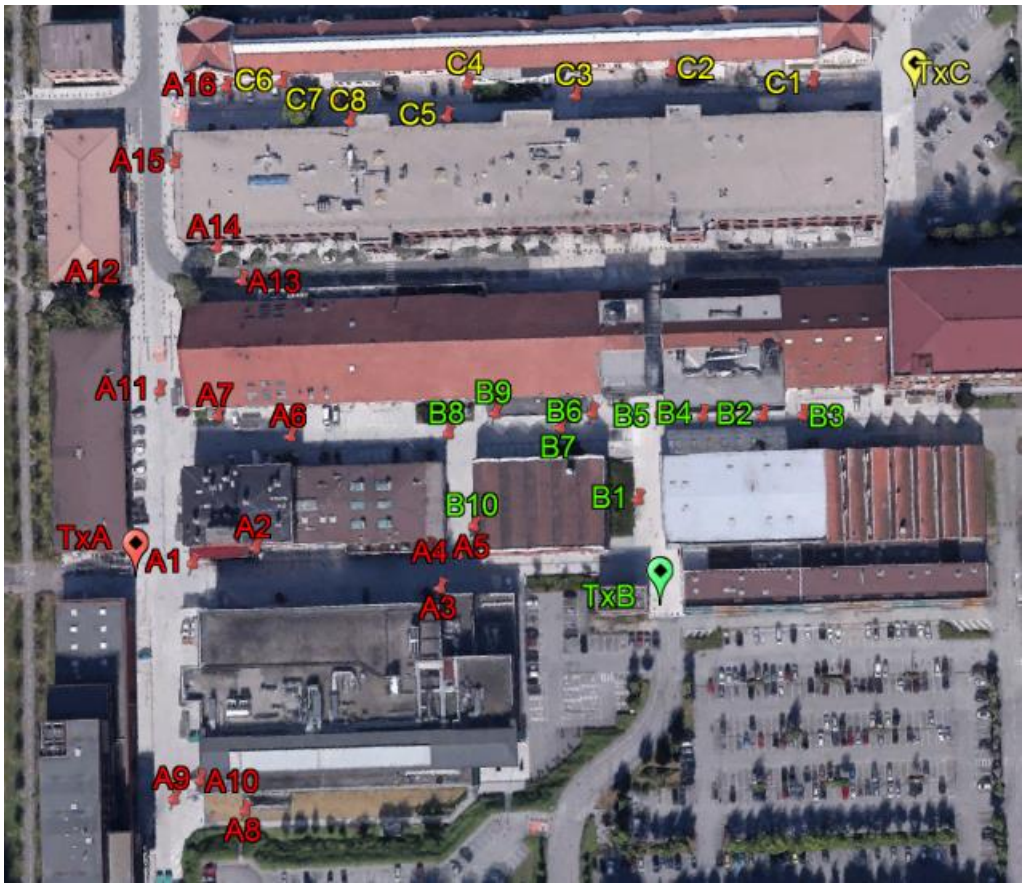

Fig. V.1.1 – Aerial map view of the outdoor measurement environment

This map view shows the three distinctive transmission points that were considered during the measurement: TxA, TxB and TxC. At each transmission point, the TX antenna was mounted on top of a van at 4 m above ground level. Then, a set of LoS and NLoS measurements were performed with the RX antenna placed at different positions as shown in **Fig. V.1.1**. A1 to A16 denote the RX antenna positions for the transmission point TxA, B1 to B11 for TxB and C1 to C8 for TxC. The RX antenna height was kept at mobile user level i.e. 1.5 m high above ground level. The distance between the TX and the 35 RX positions ranged from 16 to 200 m, illustrating an UMi scenario. In the remainder of this chapter, the TX and RX will also be referred to as the BS and MS respectively.

1.2. Measurement setups

The measurements were performed with the same channel sounder [112] as the one used in the previous campaign described in **Chapter IV**. Both directional and omnidirectional antennas were used at both ends. In addition to enabling more dynamic range at higher

frequencies, the directional measurements performed in this campaign also aim at studying the directional characteristics of the radio propagation channel, important for future 5G mm–Wave systems as argued in **Chapter II**, **Section 3.3**.

Similarly to the O2I measurements, two setups were considered depending on the MS antenna radiation patterns, as shown in **Table V.1.1**. For setup S1, omnidirectional MS antennas were used while setup S2 used directional MS antennas, with 90° HPBW.

On the BS side, irrespective of the setup, an omnidirectional antenna was used at 3 GHz while directional antennas, with 30° HPBW, were used at 17 and 60 GHz. The antenna gains are given in **Table V.1.1**.

Table V.1.1 – Urban outdoor measurement setup parameters

Parameters	Measurement Setups				
	S1			S2	
	3 GHz	17 GHz	60 GHz	17 GHz	60 GHz
Frequency [GHz]	3.6 – 3.725	17.3 – 17.425	59.875 – 60.125	17.3 – 17.425	59.875 – 60.125
RX/MS Antenna	Omni. 1 dBi	Omni. 0 dBi	Omni. 0 dBi	90° HPBW 7 dBi	90° HPBW 6 dBi
TX/BS Antenna	Omni. 1 dBi	30° HPBW 13 dBi	30° HPBW 15 dBi	30° HPBW 13 dBi	30° HPBW 15 dBi
Antenna Polarization	Vertical				
Bandwidth [MHz]	125 (250 at 60 GHz)				
TX power	From 20 dBm (60 GHz) to 30 dBm (3 GHz)				

Omni. : Omnidirectional

Fig. V.1.2 and **Fig. V.1.3** below display the TX/BS and RX/MS measurement equipments respectively, at 17 and 60 GHz. The measurement equipment at 3 GHz is the same as the one presented in **Chapter IV** for the O2I measurement campaign.

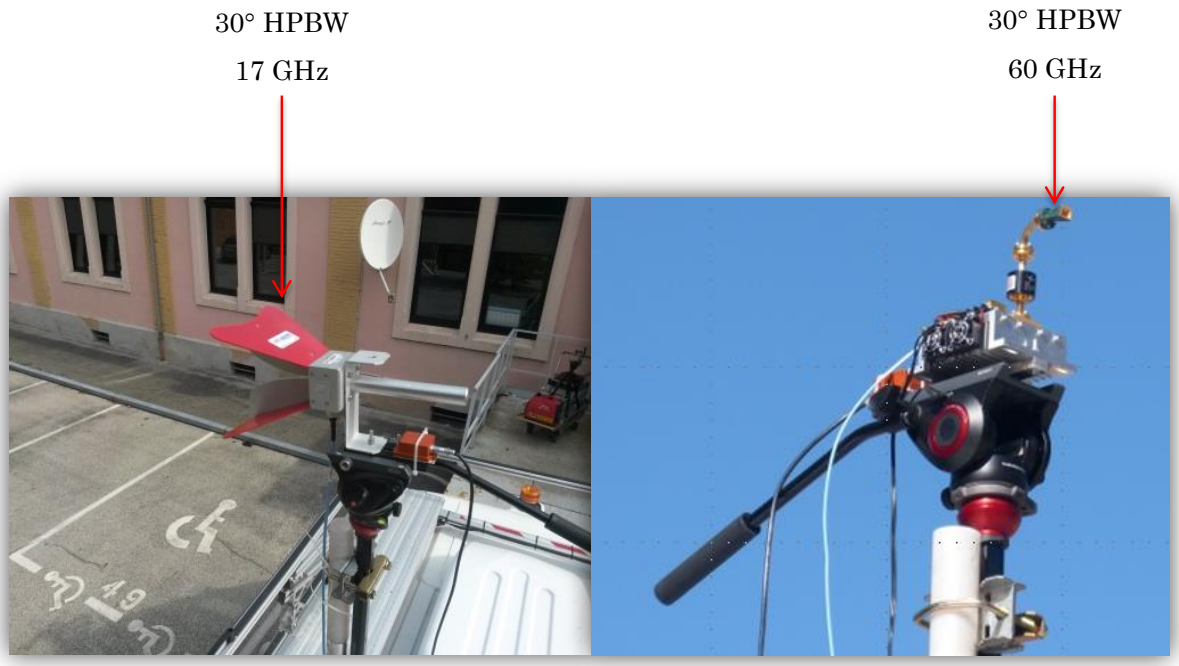

Fig. V.1.2 – TX/BS outdoor measurement equipment

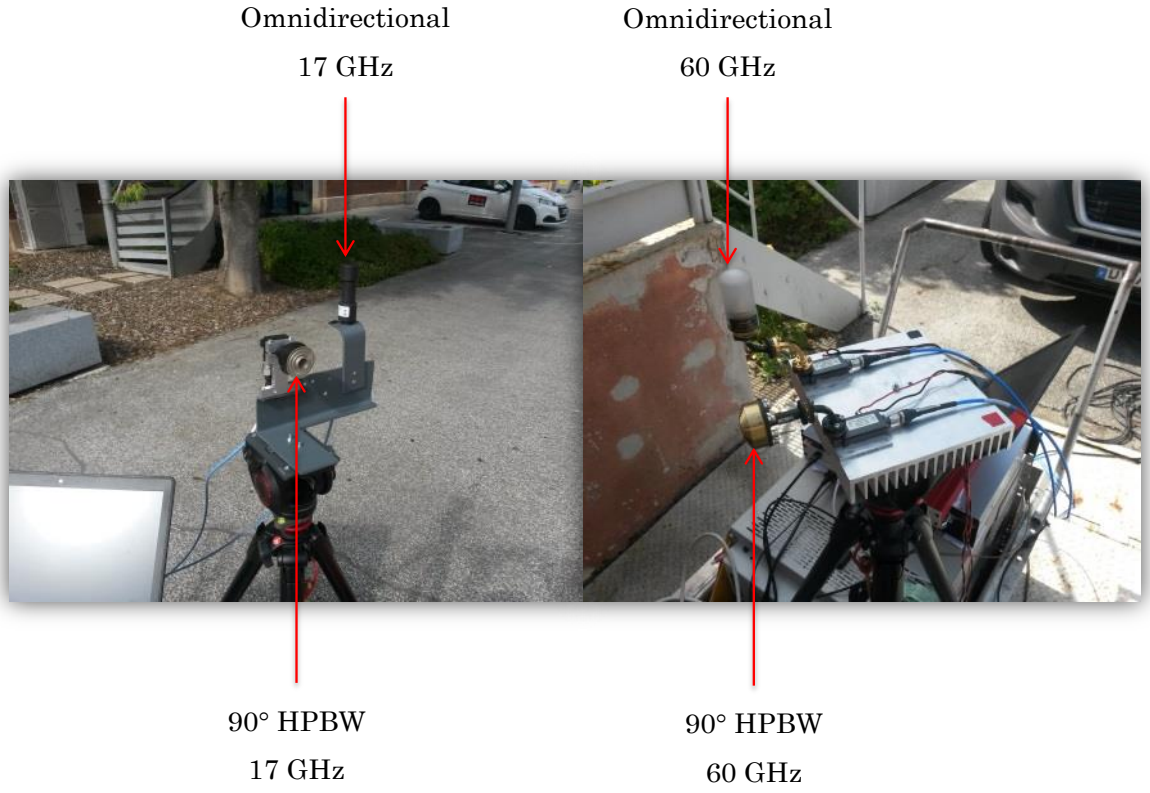

Fig. V.1.3 – RX/MS outdoor measurement equipment

1.3. Measurement procedure

At 3 GHz, the omnidirectional BS antenna was fixed and the MS antenna was slightly moved over a few tens of λ, where λ denotes the radio signal wavelength, while channel CIRs were being collected.

At 17 and 60 GHz, the measurement procedure was the same. Both the omnidirectional and the 90° HPBW MS antennas were steered into four distinctive sectors, with a 90° angular step. In each sector, the 30° HPBW directional BS antenna was scanning the entire azimuth dimension while CIRs were being collected on each of the two MS antennas, simultaneously. With an angular step equal to about 10°, a total of 36 pointing angles could be counted on the BS side. This is illustrated in **Fig. V.1.4** below.

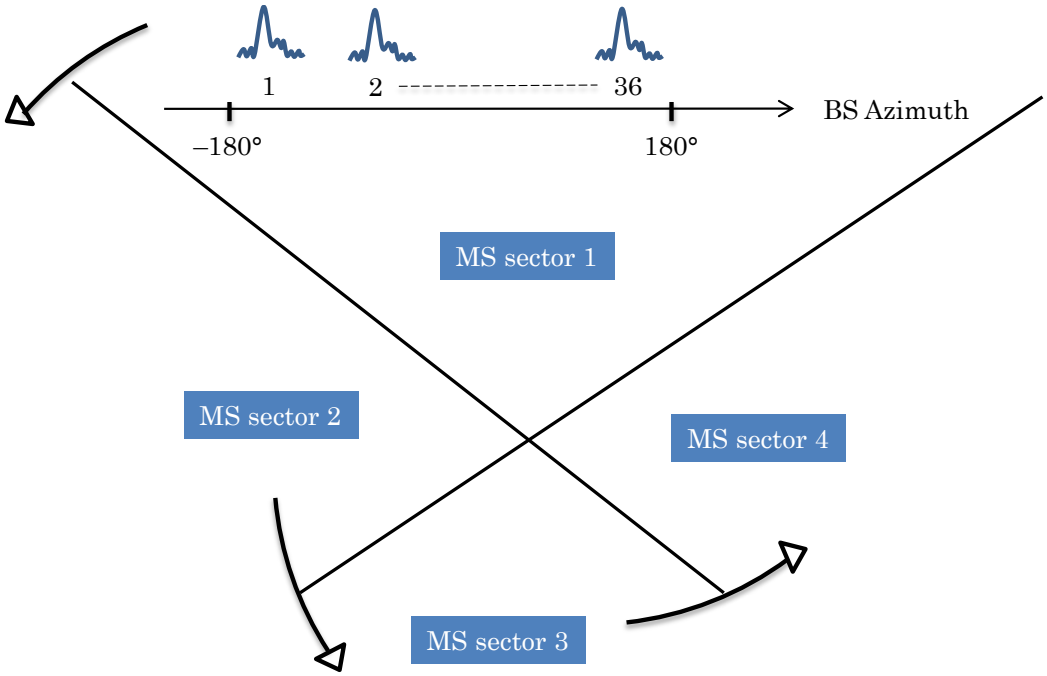

Fig. V.1.4 – Illustration of the measurement procedure for S2

2. Measurement data processing

In this section, both omnidirectional and directional propagation channel characteristics are presented. First, omnidirectional PDPs are computed at 3, 10 and 60 GHz. The channel parameters extracted from such characteristics give an interesting insight into the propagation channel at mm–Wave frequencies. However, they are not very representative of

envisioned 5G mm–Wave systems, where directional antennas are expected to be used. Therefore directional PDPs have also been computed from the directional measurements performed at 17 and 60 GHz in this regard.

2.1. Omnidirectional power delay profiles (PDPs)

At 3 GHz, let $h_n^{Omni}(\tau)$ denote the n^{th} CIR measured during the MS antenna motion with τ denoting the propagation delay. Let N, equal to a few hundred, denote the total number of CIRs collected during the MS antenna motion. The omnidirectional PDP, denoted by $PDP^{Omni}(\tau)$, is computed as the average gain, associated with each propagation path, between the N measured CIRs (**Eq. V.2.1**). As argued in **Chapter IV**, this practice contributes to the lowering of the multi–path fading effects.

$$PDP^{Omni}(\tau) = \frac{1}{N}\sum_{n=1}^{N}\left|h_n^{Omni}(\tau)\right|^2 \qquad \textbf{(Eq. V.2.1)}$$

At 17 and 60 GHz, a 30° (BS antenna HPBW) spaced BS–grid is first synthesized in the azimuth domain from S2 measurements illustrated in **Fig. V.1.4**, where a 10° step was considered. We thus denote by $h_{p,k}^{Dir}(\phi_{BS}(p), \phi_{MS}(k), \tau)$ the CIR measured at the p^{th} BS antenna pointing angle $\phi_{BS}(p)$ and the k^{th} MS antenna pointing angle $\phi_{MS}(k)$. Let P, equal to 12, and K, equal to 4, denote the total number of BS and MS pointing angles respectively.

The omnidirectional PDP denoted by $PDP^{Omni}(\tau)$ is derived in two ways depending on the MS antenna radiation patterns (i.e. measurement setups), as indicated in (**Eq. V.2.2**). With the 90° HPBW directional antenna (setup S2), the omnidirectional PDP is obtained by summing the contributions from the four different MS antenna pointing angles since the angular step is equal to the MS antenna HPBW. With the omnidirectional antenna (setup S1), the four contributions from the four different MS pointing angles are averaged. On the BS side, irrespective of the setup, the contributions from the P pointing angles are summed since the angular step of the synthesized BS–grid is equal to the BS antenna HPBW. These synthesizing methods are based on the same approach described in **Chapter IV**.

$$PDP^{Omni}(\tau)=\begin{cases}\sum_{p=1}^{P}\left(\frac{1}{K}\sum_{k=1}^{K}\left|h_{p,k}^{Dir}\left(\phi_{BS}(p),\phi_{MS}(k),\tau\right)\right|^2\right), \text{ for setup S1}\\ \sum_{p=1}^{P}\left(\sum_{k=1}^{K}\left|h_{p,k}^{Dir}\left(\phi_{BS}(p),\phi_{MS}(k),\tau\right)\right|^2\right), \text{for setup S2}\end{cases} \quad \textbf{(Eq. V.2.2)}$$

2.2. Directional power delay profiles

The directional PDPs computed from the directional measurements performed at 17 and 60 GHz are of two types. On one hand omnidirectional antenna patterns are assumed at the MS end while directional antenna patterns are considered on the BS side. The computed PDPs are thus referred to as "single–directional" PDPs. On the other hand, directional antenna patterns are considered at both ends of the link (BS and MS). The computed PDPs are thus referred to as "double–directional" PDPs.

The single–directional PDP is a function of the BS antenna pointing angle $\phi_{BS}(p)$. Denoted by $PDP_{BS}^{Dir}\left(\phi_{BS}(p),\tau\right)$, its expression is given in (**Eq. V.2.3**). The omnidirectional MS antenna patterns can be synthesized in two ways as indicated in (**Eq. V.2.2**).

$$PDP_{BS}^{Dir}\left(\phi_{BS}(p),\tau\right)=\begin{cases}\frac{1}{K}\sum_{k=1}^{K}\left|h_{p,k}^{Dir}\left(\phi_{BS}(p),\phi_{MS}(k),\tau\right)\right|^2, \text{ for setup S1}\\ \sum_{k=1}^{K}\left|h_{p,k}^{Dir}\left(\phi_{BS}(p),\phi_{MS}(k),\tau\right)\right|^2, \text{for setup S2}\end{cases} \quad \textbf{(Eq. V.2.3)}$$

The double–directional PDP is a function of both the BS and MS antenna pointing angles, $\phi_{BS}(p)$ and $\phi_{MS}(k)$ respectively. It is denoted by $PDP_{BS-MS}^{Dir}\left(\phi_{BS}(p),\phi_{MS}(k),\tau\right)$ and its expression is given in (**Eq. V.2.4**). It should be noted that only the 90° HPBW MS antenna (setup S2) is considered in this case.

$$PDP_{BS-MS}^{Dir}\left(\phi_{BS}(p),\phi_{MS}(k),\tau\right)=\left|h_{p,k}^{Dir}\left(\phi_{p}^{BS},\phi_{k}^{MS},\tau\right)\right|^2 \quad \textbf{(Eq. V.2.4)}$$

2.3. Atmospheric oxygen attenuation

The 60 GHz frequency band is especially characterized by higher energy absorption due to oxygen molecules compared to lower frequencies. Thus, it is important to take into account this phenomenon in order to avoid the introduction of a bias in the comparisons between the different frequency bands. The attenuation of 16 dB per kilometer due to oxygen absorption

is usually considered. This corresponds to the attenuation $\psi_{[dB]} = 0.0048$ per nanosecond. The expression in (**Eq. V.2.5**) gives the relation between a given raw PDP, denoted by PDP_{Raw}, and the compensated PDP, denoted by PDP_{Comp}, where this oxygen attenuation is compensated for.

$$PDP_{Comp}(\tau) = PDP_{Raw}(\tau) \cdot 10^{\left(\psi_{[dB]} \cdot \tau / 1ns\right) / 10} \qquad \textbf{(Eq. V.2.5)}$$

The oxygen absorption impact can be observed in **Fig. V.2.1**. The effects of this phenomenon are more emphasized at larger delays, where MPCs undergo higher attenuation in the absence of compensation of such effects. The 60 GHz PDPs given in (**Eq. V.2.1.–V.1.4**) take into account these effects in order to ensure fairer comparisons with the lower frequency bands. It should however be noted that, for the ranges (up to 25 m) considered in the O2I campaign described in **Chapter IV**, this phenomenon is insignificant.

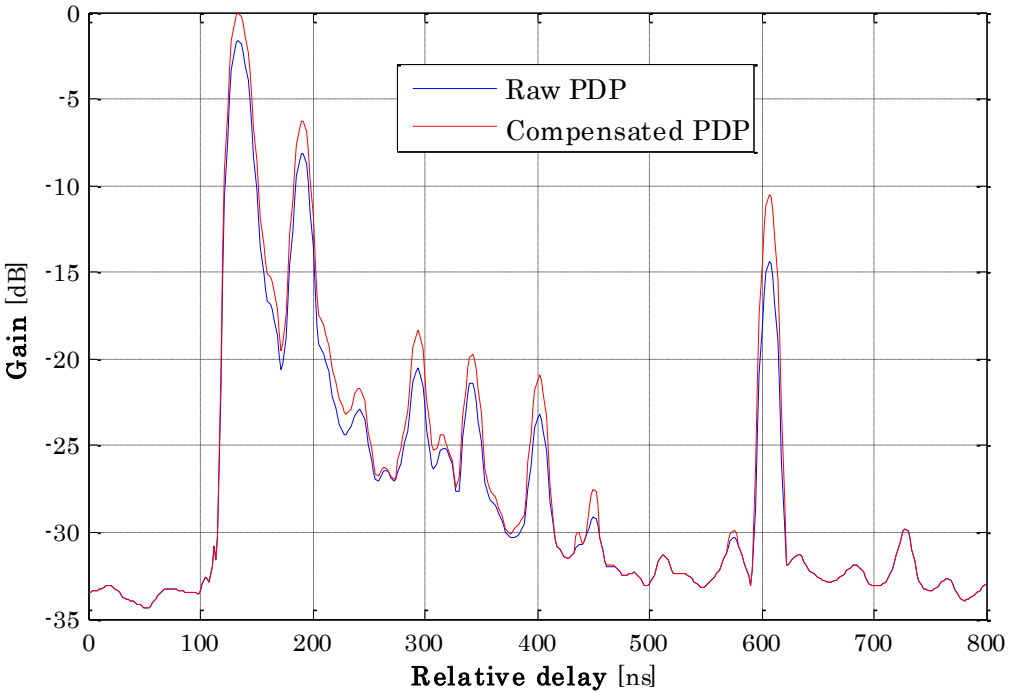

Fig. V.2.1 – Impact of oxygen absorption at 60 GHz for MS position A4

3. Result analysis

3.1. Channel delay spread (DS)

From the PDPs defined in (**Eq. V.2.1–V.1.4**), corresponding channel DS are derived accordingly to (**Eq. II.3.5**). Thus, we denote by DS^{Omni} the omnidirectional DS estimated from $PDP^{Omni}(\tau)$ at 3, 17 and 60 GHz whereas $DS_{BS}^{Dir}(\phi_{BS}(p))$ and $DS_{BS-MS}^{Dir}(\phi_{BS}(p),\phi_{MS}(k))$ denote the single–directional and double–directional DS computed from $PDP_{BS}^{Dir}(\phi_{BS}(p),\tau)$ and $PDP_{BS-MS}^{Dir}(\phi_{BS}(p),\phi_{MS}(k),\tau)$ respectively, at both 17 and 60 GHz. Similarly to the analysis in **Chapter III**, a 20 dB threshold is applied for the computation of these DS values.

3.1.1. Omnidirectional delay spread (DS)

In **Table C.1.1** given in **Annex C**, the omnidirectional DS values DS^{Omni}, computed for the 35 different MS positions are given for the 3, 17 and 60 GHz frequency bands. Their cumulative distribution functions (CDFs) are represented in **Fig. V.3.1** and **Fig. V.3.2** for the LoS and NLoS conditions respectively.

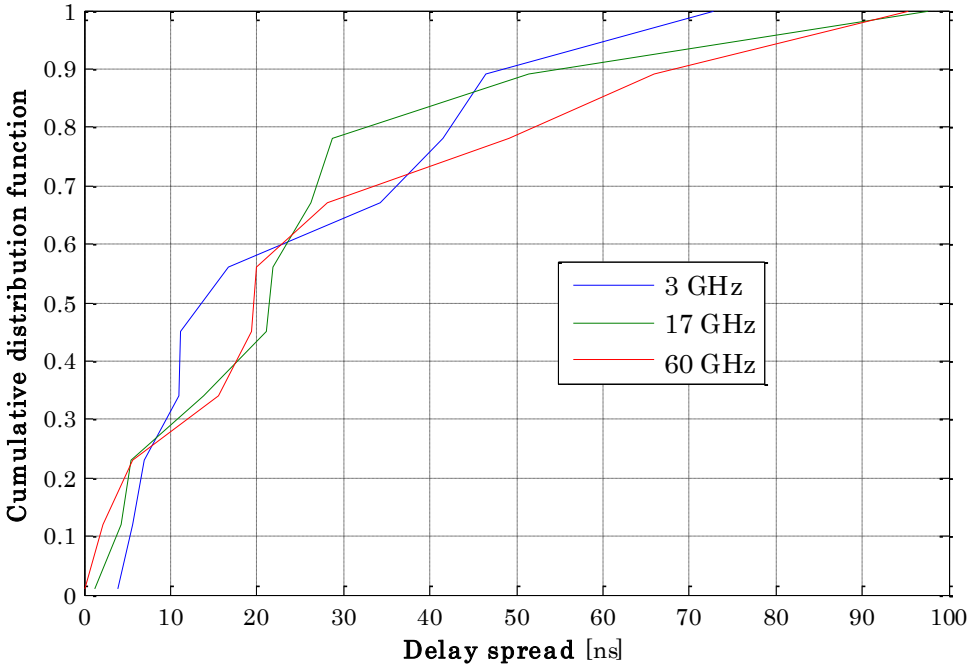

Fig. V.3.1 – CDFs of the omnidirectional channel DS in LoS

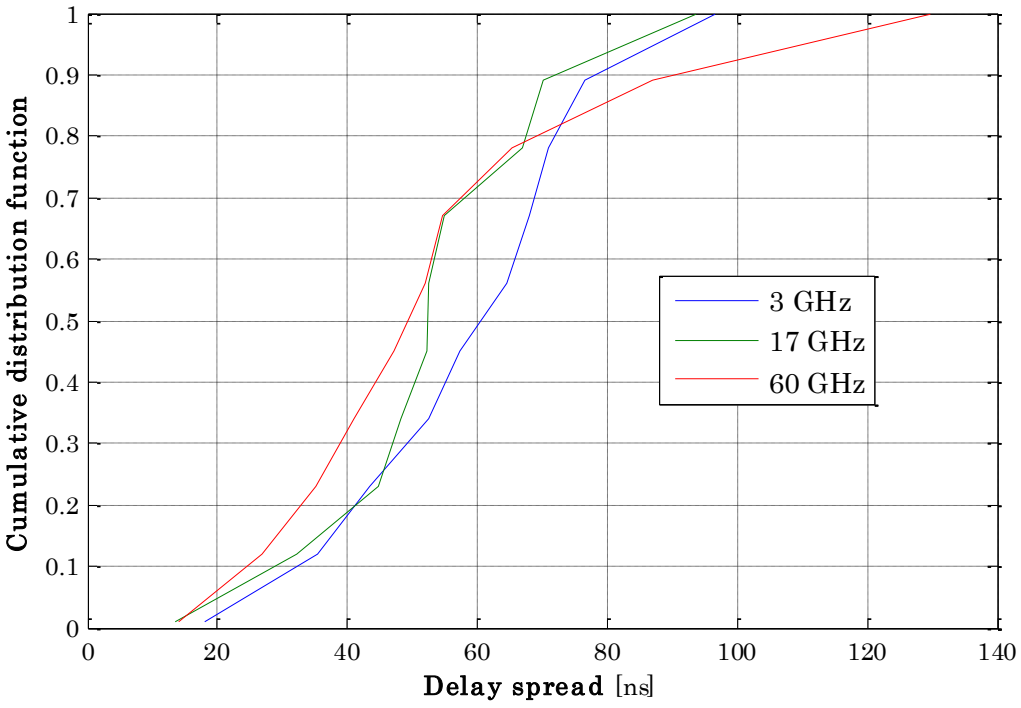

Fig. V.3.2 – CDFs of the omnidirectional channel DS in NLoS

Expectedly, DS^{Omni} is larger in NLoS than in LoS conditions. The 90 percentile is roughly comprised between 50 and 70 ns in LoS conditions whereas in NLoS conditions, it is comprised between 70 and 90 ns. Similarly, the 50 percentile is roughly comprised between 10 and 20 ns in LoS conditions and 50 and 60 ns in NLoS conditions. Statistically, the CDFs given in **Fig. V.3.1** and **Fig. V.3.2** for the LoS and NLoS conditions respectively do not indicate a significant frequency–dependence of DS^{Omni}.

In order to refine our upcoming analysis, measurements were split into three generic urban outdoor scenarios in accordance with the environment described with the transmission points TxA, TxB and TxC. In this sense, TxA defines an open square (OS), TxB a street intersection (SI) and TxC a street canyon (SC). The average values of DS^{Omni} measured in these scenarios, in both LoS and NLoS conditions, are summarized in **Table V.3.1**.

Table V.3.1 – Average DS values in the specific outdoor scenarios

Scenarios	Omnidirectional DS [ns]		
	3 GHz	17 GHz	60 GHz
LoS			
Open Square (OS)	26	30	41
Street Intersection (SI)	35	35	25
Street Canyon (SC)	9	7	6
NLoS			
Open Square (OS)	64	49	43
Street Intersection (SI)	69	63	59
Street Canyon (SC)	35	52	65

On average, as the frequency increases, only a marginal decrease of 9% from 3 to 17 GHz and 2% from 17 to 60 GHz of DS^{Omni} values can be observed in NLoS conditions whereas in LoS conditions, DS^{Omni} increases slightly by about 8% from both 3 to 17 and 17 to 60 GHz.

However, different tendencies with regards to the frequency may emerge from the different measurement scenarios including OS, SI and SC. To illustrate these trends, typical examples of PDPs are provided in **Fig. V.3.3**, **Fig. V.3.4** and **Fig. V.3.5** for OS, SI and SC respectively.

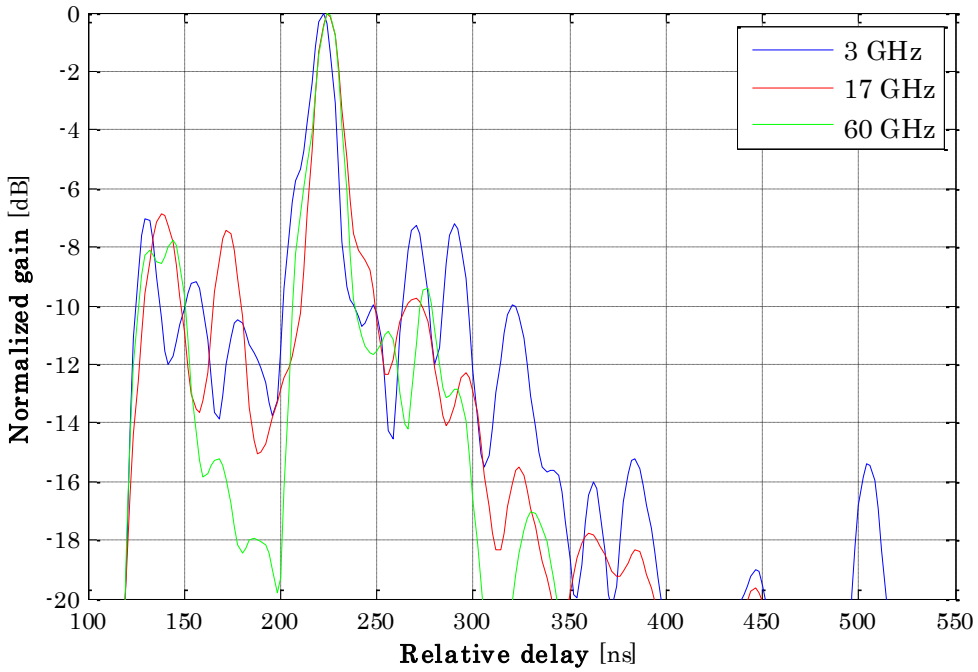

Fig. V.3.3 – PDPs at 3, 17 and 60 GHz for MS position A8 in scenario OS

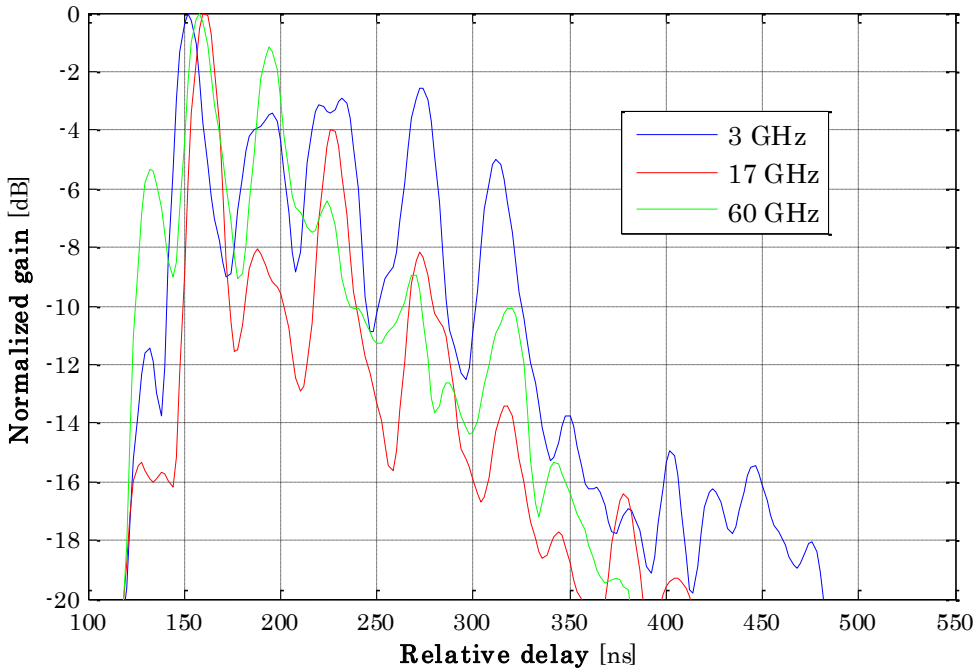

Fig. V.3.4 – PDPs at 3, 17 and 60 GHz for MS position B4 in scenario SI

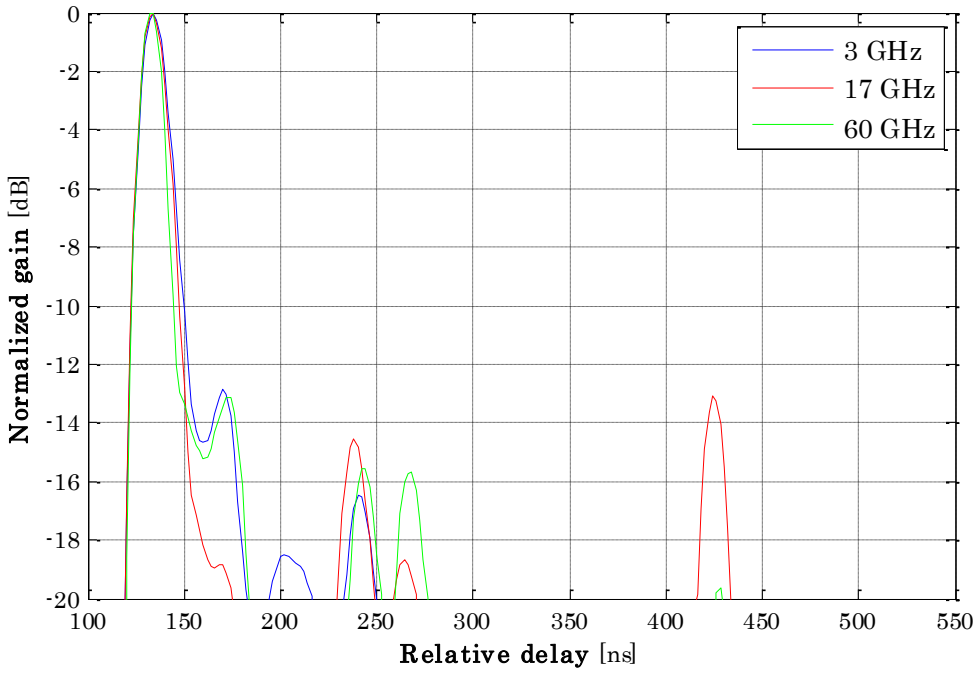

Fig. V.3.5 – PDPs at 3, 17 and 60 GHz for MS position C4 in scenario SC

For scenarios OS and SI, DS^{Omni} is larger at 3 GHz compared to 17 and 60 GHz while an opposite behavior is observed in scenario SC. Similar trends have been reported in literature results presented in **Chapter II**.

In comparison with the 3GPP channel model described in (**Eq. V.3.1**), for frequencies above 6 GHz for UMi scenarios [70], **Fig. V.3.6** shows that the measured DS values are, on average, in good agreement with the model at 60 GHz. However, at 17 GHz, the measurements result in lower DS values than those provided by the 3GPP model. This may be due to the fact that the outdoor measurement environment in Belfort is less reflective that those considered in the 3GPP studies. Additionally, whereas the 3GPP model clearly supports a decreasing behavior of the channel DS with increasing frequency, the measurement results do not indicate a distinctive trend in this regard.

$$\mu_{\lg DS} = \begin{cases} -0.24 \cdot \log_{10}\left(1 + f_{[GHz]}\right) - 7.14, \text{ for LoS} \\ -0.01 \cdot \log_{10}\left(1 + f_{[GHz]}\right) - 6.83, \text{ for NLoS} \end{cases} \quad \textbf{(Eq. V.3.1)}$$

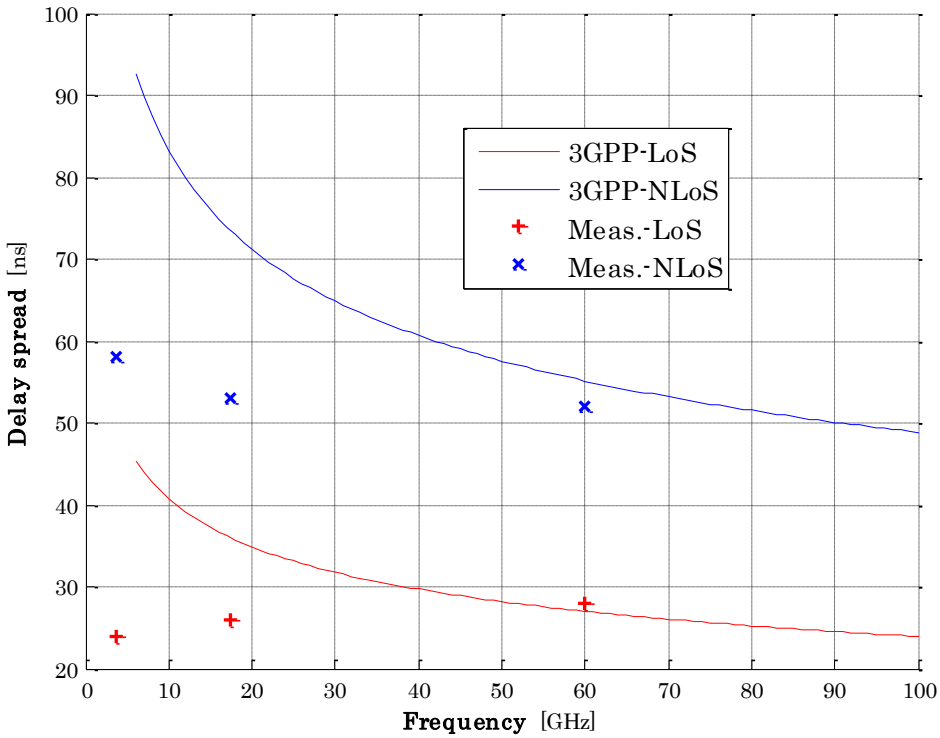

Fig. V.3.6 – Channel DS comparisons between measurements and the 3GPP model

3.1.2. Directional delay spread (DS)

The single–directional and double–directional DS, $DS_{BS}^{Dir}\left(\phi_{BS}(p)\right)$ and $DS_{BS-MS}^{Dir}\left(\phi_{BS}(p),\phi_{MS}(k)\right)$ respectively, are determined at each of the 35 different MS positions for the 17 and 60 GHz frequency bands, where directional antennas were used. The 20 dB noise threshold requirement was unfortunately not often met at 60 GHz because of the increase of propagation losses in this frequency band.

Hence, the statistical studies below are restricted to the 17 GHz frequency band.

In wireless communications scenarios, the system will typically favor the strongest beams i.e. $\phi_{BS}(p)$ and/or $\phi_{MS}(k)$ pointing angles that allow for the greatest channel gains. We thus denote by $DS_{BS,Max}^{Dir}$ and $DS_{BS-MS,Max}^{Dir}$ the corresponding channel DS values for the single–directional and double–directional cases respectively, considering these strongest beams. In **Fig. V.3.7** and **Fig. V.3.8**, plotted are $DS_{BS,Max}^{Dir}$, $DS_{BS-MS,Max}^{Dir}$ and DS^{Omni} (comparative reference)

values, measured at the different MS positions, in LoS and NLoS conditions respectively. The mean values across the different MS positions are also provided.

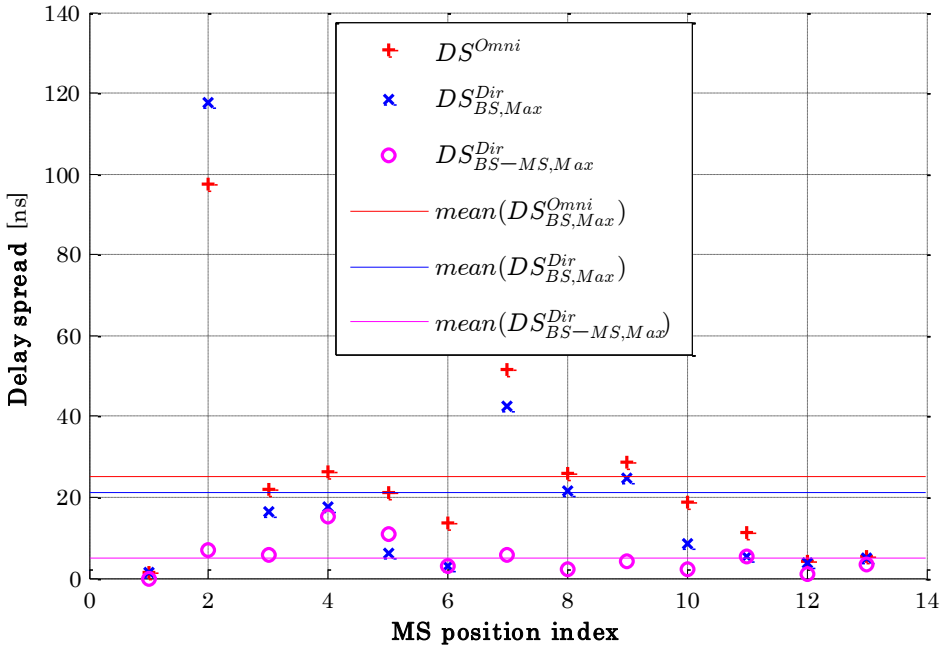

Fig. V.3.7 – Directional DS values for the strongest beams in LoS

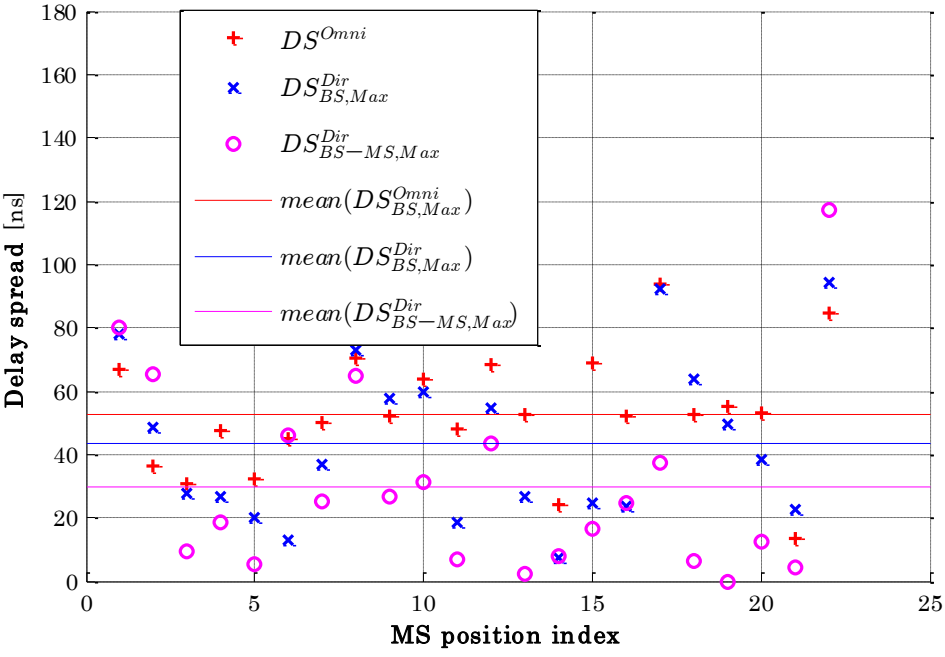

Fig. V.3.8 – Directional DS values for the strongest beams in NLoS

On average, when the strongest beams are considered, a reduced BS and/or MS antenna angular aperture results in a decrease of the channel DS. In LoS conditions, this decrease is about 16% from the omnidirectional to the single–directional case and 76% from the single–directional to the double–directional case. In NLoS conditions, the channel DS decreases by 17% from the omnidirectional to the single–directional case and by 32% from the single–directional to the double–directional case. It can thus be concluded that channel DS decreases with antenna angular aperture, in the most favorable propagation conditions.

However, assuming the strongest beams become obstructed due to blockage phenomena, the wireless system may consider alternative beam configurations, referred to as secondary beams herein, with greater channel gains. To assess the impact of these phenomena on the channel DS, $DS_{BS}^{Dir}\left(\phi_{BS}(p)\right)$ and $DS_{BS-MS}^{Dir}\left(\phi_{BS}(p),\phi_{MS}(k)\right)$, the directional DS values measured for all possible beams, are given in **Fig. V.3.9** and **Fig. V.3.10** respectively, for a typical NLoS example. $DS_{BS,Max}^{Dir}$, $DS_{BS-MS,Max}^{Dir}$ and DS^{Omni} are also provided as comparative references.

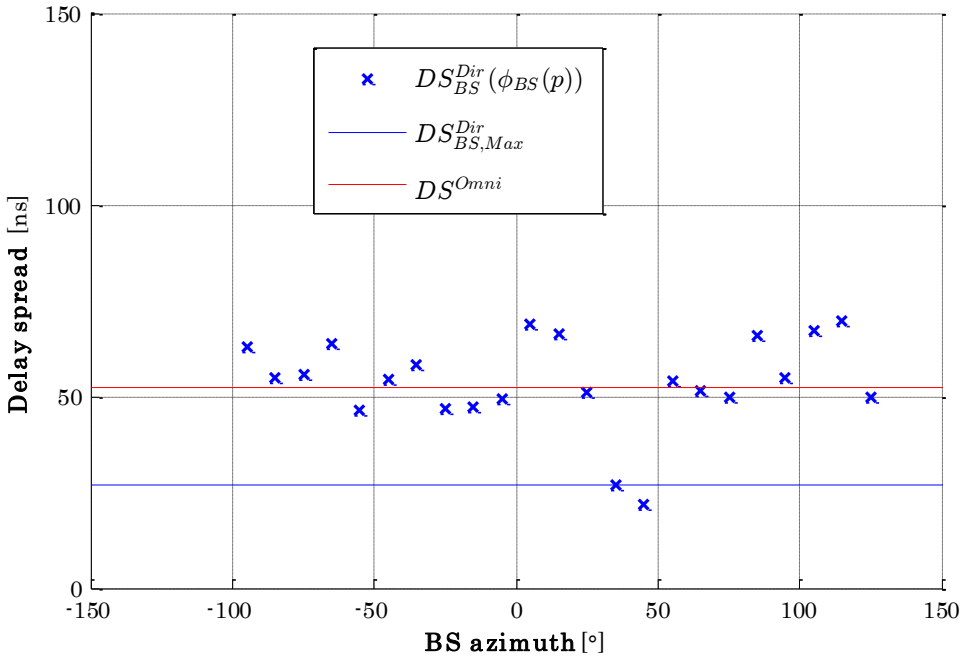

Fig. V.3.9 – Single–directional DS for MS position B4 in NLoS

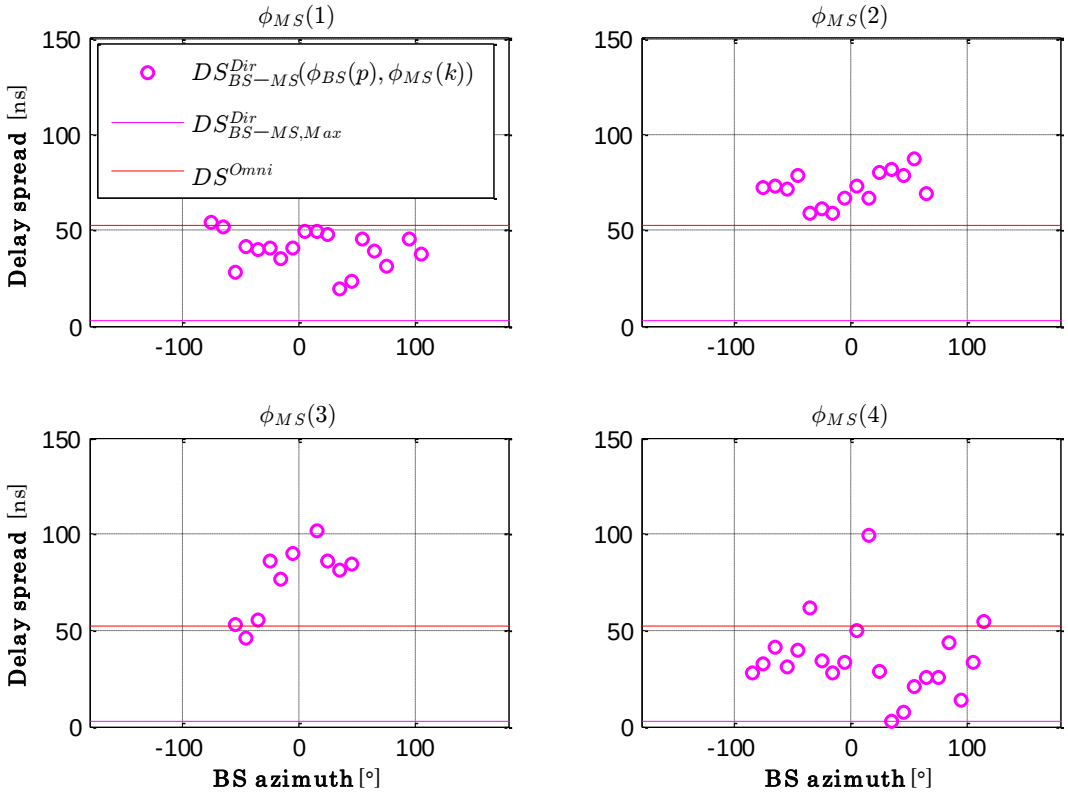

Fig. V.3.10 – Double–directional DS for MS position B4 in NLoS

It can be observed that the secondary beams result in higher DS values compared to the strongest beams. In fact, when the strongest beams are obstructed, the direct component power level decreases. This situation results in an increased importance of the secondary MPCs and, consequently, in larger channel DS values. There is also an important dispersion the DS values provided by these secondary beams, even more in the double–directional case. However, they remain overall more or less evenly spread around the omnidirectional DS value. To further illustrate this latest observation, differential values between the DS provided by the secondary beams and the omnidirectional DS, denoted by $\delta DS^{Dir}_{BS}\left(\phi_{BS}(p)\right)$ and $\delta DS^{Dir}_{BS-MS}\left(\phi_{BS}(p),\phi_{MS}(k)\right)$, for the single–directional and double–directional cases respectively, are defined for all MS positions, in (**Eq. V.3.2–V.3.3**).

$$\delta DS^{Dir}_{BS}\left(\phi_{BS}(p)\right) = DS^{Dir}_{BS}\left(\phi_{BS}(p)\right) - DS^{Omni} \qquad \textbf{(Eq. V.3.2)}$$

$$\delta DS^{Dir}_{BS-MS}\left(\phi_{BS}(p),\phi_{MS}(k)\right) = DS^{Dir}_{BS-MS}\left(\phi_{BS}(p),\phi_{MS}(k)\right) - DS^{Omni} \qquad \textbf{(Eq. V.3.3)}$$

The probability density functions (PDFs) of $\delta DS_{BS}^{Dir}\left(\phi_{BS}(p)\right)$ and $\delta DS_{BS-MS}^{Dir}\left(\phi_{BS}(p),\phi_{MS}(k)\right)$ are roughly similar to one another, as shown in **Fig. V.3.11**. Therefore, in both the single–directional and the double–directional cases, it can be concluded that the channel DS provided by the secondary beams are evenly distributed around the omnidirectional DS.

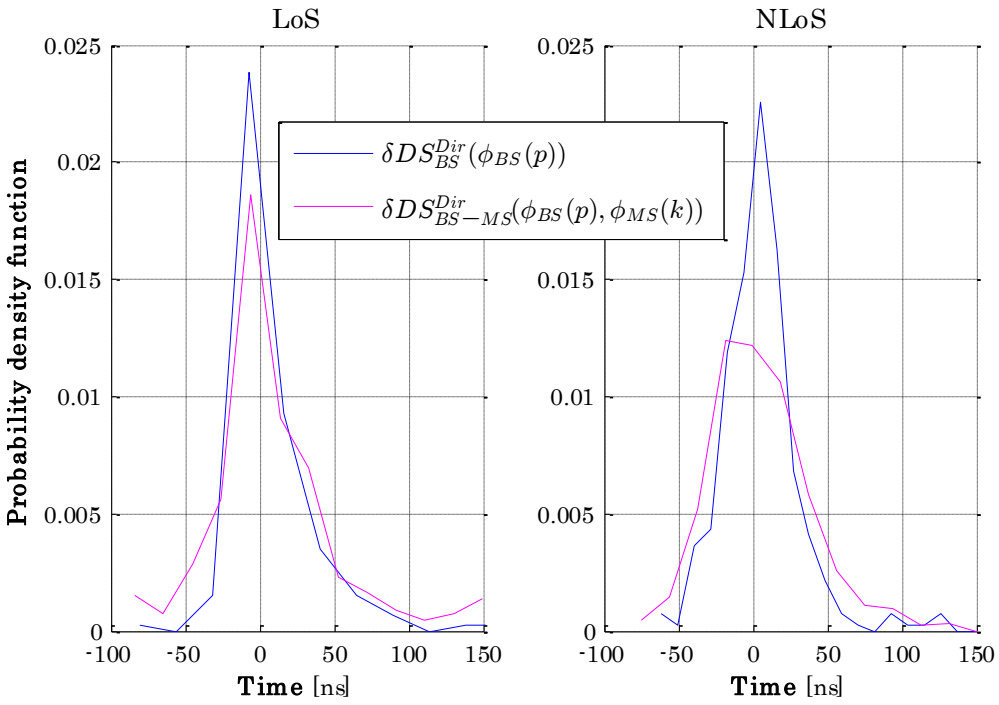

Fig. V.3.11 – PDFs of the directional DS relative to the omnidirectional DS

3.2. Azimuth–delay power profile (ADPP)

The ADPP is studied at 17 and 60 GHz in order to enable further comparisons between these two frequency bands. Defined as a function of the BS antenna pointing angle $\phi_{BS}(p)$ and the propagation delay τ, the ADPP corresponds with $PDP_{BS}^{Dir}\left(\phi_{BS}(p),\tau\right)$, the single–directional PDP defined in (**Eq. V.2.3**).

In **Fig. V.3.12–V.3.13**, **Fig. V.3.14–V.3.15** and **Fig. V.3.16–V.3.17**, typical examples of ADPPs are given for the different scenarios including OS, SI and SC respectively, in both LoS and NLoS conditions. The dotted "magenta" line represents the azimuth of the direct path between the BS and the MS.

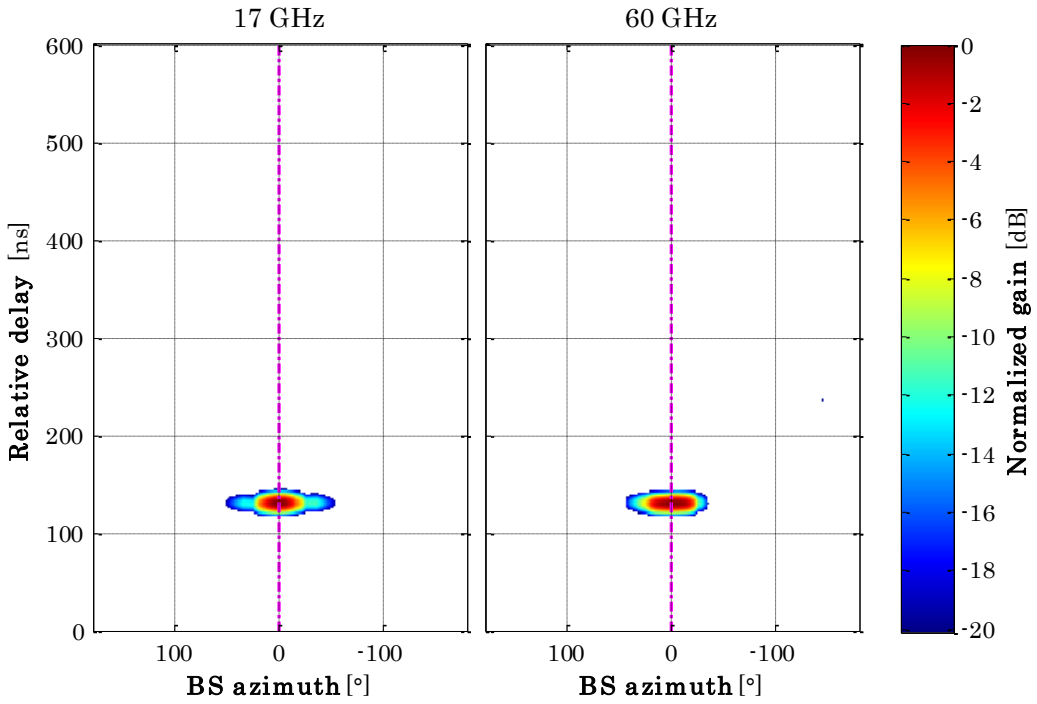

Fig. V.3.12 – ADPPs at 17 and 60 GHz for MS position A1 in OS (LoS)

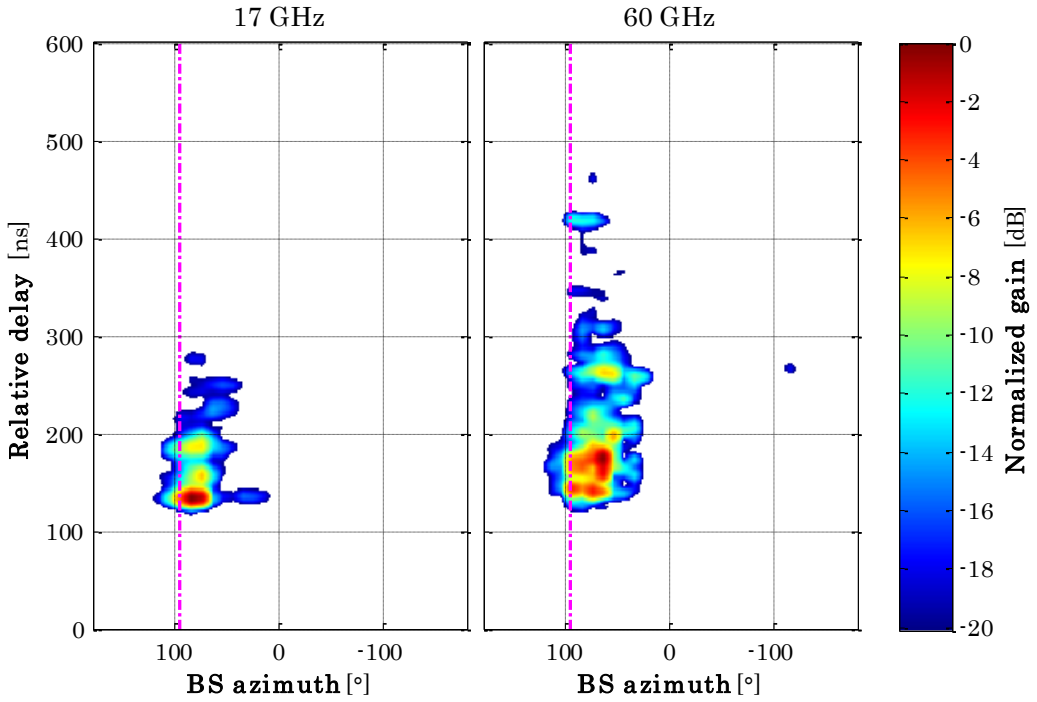

Fig. V.3.13 – ADPPs at 17 and 60 GHz for MS position A12 in OS (NLoS)

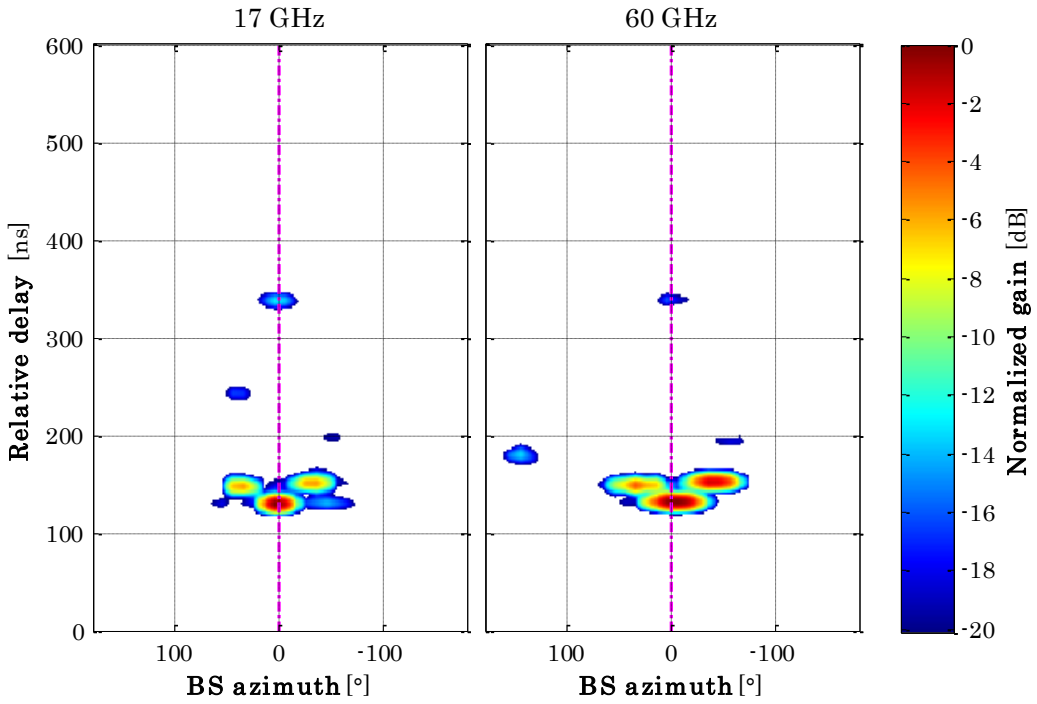

Fig. V.3.14 – ADPPs at 17 and 60 GHz for MS position B1 in SI (LoS)

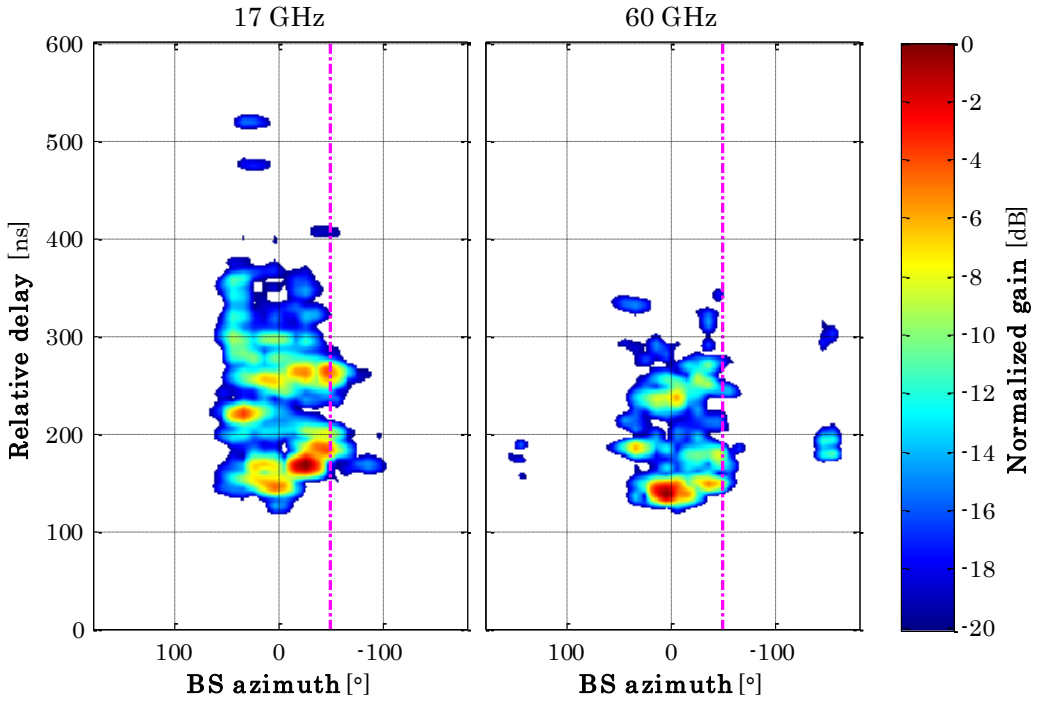

Fig. V.3.15 – ADPPs at 17 and 60 GHz for MS position B3 in SI (NLoS)

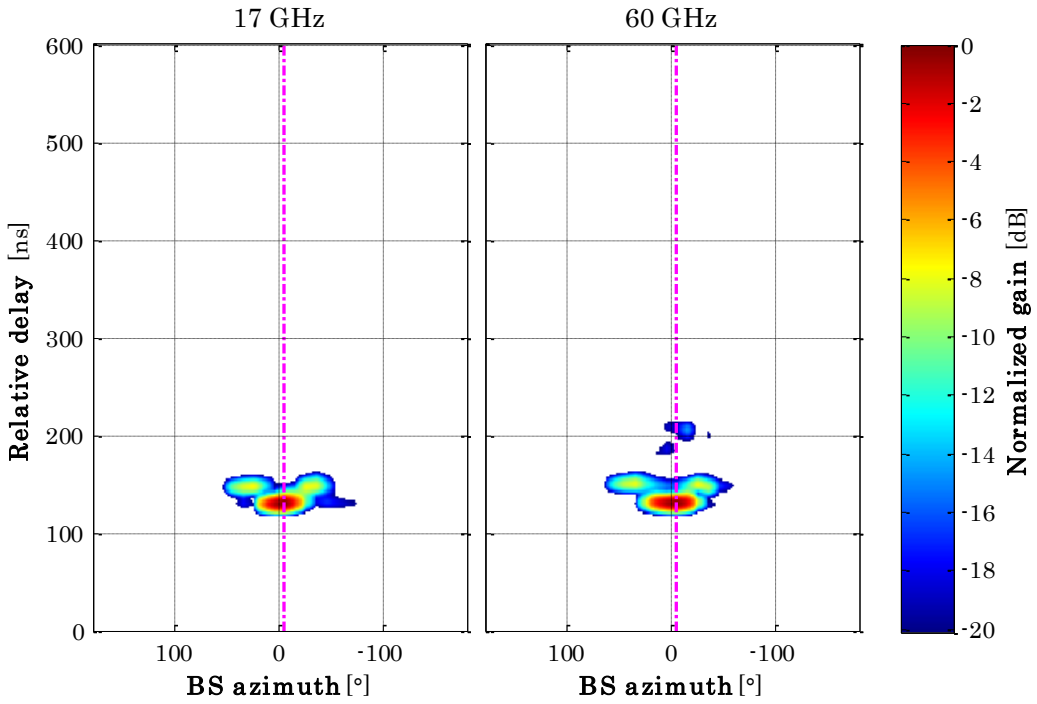

Fig. V.3.16 – ADPPs at 17 and 60 GHz for MS position C1 in SC (LoS)

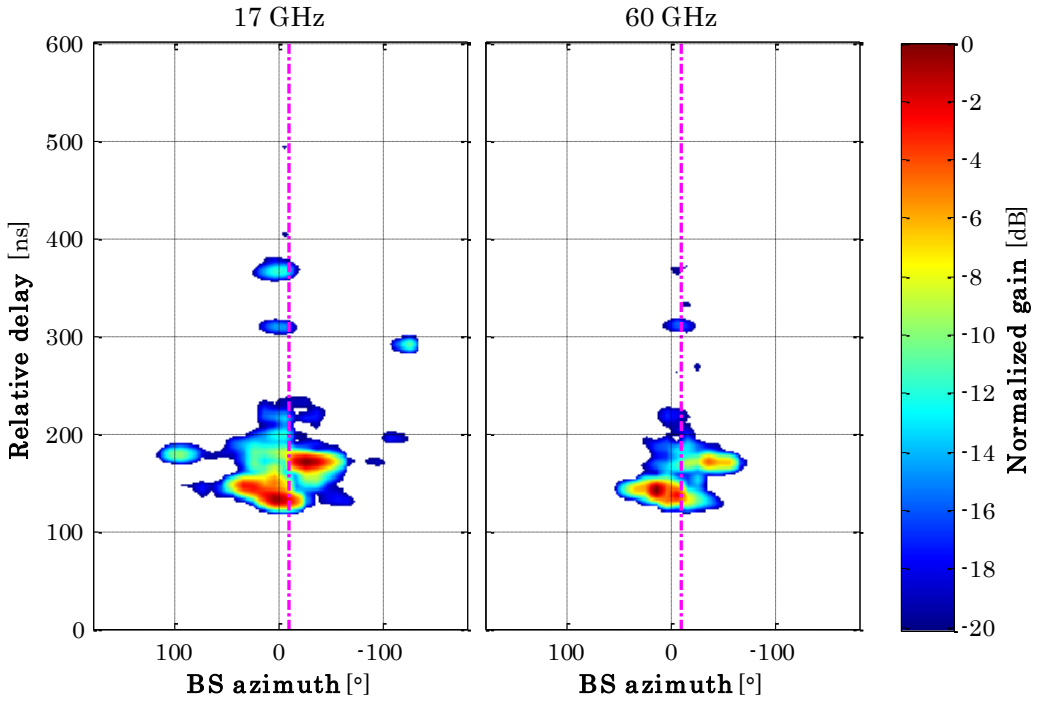

Fig. V.3.17 – ADPPs at 17 and 60 GHz for MS position C2 in SC (NLoS)

In LoS conditions, the ADPPs computed at 17 and 60 GHz are very similar. There is usually a main component in the direction of the LoS azimuth which is the direct path. However, there can also be significant secondary MPCs besides the main path.

Similarly, in NLoS conditions, it can be observed that the angular–temporal profiles at the two frequencies are highly correlated. However, the main path does not necessarily correspond with the direct path between the BS and MS. Furthermore, the dispersion of the MPCs is more important than in LoS conditions.

The conclusions regarding the 17 GHz directional DS values, made in **Section 3.1**, may thus be extendable to 60 GHz since the propagation channel characteristics between these two frequencies are overall very similar, according to the results presented above. More details on the ADPPS for these MS positions are provided in **Annex C, Section 2**.

3.3. Channel azimuth spread (AS)

The channel AS on the BS side, denoted by AS, has also been evaluated at 17 and 60 GHz. $PDP_{BS}^{Dir}\left(\phi_{BS}(p),\tau\right)$, the single–directional defined in (**Eq. V.2.3**), is considered to determine this parameter according to the relations given in (**Eq. II.3.6–II.3.7**).

In **Table C.1.2** given in **Annex C**, AS values, determined for the 35 MS positions, are provided. The average values measured in the different scenarios including OS, SI and SC are summarized in **Table V.3.2** in both LoS and NLoS conditions.

Table V.3.2 – Average AS values in the specific outdoor scenarios

Scenarios	AS [°]	
	17 GHz	60 GHz
LoS		
Open Square (OS)	24	34
Street Intersection (SI)	28	41
Street Canyon (SC)	17	18

Scenarios	AS [°]	
	17 GHz	60 GHz
NLoS		
Open Square (OS)	27	24
Street Intersection (SI)	38	46
Street Canyon (SC)	21	14

The average *AS* values given in **Table V.3.2** are relatively low (less than 50° and around 30° on average). There is overall no indication of a clear frequency–dependence of this parameter. However *AS* values recorded in SC are lower than those in SI or OS, where there are more reflectors. Additionally, **Fig. V.3.18** shows that the AS tends to decrease as the distance increases. This can be explained by the fact that far away reflectors result in weak MPCs.

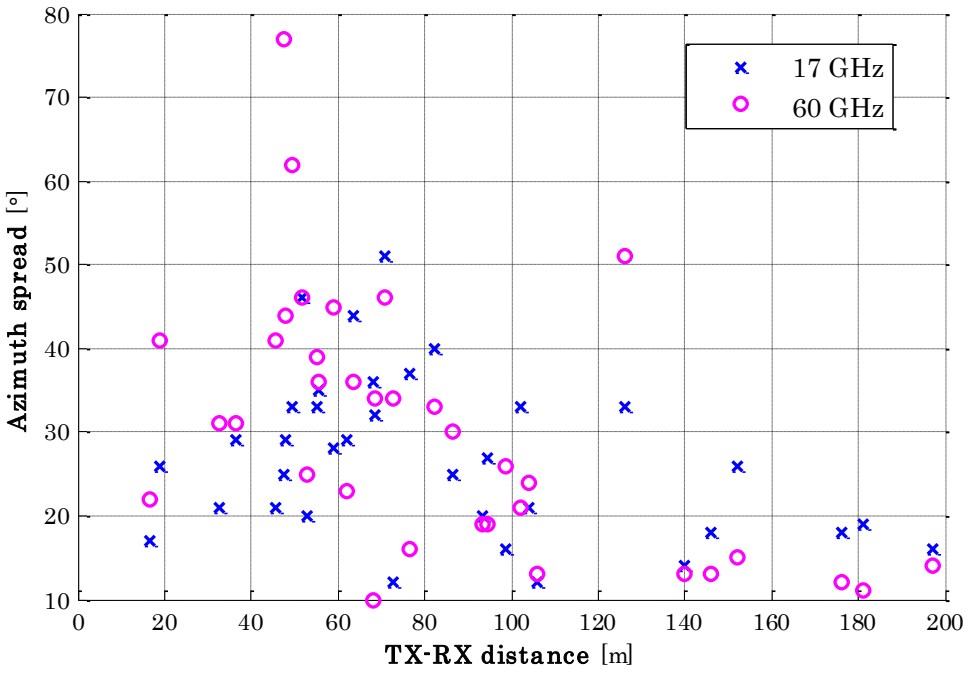

Fig. V.3.18 – Channel AS at 17 and 60 GHz vs distance

3.4. Propagation path–loss (PL)

Studies of the propagation PL, denoted by $PL_{[dB]}$, have also been conducted at 3, 17 and 60 GHz. $PL_{[dB]}$ is computed from the omnidirectional PDP, $PDP^{Omni}(\tau)$, defined in (**Eq. V.2.1**) for the 3 GHz frequency band and in (**Eq. V.2.2**) for the 17 and 60 GHz frequency bands. Its expression is given in (**Eq. II.3.3**).

In LoS conditions, the measured $PL_{[dB]}$ values more or less follow Friis' free–space attenuation model described in (**Eq. III.2.3**), as indicated in **Fig. V.3.19**. The presence of $PL_{[dB]}$ values well below the free–space model shows that, even in these LoS conditions, there can be reflected paths that interfere with the main LoS path in a constructive manner. These reflected paths may either be caused by elements present in the surrounding environment or be the result of ground reflection phenomena. Similar claims have been made in the studies reported in **Chapter II**.

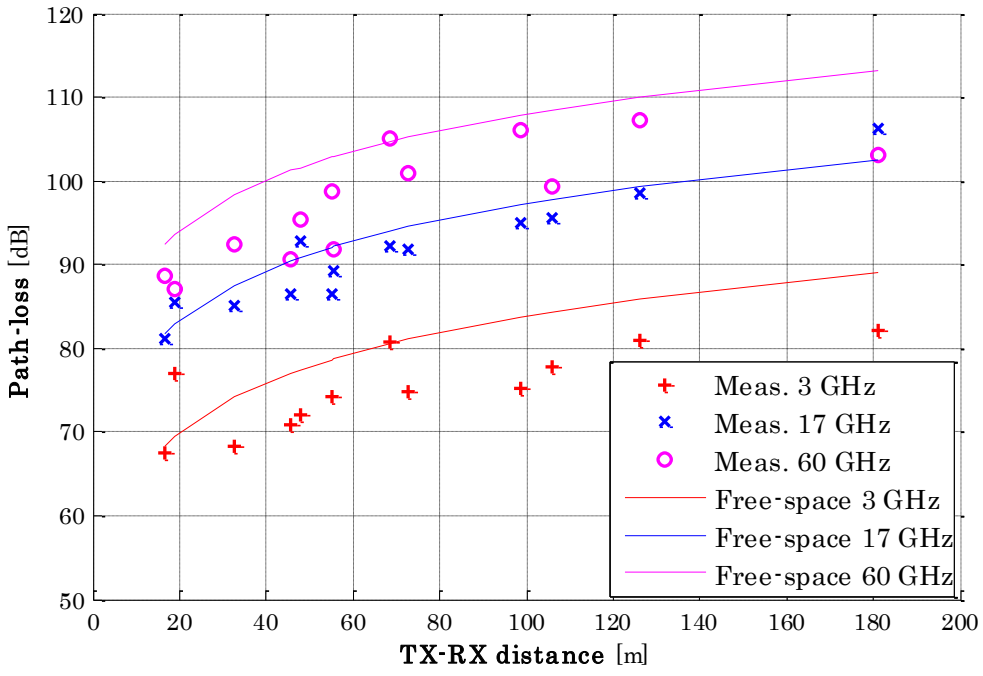

Fig. V.3.19 – Propagation PL vs distance in LoS

In NLoS conditions, there are about 15 dB more attenuation, on average, than in LoS conditions. The proposed linear fitting model for the measured NLoS values is the ABG

model described in (**Eq. II.3.8**) and characterized by its parameters α, β and γ. For the urban outdoor measurements presented herein, an ABG model, defined for distances up to 200 m in the frequency bands between 3 and 60 GHz, is proposed. The estimated values of α, β and γ are given in **Table V.3.3**.

Table V.3.3 – ABG PL model parameters

ABG model		
α	$\beta_{[dB]}$	γ
2.66	–163.25	2.12

A good agreement is observed between the measurements and the ABG model, as illustrated in **Fig. V.3.20**. It is thus reasonable to assume that the propagation conditions in these different frequency bands are overall similar since the difference regarding the PL can be quantified by an offset caused by the frequency, similarly to Friis' free–space model.

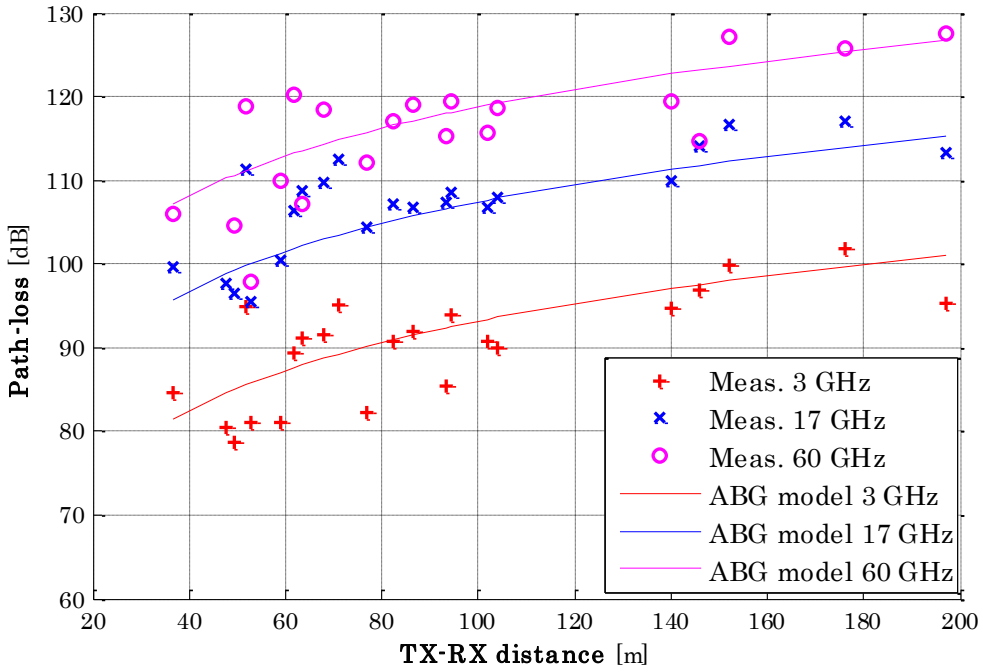

Fig. V.3.20 – Propagation PL vs distance in NLoS

4. Summary

The radio propagation channel properties have been studied at 3, 17 and 60 GHz in an UMi outdoor environment in the industrial area "Techn'hom", in Belfort. The outdoor environment describes three different scenarios including OS, SI and SC. Channel LSPs such as DS, AS and PL have been evaluated.

A slight decrease of the channel DS with increasing frequency has been observed in the overall measurements, although the different specific outdoor scenarios have revealed different trends. Larger DS values were recorded at 3 GHz compared to 17 and 60 GHz in scenarios OS and SI whereas scenario SC revealed the opposite. It has also been demonstrated, at 17 GHz, that the channel DS can be reduced by the use of directional antennas with small angular aperture (such as 30° HPBW). However, obstructions represent a limiting cause in the endeavor. In fact, when the strongest beam is highly attenuated, the channel DS may increase in comparison to that of omnidirectional antennas. Furthermore, it has been observed that both the channel ADPPs and AS are very similar at 17 and 60 GHz. When 30° HPBW antenna are used, the average measured AS is around 30°. Moreover, while the measured LoS propagation PL is generally in accordance with Friis' free–space law, in NLoS conditions, the ABG model shows that the difference in PL between the frequency bands from 3 and 60 GHz is caused by the frequency, similarly to the free–space model.

These findings show that the propagation channel characteristics in UMi environments are overall similar between 3 and 60 GHz. The additional propagation PL caused by the increase of the frequency can be compensated by the use of directional antennas, as envisioned in future 5G systems.

Conclusion

Propagation channel studies are an important component for the design and evaluation of the performances of wireless systems. In the context of the next generation (5G) mobile and wireless communications systems, millimeter–Wave (mm–Wave) bands are considered as a potential candidate for providing high communications data rates. This is mainly due to the large frequency bandwidth available in this range in comparison to the lower frequency bands, i.e. sub–6 GHz bands, where spectrum shortage is looming. It is thus necessary to precisely characterize the mm–Wave radio propagation channel in order to reach 5G expectations.

In the past, mm–Wave frequencies have been deemed to be ill–suited for mobile communications for various reasons including severe propagation conditions usually associated with high frequencies. However, thanks to recent advancements on antenna design with high gain directional antennas and signal processing techniques such as beamforming, the wireless industry is reconsidering the feasibility of mm–Wave mobile communications. In this sense, this Ph.D. project has aimed at providing a contribution to this endeavor.

In **Chapter I**, an overview on 5G technology is provided. The three main targeted use cases, including enhanced mobile broadband (eMBB), massive machine–type communications (mMTCs) and ultra–reliable low latency communications (URLLCs) are first discussed. The vision of major telecommunications operators and/or equipment vendors, including Orange, Huawei, Ericsson, Nokia, etc., has thus been laid out. These use cases have very diverse requirements such as high data rates for eMBB services, massive connectivity with low cost components for mMTCs and extremely low latency for URLLCs. Therefore, some of the key technologies identified to meet these requirements, especially the need for higher data rates, are described. They include, but are not limited to, radio access technologies (RATs) such as massive multiple–input multiple–output (MIMO) systems and mm–Wave communications and novel network concepts such as small–cells densification, cloud–based

radio access network (C–RAN) and network functions virtualization (NFV). It has been shown that these technologies are very promising for achieving 5G targets but there are still some challenges that need to be overcome.

Thereafter, the emphasis is put on mm–Wave communications and the characterization of the propagation channel in these frequency bands. The frequency–dependence of channel large scale parameters (LSPs) in envisioned 5G deployment scenarios such as outdoor–to–indoor (O2I) and urban outdoor environments, in the frequency range between 3 and 60 GHz, has been the main discussed issue. The investigated channel LSPs include the building penetration losses (PELs), the channel delay spread (DS), the channel azimuth spread (AS), and the propagation path–loss (PL), which describe the main characteristics of the radio propagation channel.

Therefore, in **Chapter II**, literature measurements and studies on such channel parameters are reported. In O2I scenarios, the building PELs are essentially documented. The results mainly highlight the difference on the PELs measured between EE modern building and standard old buildings. The general consensus is that coated windows, usually found in modern buildings, result in about 20 – 30 dB more PELs than standard windows which are found in standard buildings. While a frequency–independence of the building PELs is usually claimed, some studies have reported an increasing behavior of the PELs with increasing frequency. However, this impact of the frequency on these PELs remains marginal in comparison to that of the building material composition.

In urban outdoor scenarios, the channel DS is the main discussed topic. The frequency–dependence of such a parameter has been the subject of intensive discussions within the channel modeling community. The majority of the studies claim either a frequency–independence or a decreasing behavior of the channel DS with increasing frequency, especially in open areas. However, in street canyons for example, the DS has been observed to slightly increase with the frequency. Either way, the variations observed in the channel DS parameter, within the frequency range between 2 and 86 GHz, are relatively small. Similar conclusions have been drawn regarding the other channel LSPs discussed in the literature reported in **Chapter II**.

The studies presented in **Chapter II** are, however, limited due to the lack of fully comparable measurements in the literature. The differences in hardware equipments, environment characteristics and measurement setting parameters among others prevent comprehensive comparisons across different measurement campaigns. It has thus been our objective to characterize the frequency–dependence of the radio propagation channel in a more consistent manner.

First, through theoretical studies presented in **Chapter III**, the frequency–dependence of the geometric model, adopted by standard bodies such as 3GPP and the ITU, is investigated. Specifically, the main radio propagation phenomena including reflection, transmission and diffraction are modeled thanks to the geometrical optics (GO) theory and the geometrical/uniform theory of diffraction (GTD/UTD). Their frequency–dependence has been discussed. The findings of these studies offer a good insight into the propagation channel characteristics in the mm–Wave bands. However, complex interactions between radio signals and the elements present environment are not **necessarily** accounted for in this geometrical approach.

In response to these limitations, experimental characterizations of the radio propagation channel have been conducted and described in **Chapter IV–V**. Contrary to most studies reported in **Chapter II**, the measurement results presented in **Chapter IV–V** fulfill a certain number of requirements to ensure full comparability across the different frequency bands. These requirements include similar hardware equipments, same exact measurement environments, measurement parameters, settings and procedures. Any differences in these aspects were consistently compensated for in the data processing.

In this sense, **Chapter IV** covers an O2I propagation scenario at 3, 10, 17 and 60 GHz. On the building PELs, the findings are very much in line with literature results. Double–layered standard glass windows have been observed to result in relatively low PELs, lesser than 10 dB, while the PELs measured for 2–layered coated glass windows are around 30 dB. For standard windows, little to no frequency–dependence of the PELs is recorded whereas the PELs measured for the coated windows tend to slightly increase with increasing frequency. These conclusions are also supported by the theoretical studies presented in **Chapter III**.

In **Chapter V**, urban outdoor scenarios are tested at 3, 17 and 60 GHz. Regarding the frequency–dependence of the channel DS, different tendencies are observed in the different scenarios. For the open square (OS) and street intersection (SI) scenarios, the channel DS slightly decreases with increasing frequency while the opposite behavior is observed in the street canyon (SC) scenario. This is in agreement with the literature reports in **Chapter II**. Additionally, studies on the impact of antenna angular aperture on the channel DS have been conducted. As directional antennas are envisioned for future 5G systems, their impact on channel parameters needs to be evaluated. The results have revealed that, so long as the main propagation path is not obstructed, a reduce antenna angular aperture leads to smaller channel DS. However, when this main path is obstructed, the channel DS tends to increase but, on average, remains similar to the DS measured with omnidirectional antennas. Further comparisons between the 17 and 60 GHz frequency bands have also been performed in **Chapter V**. The channel AS and azimuth power delay profile (ADPP) characteristics between these two frequency bands have been found to be overall similar. Finally, regarding the propagation PL parameter, the frequency offset was found to be the main factor for the different attenuation values measured between 3 and 60 GHz.

In summary, the studies conducted in this project represent a significant contribution on the quest for better knowledge of the radio propagation channel characteristics in the mm–Wave frequency bands. According to the results provided herein, there is a strong case for mm–Wave communications to be considered for achieving 5G data rates, especially with the use of directional antennas and, potentially, advanced signal processing techniques. However, these features may require deeper knowledge of the propagation channel angular or directional characteristics. In this regard, further analysis of the radio signal directions of arrival and/or departure can contribute to this endeavor and validate some of the physical and geometrical interpretations made herein. In this sense, the use of massive MIMO antennas and their related technical challenges can be targeted. In parallel, a possible area of future investigations is the use of adaptive antenna arrays in order to evaluate the potential of beamforming in mm–Wave communications. This requires the study of the temporal variability of the propagation channel in order to account for the impact of user mobility, human body blockage and also moving objects such as vehicles. Finally, additional measurements and drive tests may be necessary in order to collect enough data and provide a more reliable statistical analysis of the radio propagation channel.

Annex A

A. Channel Measurement Campaigns and Results for 5G

Details on the measurement campaigns discussed in **Section 3.2–3.3** of **Chapter II** are provided herein. O2I propagation scenarios are described in **Table A.1** where the building PELs are reported. In **Table A.2**, studies on the channel DS in urban outdoor scenarios are provided.

Table A.1 – Literature measurement results on PELs in O2I scenarios

References	**Frequency bands**	**TX/RX height** h **TX–RX distance** d	**TX antenna**	**Main measurement results**
	Test scenario	**PELs estimation procedure**	**RX antenna**	
[75]	Frequency : **28 GHz**	h = 1.5/1.5 m d = 5 m	TX : 24 dBi gain, 10° HPBW	✦ Clear glass (< 1.3 cm thick) PELs = 3.6 – 3.9 dB ✦ Tinted glass (1.3 and 3.8 cm thick) PELs = 24.5 and 40.1 dB ✦ Drywall (38.1 cm thick) PELs = 6.8 dB ✦ Brick pillar (185.4 cm thick) PELs = 28.3 dB
	Different outdoor and indoor building materials (clear glass, tinted glass, brick and drywall) tested	PELs as difference between measured PL (with obstructing materials) and free–space measurements	RX : 24 dBi gain, 10° HPBW	

References	**Frequency bands** **Test scenario**	**TX/RX height** h **TX–RX distance** d **PELs estimation procedure**	**TX antenna** **RX antenna**	**Main measurement results**
[76]	Frequency : **15 GHz** Bandwidth : 200 MHz	h = 12/1.5 m RX across the street from where TX is located	TX : 15 dBi gain, 90° azimuth HPBW, 8.6° elevation HPBW, Dual–polarized 2–element arrays	▪ 3–layered standard glass window PELs = 6 dB ▪ 3–layered IRR coated glass window PELs = 24 dB ▪ Standard window (closed blinds) PELs = 14 dB ▪ Metallic white board, 0.5 m wide concrete pillar or human body (30 cm away from RX) PELs = 8 – 10 dB
	O2I scenario with PELs for normal and IRR coated glass windows, human body, metallic whiteboard and concrete pillar measured	PELs as difference between measured PL (with obstructing materials) and free–space measurements	RX : Omnidirectional, Dual–polarized 2–element arrays	
[77]	Frequencies : **0.8 to 18 GHz** (at 800 MHz and, then, from 2 to 18 GHz) 1 GHz step	Same TX/RX height d = 3.6, 5.4, 13 m	TX : Horn antennas	▪ 1–layered standard glass window PELs = 5.16 dB (in average) ▪ 2–layered EE glass windows PELs = 24.86 – 28.43 dB (in average) ▪ 3–layered EE glass panels and doors PELs = 31.98 dB (in average) ▪ 45 cm thick multi–layered reinforced–concrete and brick walls High PELs with rapid increase with frequency
	O2I scenario with PELs caused by old and modern building materials measured	PELs as difference between measured PL (with obstructing materials) and free–space measurements	RX : Horn antennas	

References	**Frequency bands** **Test scenario**	**TX/RX height** h **TX–RX distance** d **PELs estimation procedure**	**TX antenna** **RX antenna**	**Main measurement results**
[78]	Frequency : **28 GHz** Bandwidth : 50 MHz	h : Rooftop/3rd floor d = 70 m	TX1 : 22 dBi gain, 60° azimuth HPBW, 4.3° elevation HPBW TX2 : 34 dBi gain, 3.3° HPBW	✚ Standard glass windows PELs = 3 – 5 dB ✚ Coated glass windows PELs = 30 dB
	O2I scenario with PELs for standard and coated glass windows measured	PELs as difference between measured PL (with obstructing materials) and free–space measurements	RX : 34 dBi gain 3.3° HPBW	
[79]	Frequency : **10.1 GHz** Bandwidth : 500 MHz	h = 1.3–5.1/1.3 m	TX : Horn antenna, 13 dBi gain	✚ 2–layered standard glass window PELs = 5 dB at 90° grazing angle PELs = 28 dB at 0° grazing angle ✚ Concrete wall PELs = 24 at 90° grazing angle PELs > 50° at 0° grazing angle
	O2I PELs model derived from measurements	PELs modeled from measured PL (with obstructing materials)	RX : Dipole antennas, 2.1 dBi gain	
[80]	Frequencies : **0.8, 2.2, 4.7, 8.4, 26.3 and 37.0 GHz**	h = 2.5, 11.5/1.5 m	TX : Sleeve antennas	✚ Material composition not specified PELs = 6.8 dB at 0° incidence

References	**Frequency bands** **Test scenario**	**TX/RX height** h **TX–RX distance** d **PELs estimation procedure**	**TX antenna** **RX antenna**	**Main measurement results**
	O2I PELs modeling from measurements	PELs modeled from measured PL (with obstructing materials)	RX : Sleeve antennas	angle PELs = 21.9 dB at 90° incidence angle
[81]	Frequency **38 GHz** Bandwidth : 28 MHz	h = 1.75/1.75 m	TX : 40 dBi gain, 1.5° HPBW	✦ 2–layered EE glass window PELs = 22 – 25 dB ✦ 3–layered EE glass door PELs = 35 – 40 dB ✦ 45 cm thick multi–layered reinforced–concrete and brick wall PELs > 91 dB
	O2I scenario with PELs caused by modern window and door and concrete wall measured	PELs as difference between measured PL (with obstructing materials) and free–space measurements	RX : 40 dBi gain, 1.5° HPBW	
[82]	Frequencies : **9.6, 28.8 and 57.6 GHz** Sequence rate : 500 Mb/s	TX/RX on opposite side of the building, set on a line perpendicular to the building d up to 260 m	TX : 10° beamwidth	✦ Clear glass walls PELs small at all frequencies ✦ Coated glass walls PELs increase by 25 – 50 dB per layer of metal coating ✦ Reinforced–concrete and brick walls No signal detected
	O2I scenario with PELs caused by building materials (clear and coated glass, concrete)	PELs as difference between obstructed PL measurements and free–space	RX : 4.8° beamwidth at 9.6 GHz and 1.2° beamwidth at 28.8 and 57.6 GHz	
[84]	Frequencies : **28 and 40 GHz**	Same TX/RX height d = 30 cm	TX : 15 dBi gain, 30° HPBW	✦ 1–inch (~2.54 cm) wood PELs = 5 and 7 dB at 28 and

References	**Frequency bands** **Test scenario**	**TX/RX height** h **TX–RX distance** d **PELs estimation procedure**	**TX antenna** **RX antenna**	**Main measurement results**
	Different materials (wood, human body) tested	PELs as difference between measured PL (with obstructing materials) and free–space	RX : 15 dBi gain, 30° HPBW	40 GHz resp. - Human body PELs = 30 and 40 dB at 28 and 40 GHz resp. (obstacle about 1 cm away from RX) PELs = 15 and 25 dB at 28 and 40 GHz resp. (obstacle about 10 cm away from RX)
[83]	Frequency : **73.5 GHz** Bandwidth : 1 GHz	h = 1.5/1.5 m TX/RX on opposite side of tested materials d = 3 m	TX : 20 dBi gain, 15° HPBW	- 1 cm thick clear glass windows and glass doors PELs = 7.1 and 5.1 dB resp. - 13.7 cm thick plasterboard walls PELs = 10.6 dB - 7 cm thick closet doors, 5.3 cm thick steel doors and 21.4 cm thick whiteboard walls PELs = 32.3, 52.2 and 73.8 dB resp.
	Different materials (glass doors, glass windows, closet doors, steel doors, and whiteboard writing walls) tested	PELs as difference between obstructed measured PL and free–space	RX : 20 dBi gain, 15° HPBW	
[69]	Frequencies : **2, 6, 15 and 60 GHz** Bandwidth (in processing) : 80 MHz	h = 1.5/1.5 m d up to 75 m	TX (2 and 6 GHz) : patch with 7 dBi gain TX (15 and 60 GHz) : open wave guide	- 3–layered pure glass (without metallization) PELs = 2, 0, 10 and 6 dB at 2, 6, 15 and 60 GHz resp.
	O2I scenario where PELs caused by glass windows measured	PELs as loss in excess of free–space	RX : Omnidirectional, 2 dBi gain	

References	Frequency bands Test scenario	TX/RX height h TX–RX distance d PELs estimation procedure	TX antenna RX antenna	Main measurement results
[70]	Frequencies from 6 to 100 GHz O2I building PeLs modeling			▪ Standard glass windows PELs = 4, 8 and 14 dB at 10, 30 and 60 GHz resp. ▪ Modern glass windows PELs = 26, 32 and 41 dB at 10, 30 and 60 GHz resp. ▪ Concrete wall PELs = 45 dB at 10 GHz with very rapid increase with the frequency

Table A.2 – Literature measurement results on the channel DS in urban outdoor environments

References	Frequency bands Environments	TX/RX height h TX–RX distance d	TX antenna RX antenna	Main measurement results
[73]	Frequencies : **28, 38 and 73 GHz** Bandwidth : 800 MHz 28, 73 GHz : dense urban (downtown Manhattan and Brooklyn) 38 GHz : urban (UTA campus, Austin)	28 GHz h = 7, 17, 40/1.5 m d up to 200 m 38 GHz h = 8, 23, 36/1.5 m d up to 930 m 73 GHz h = 7, 17/2, 4.06 m d up to 200 m	TX : 15 – 27 dBi gain, 7 – 28.8° azimuth HPBW, 7 – 30 ° elevation HPBW RX : 13.3 – 27 dBi gain, 7 – 49.4° azimuth HPBW, 7 – 49.4 ° elevation HPBW	**Directional DS** ▪ LoS (28 and 73 GHz) : virtually no DS i.e. DS = width of the sounder impulse response) ▪ NLoS 28 GHz : 90% DS < 50 ns with mean DS = 15.6 – 17.4 ns 73 GHz : DS < 25 ns (in general) with mean DS = 9.4 – 11.1 ns 38 GHz : 90% DS < 40 ns with mean DS = 7.7 – 11.4 ns

References	**Frequency bands** **Environments**	**TX/RX height** h **TX–RX distance** d	**TX antenna** **RX antenna**	**Main measurement results**
[87]	Frequencies : **71–76 and 81–86 GHz** Bandwidth : 5 GHz	Street canyon same TX/RX height d up to 685 m Long street canyon same TX/RX height d up to 1100 m	TX : parabolic antennas, 45 dBi gain, 0.8° HPBW	**Directional DS** Street canyon Meas. : mean DS = 0.10 ns Model : mean DS = 0.089 Long street canyon Meas. : mean DS = 0.125 ns Model : mean DS = 0.098 ns
	LoS Street Canyon (Eerikinkatu) LoS Long street canyon (Unioninkatu)		RX : parabolic antennas, 45 dBi gain, 0.8° HPBW	
[69]	Frequencies : **10, 28, 41 and 82 GHz** Bandwidth : 500 MHz	h = 5/1.5 m d up to 300 m	TX : Omnidirectional antennas	**Omnidirectional DS** 20 dB threshold : ≈ 90% DS < 40 ns at 10, 28 and 41 GHz 15 dB threshold : lower DS at 82 GHz 25 dB threshold : higher DS at 10 GHz
	LoS street canyon (downtown Berlin)		RX : Omnidirectional antennas	
[88]	Frequency : **59 GHz** Bandwidth : 200 MHz	h = 3.1 – 11/2.2 m d up to ≈ 200 m	TX : 90° horn antenna, 20° vertical HPBW	**Omnidirectional DS** Empty street (no major reflectors) 90 % DS < 20 ns Parked bus in the street Larger DS than in an empty street 90% DS < 50 ns
	Seven city streets (downtown Oslo)		RX: Omnidirectional, 20° vertical HPBW	
[89]	Frequency : **59 GHz** Bandwidth : 200 MHz	h = 4/2.2 m d up to ≈ 200 m	TX : 90° horn antenna, 20° vertical HPBW	**Omnidirectional DS** City streets **[NTR..94]** 90% DS < 20 ns City squares and parking garage

References	Frequency bands Environments	TX/RX height h TX–RX distance d	TX antenna RX antenna	Main measurement results
	City streets, city squares, parking garage, tunnel road		RX : Omnidirectional, 20° vertical HPBW	More DS than in city streets Road tunnel Similar to city streets
[90]	Frequencies : **10 and 60 GHz** Bandwidth : 250 MHz	h = 5/1.5 m d up to 200 m	TX : Omnidirectional, (– 0 .7) – 0 dBi gain	**Omnidirectional DS** LoS (25 dB threshold) 10 GHz : 90% DS < 35 ns 60 GHz : 90% DS < 25 ns NLoS (25 dB threshold) 10 GHz : 90% DS < 65 ns 60 GHz : 90% DS < 45 ns
	Urban street canyon (Kreuzberg in Berlin)		RX : Omnidirectional, (– 0 .7) – 0 dBi gain	
[91]	Frequencies : **28 and 38 GHz** Bandwidth : 500 MHz	h = 10/1.5 m d up to 180 m	TX : 24 .4 –24.6 dBi gain, 10° HPBW	**Directional DS** LoS : 90% DS < 30 ns NLoS : 90% DS < 90 ns
	UMi environment (downtown Daejeon city in Korea)		RX : 15.4 – 16.4 dBi gain, 30° HPBW	
[92]	Frequencies : **15, 28 and 60 GHz** Bandwidth : 0.5, 0.9 and 4 GHz at 15, 28 and 60 GHz resp	h = 2.57/2.57 m d up to 120 m	TX : Omnidirectional antenna	**Omnidirectional DS** LoS links DS < 30 ns Presence of major obstacles at 15 and 60 GHz Less DS than at 28 GHz
	UMi street canyon		RX : 19 dBi gain, 10° azimuth HPBW, 40° elevation HPBW	

References	**Frequency bands** **Environments**	**TX/RX height** h **TX–RX distance** d	**TX antenna** **RX antenna**	**Main measurement results**
[69]	Frequencies : **15, 28 60 and 86 GHz** Bandwidth : 0.5, 0.9, 4 and 4 GHz at 15, 28, 60 and 86 GHz resp.	Street canyon h = 2.57/2.57 m d up to 120 m Open square h = 1.6/5 m d up to 60 m	TX : Omnidirectional, 2 dBi gain, 60° elevation HPBW	**Omnidirectional DS** Street canyon (LoS links) 15 GHz : mean DS = 15.1 ns 28 GHz : mean DS = 14.3 ns 60 GHz : mean DS = 14.2 ns 86 GHz : mean DS = 10.8 ns Open square 28 GHz : mean DS = 45.9 ns 86 GHz : mean DS = 36.8 ns
	15, 28, 60 and 86 GHz UMi street canyon (Espoo, Helsinki) 28 and 86 GHz UMi open square (Centre of Helsinki)		RX : 19 dBi gain, 10° azimuth HPBW, 40° elevation HPBW	
[93]	Frequency : **60 GHz** Bandwidth : 1 GHz	h = 1.8/12, 8 m d up to 405 m	TX : Standard gain horn antenna, 18 – 19° HPBW	**Directional DS** Strongest path LoS : DS < 12 ns NLoS : DS < 22 ns Secondary paths LoS : 90% DS < 12 ns NLoS : 90% DS < 20 ns
	UMi street canyons (Camelia and Florida streets in Vigo)		RX : Horn antenna, 20 dBi gain	
[94]	Frequency : **28 GHz** Bandwidth : 250 MHz	h =15 m/user level d up to 200 m	TX : Horn antennas, 24.5 dBi gain, 10° HPBW	**Omnidirectional DS** NLoS (only 11 valid locations) DS < 100 ns (in general) Mean DS = 22.29 ns
	Urban area (downtown Daejeon in Korea)		RX : Horn antennas, 24.5 dBi gain, 10° HPBW	

References	Frequency bands Environments	TX/RX height h TX–RX distance d	TX antenna RX antenna	Main measurement results
[95]	Frequency : **11 GHz** Bandwidth : 400 MHz Urban environments (UMi, UMa and street cell in Ishigaki city, Okinawa)	UMa : h = 3/28 m d up to ≈ 1000 m UMi : h = 3/9 m d up to ≈ 200 m Street cell : h = 3/3 m d up to ≈ 200 m	TX : Dual polarized 12–element uniform circular arrays (24 x 24 full MIMO sounding) RX : Dual polarized 12–element uniform circular arrays (24 x 24 full MIMO sounding)	**Directional DS** UMa, UMi, street–cell Mean DS < 20 ns Smaller DS in street–cell than in UMi and UMa environments
[96]	Frequency **: 3–18 GHz** (per step of 500 MHz) Bandwidth : 1 GHz UMi and UMa environments (on the USC campus)	UMa : h = 31/1.5 m d up to 120 m UMi : h = 8.5, 11.5, 14/1.5 m d up to 90 m	TX : Bi-conical antennas, Isotropic in azimuth, 65 – 45 ° elevation HPBW from 3 – 18 GHz RX : Bi-conical antennas, Isotropic in azimuth, 65 – 45 ° elevation HPBW from 3 – 18 GHz	**Omnidirectional DS** LoS UMa : DS < 50 ns, UMi : DS < 30 ns DS decreases from 3 to 18 GHz (46 to 29 ns for e.g. in UMa and 29 to 25 ns for e.g. in UMi) NLoS UMa : DS < 300 ns, UMi : DS < 125 ns DS ≈ the same from 3 to 18 GHz In UMi, DS ≈ from 70 to 120 ns for TX height from 8.5 to 14 m
[97]	Frequency : **28 GHz** Sequence rate : 250 Mcps	h = 15m/user level d up to 209 m	TX : Horn antennas, 24.5 dBi gain, 10° HPBW	**Omnidirectional DS** NLoS (38 valid locations) DS < 200 ns (in general) mean DS = 55.43 ns

References	**Frequency bands** **Environments**	**TX/RX height** h **TX–RX distance** d	**TX antenna** **RX antenna**	**Main measurement results**
	Urban area (downtown Daejeon, Korea)		RX : Horn antennas, 24.5 dBi gain, 10° HPBW	
[69]	Frequency : **2, 15 and 60 GHz** Bandwidth : 80 MHz	h = 1.5/1.5 m d up to 209 m	TX : Vertical dipole antennas, 2 dBi gain	**Omnidirectional DS** LoS (2, 15 and 60 GHz) DS = 20 – 50 ns NLoS (2, 15 and 60 GHz) DS = 75 – 200 ns
	UMi street canyon (Kista, Stockholm)		RX : Vertical dipole antennas, 2 dBi gain	
[98]	Frequency : **28 GHz** Bandwidth : 400 MHz	h = 1.66/13.38 m d up to 137 m	TX : 2 dBi gain, 360° azimuth. HPBW, 40° elevation HPBW	**Directional DS** LoS : mean DS = 29.51 ns NLoS : mean DS = 37.15 ns
	UMi scenario (campus of the Beijing University)		RX : 8 dBi gain 90° azimuth HPBW, 40° elevation HPBW	
[99]	Frequency : **60 GHz** Bandwidth : 2.2 GHz	h = 5/1.7 m d up to 50 m	TX : Directional, 18 dBi gain	**Directional DS** 50% percentile DS ≈ 20 ns 90% percentile DS > 50 ns
	Outdoor LoS small–cell on the campus of Durham University		RX : Highly directional, 36 dBi gain, 5° beamwidth	

Annex B

B. Outdoor–to–Indoor (O2I) Measurement Results in Belfort

In this annex, details regarding the O2I measurements discussed in **Chapter IV** are given. The measurements were conducted in Belfort at 3, 10, 17 and 60 GHz. The building PELs measured for each RX/MS position are provided in **Table B.1** while the corresponding channel DS are given in **Table B.2**.

Table B.1 – PELs values measured in the O2I scenario in Belfort

RX positions	PELs [dB]					
	S1			S2		S3
	3 GHz	10 GHz	17 GHz		60 GHz	
Corridor (Co)						
R1	18	18	17	22	N/A	N/A
R2	20	19	21	22	N/A	N/A
R3	18	19	22	17	N/A	N/A
R4	21	22	23	23	N/A	N/A
R5	21	22	21	23	N/A	N/A
Flat (Fl)						
R6	27	31	33	30	N/A	N/A
R7	28	31	35	36	N/A	N/A

RX positions	**PELs** [dB]					
	S1			**S2**		**S3**
	3 GHz	**10 GHz**	**17 GHz**		**60 GHz**	
R8	29	31	34	36	N/A	N/A
R9	25	29	34	33	N/A	N/A
R10	28	32	30	33	N/A	N/A
R11	27	26	31	28	N/A	N/A
R12	25	29	33	27	N/A	N/A
R13	26	29	35	38	N/A	N/A
R14†	27	30	35	35	N/A	39
R15	27	31	35	37	N/A	N/A
R16	23	30	37	N/A	N/A	N/A
R17†	27	28	33	40	N/A	39
R18	29	31	33	38	N/A	N/A
R19	26	31	32	33	N/A	N/A
Break–room (BR)						
R20‡	17	16	16	12	18	20
R21†	7	4	2	0	5	6
R22‡	12	6	14	9	17	14
R23†	7	5	2	0	5	4
R24‡	20	22	18	19	23	N/A
R25	5	3	2	N/A	6	4

RX positions	PELs [dB]					
	S1			S2		S3
	3 GHz	10 GHz	17 GHz		60 GHz	
R26	19	18	16	14	24	20
R27	9	4	2	N/A	4	5
R28	10	6	7	2	5	9
R29	11	12	8	9	20	17
R30	4	6	–1	N/A	7	2
Large office 1 (LO1)						
R31	13	19	19	19	22	22
R32	17	21	18	19	25	18
R33	17	20	22	N/A	24	18
R34†	7	8	8	16	8	5
Large office 2 (LO2)						
R35	19	19	18	N/A	30	22
R36	18	19	17	16	27	23
R37	19	24	19	N/A	33	21
R38†	23	25	27	31	N/A	N/A

† Behind windows, ‡behind walls, N/A: not performed or lack of sufficient dynamic range

Table B.2 – Channel DS values measured in the O2I scenario in Belfort

RX positions	DS [ns]					
	S1			S2		S3
	3 GHz	10 GHz	17 GHz		60 GHz	
Corridor (Co)						
R1	13	18	16	16	N/A	N/A
R2	24	18	20	22	N/A	N/A
R3	16	25	22	14	N/A	N/A
R4	24	18	20	23	N/A	N/A
R5	20	17	18	19	N/A	N/A
Flat (Fl)						
R6	22	22	20	15	N/A	N/A
R7	23	22	21	23	N/A	N/A
R8	25	22	19	20	N/A	N/A
R9	19	16	16	15	N/A	N/A
R10	24	23	12	18	N/A	N/A
R11	22	14	17	14	N/A	N/A
R12	21	19	17	9	N/A	N/A
R13	20	21	24	31	N/A	N/A
R14†	20	26	23	24	N/A	8
R15	23	19	21	23	N/A	N/A

RX positions	DS [ns]					
	S1			S2		S3
	3 GHz	10 GHz	17 GHz		60 GHz	
R16	19	20	24	N/A	N/A	N/A
R17†	24	12	22	24	N/A	7
R18	24	20	18	22	N/A	N/A
R19	21	20	17	15	N/A	N/A
Break–room (BR)						
R20‡	30	29	28	29	26	27
R21†	18	14	9	0	4	8
R22‡	23	15	36	19	18	22
R23†	17	14	14	9	9	11
R24‡	27	29	31	31	22	N/A
R25	11	6	9	N/A	7	7
R26	30	29	32	25	19	14
R27	9	10	15	N/A	2	3
R28	14	10	23	16	8	9
R29	17	19	14	23	19	23
R30	6	9	9	N/A	6	6
Large office 1 (LO1)						
R31	9	15	17	16	10	21
R32	16	21	16	21	17	14

RX positions	DS [ns]					
	S1			S2		S3
	3 GHz	10 GHz	17 GHz		60 GHz	
R33	20	17	22	N/A	16	19
R34†	12	7	6	11	7	7
Large office 2 (LO2)						
R35	26	23	17	N/A	20	14
R36	23	21	20	15	13	14
R37	28	25	19	N/A	21	10
R38†	37	36	33	41	N/A	N/A

† Behind windows, ‡behind walls, N/A: not performed or lack of sufficient dynamic range

Annex C

C. Urban Outdoor Measurement Results in Belfort

Herein, detailed results regarding the measurement campaign described in **Chapter V** are provided. The measurements were performed at 3, 17 and 60 GHz in an urban outdoor environment in Belfort.

1. Delay spread (DS) and azimuth spread (AS) values

In this section, channel DS and AS values, measured at each of the RX/MS position, are summarized in **Table C.1.1** and **Table C.1.2** respectively.

Table C.1.1 – Channel DS values measured in the urban outdoor environment in Belfort

RX positions	Omnidirectional DS [ns]		
	3 GHz	17 GHz	60 GHz
Open Square (OS) – LoS			
A1	11	1	6
A4	73	98	95
A9	9	22	13
A10	47	26	49
A11	11	21	19
A15	6	14	66
Open Square (OS) – NLoS			
A2	63	67	49
A3	68	36	30
A5	35	31	27
A6	57	48	43
A7	71	32	14
A8	70	45	41
A12	87	50	65
A13	76	70	66

RX positions	Omnidirectional DS [ns]		
	3 GHz	17 GHz	60 GHz
A14	53	52	35
A16	57	64	57
Street Intersection (SI) – LoS			
B1	42	51	20
B5	34	26	28
B6	30	29	27
B11	N/A	19	19
Street Intersection (SI) – NLoS			
B2	44	48	47
B3	66	69	55
B4	64	53	52
B7	34	24	N/A
B8	86	69	N/A

RX positions	Omnidirectional DS [ns]		
	3 GHz	17 GHz	60 GHz
B9	74	52	53
B10	97	94	87
Street Canyon (SC) – LoS			
C1	17	11	15
C3	4	4	0
C7	7	5	2
Street Canyon (SC) – NLoS			
C2	18	52	41
C4	24	55	37
C5	43	53	20
C6	37	13	96
C8	52	84	130

Table C.1.2 – Channel AS values measured in the urban outdoor environment in Belfort

RX positions	AS [°]	
	17 GHz	60 GHz
Open Square (OS) – LoS		
A1	17	22
A4	16	26

RX positions	AS [°]	
	17 GHz	60 GHz
A9	12	34
A10	32	34
A11	33	39

RX positions	AS [°]	
	17 GHz	60 GHz
A15	33	51
Open Square (OS) – NLoS		
A2	29	31
A3	20	19
A5	21	24
A6	29	23
A7	20	25
A8	40	33
A12	25	30
A13	27	19
A14	33	21
A16	26	15
Street Intersection (SI) – LoS		
B1	26	41
B5	21	41
B6	29	44
B11	35	36
Street Intersection (SI) – NLoS		
B2	28	45
B3	36	10
B4	33	62
B7	25	77
B8	51	46
B9	44	36
B10	46	46
Street Canyon (SC) – LoS		
C1	21	31
C3	12	13
C7	19	11
Street Canyon (SC) – NLoS		
C2	37	16
C4	14	13
C5	18	13
C6	16	14
C8	18	12

N/A: not performed or lack of sufficient dynamic range

2. Azimuth–delay power profiles (ADPPs)

In this section, details on the ADPPs are provided according the format specified below. These characteristics are given for the same MS positions as given in **Section 3.2** of **Chapter V**.

Aerial map view of BS and MS positions

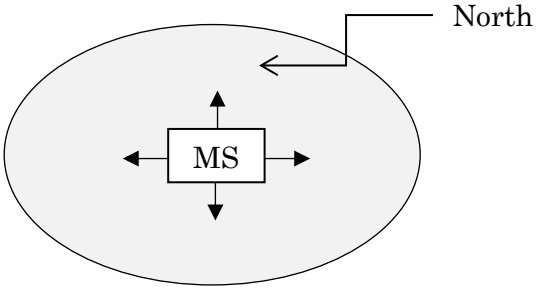

Mean ADPP derived from both setups (S1 and S2), assuming omnidirectional MS antenna patterns

S2

ADPPs measured in the four different sectors with the 90° HPBW MS antenna via setup S2

ADPPs obtained from S2, assuming omnidirectional MS antenna patterns (**Eq. V.2.3**) – setup S2

S1

ADPPs measured in the four different sectors with the omnidirectional MS antenna via setup S1

ADPPs obtained from S1, assuming omnidirectional MS antenna patterns (**Eq. V.2.3**) – setup S1


17 GHz
TxA
A1

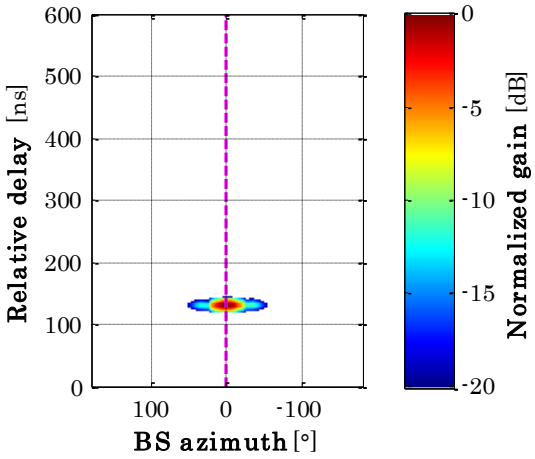
Relative delay [ns]
BS azimuth [°]
Normalized gain [dB]

S2

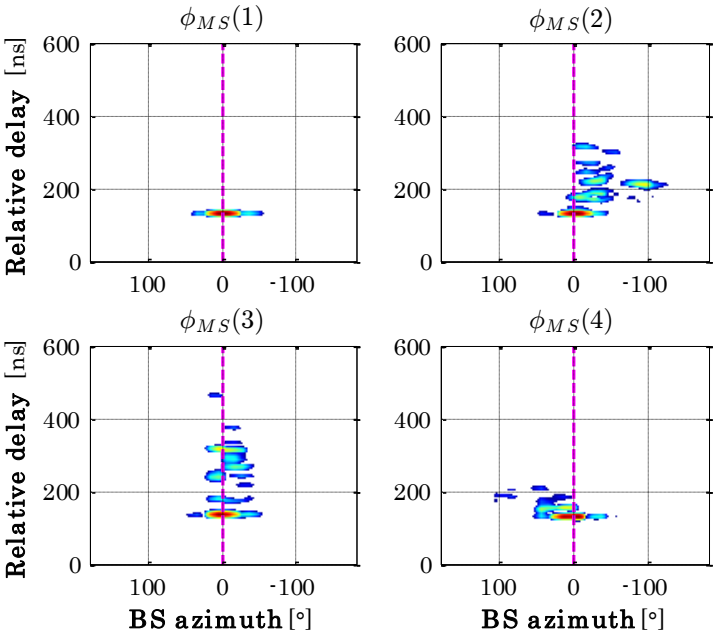
$\phi_{MS}(1)$
$\phi_{MS}(2)$
$\phi_{MS}(3)$
$\phi_{MS}(4)$
Relative delay [ns]
BS azimuth [°]

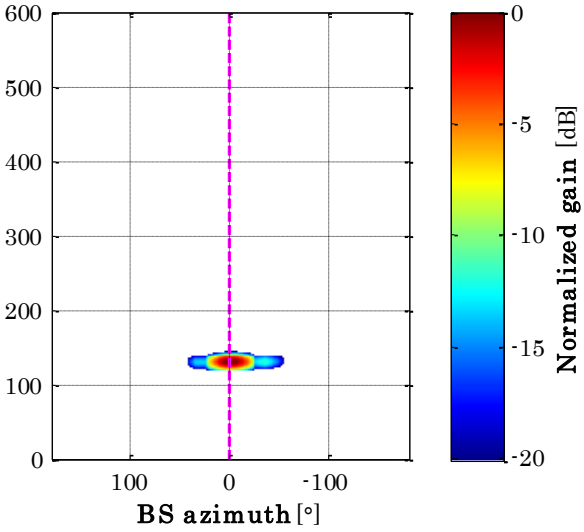
BS azimuth [°]
Normalized gain [dB]

S1

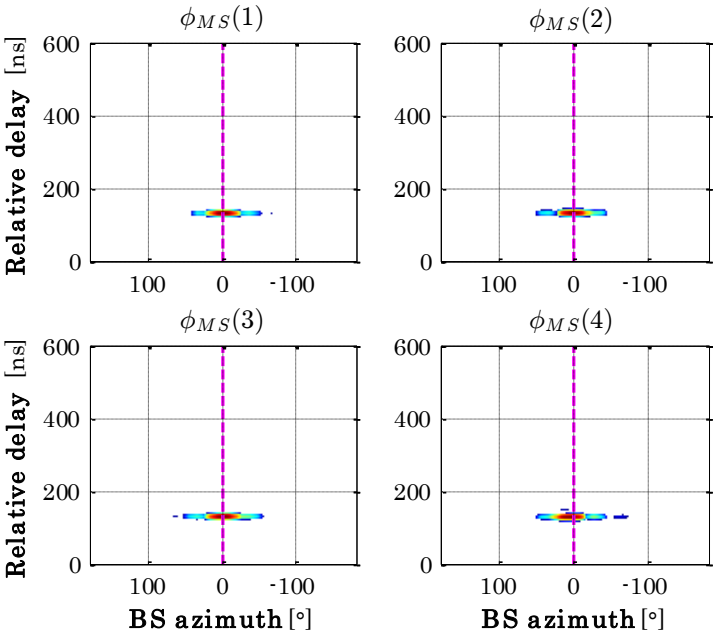
$\phi_{MS}(1)$
$\phi_{MS}(2)$
$\phi_{MS}(3)$
$\phi_{MS}(4)$
Relative delay [ns]
BS azimuth [°]

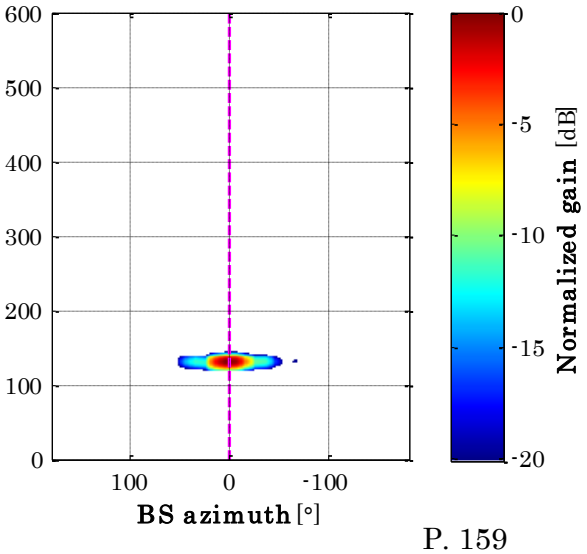
BS azimuth [°]
Normalized gain [dB]


17 GHz
TxA
A2

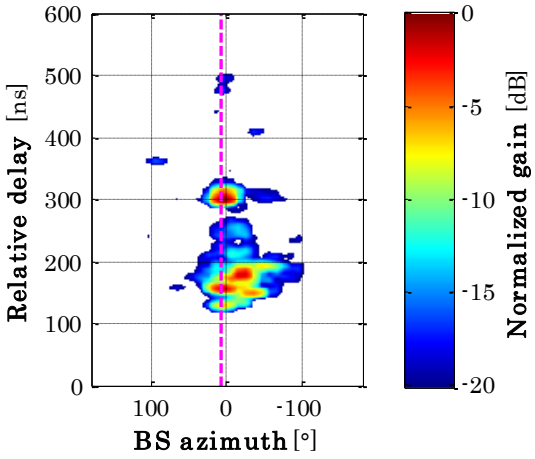
Relative delay [ns]
BS azimuth [°]
Normalized gain [dB]

S2

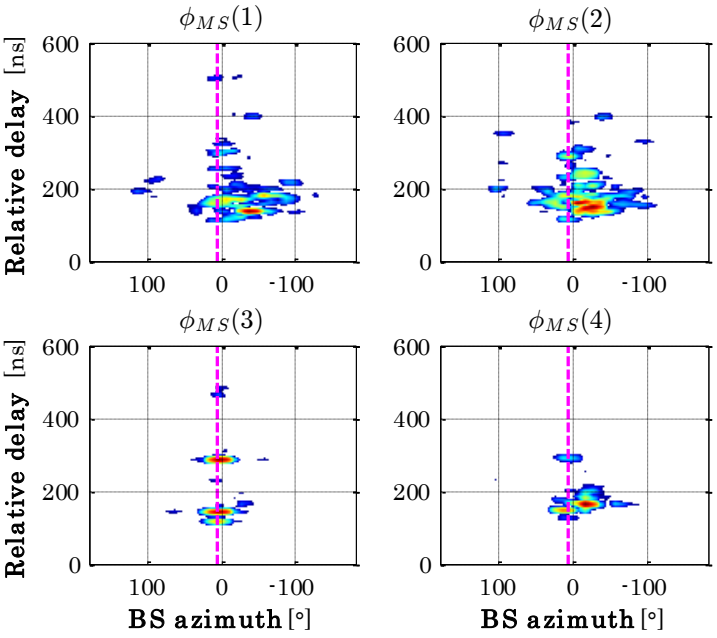
$\phi_{MS}(1)$
$\phi_{MS}(2)$
$\phi_{MS}(3)$
$\phi_{MS}(4)$
Relative delay [ns]
BS azimuth [°]

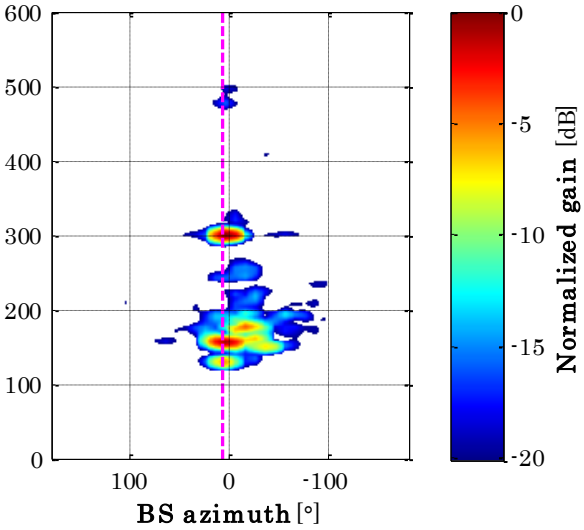
BS azimuth [°]
Normalized gain [dB]

S1

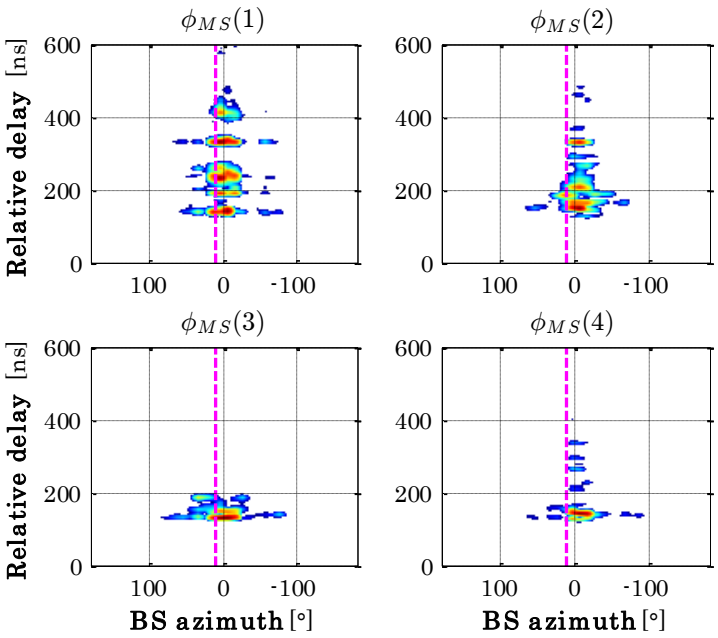
$\phi_{MS}(1)$
$\phi_{MS}(2)$
$\phi_{MS}(3)$
$\phi_{MS}(4)$
Relative delay [ns]
BS azimuth [°]

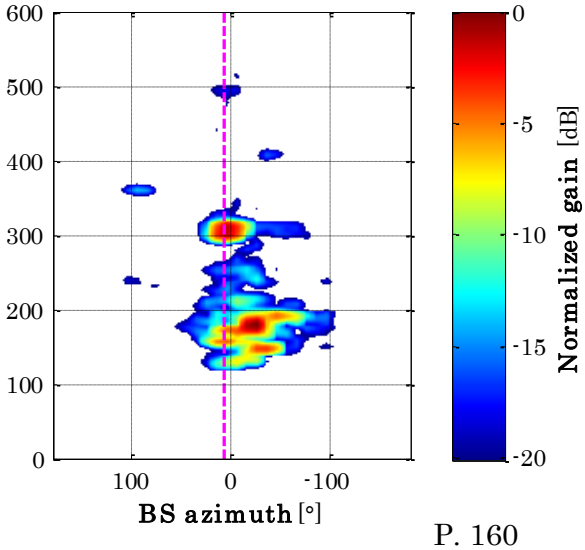
BS azimuth [°]
Normalized gain [dB]


17 GHz
TxA
A3

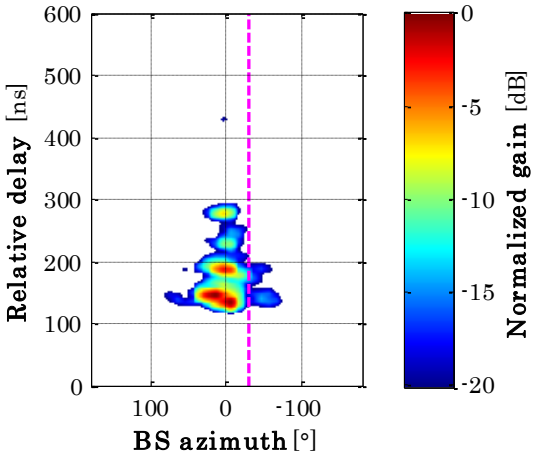
Relative delay [ns]
BS azimuth [°]
Normalized gain [dB]

S2

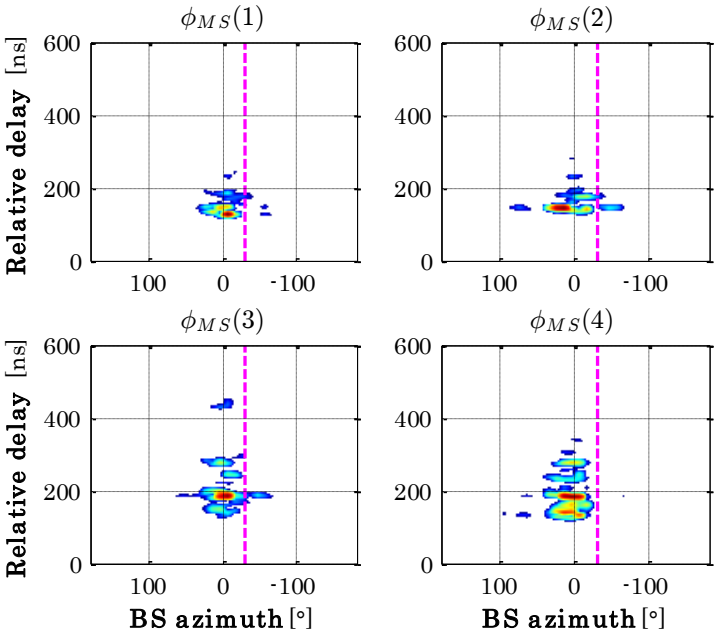
$\phi_{MS}(1)$
$\phi_{MS}(2)$
$\phi_{MS}(3)$
$\phi_{MS}(4)$
Relative delay [ns]
BS azimuth [°]

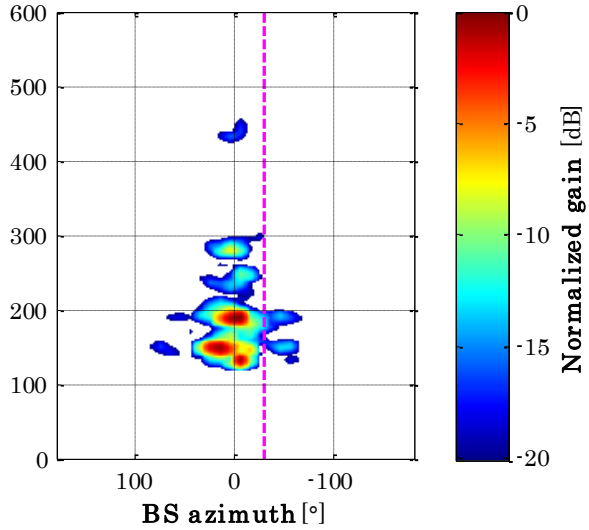
Relative delay [ns]
BS azimuth [°]
Normalized gain [dB]

S1

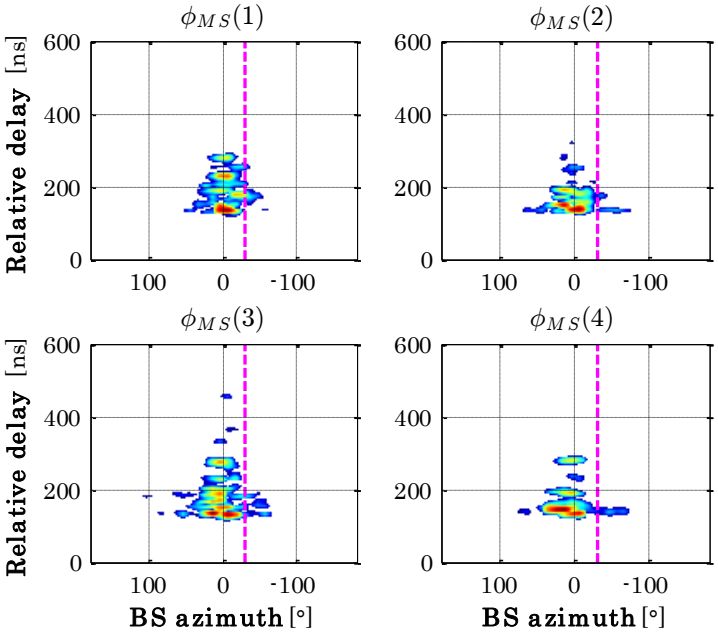
$\phi_{MS}(1)$
$\phi_{MS}(2)$
$\phi_{MS}(3)$
$\phi_{MS}(4)$
Relative delay [ns]
BS azimuth [°]

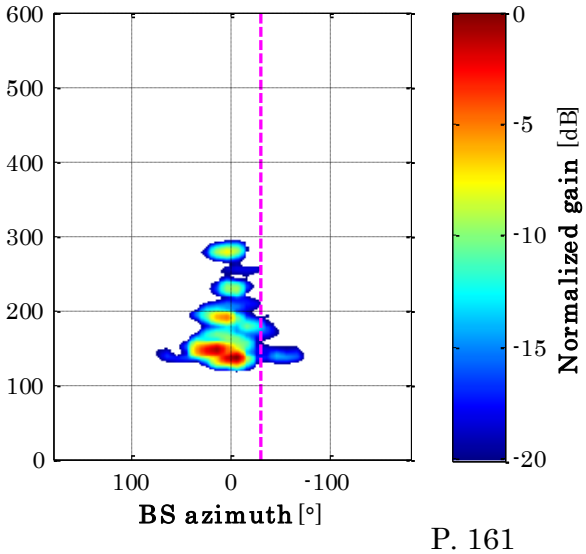
Relative delay [ns]
BS azimuth [°]
Normalized gain [dB]

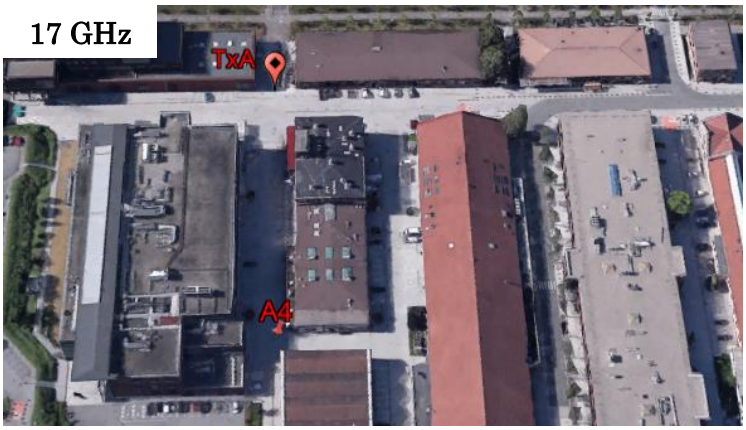
17 GHz
TxA
A4

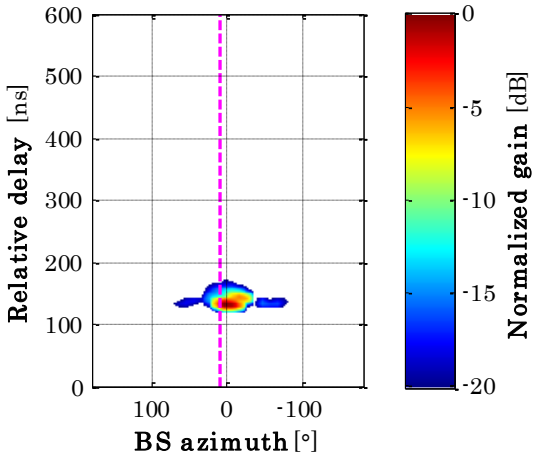
Relative delay [ns]
BS azimuth [°]
Normalized gain [dB]

S2

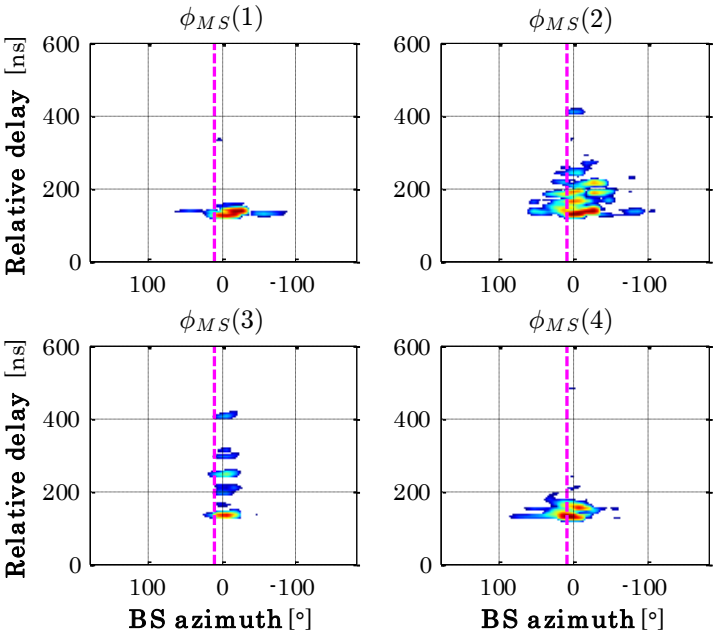
$\phi_{MS}(1)$
$\phi_{MS}(2)$
$\phi_{MS}(3)$
$\phi_{MS}(4)$
Relative delay [ns]
BS azimuth [°]

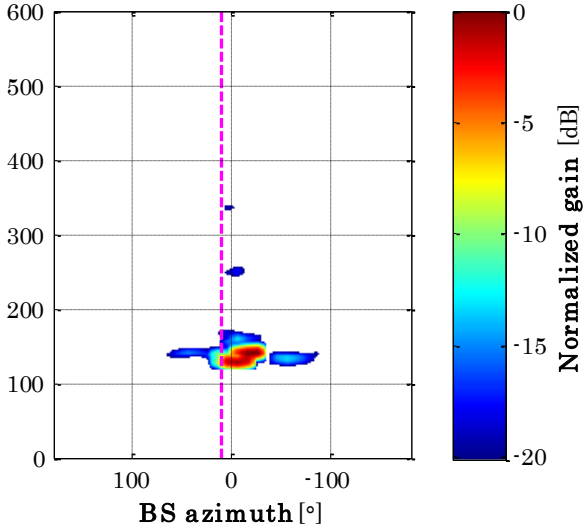
BS azimuth [°]
Normalized gain [dB]

S1

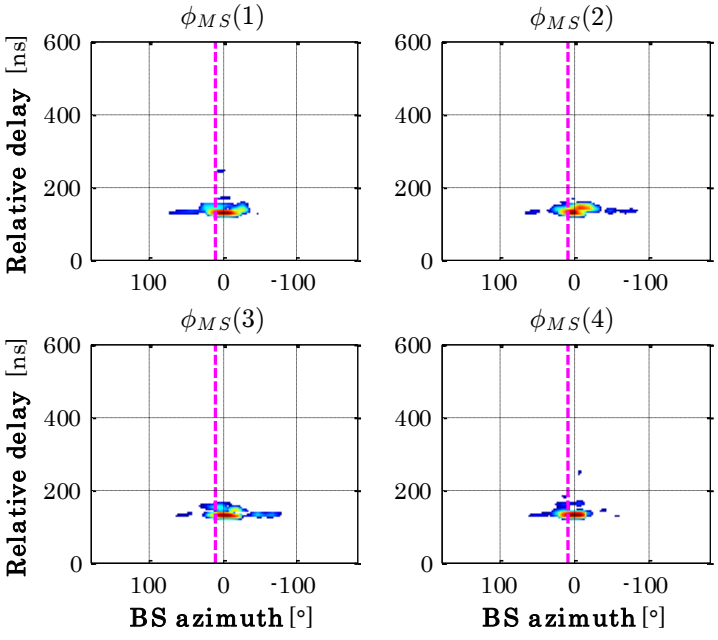
$\phi_{MS}(1)$
$\phi_{MS}(2)$
$\phi_{MS}(3)$
$\phi_{MS}(4)$
Relative delay [ns]
BS azimuth [°]

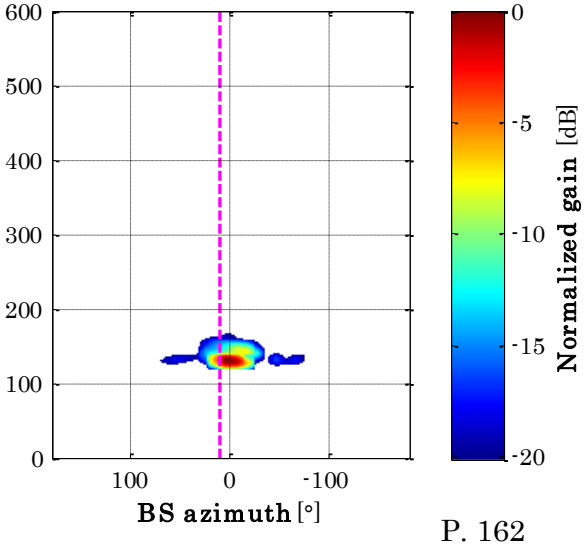
BS azimuth [°]
Normalized gain [dB]

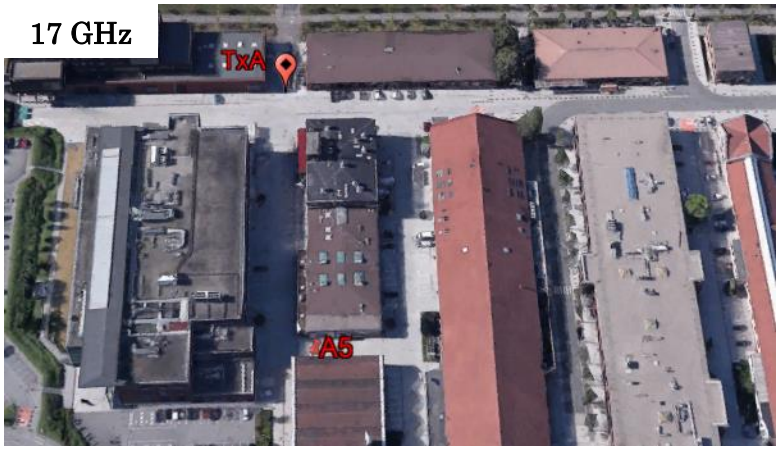
17 GHz
TxA
A5

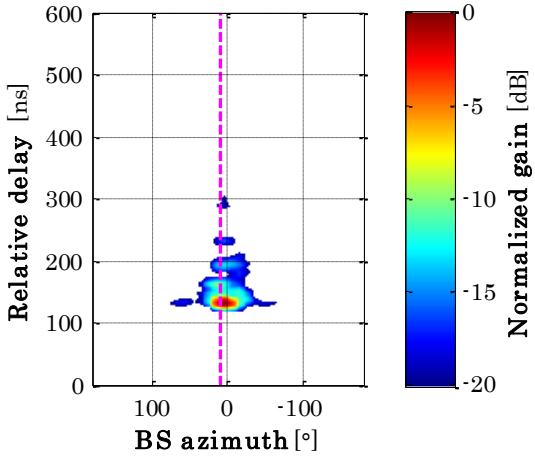
Relative delay [ns]
BS azimuth [°]
Normalized gain [dB]

S2

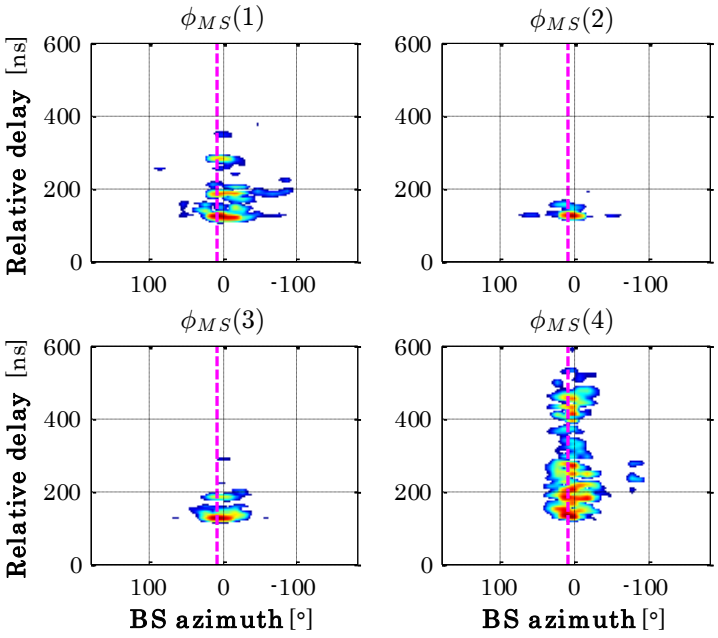
$\phi_{MS}(1)$
$\phi_{MS}(2)$
$\phi_{MS}(3)$
$\phi_{MS}(4)$
Relative delay [ns]
BS azimuth [°]

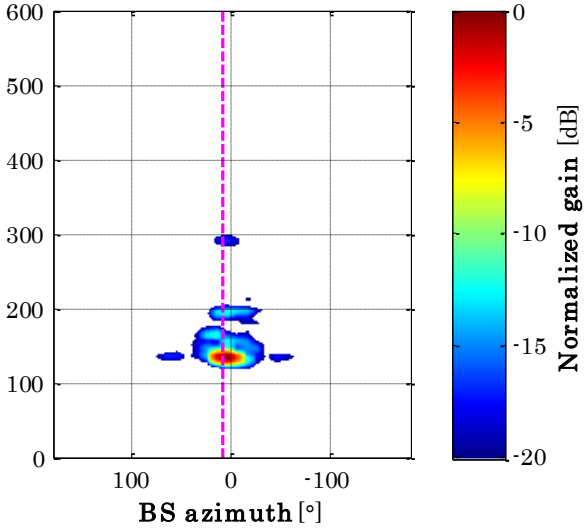
Relative delay [ns]
BS azimuth [°]
Normalized gain [dB]

S1

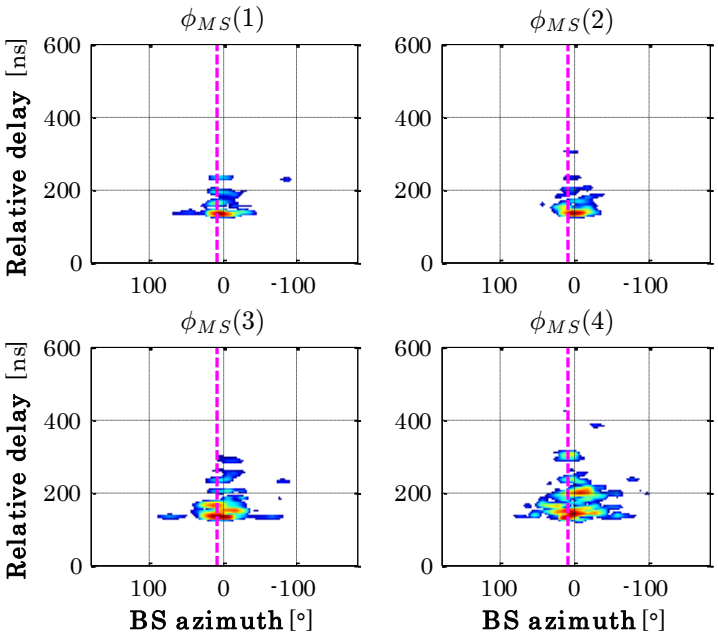
$\phi_{MS}(1)$
$\phi_{MS}(2)$
$\phi_{MS}(3)$
$\phi_{MS}(4)$
Relative delay [ns]
BS azimuth [°]

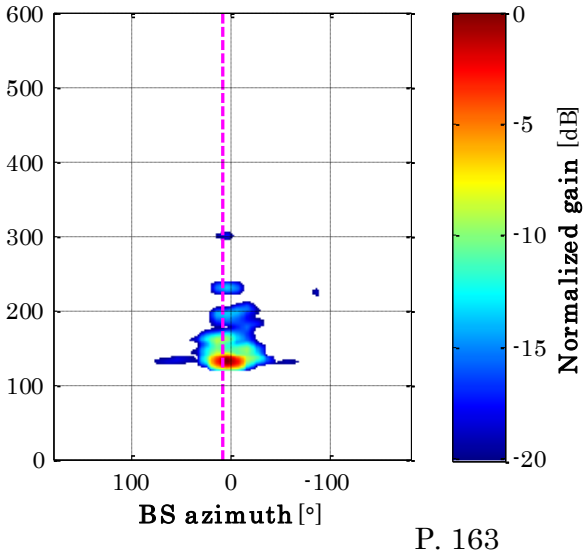
Relative delay [ns]
BS azimuth [°]
Normalized gain [dB]


17 GHz
TxA
A6

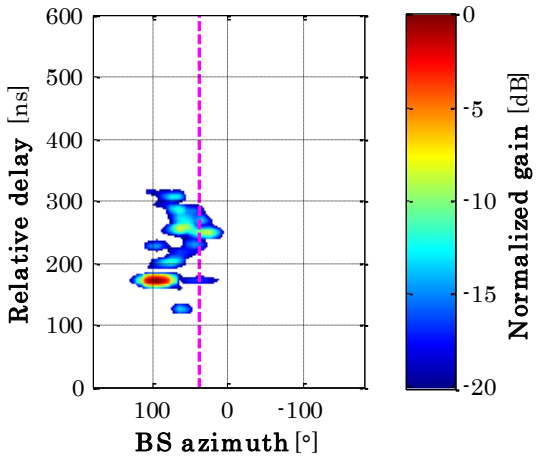
Relative delay [ns]
BS azimuth [°]
Normalized gain [dB]

S2

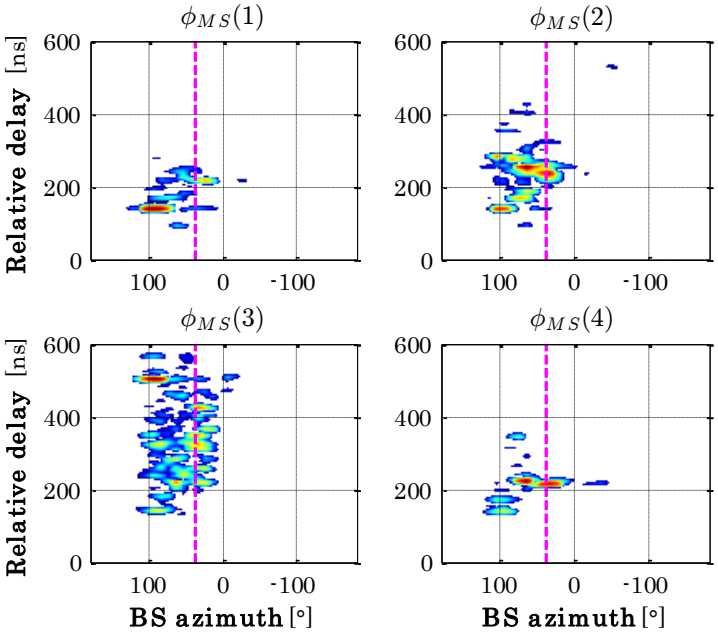
$\phi_{MS}(1)$
$\phi_{MS}(2)$
$\phi_{MS}(3)$
$\phi_{MS}(4)$
Relative delay [ns]
BS azimuth [°]

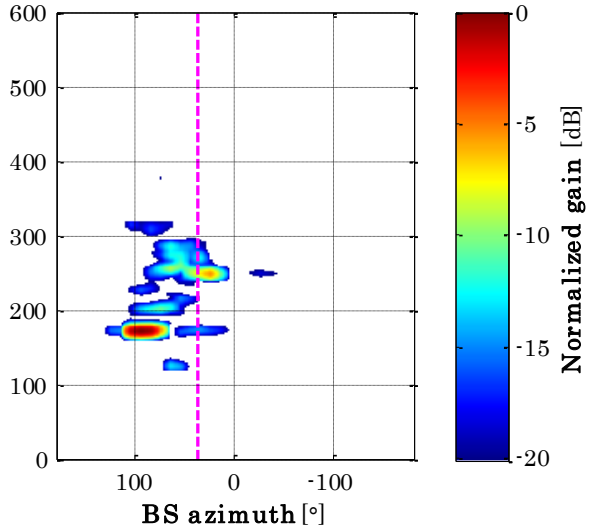
BS azimuth [°]
Normalized gain [dB]

S1

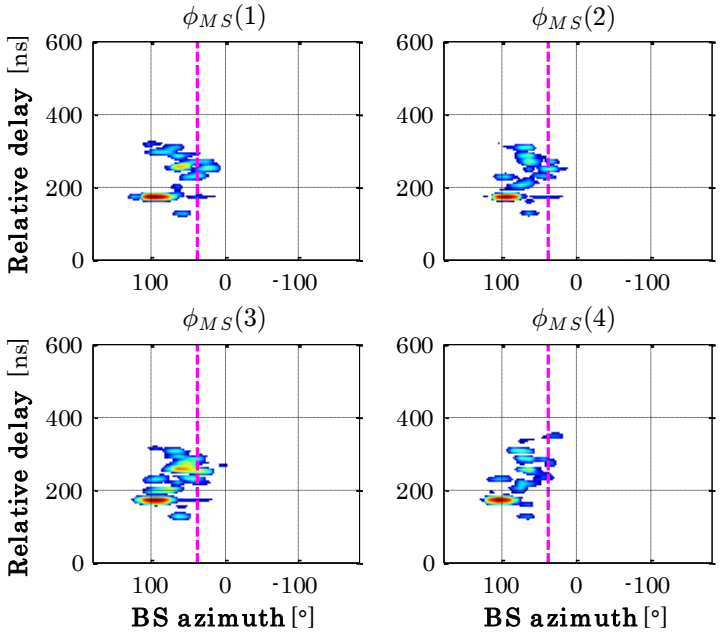
$\phi_{MS}(1)$
$\phi_{MS}(2)$
$\phi_{MS}(3)$
$\phi_{MS}(4)$
Relative delay [ns]
BS azimuth [°]

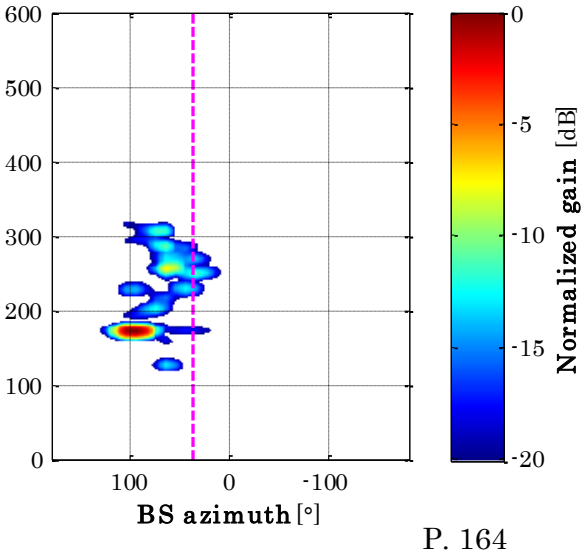
BS azimuth [°]
Normalized gain [dB]


17 GHz
TxA
A7

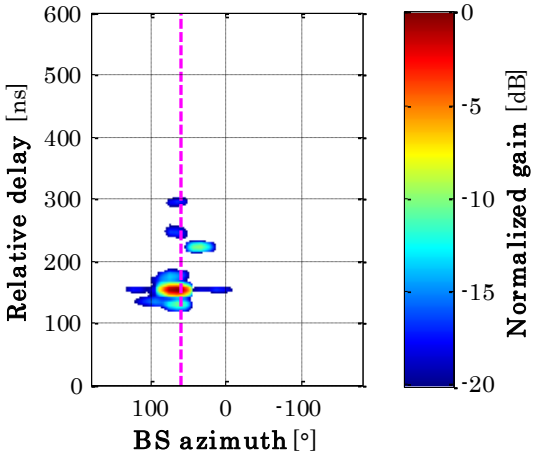
Relative delay [ns]
BS azimuth [°]
Normalized gain [dB]

S2

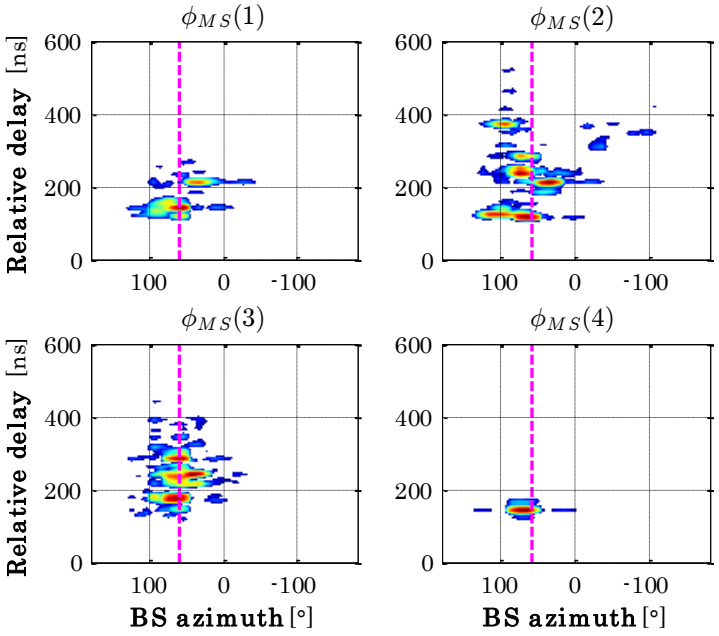
$\phi_{MS}(1)$
$\phi_{MS}(2)$
$\phi_{MS}(3)$
$\phi_{MS}(4)$
Relative delay [ns]
BS azimuth [°]

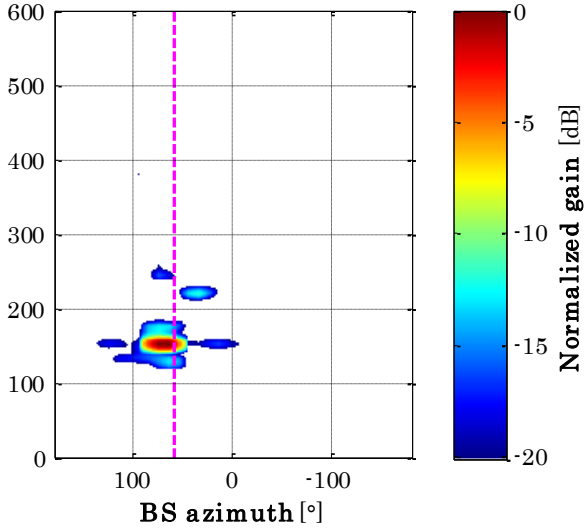
BS azimuth [°]
Normalized gain [dB]

S1

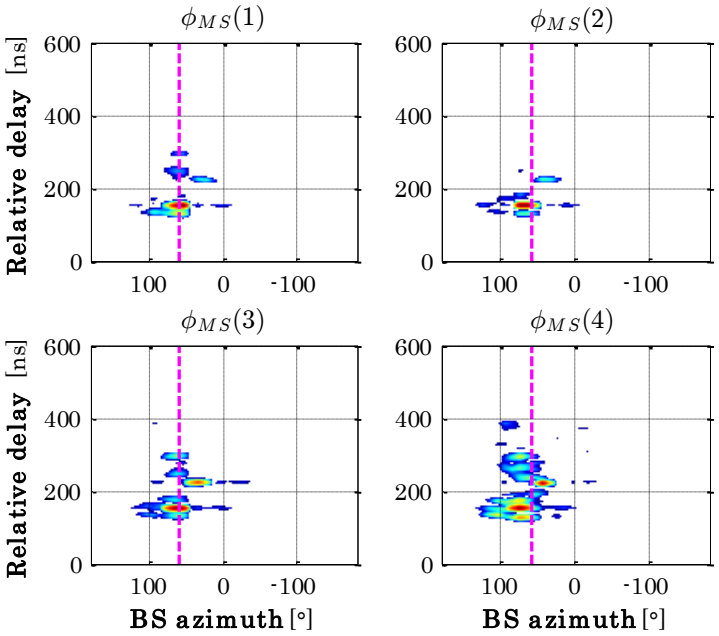
$\phi_{MS}(1)$
$\phi_{MS}(2)$
$\phi_{MS}(3)$
$\phi_{MS}(4)$
Relative delay [ns]
BS azimuth [°]

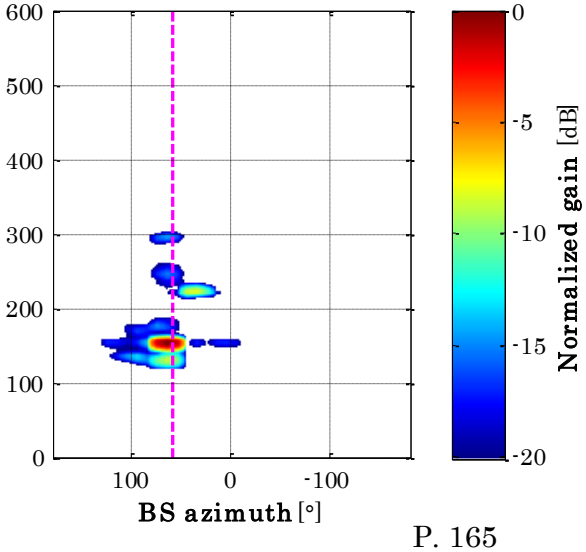
BS azimuth [°]
Normalized gain [dB]


17 GHz
TxA
A8

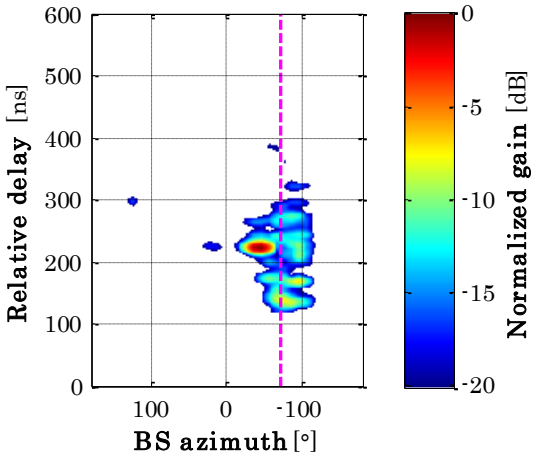
Relative delay [ns]
BS azimuth [°]
Normalized gain [dB]

S2

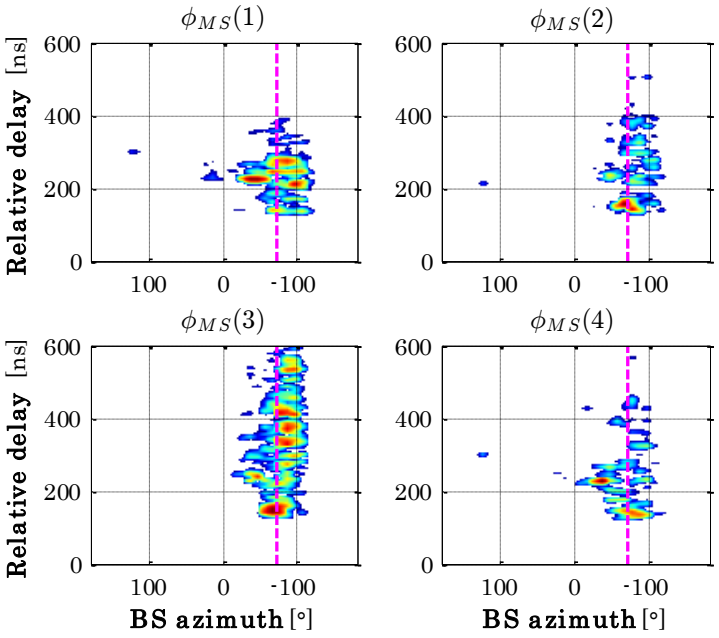
$\phi_{MS}(1)$
$\phi_{MS}(2)$
$\phi_{MS}(3)$
$\phi_{MS}(4)$
Relative delay [ns]
BS azimuth [°]

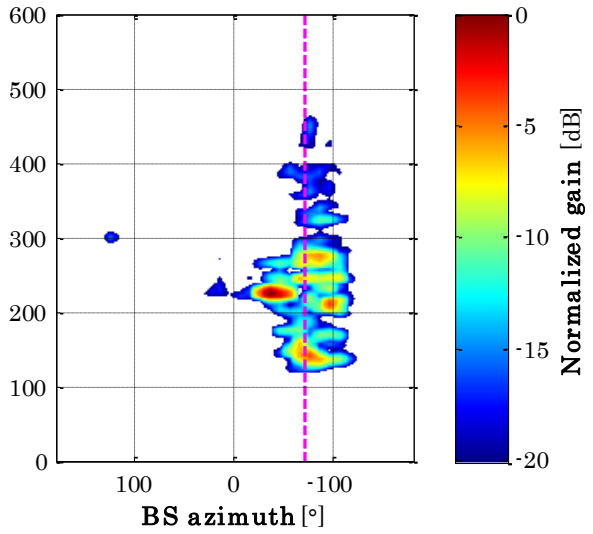
BS azimuth [°]
Normalized gain [dB]

S1

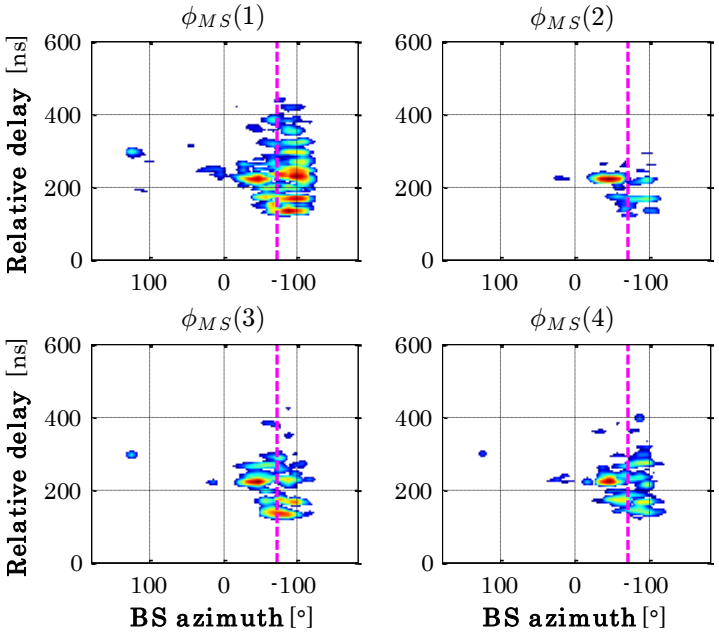
$\phi_{MS}(1)$
$\phi_{MS}(2)$
$\phi_{MS}(3)$
$\phi_{MS}(4)$
Relative delay [ns]
BS azimuth [°]

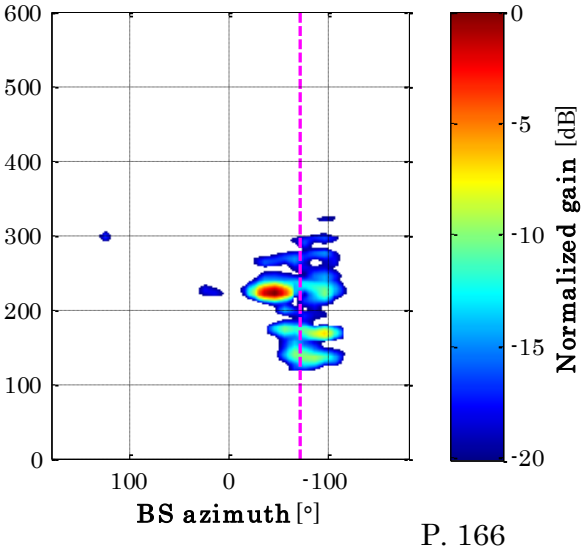
BS azimuth [°]
Normalized gain [dB]

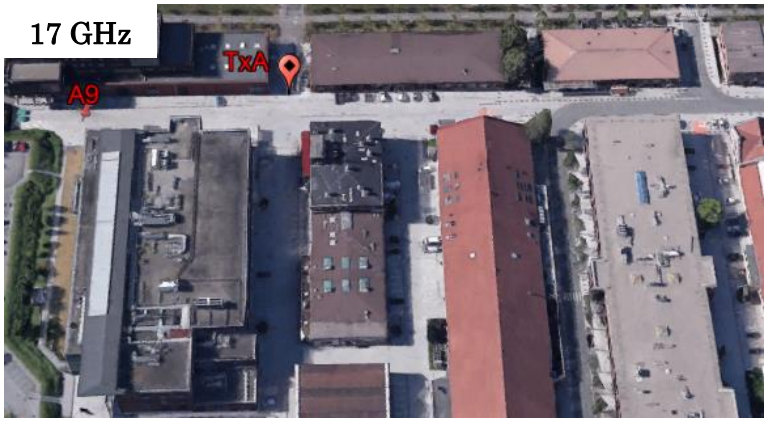
17 GHz
TxA
A9

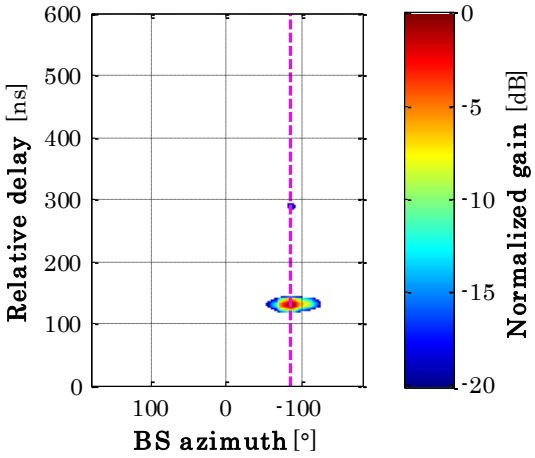
Relative delay [ns]
BS azimuth [°]
Normalized gain [dB]

S2

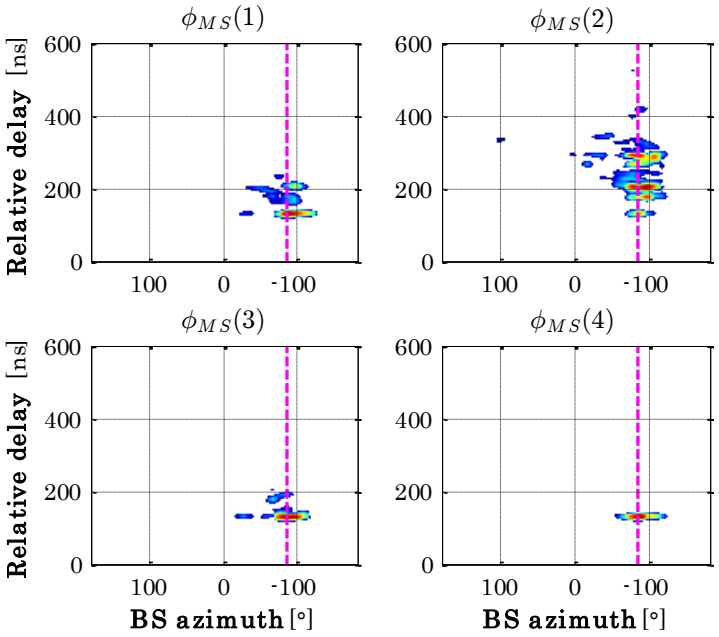
$\phi_{MS}(1)$
$\phi_{MS}(2)$
$\phi_{MS}(3)$
$\phi_{MS}(4)$
Relative delay [ns]
BS azimuth [°]

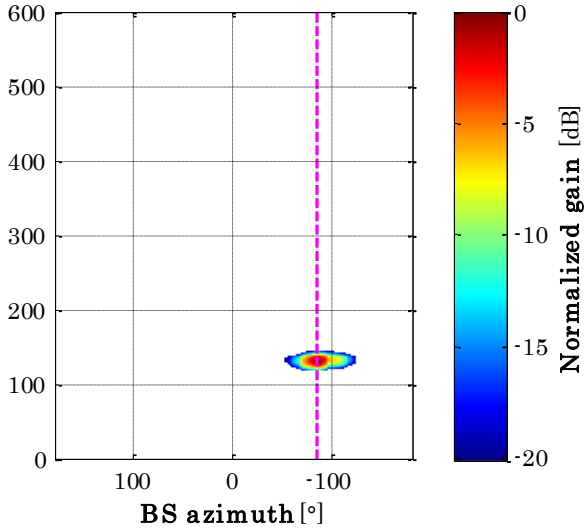
BS azimuth [°]
Normalized gain [dB]

S1

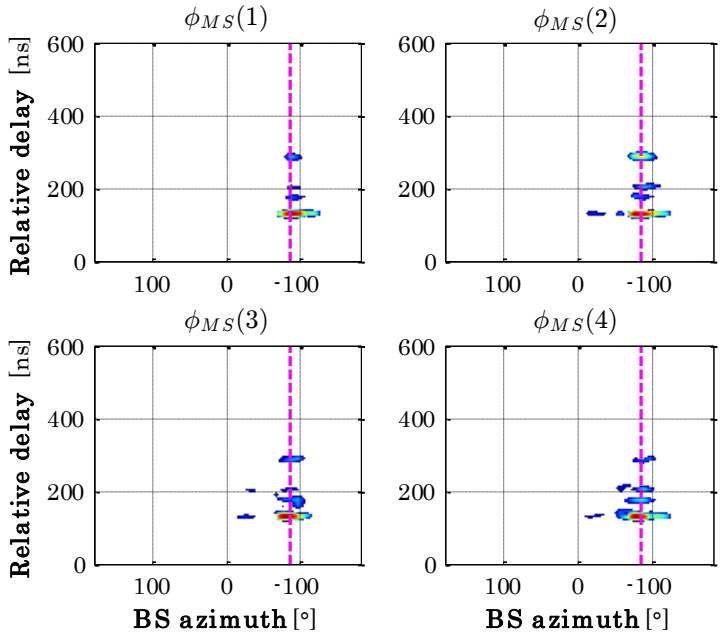
$\phi_{MS}(1)$
$\phi_{MS}(2)$
$\phi_{MS}(3)$
$\phi_{MS}(4)$
Relative delay [ns]
BS azimuth [°]

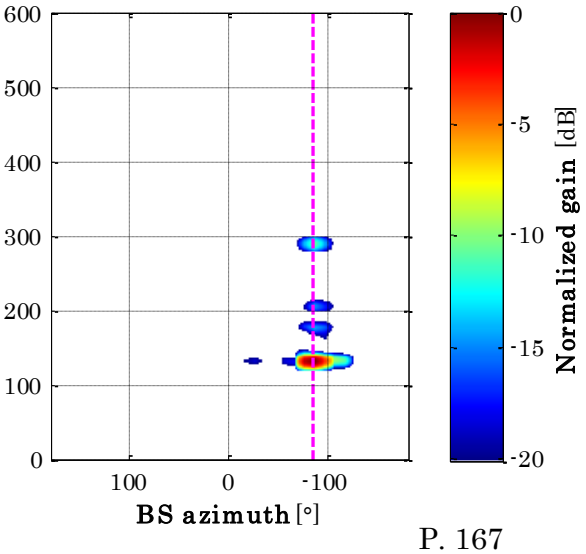
BS azimuth [°]
Normalized gain [dB]


17 GHz
TxA
A10

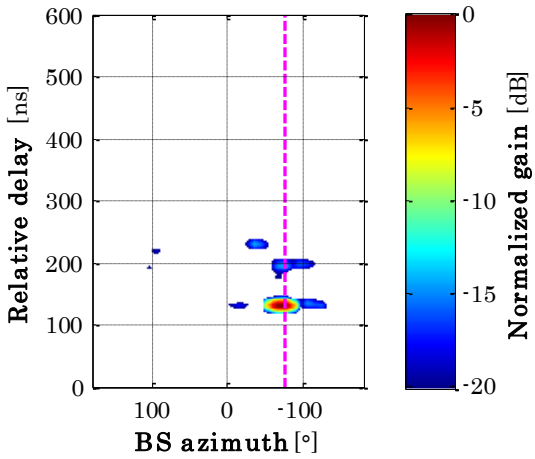
Relative delay [ns]
BS azimuth [°]
Normalized gain [dB]

S2

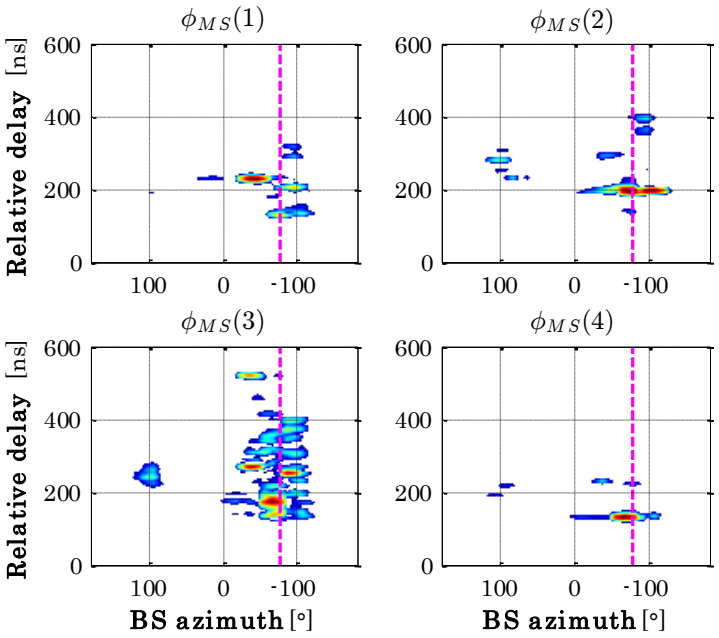
$\phi_{MS}(1)$
$\phi_{MS}(2)$
$\phi_{MS}(3)$
$\phi_{MS}(4)$
Relative delay [ns]
BS azimuth [°]

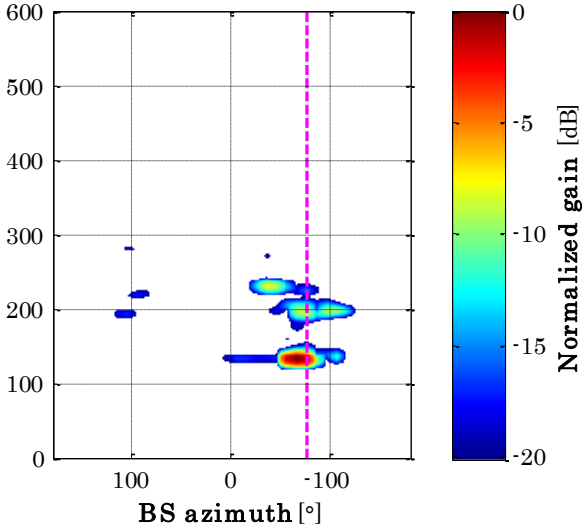
Relative delay [ns]
BS azimuth [°]
Normalized gain [dB]

S1

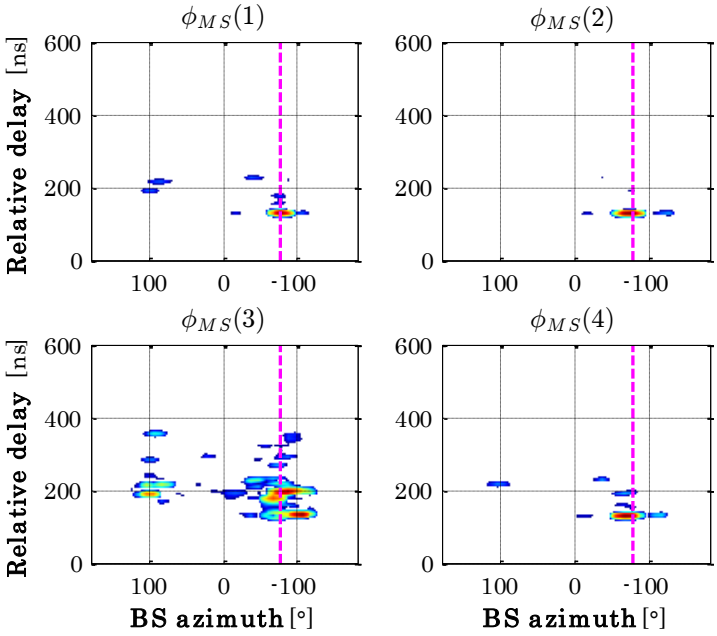
$\phi_{MS}(1)$
$\phi_{MS}(2)$
$\phi_{MS}(3)$
$\phi_{MS}(4)$
Relative delay [ns]
BS azimuth [°]

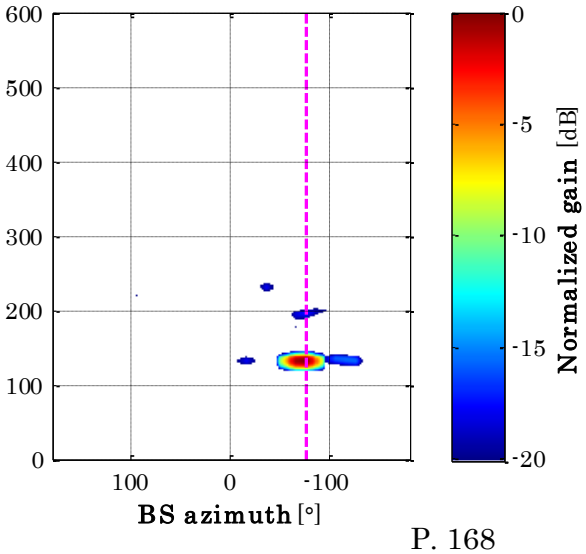
Relative delay [ns]
BS azimuth [°]
Normalized gain [dB]


17 GHz
TxA
A11

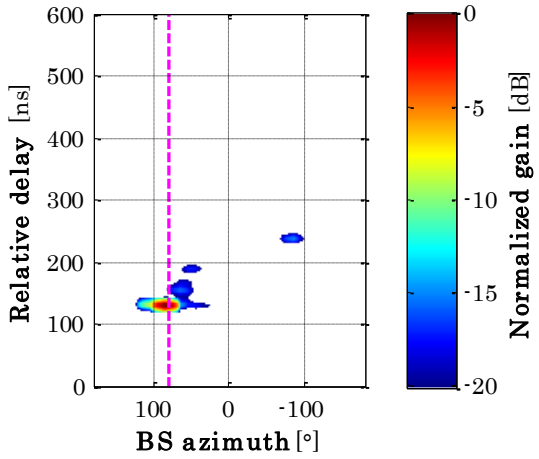
Relative delay [ns]
BS azimuth [°]
Normalized gain [dB]

S2

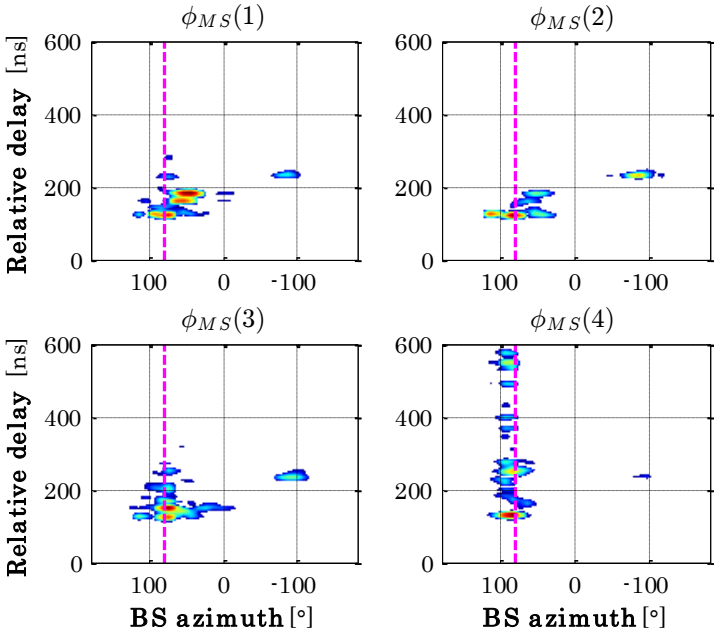
$\phi_{MS}(1)$
$\phi_{MS}(2)$
$\phi_{MS}(3)$
$\phi_{MS}(4)$
Relative delay [ns]
BS azimuth [°]

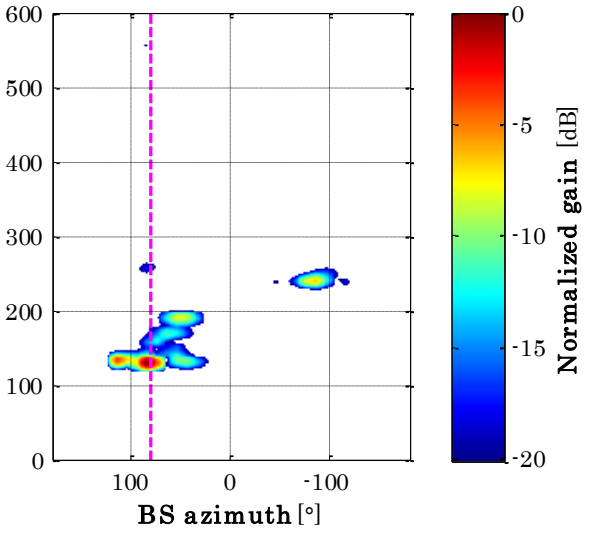
Relative delay [ns]
BS azimuth [°]
Normalized gain [dB]

S1

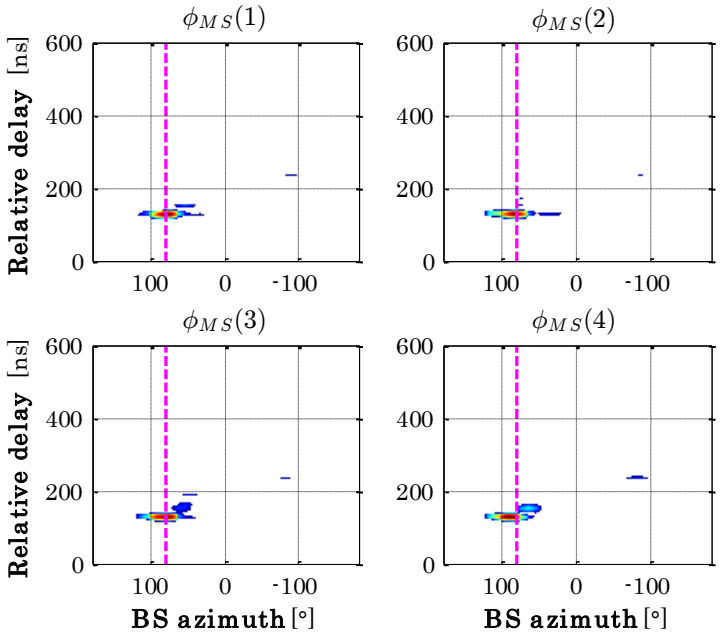
$\phi_{MS}(1)$
$\phi_{MS}(2)$
$\phi_{MS}(3)$
$\phi_{MS}(4)$
Relative delay [ns]
BS azimuth [°]

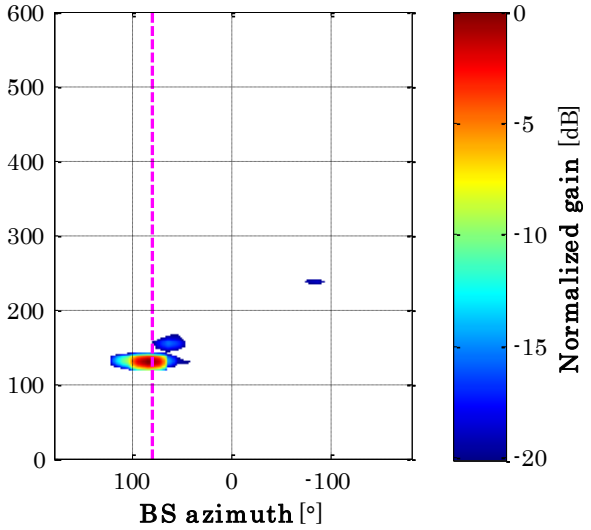
Relative delay [ns]
BS azimuth [°]
Normalized gain [dB]

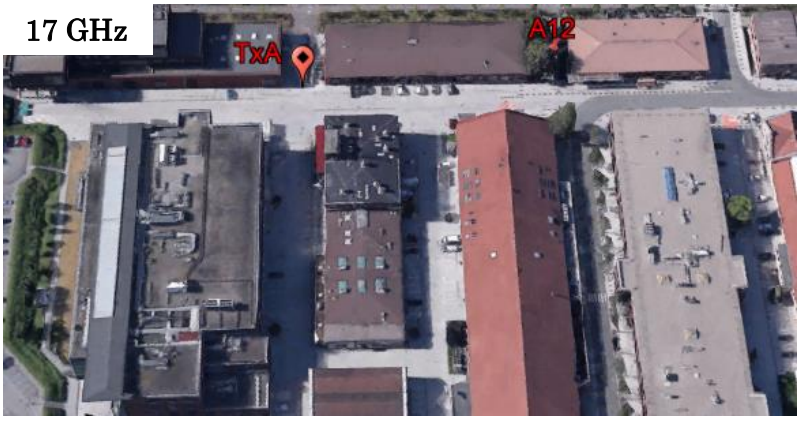
17 GHz
TxA
A12

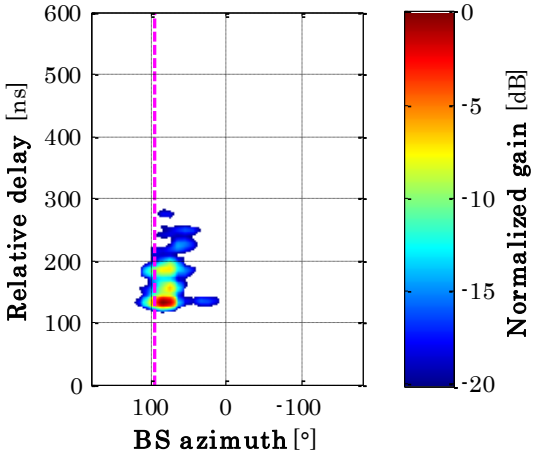
Relative delay [ns]
BS azimuth [°]
Normalized gain [dB]

S2

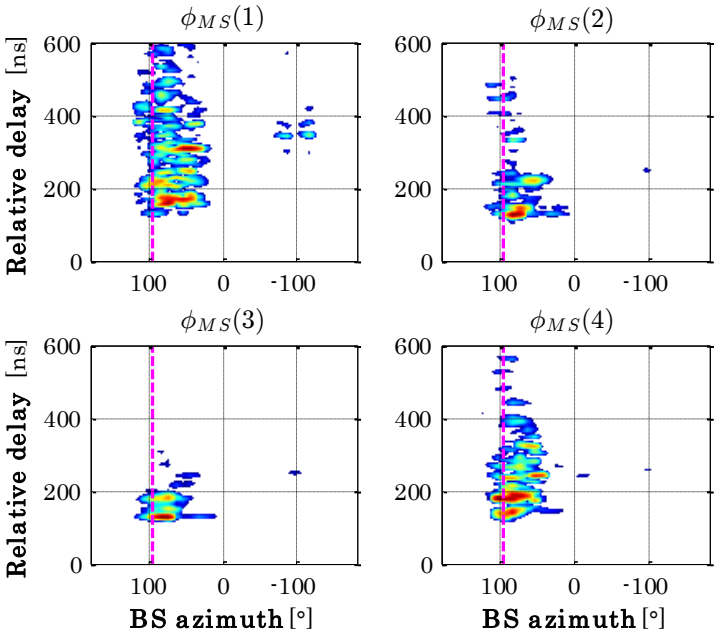
$\phi_{MS}(1)$
$\phi_{MS}(2)$
$\phi_{MS}(3)$
$\phi_{MS}(4)$
Relative delay [ns]
BS azimuth [°]

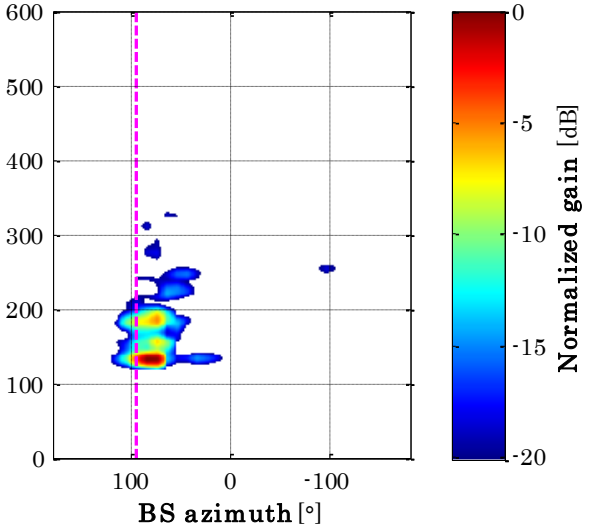
BS azimuth [°]
Normalized gain [dB]

S1

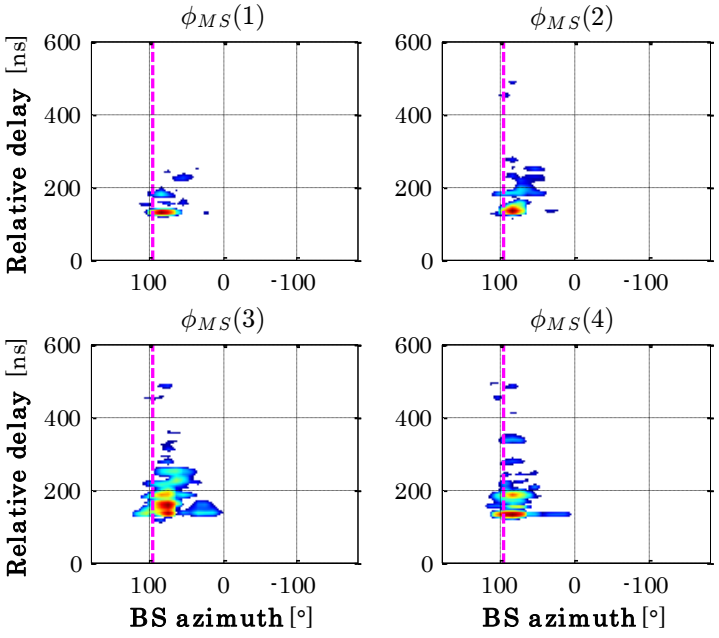
$\phi_{MS}(1)$
$\phi_{MS}(2)$
$\phi_{MS}(3)$
$\phi_{MS}(4)$
Relative delay [ns]
BS azimuth [°]

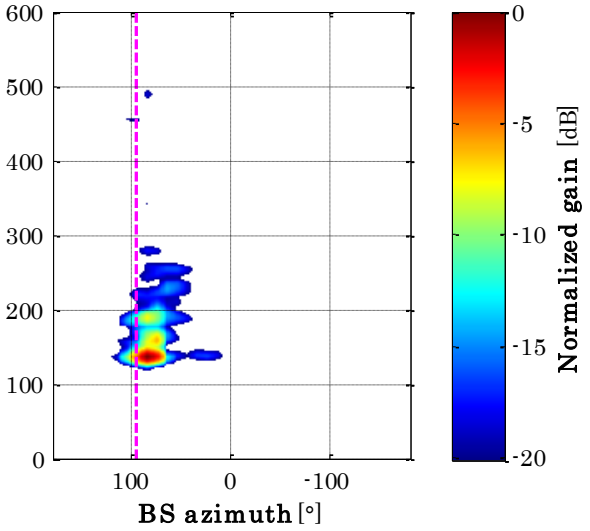
BS azimuth [°]
Normalized gain [dB]


17 GHz
TxA
A13

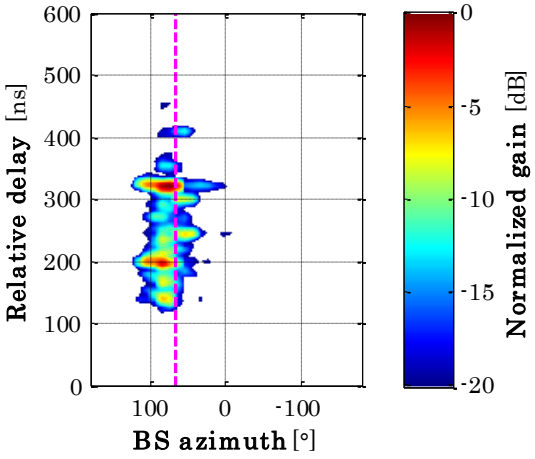
Relative delay [ns]
BS azimuth [°]
Normalized gain [dB]

S2

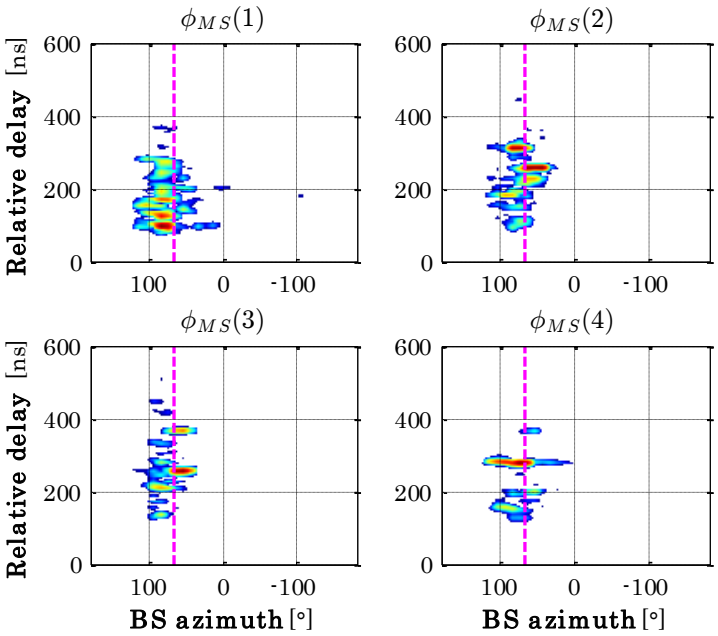
$\phi_{MS}(1)$
$\phi_{MS}(2)$
$\phi_{MS}(3)$
$\phi_{MS}(4)$
Relative delay [ns]
BS azimuth [°]

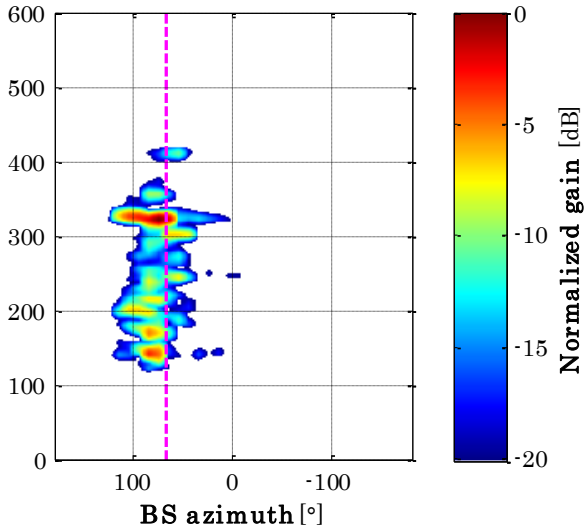
Relative delay [ns]
BS azimuth [°]
Normalized gain [dB]

S1

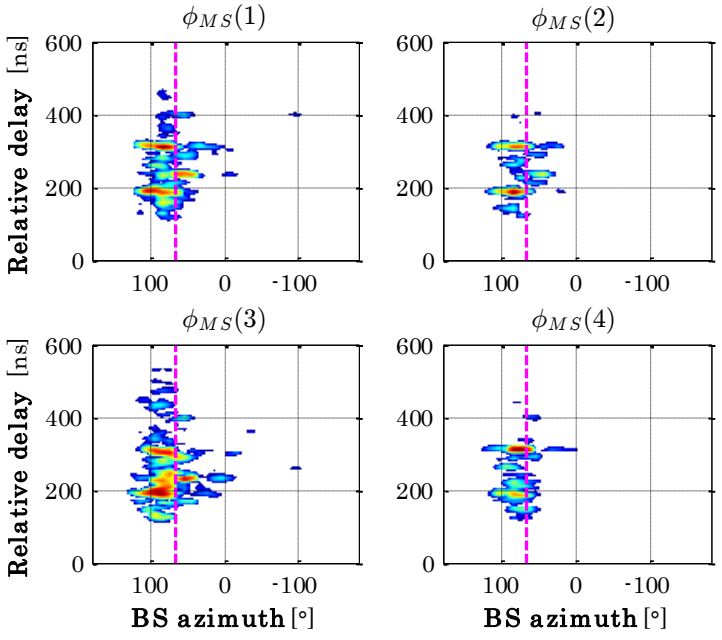
$\phi_{MS}(1)$
$\phi_{MS}(2)$
$\phi_{MS}(3)$
$\phi_{MS}(4)$
Relative delay [ns]
BS azimuth [°]

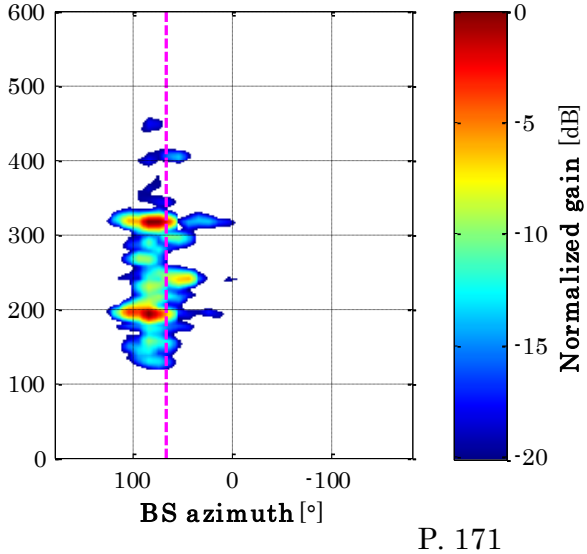
Relative delay [ns]
BS azimuth [°]
Normalized gain [dB]

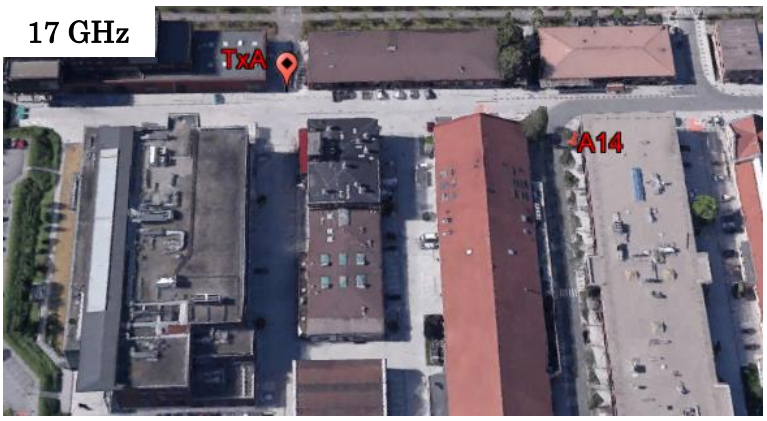
17 GHz
TxA
A14

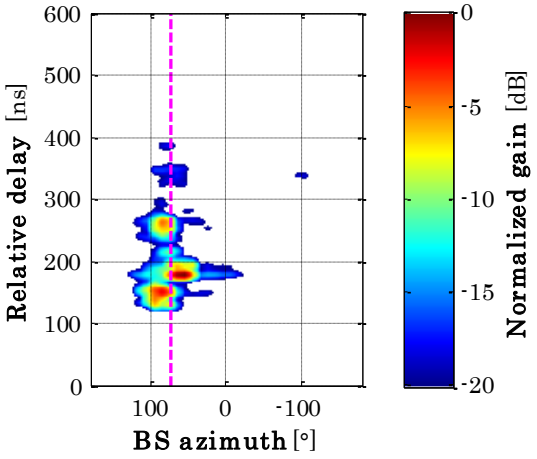
Relative delay [ns]
BS azimuth [°]
Normalized gain [dB]

S2

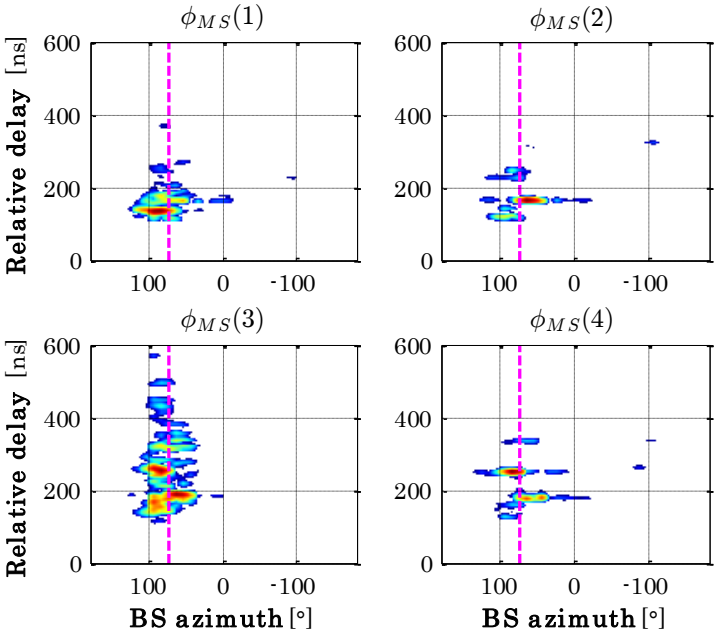
$\phi_{MS}(1)$
$\phi_{MS}(2)$
$\phi_{MS}(3)$
$\phi_{MS}(4)$
Relative delay [ns]
BS azimuth [°]

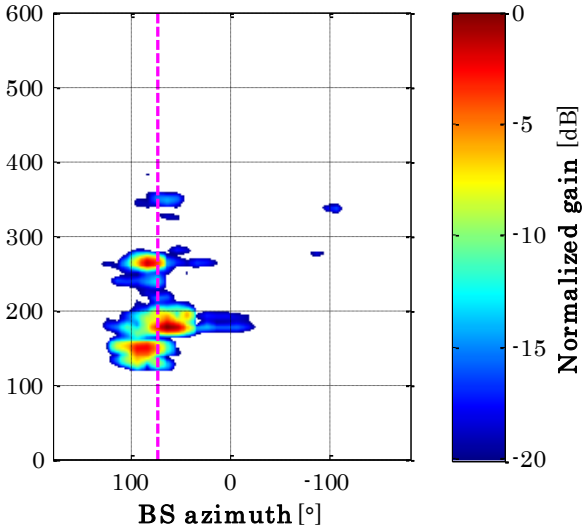
Relative delay [ns]
BS azimuth [°]
Normalized gain [dB]

S1

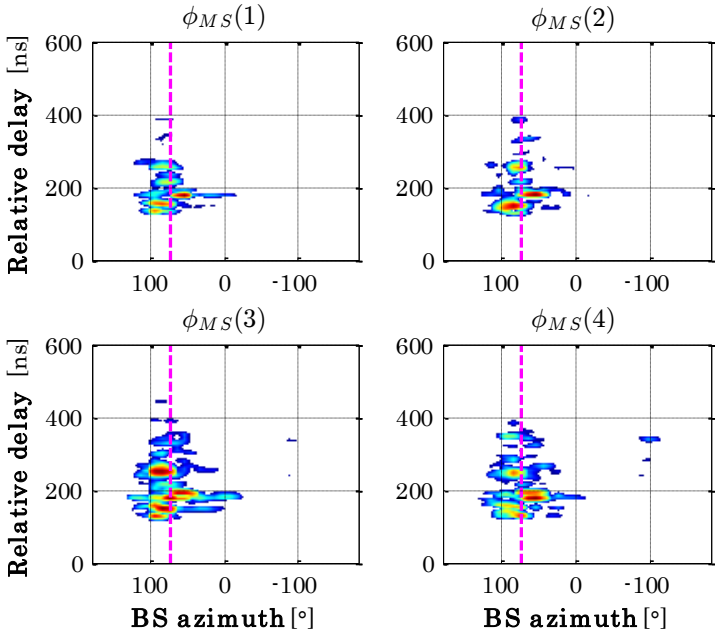
$\phi_{MS}(1)$
$\phi_{MS}(2)$
$\phi_{MS}(3)$
$\phi_{MS}(4)$
Relative delay [ns]
BS azimuth [°]

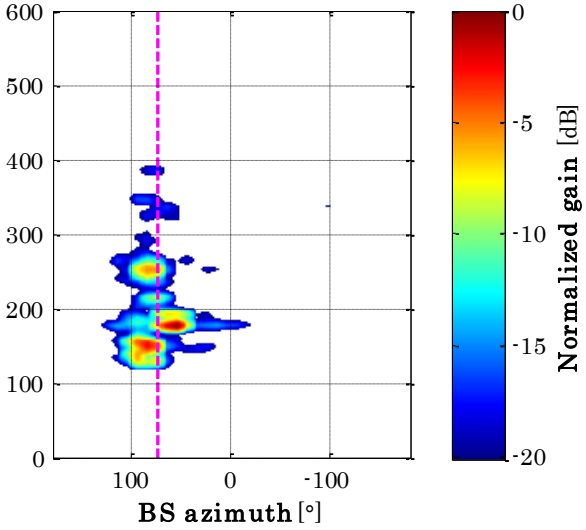
Relative delay [ns]
BS azimuth [°]
Normalized gain [dB]


17 GHz
TxA
A16

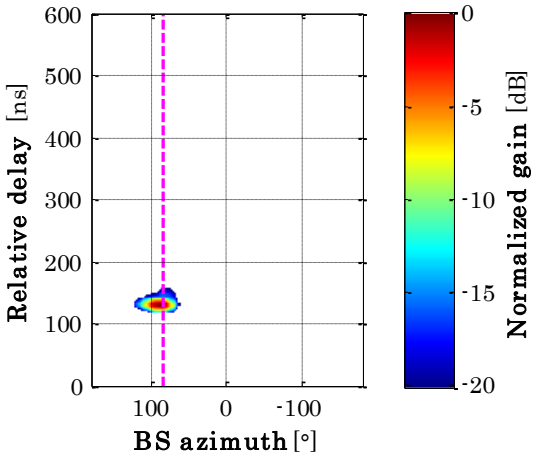
Relative delay [ns]
BS azimuth [°]
Normalized gain [dB]

S2

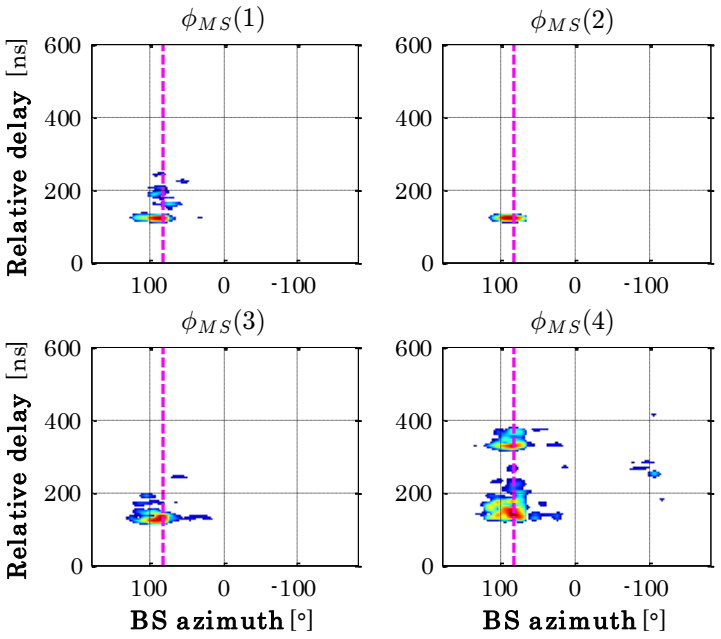
$\phi_{MS}(1)$
$\phi_{MS}(2)$
$\phi_{MS}(3)$
$\phi_{MS}(4)$
Relative delay [ns]
BS azimuth [°]

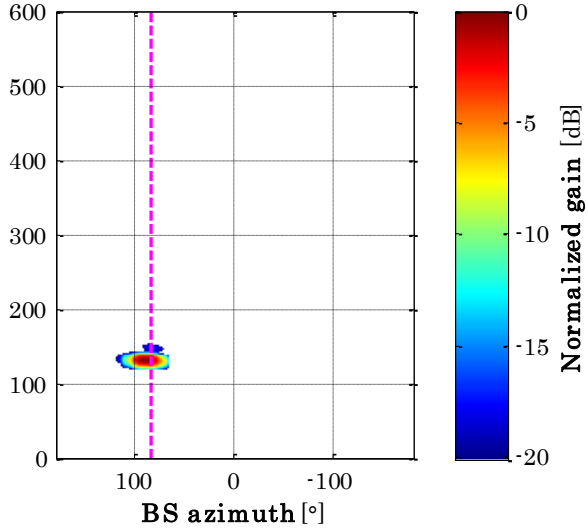
BS azimuth [°]
Normalized gain [dB]

S1

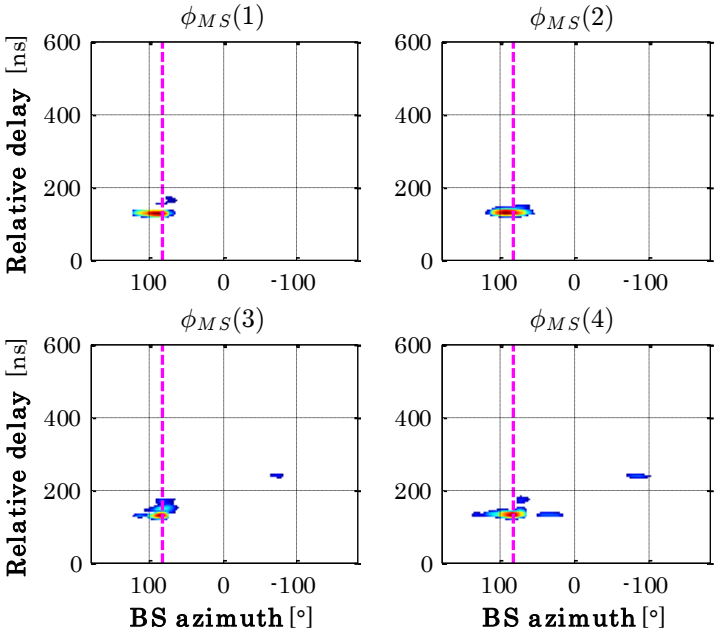
$\phi_{MS}(1)$
$\phi_{MS}(2)$
$\phi_{MS}(3)$
$\phi_{MS}(4)$
Relative delay [ns]
BS azimuth [°]

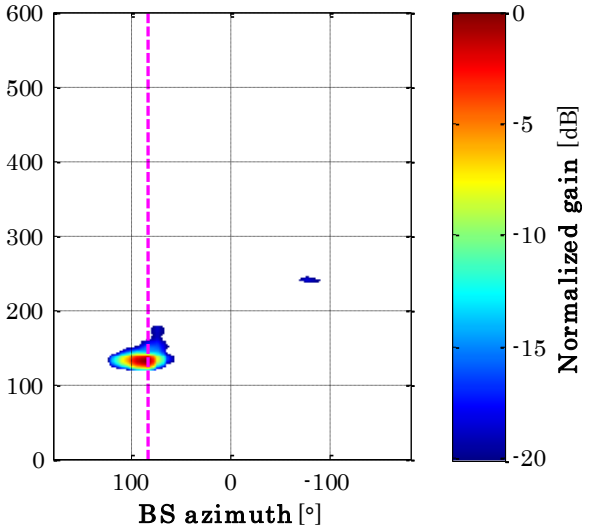
BS azimuth [°]
Normalized gain [dB]

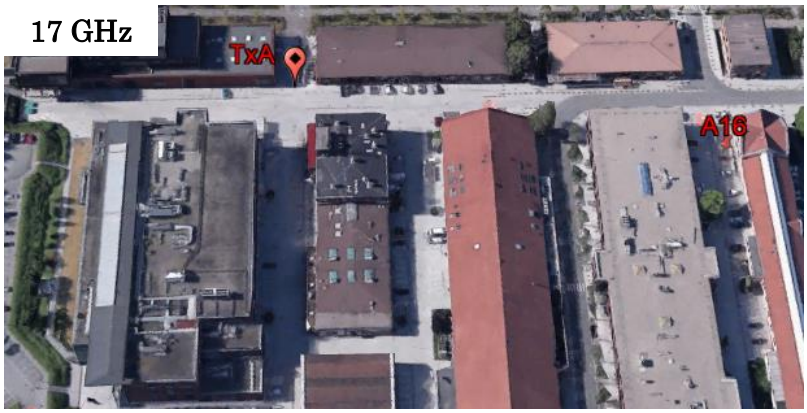
17 GHz
TxA
A16

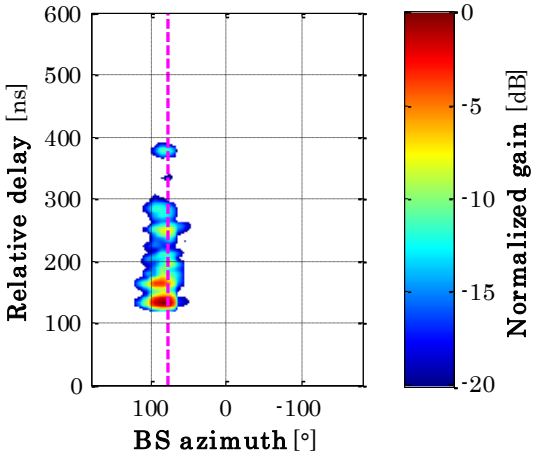
Relative delay [ns]
BS azimuth [°]
Normalized gain [dB]

S2

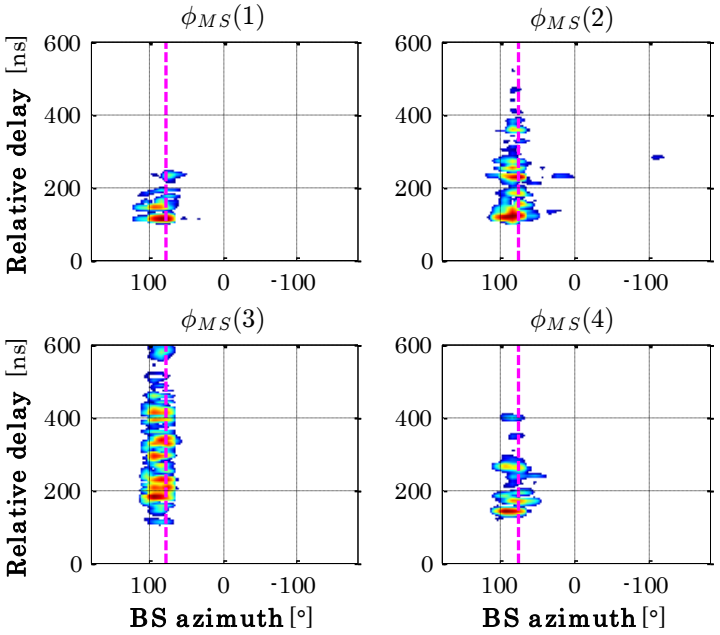
$\phi_{MS}(1)$
$\phi_{MS}(2)$
$\phi_{MS}(3)$
$\phi_{MS}(4)$
Relative delay [ns]
BS azimuth [°]

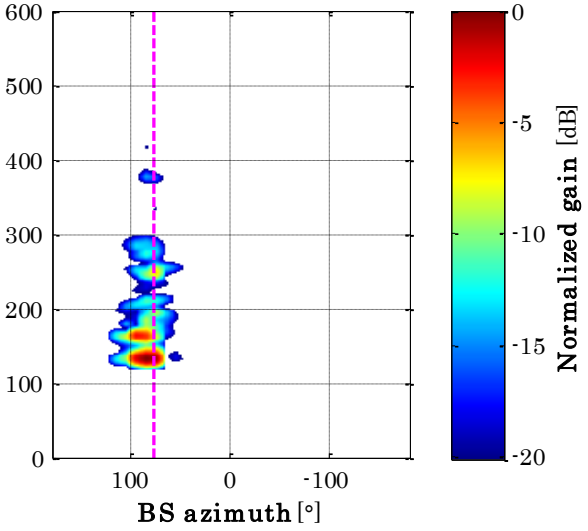
Relative delay [ns]
BS azimuth [°]
Normalized gain [dB]

S1

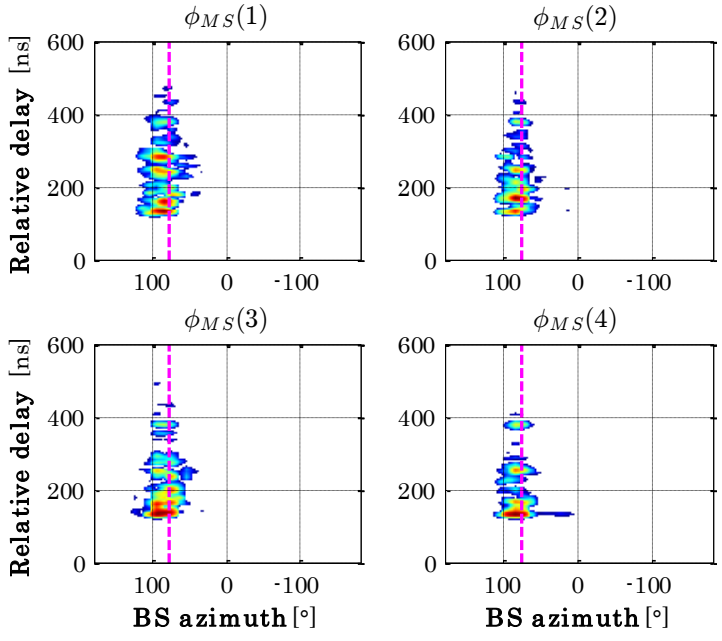
$\phi_{MS}(1)$
$\phi_{MS}(2)$
$\phi_{MS}(3)$
$\phi_{MS}(4)$
Relative delay [ns]
BS azimuth [°]

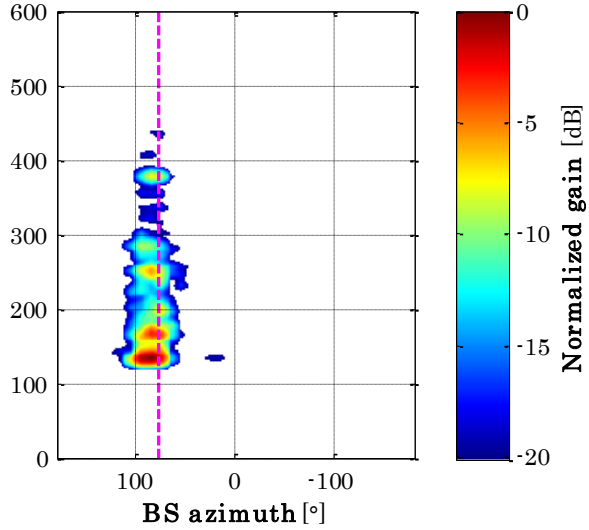
Relative delay [ns]
BS azimuth [°]
Normalized gain [dB]


17 GHz
TxB
B1

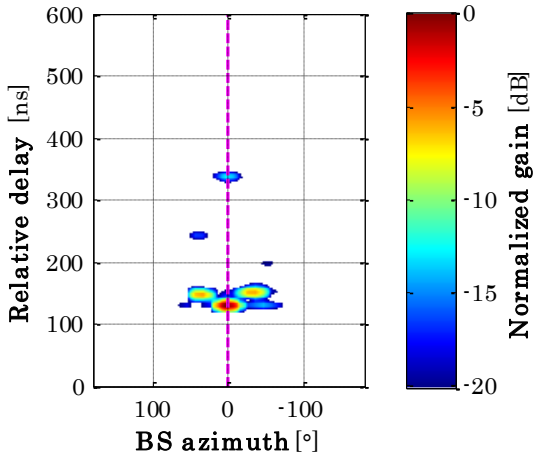
Relative delay [ns]
BS azimuth [°]
Normalized gain [dB]

S2

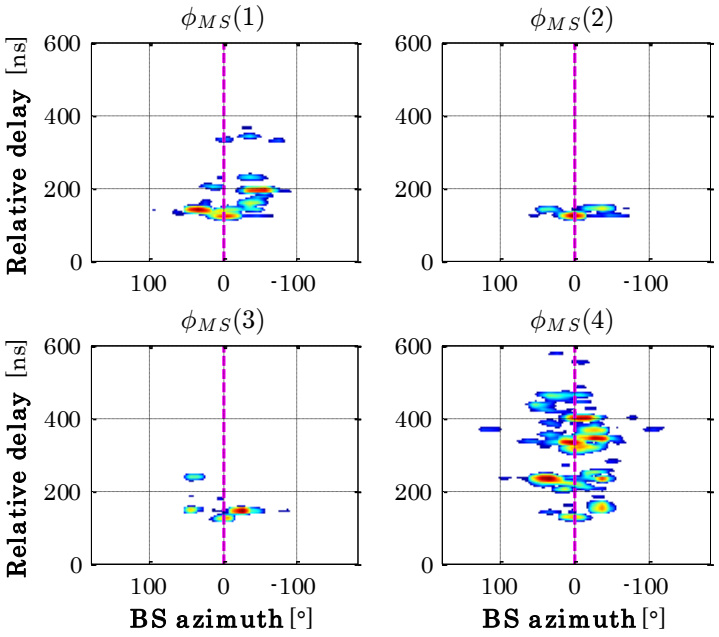
$\phi_{MS}(1)$
$\phi_{MS}(2)$
$\phi_{MS}(3)$
$\phi_{MS}(4)$
Relative delay [ns]
BS azimuth [°]

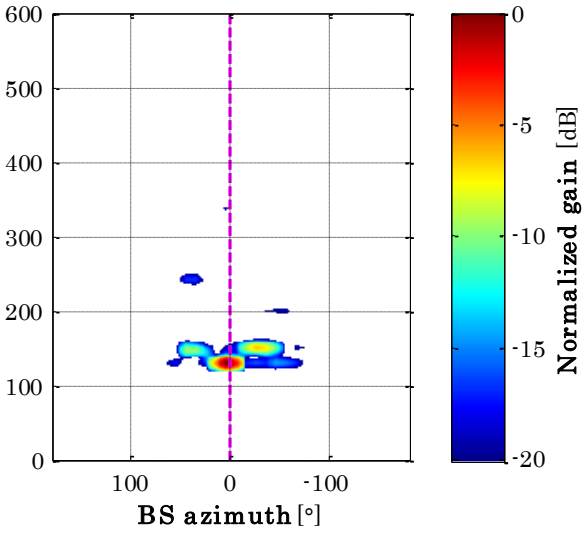
Relative delay [ns]
BS azimuth [°]
Normalized gain [dB]

S1

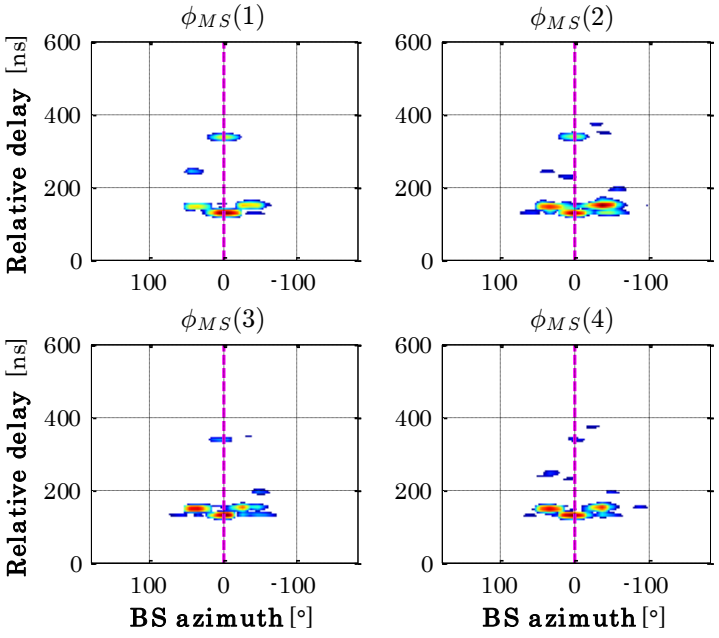
$\phi_{MS}(1)$
$\phi_{MS}(2)$
$\phi_{MS}(3)$
$\phi_{MS}(4)$
Relative delay [ns]
BS azimuth [°]

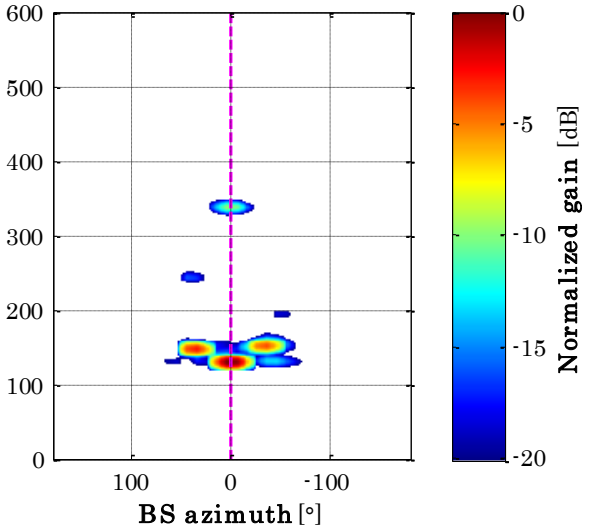
Relative delay [ns]
BS azimuth [°]
Normalized gain [dB]


17 GHz
TxB
B2

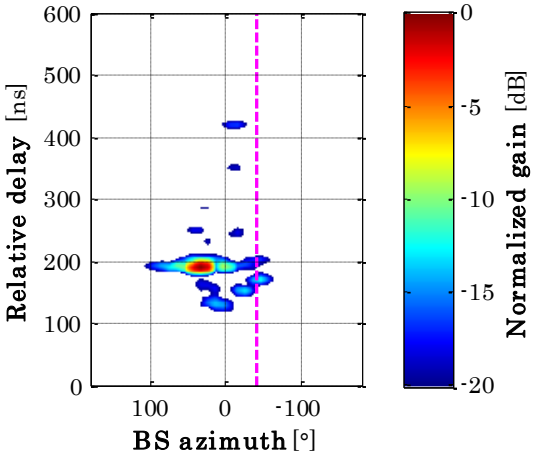
Relative delay [ns]
BS azimuth [°]
Normalized gain [dB]

S2

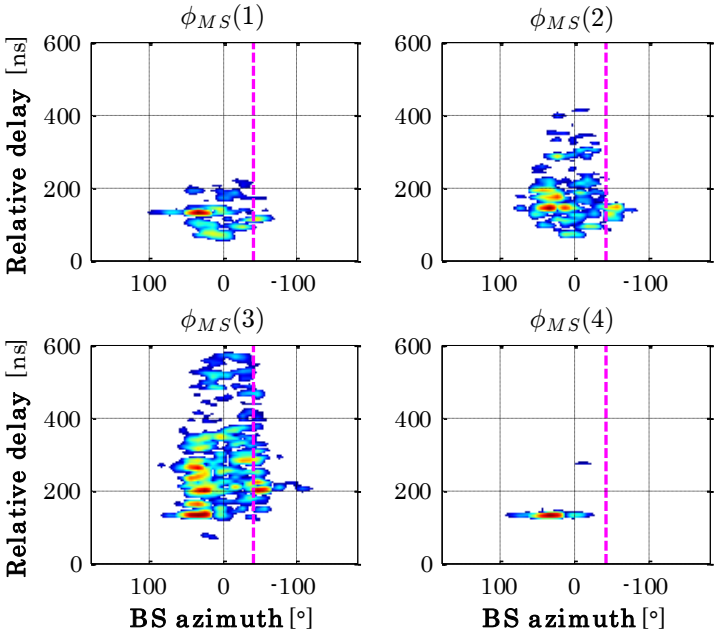
$\phi_{MS}(1)$
$\phi_{MS}(2)$
$\phi_{MS}(3)$
$\phi_{MS}(4)$
Relative delay [ns]
BS azimuth [°]

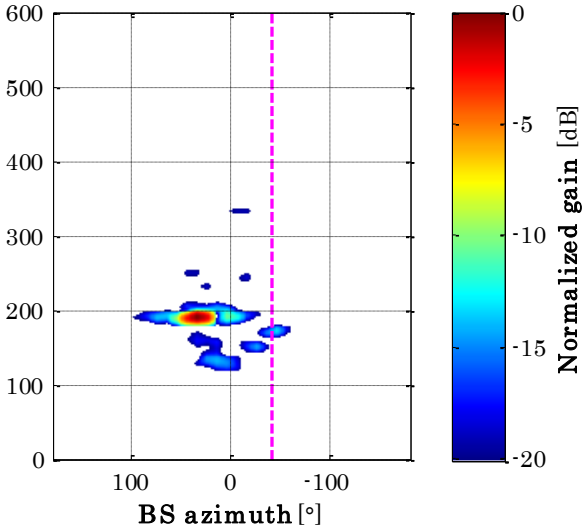
Relative delay [ns]
BS azimuth [°]
Normalized gain [dB]

S1

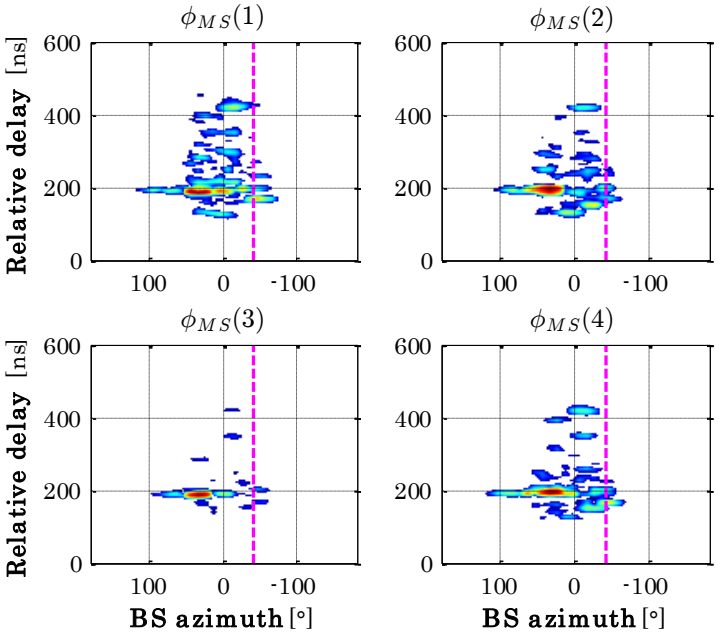
$\phi_{MS}(1)$
$\phi_{MS}(2)$
$\phi_{MS}(3)$
$\phi_{MS}(4)$
Relative delay [ns]
BS azimuth [°]

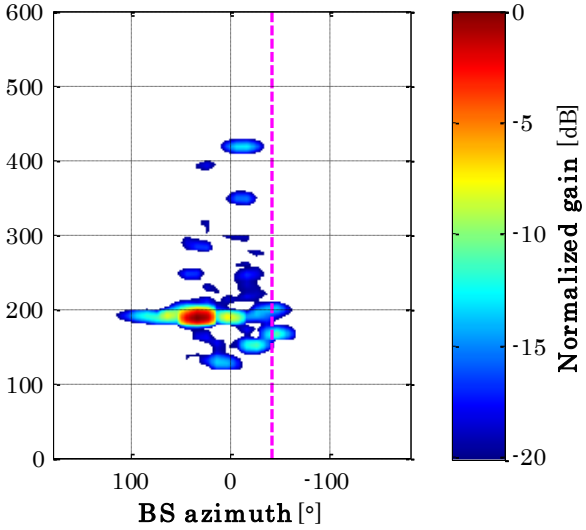
Relative delay [ns]
BS azimuth [°]
Normalized gain [dB]

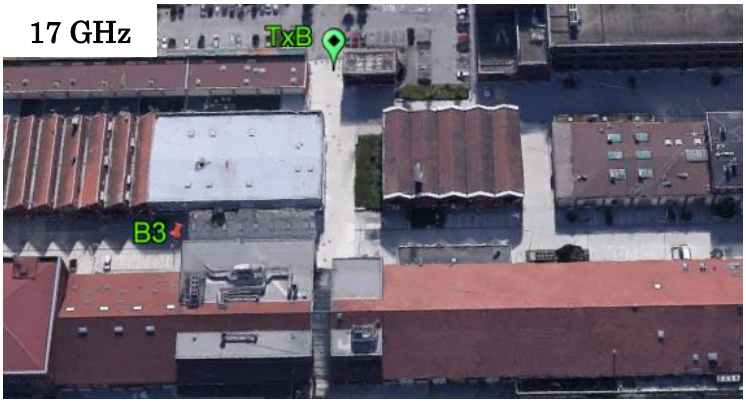
17 GHz
TxB
B3

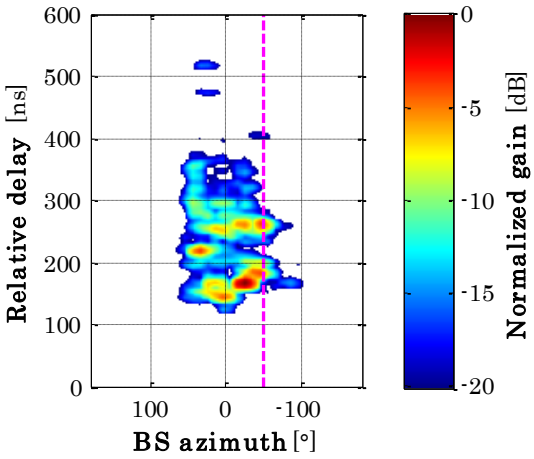
Relative delay [ns]
BS azimuth [°]
Normalized gain [dB]

S2

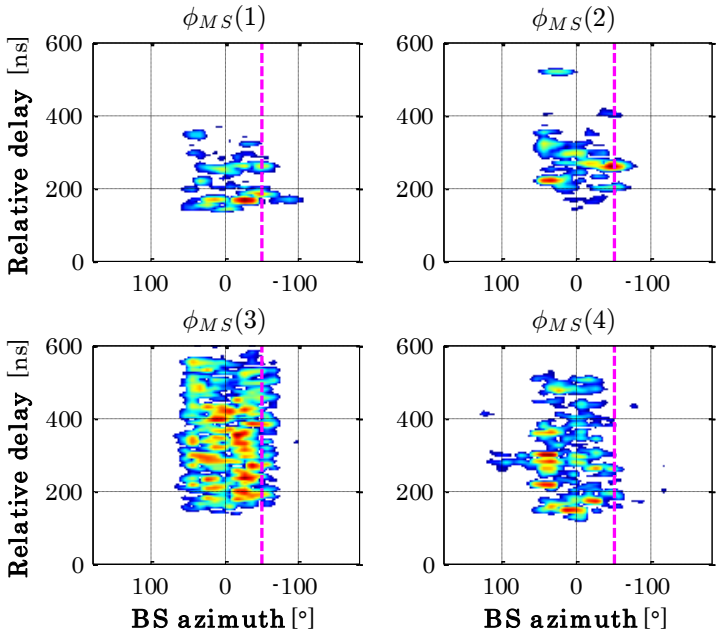
$\phi_{MS}(1)$
$\phi_{MS}(2)$
$\phi_{MS}(3)$
$\phi_{MS}(4)$
Relative delay [ns]
BS azimuth [°]

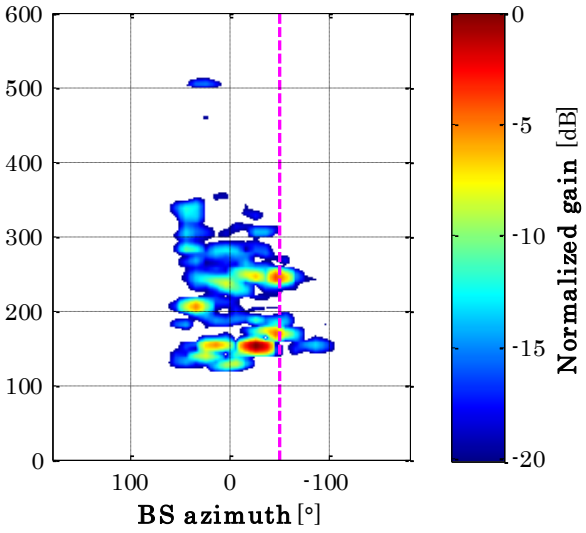
BS azimuth [°]
Normalized gain [dB]

S1

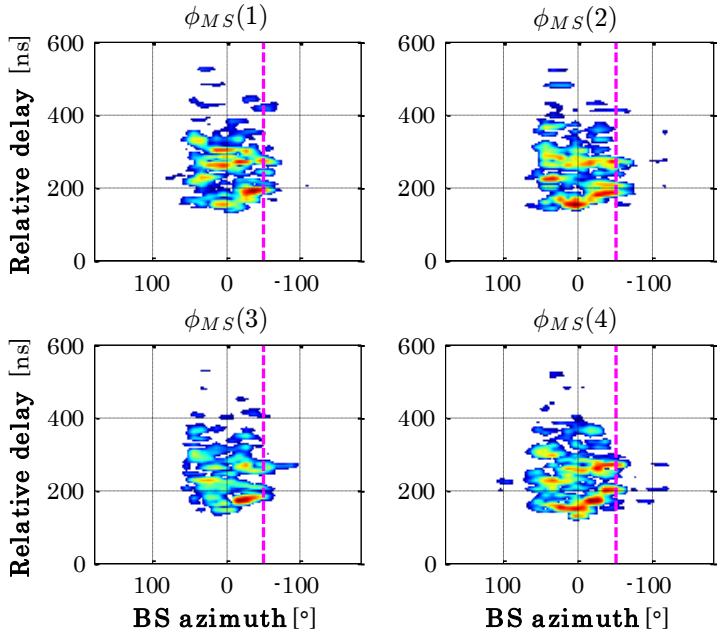
$\phi_{MS}(1)$
$\phi_{MS}(2)$
$\phi_{MS}(3)$
$\phi_{MS}(4)$
Relative delay [ns]
BS azimuth [°]

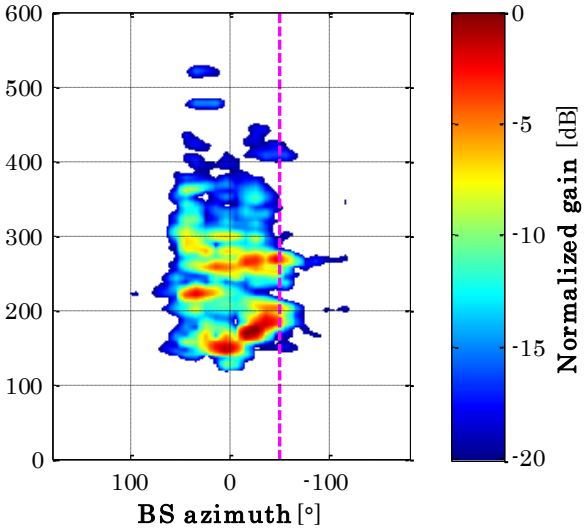
BS azimuth [°]
Normalized gain [dB]


17 GHz
TxB
B4

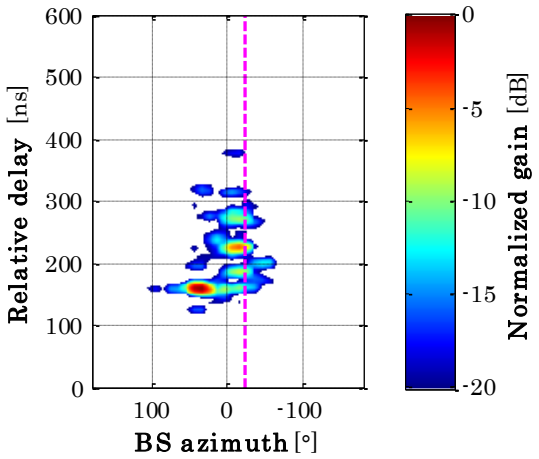
Relative delay [ns]
BS azimuth [°]
Normalized gain [dB]

S2

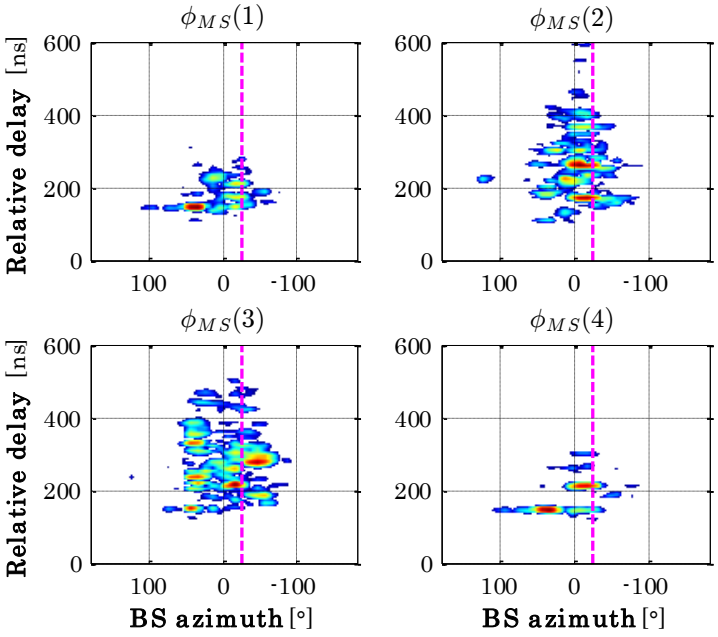
$\phi_{MS}(1)$
$\phi_{MS}(2)$
$\phi_{MS}(3)$
$\phi_{MS}(4)$
Relative delay [ns]
BS azimuth [°]

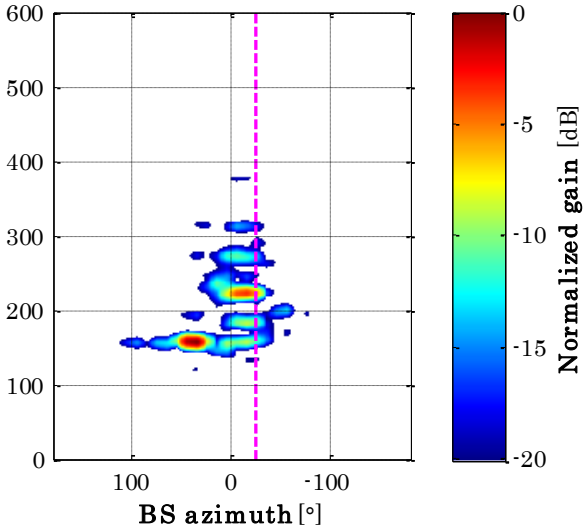
Relative delay [ns]
BS azimuth [°]
Normalized gain [dB]

S1

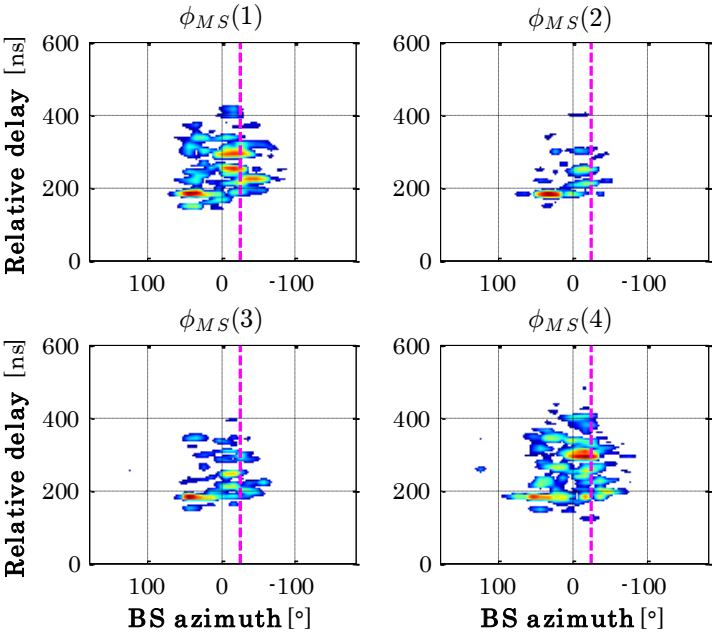
$\phi_{MS}(1)$
$\phi_{MS}(2)$
$\phi_{MS}(3)$
$\phi_{MS}(4)$
Relative delay [ns]
BS azimuth [°]

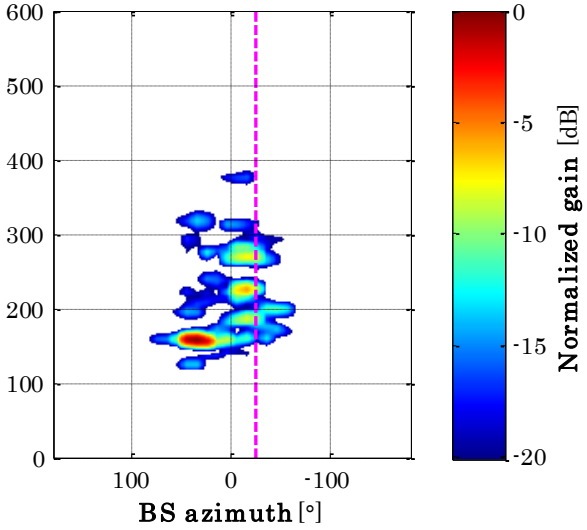
Relative delay [ns]
BS azimuth [°]
Normalized gain [dB]


17 GHz
TxB
B5

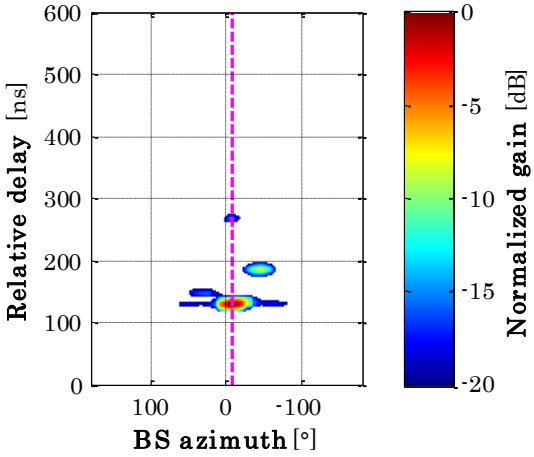
Relative delay [ns]
BS azimuth [°]
Normalized gain [dB]

S2

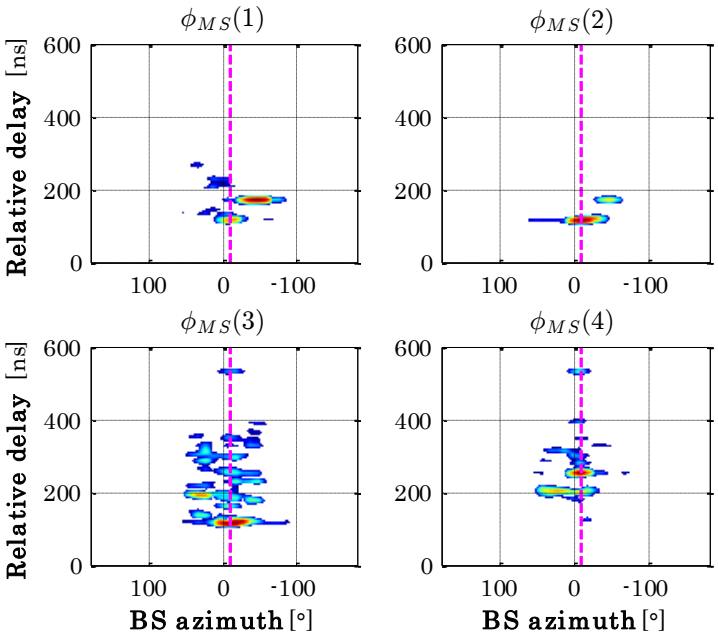
$\phi_{MS}(1)$
$\phi_{MS}(2)$
$\phi_{MS}(3)$
$\phi_{MS}(4)$
Relative delay [ns]
BS azimuth [°]

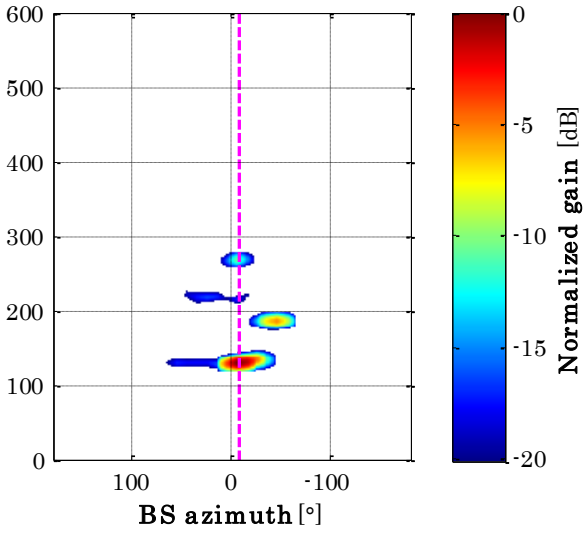
Relative delay [ns]
BS azimuth [°]
Normalized gain [dB]

S1

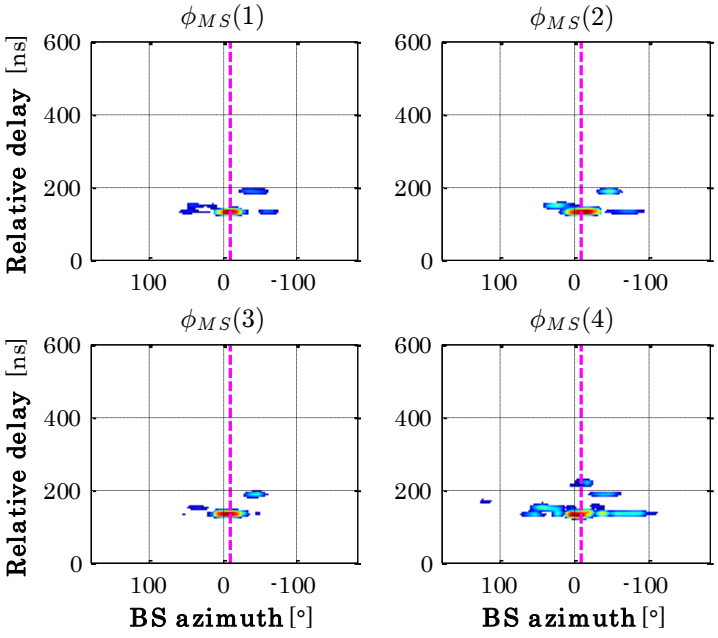
$\phi_{MS}(1)$
$\phi_{MS}(2)$
$\phi_{MS}(3)$
$\phi_{MS}(4)$
Relative delay [ns]
BS azimuth [°]

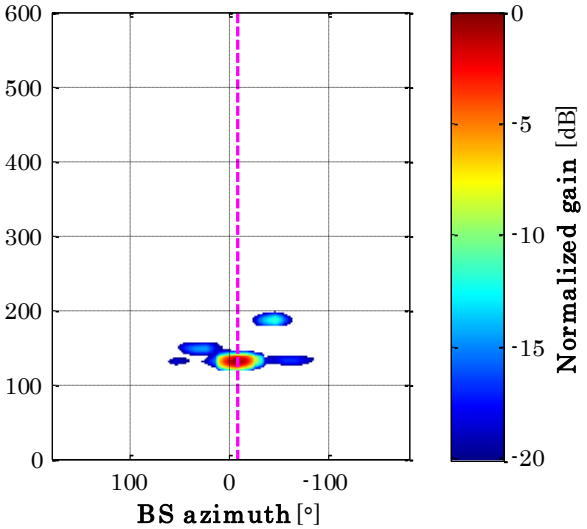
Relative delay [ns]
BS azimuth [°]
Normalized gain [dB]


17 GHz
TxB
B6

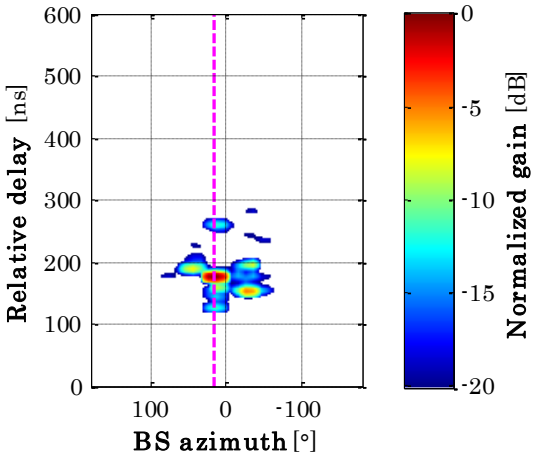
Relative delay [ns]
BS azimuth [°]
Normalized gain [dB]

S2

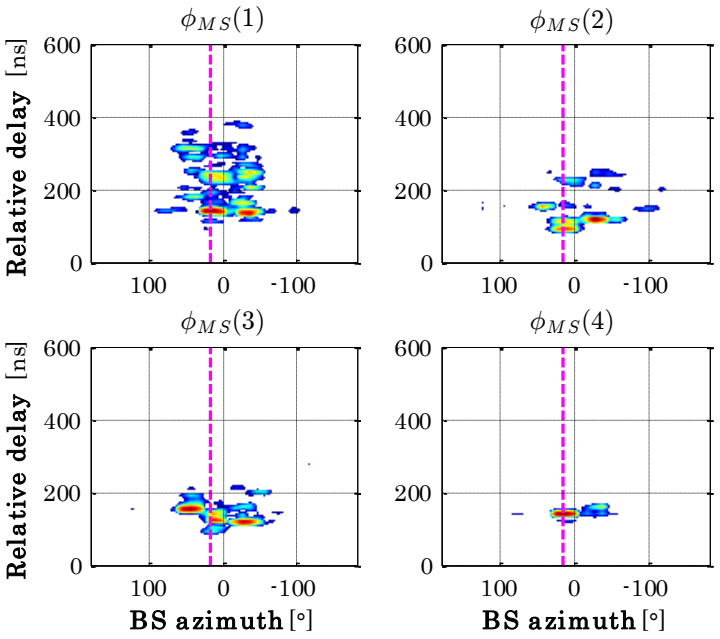
$\phi_{MS}(1)$
$\phi_{MS}(2)$
$\phi_{MS}(3)$
$\phi_{MS}(4)$
Relative delay [ns]
BS azimuth [°]

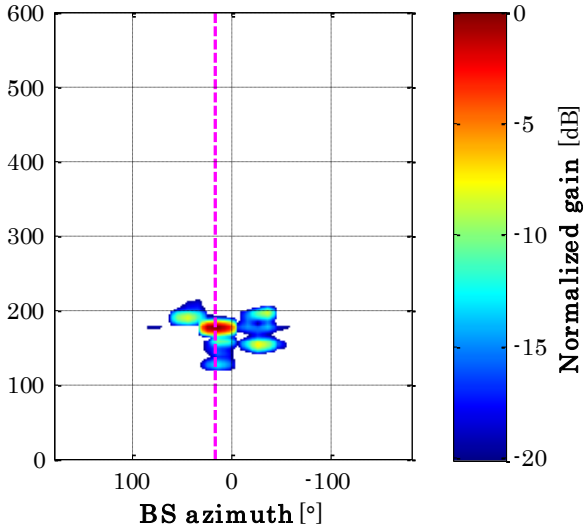
Relative delay [ns]
BS azimuth [°]
Normalized gain [dB]

S1

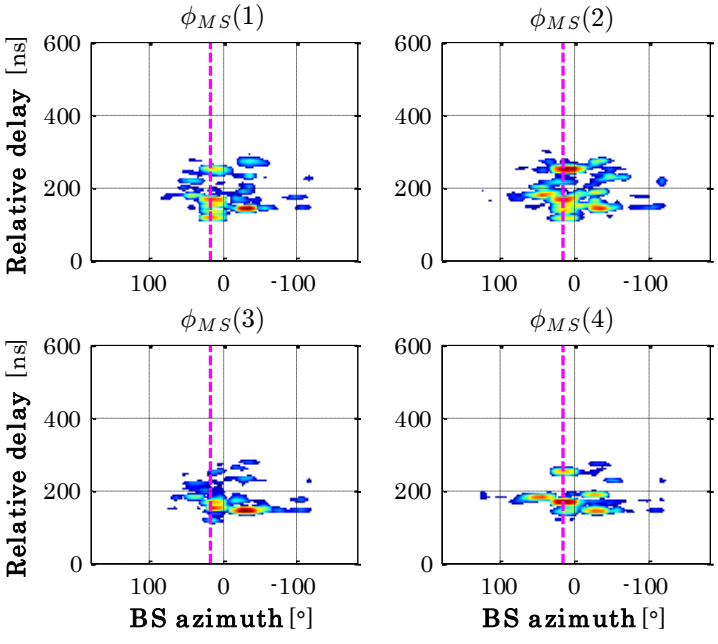
$\phi_{MS}(1)$
$\phi_{MS}(2)$
$\phi_{MS}(3)$
$\phi_{MS}(4)$
Relative delay [ns]
BS azimuth [°]

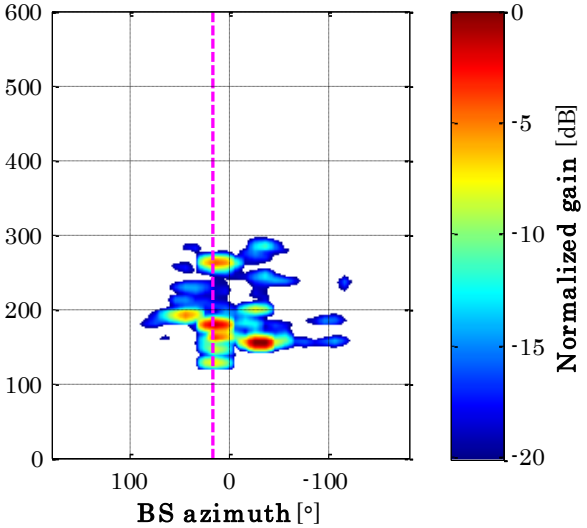
Relative delay [ns]
BS azimuth [°]
Normalized gain [dB]


17 GHz
TxB
B7

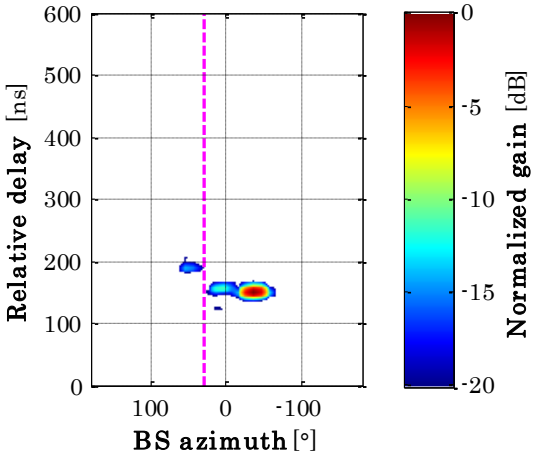
Relative delay [ns]
BS azimuth [°]
Normalized gain [dB]

S2

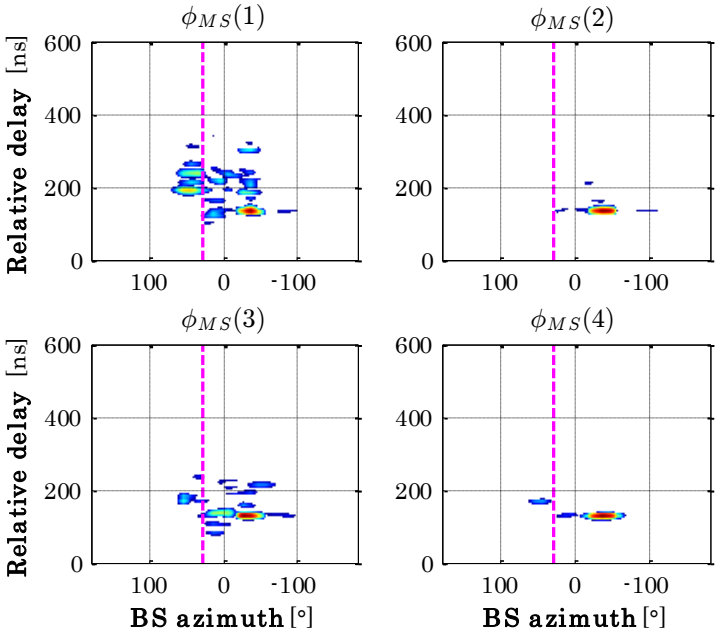
$\phi_{MS}(1)$
$\phi_{MS}(2)$
$\phi_{MS}(3)$
$\phi_{MS}(4)$
Relative delay [ns]
BS azimuth [°]

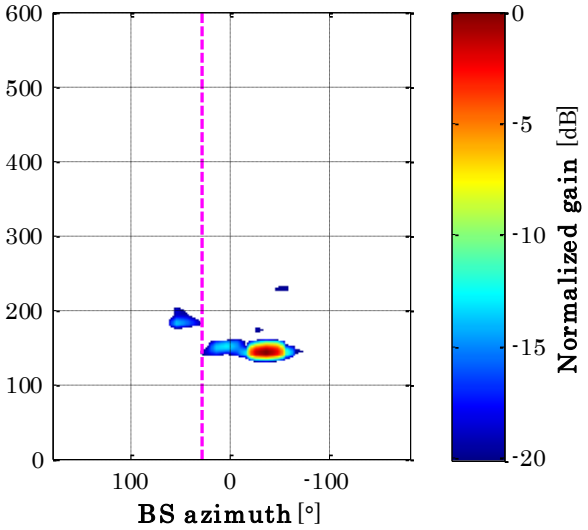
BS azimuth [°]
Normalized gain [dB]

S1

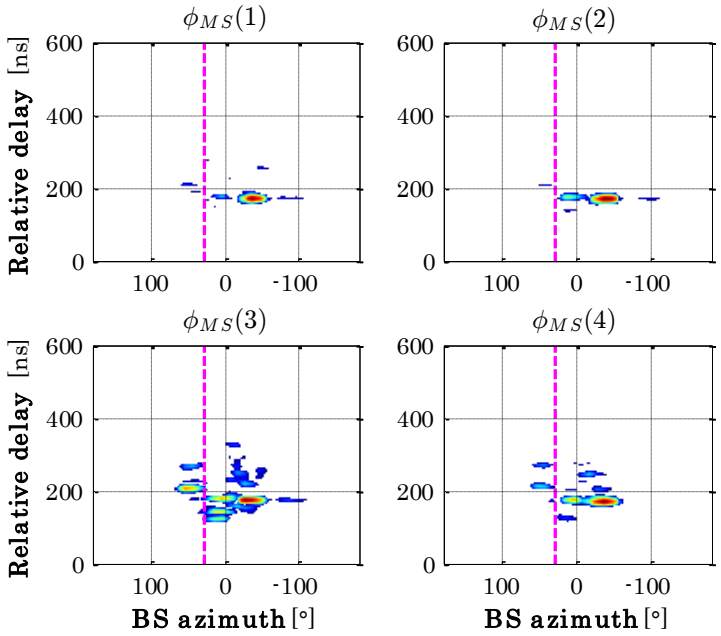
$\phi_{MS}(1)$
$\phi_{MS}(2)$
$\phi_{MS}(3)$
$\phi_{MS}(4)$
Relative delay [ns]
BS azimuth [°]

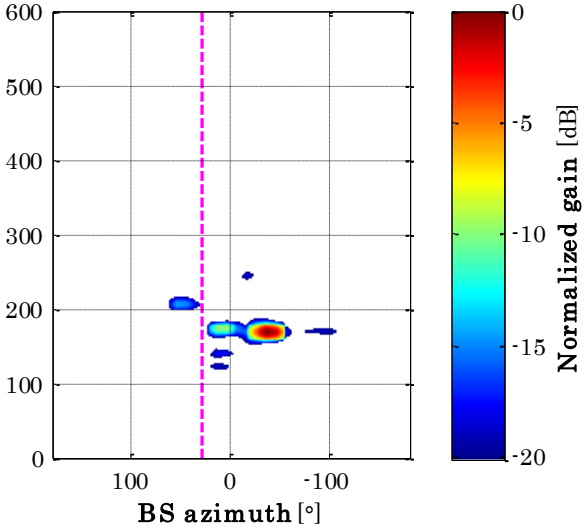
BS azimuth [°]
Normalized gain [dB]


17 GHz
TxB
B8

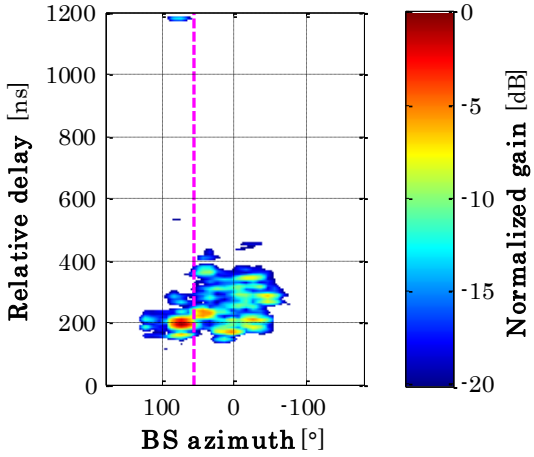
Relative delay [ns]
BS azimuth [°]
Normalized gain [dB]

S2

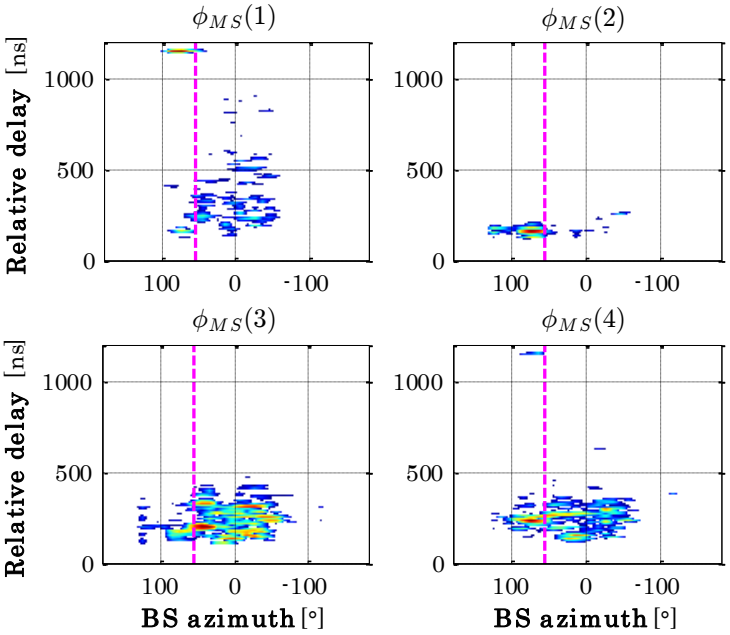
$\phi_{MS}(1)$
$\phi_{MS}(2)$
$\phi_{MS}(3)$
$\phi_{MS}(4)$
Relative delay [ns]
BS azimuth [°]

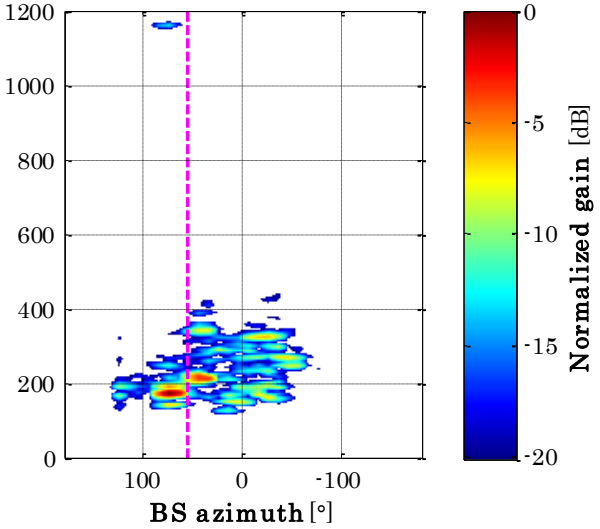
Relative delay [ns]
BS azimuth [°]
Normalized gain [dB]

S1

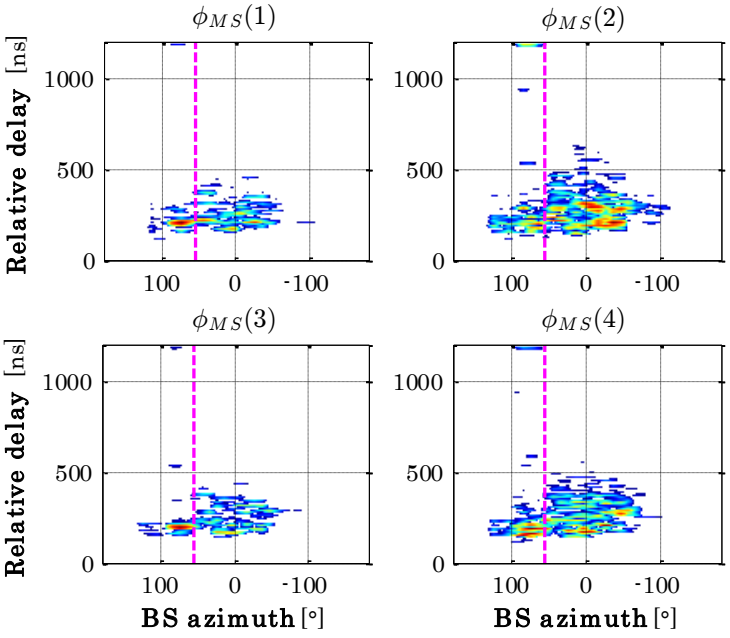
$\phi_{MS}(1)$
$\phi_{MS}(2)$
$\phi_{MS}(3)$
$\phi_{MS}(4)$
Relative delay [ns]
BS azimuth [°]

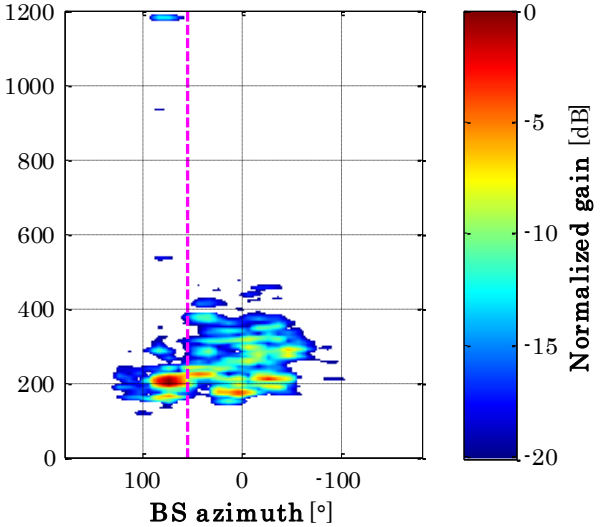
Relative delay [ns]
BS azimuth [°]
Normalized gain [dB]


17 GHz
TxB
B9

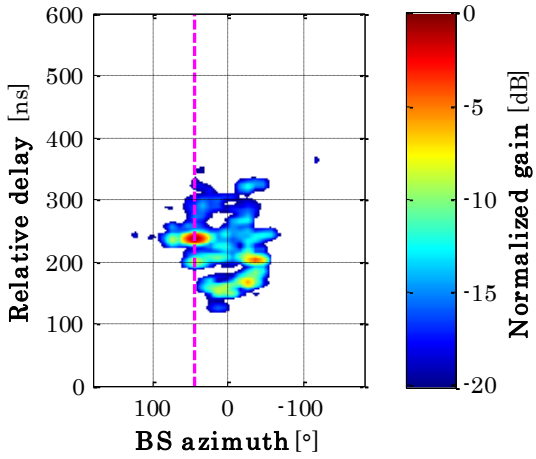
Relative delay [ns]
BS azimuth [°]
Normalized gain [dB]

S2

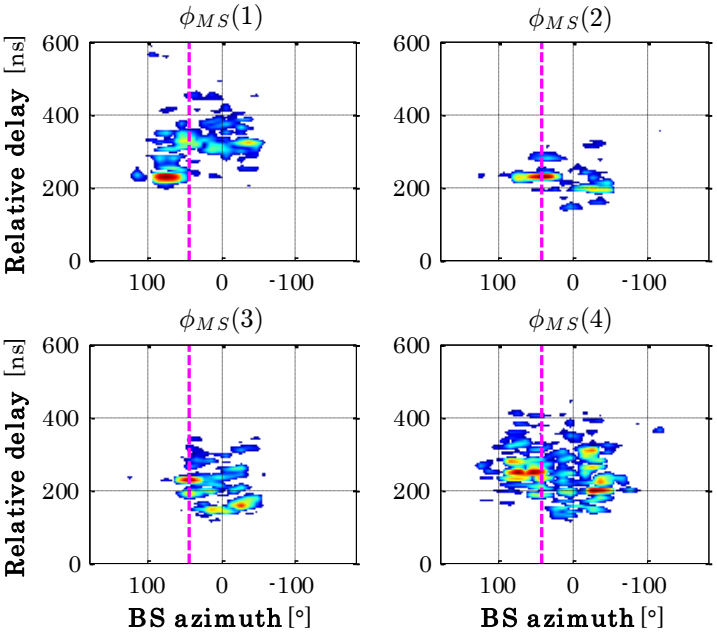
$\phi_{MS}(1)$
$\phi_{MS}(2)$
$\phi_{MS}(3)$
$\phi_{MS}(4)$
Relative delay [ns]
BS azimuth [°]

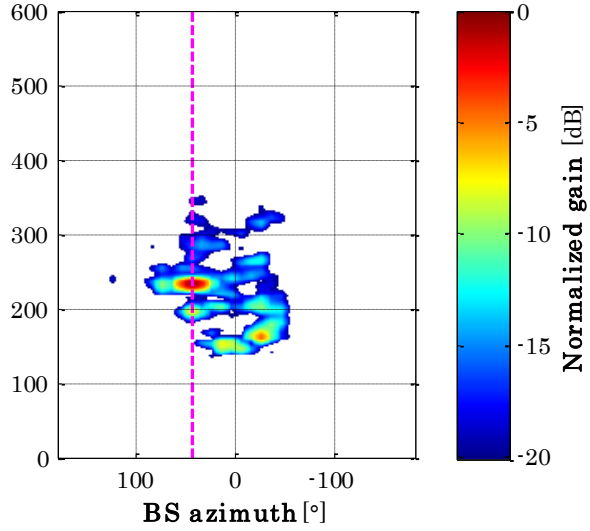
BS azimuth [°]
Normalized gain [dB]

S1

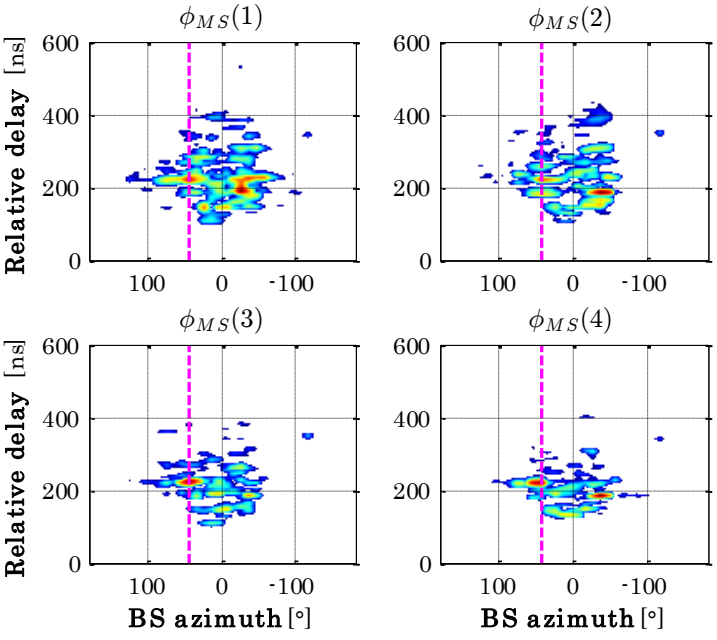
$\phi_{MS}(1)$
$\phi_{MS}(2)$
$\phi_{MS}(3)$
$\phi_{MS}(4)$
Relative delay [ns]
BS azimuth [°]

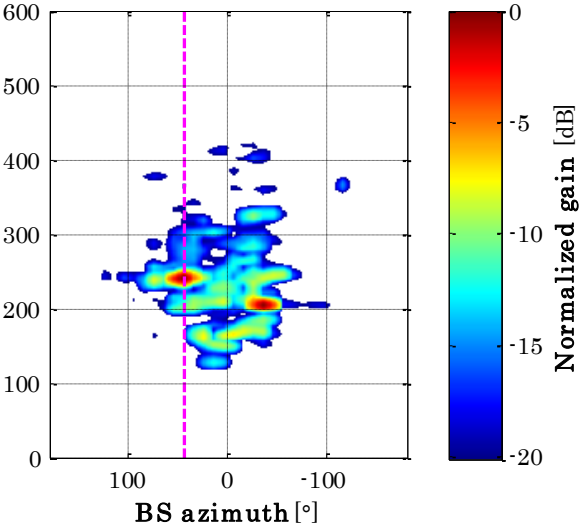
BS azimuth [°]
Normalized gain [dB]


17 GHz
TxB
B10

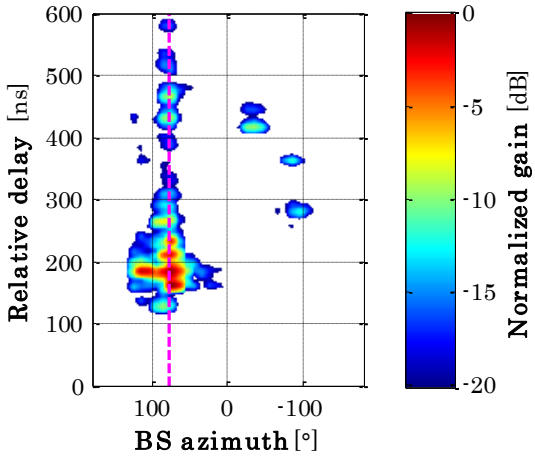
Relative delay [ns]
BS azimuth [°]
Normalized gain [dB]

S2

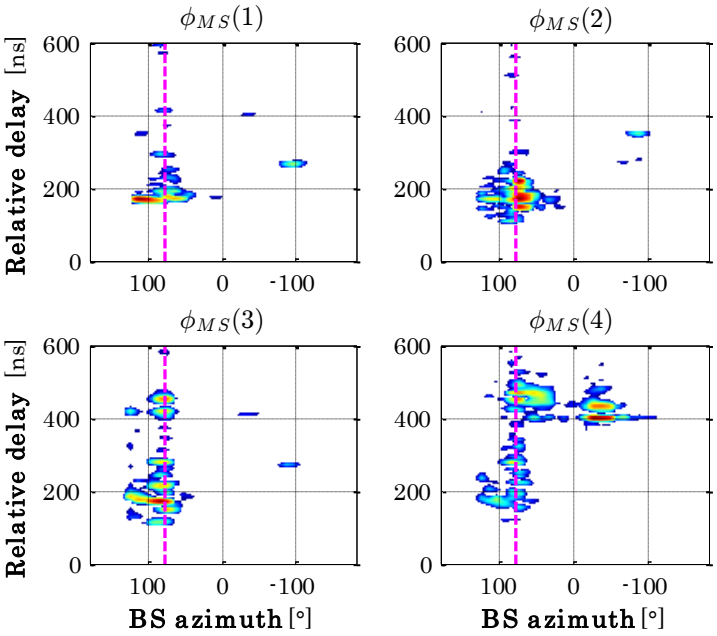
$\phi_{MS}(1)$
$\phi_{MS}(2)$
$\phi_{MS}(3)$
$\phi_{MS}(4)$
Relative delay [ns]
BS azimuth [°]

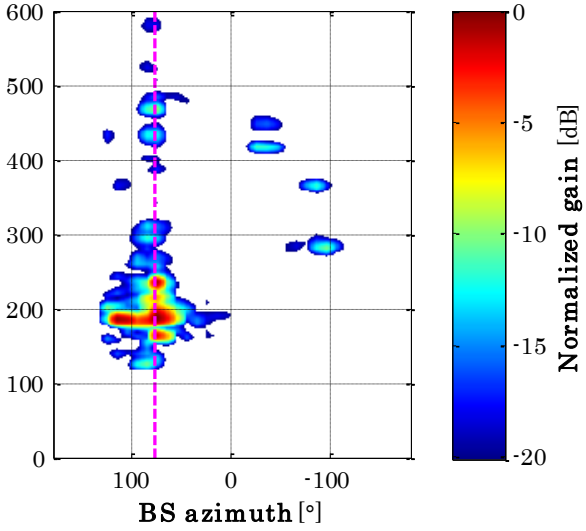
Relative delay [ns]
BS azimuth [°]
Normalized gain [dB]

S1

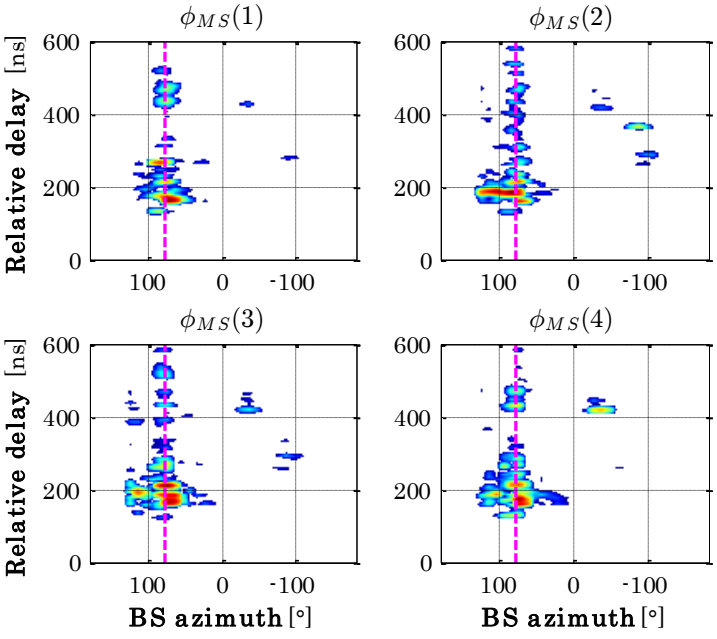
$\phi_{MS}(1)$
$\phi_{MS}(2)$
$\phi_{MS}(3)$
$\phi_{MS}(4)$
Relative delay [ns]
BS azimuth [°]

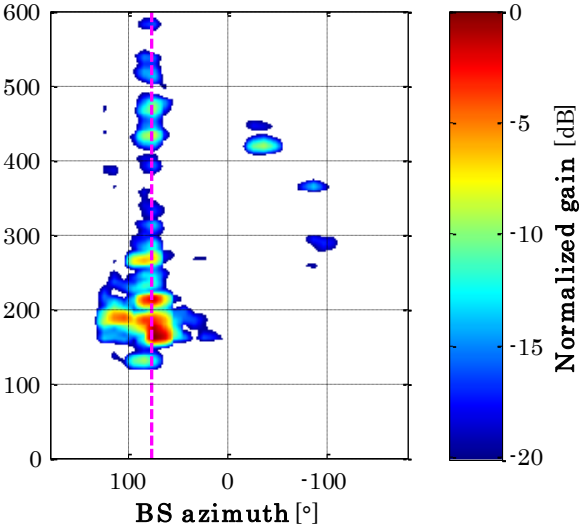
Relative delay [ns]
BS azimuth [°]
Normalized gain [dB]


17 GHz
TxB
B11

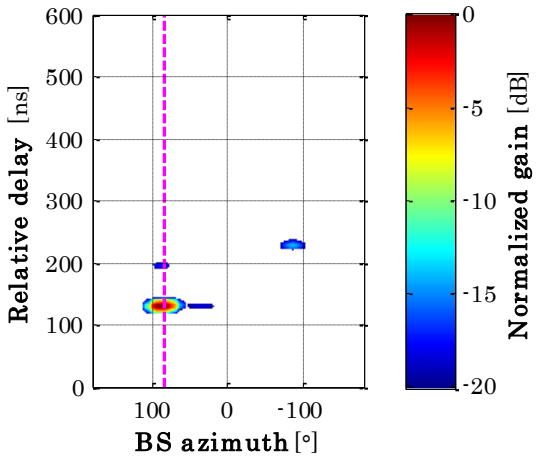
Relative delay [ns]
BS azimuth [°]
Normalized gain [dB]

S2

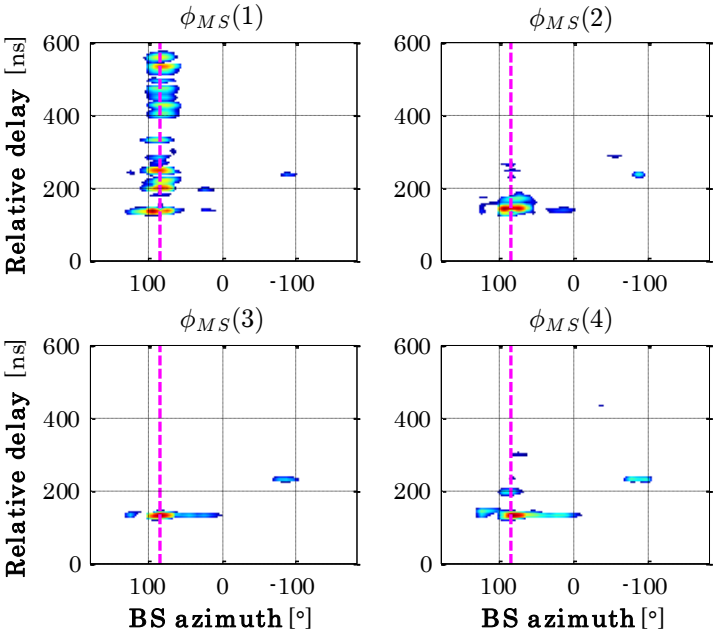
$\phi_{MS}(1)$
$\phi_{MS}(2)$
$\phi_{MS}(3)$
$\phi_{MS}(4)$
Relative delay [ns]
BS azimuth [°]

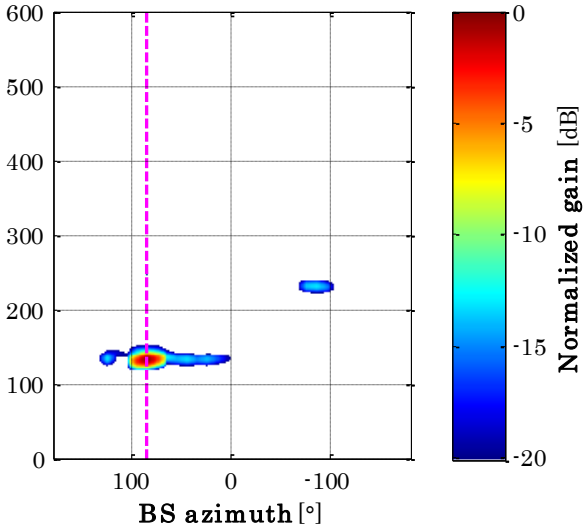
Relative delay [ns]
BS azimuth [°]
Normalized gain [dB]

S1

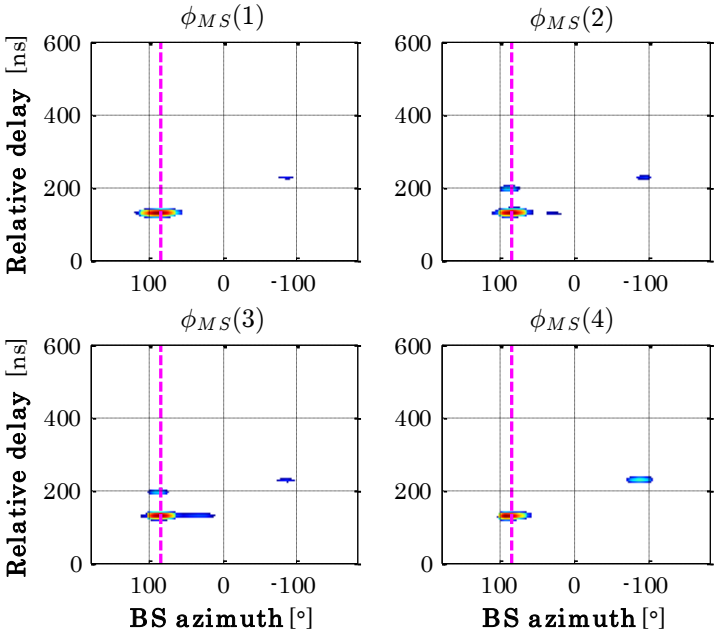
$\phi_{MS}(1)$
$\phi_{MS}(2)$
$\phi_{MS}(3)$
$\phi_{MS}(4)$
Relative delay [ns]
BS azimuth [°]

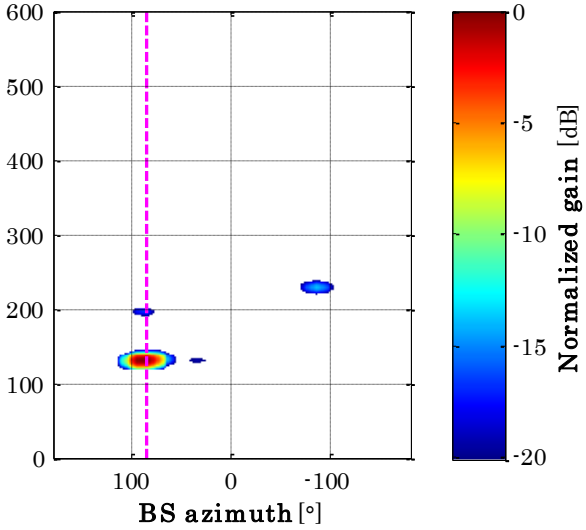
Relative delay [ns]
BS azimuth [°]
Normalized gain [dB]


17 GHz
TxC
C1

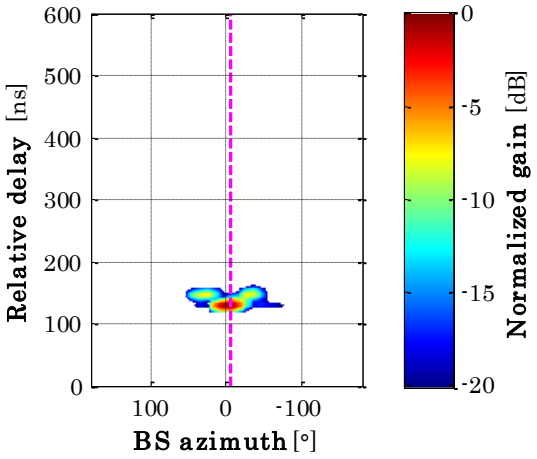
Relative delay [ns]
BS azimuth [°]
Normalized gain [dB]

S2

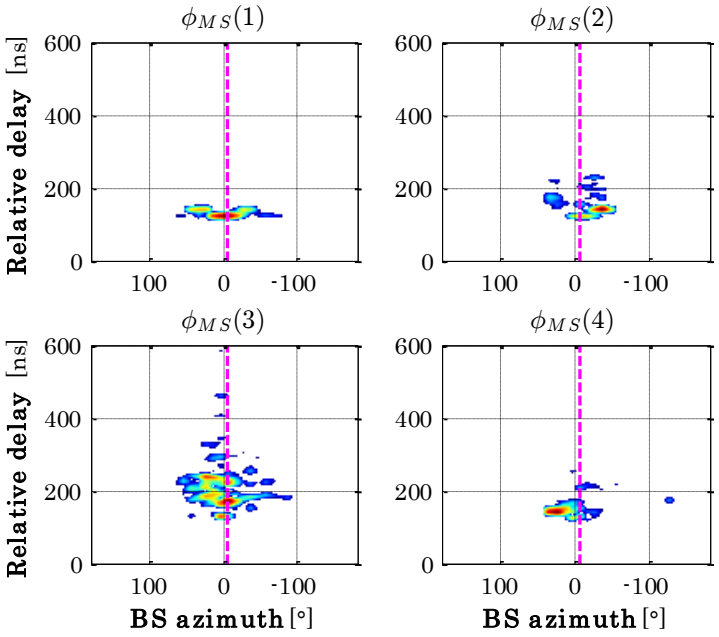
$\phi_{MS}(1)$
$\phi_{MS}(2)$
$\phi_{MS}(3)$
$\phi_{MS}(4)$
Relative delay [ns]
BS azimuth [°]

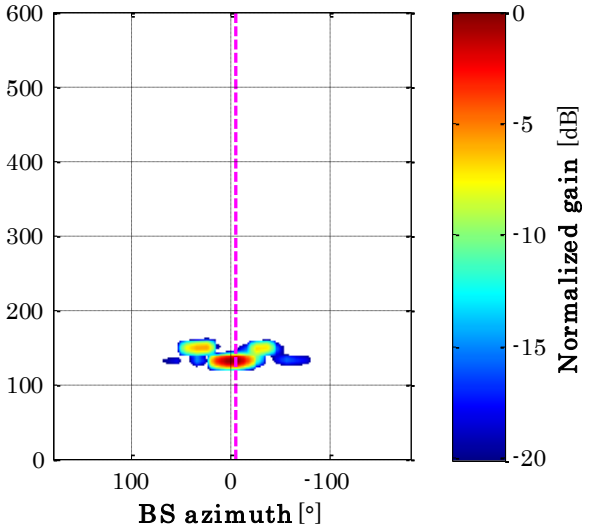
BS azimuth [°]
Normalized gain [dB]

S1

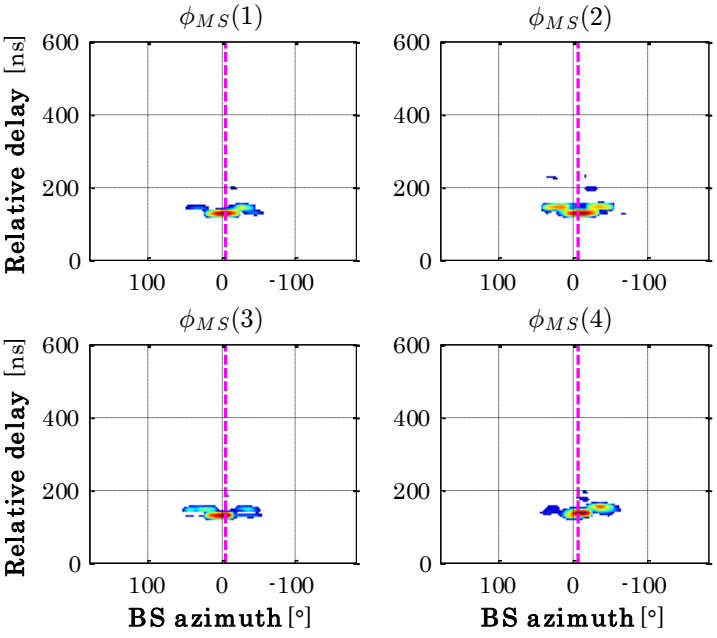
$\phi_{MS}(1)$
$\phi_{MS}(2)$
$\phi_{MS}(3)$
$\phi_{MS}(4)$
Relative delay [ns]
BS azimuth [°]

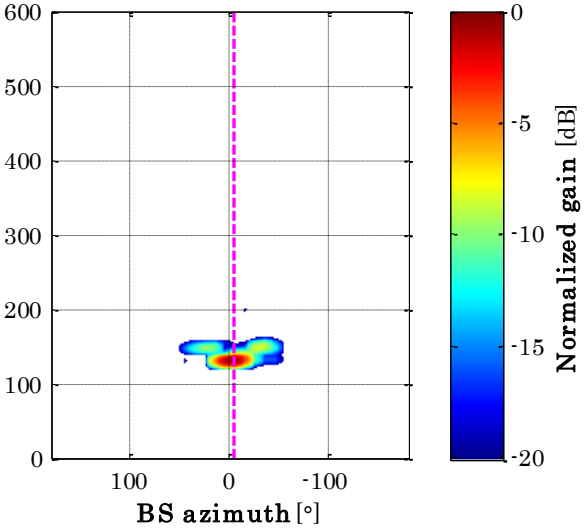
BS azimuth [°]
Normalized gain [dB]


17 GHz
TxC
C2

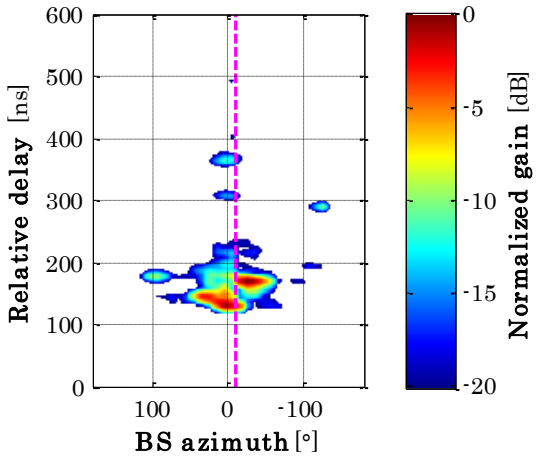
Relative delay [ns]
BS azimuth [°]
Normalized gain [dB]

S2

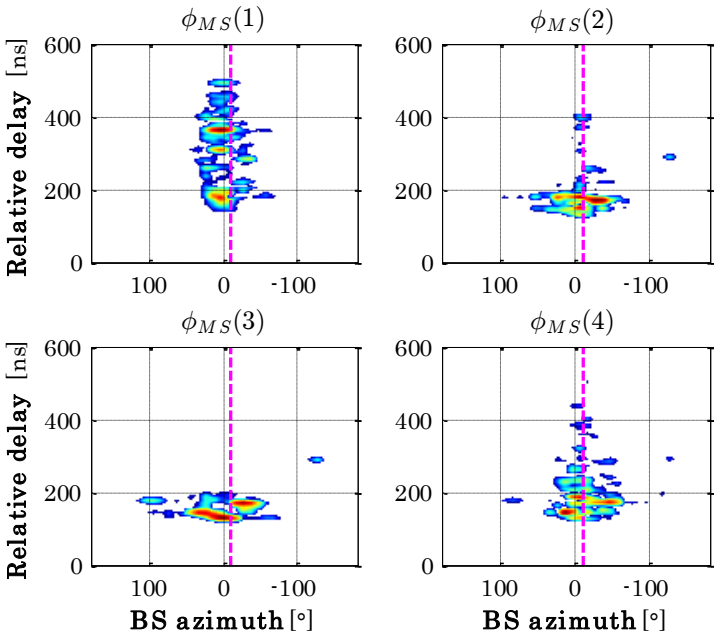
$\phi_{MS}(1)$
$\phi_{MS}(2)$
$\phi_{MS}(3)$
$\phi_{MS}(4)$
Relative delay [ns]
BS azimuth [°]

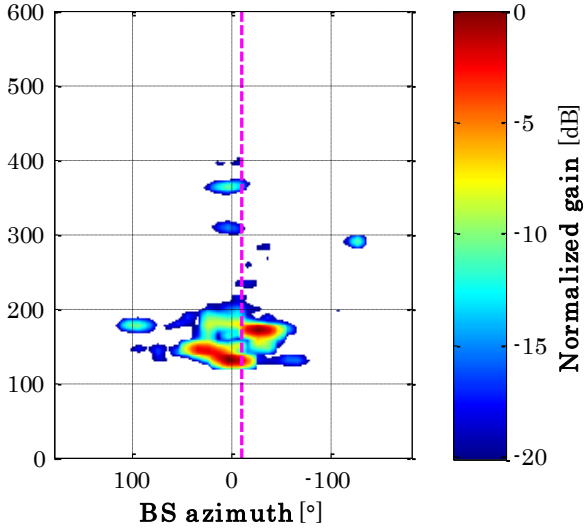
Relative delay [ns]
BS azimuth [°]
Normalized gain [dB]

S1

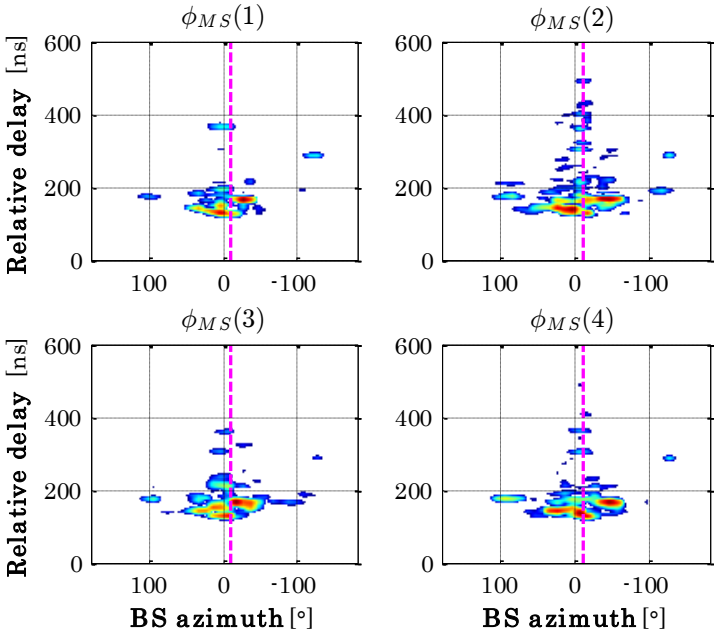
$\phi_{MS}(1)$
$\phi_{MS}(2)$
$\phi_{MS}(3)$
$\phi_{MS}(4)$
Relative delay [ns]
BS azimuth [°]

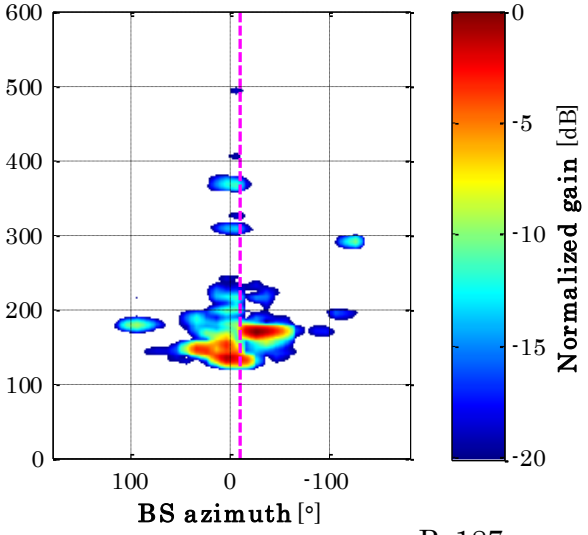
Relative delay [ns]
BS azimuth [°]
Normalized gain [dB]


17 GHz
TxC
C3

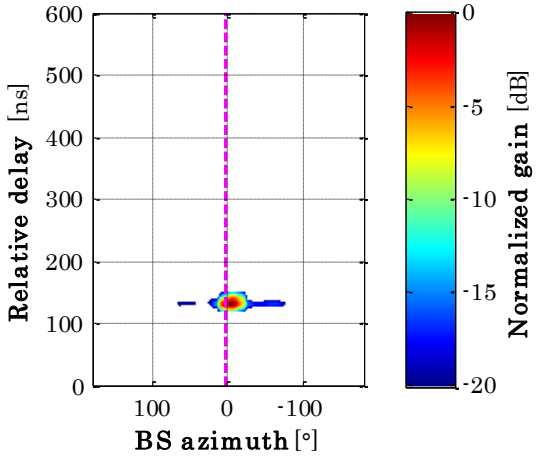
Relative delay [ns]
BS azimuth [°]
Normalized gain [dB]

S2

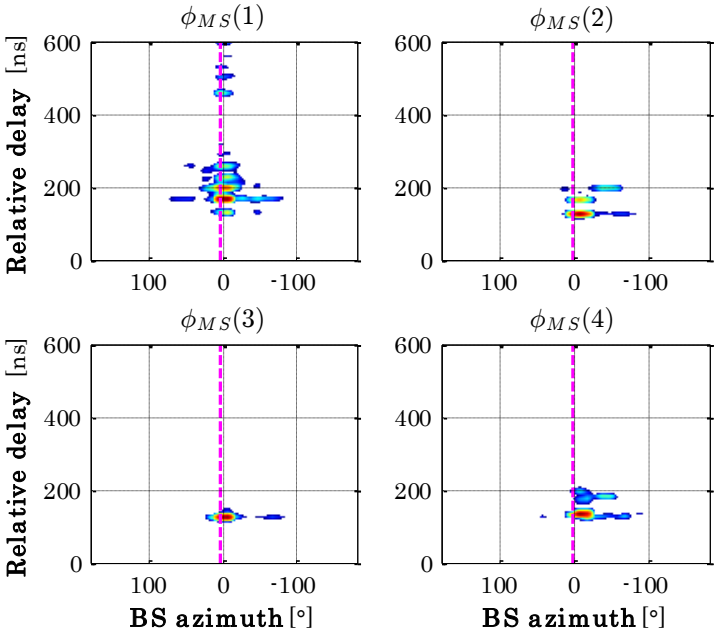
$\phi_{MS}(1)$
$\phi_{MS}(2)$
$\phi_{MS}(3)$
$\phi_{MS}(4)$
Relative delay [ns]
BS azimuth [°]

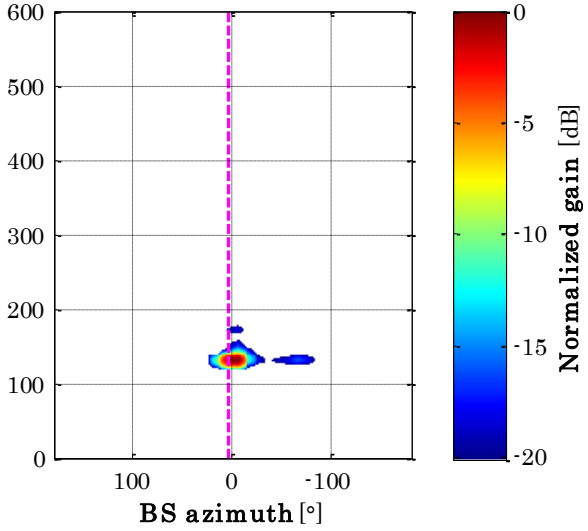
BS azimuth [°]
Normalized gain [dB]

S1

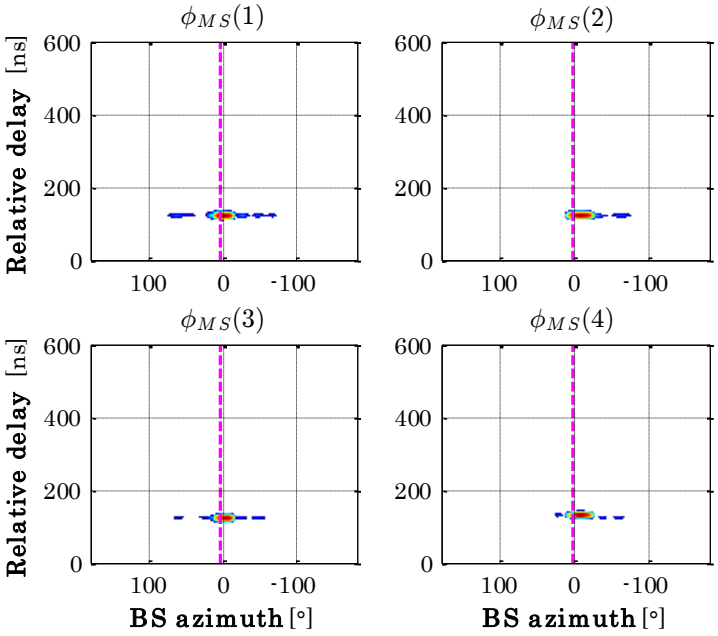
$\phi_{MS}(1)$
$\phi_{MS}(2)$
$\phi_{MS}(3)$
$\phi_{MS}(4)$
Relative delay [ns]
BS azimuth [°]

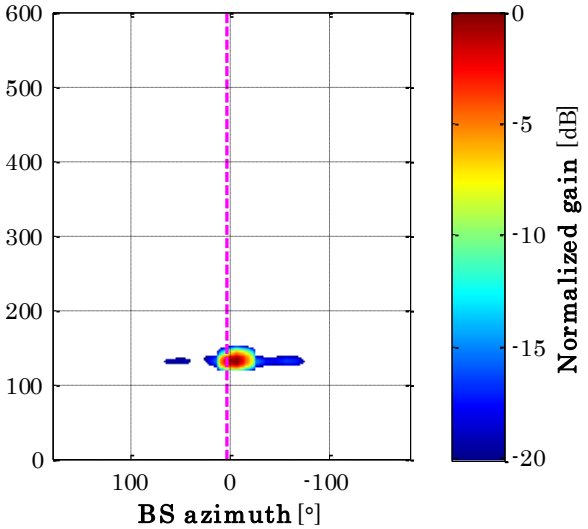
BS azimuth [°]
Normalized gain [dB]


17 GHz
TxC
C4

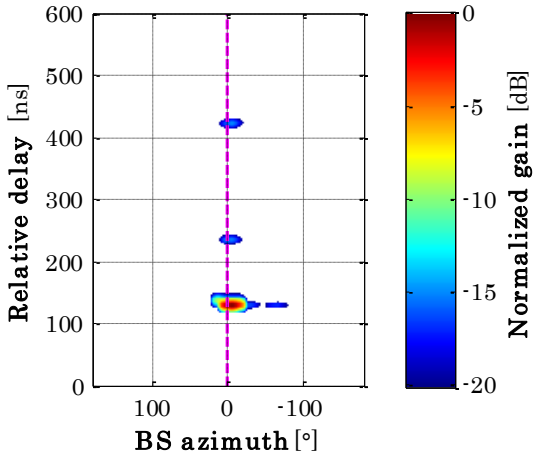
Relative delay [ns]
BS azimuth [°]
Normalized gain [dB]

S2

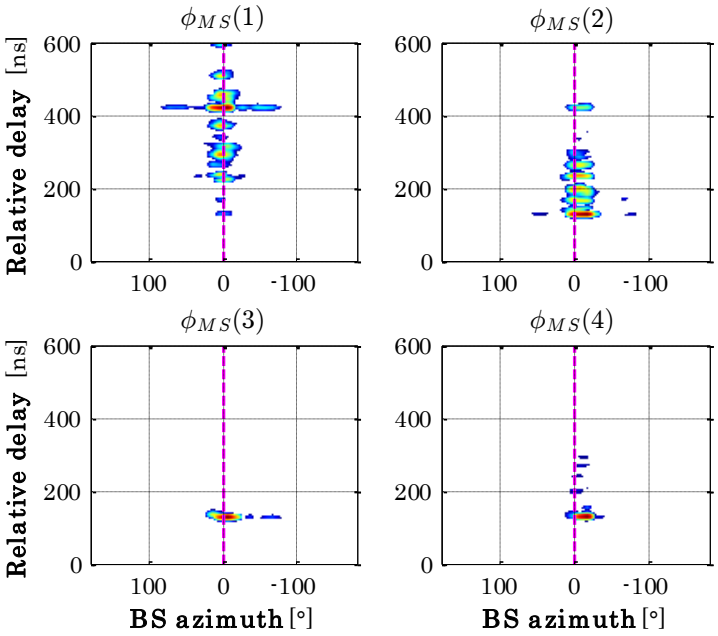
$\phi_{MS}(1)$
$\phi_{MS}(2)$
$\phi_{MS}(3)$
$\phi_{MS}(4)$
Relative delay [ns]
BS azimuth [°]

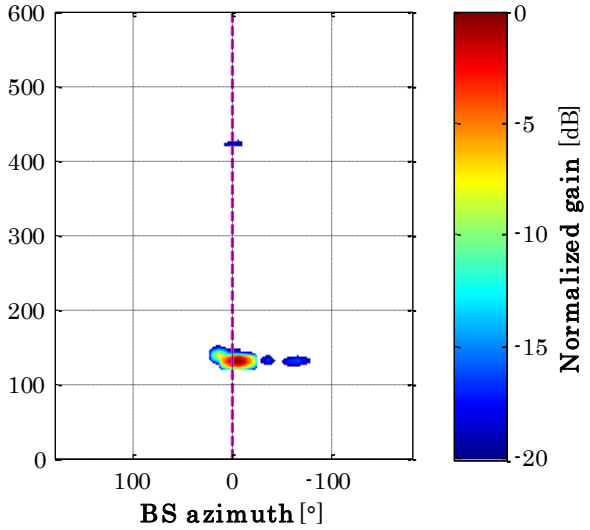
Relative delay [ns]
BS azimuth [°]
Normalized gain [dB]

S1

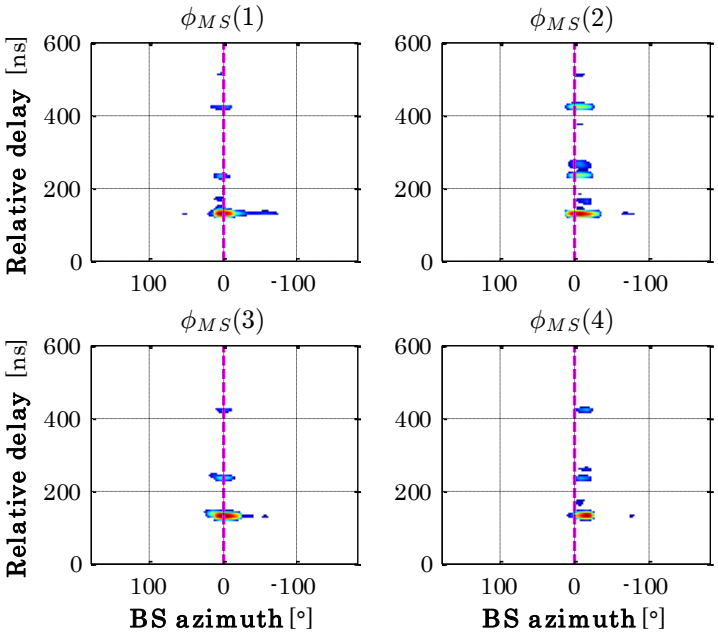
$\phi_{MS}(1)$
$\phi_{MS}(2)$
$\phi_{MS}(3)$
$\phi_{MS}(4)$
Relative delay [ns]
BS azimuth [°]

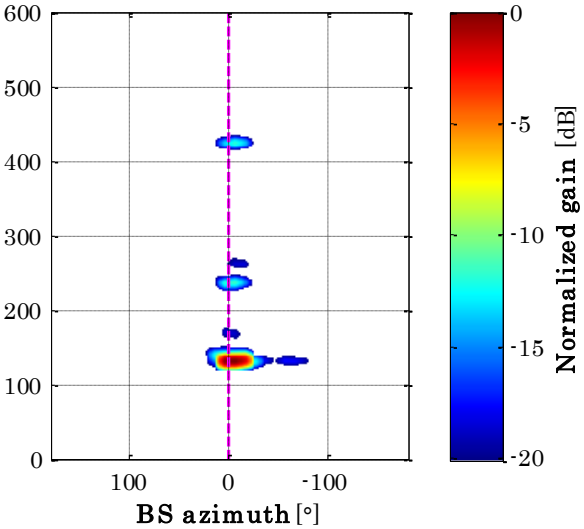
Relative delay [ns]
BS azimuth [°]
Normalized gain [dB]


17 GHz
TxC
C5

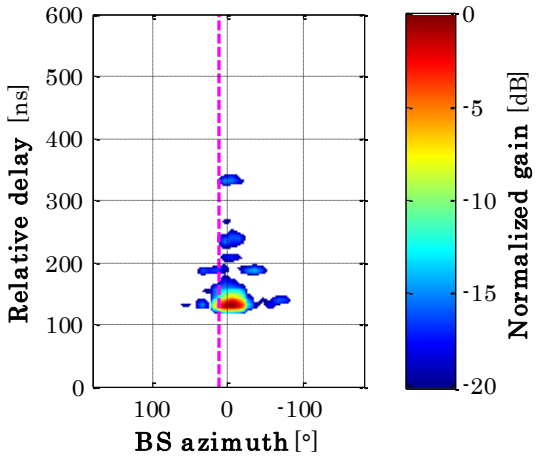
Relative delay [ns]
BS azimuth [°]
Normalized gain [dB]

S2

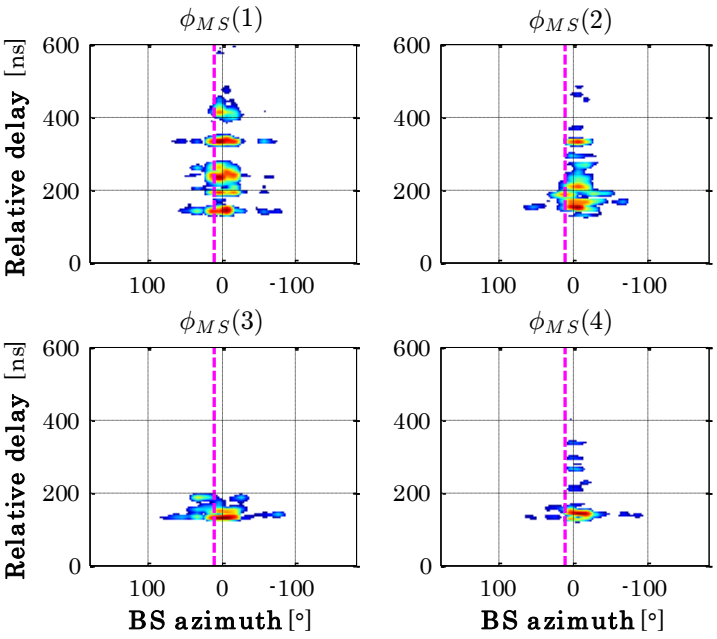
$\phi_{MS}(1)$
$\phi_{MS}(2)$
$\phi_{MS}(3)$
$\phi_{MS}(4)$
Relative delay [ns]
BS azimuth [°]

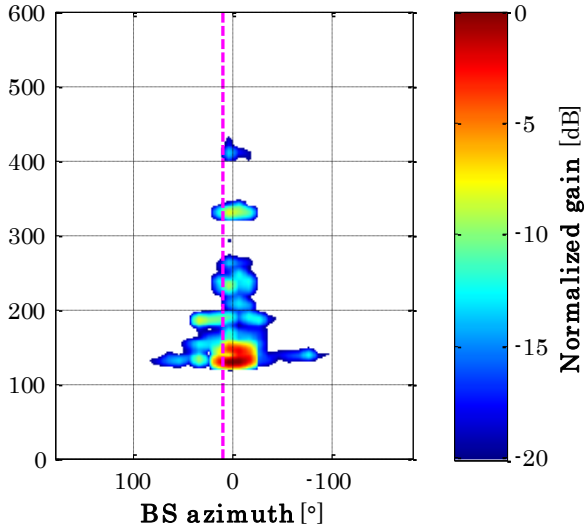
Relative delay [ns]
BS azimuth [°]
Normalized gain [dB]

S1

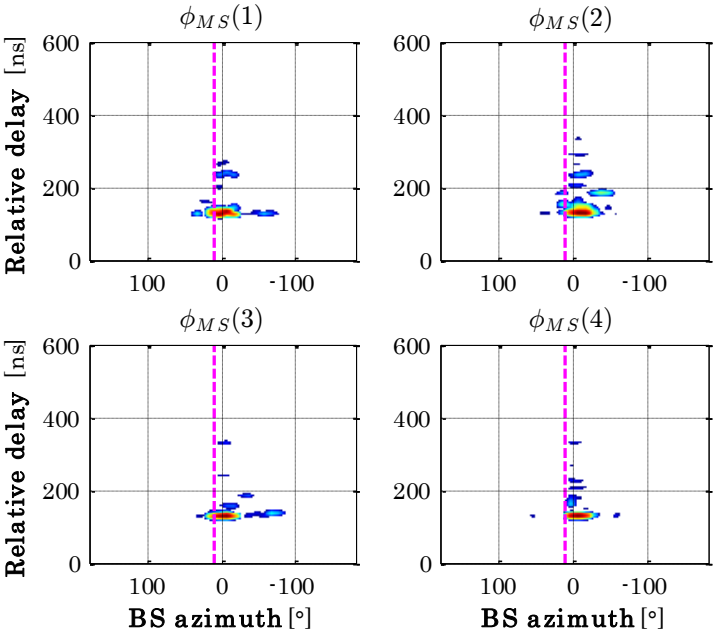
$\phi_{MS}(1)$
$\phi_{MS}(2)$
$\phi_{MS}(3)$
$\phi_{MS}(4)$
Relative delay [ns]
BS azimuth [°]

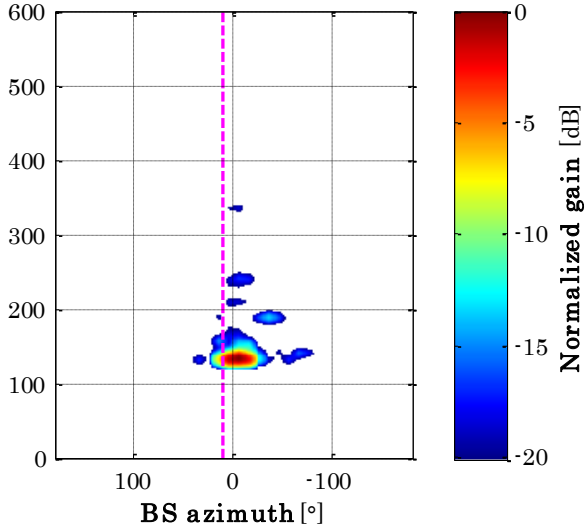
Relative delay [ns]
BS azimuth [°]
Normalized gain [dB]


17 GHz
TxC
C6

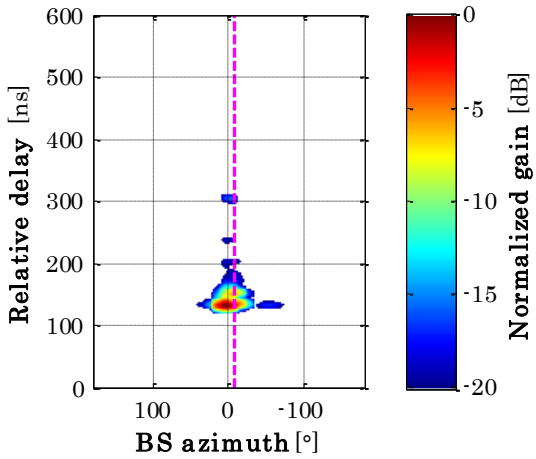
Relative delay [ns]
BS azimuth [°]
Normalized gain [dB]

S2

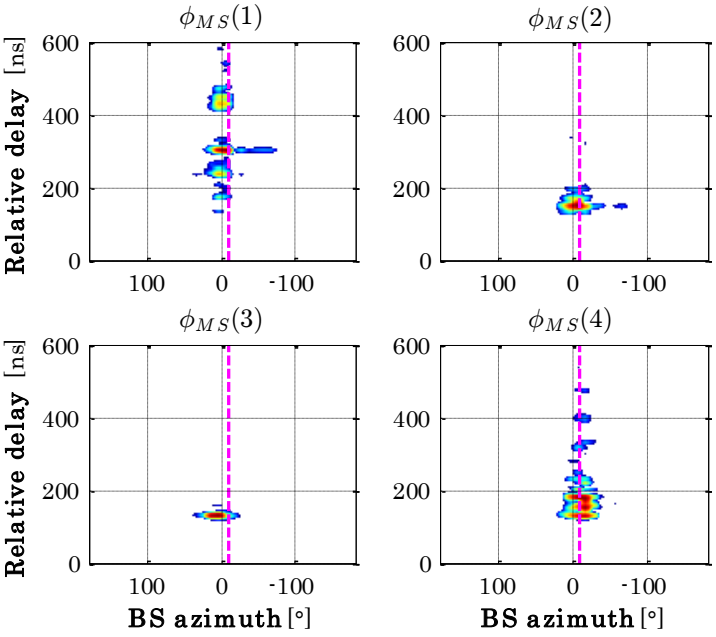
$\phi_{MS}(1)$
$\phi_{MS}(2)$
$\phi_{MS}(3)$
$\phi_{MS}(4)$
Relative delay [ns]
BS azimuth [°]

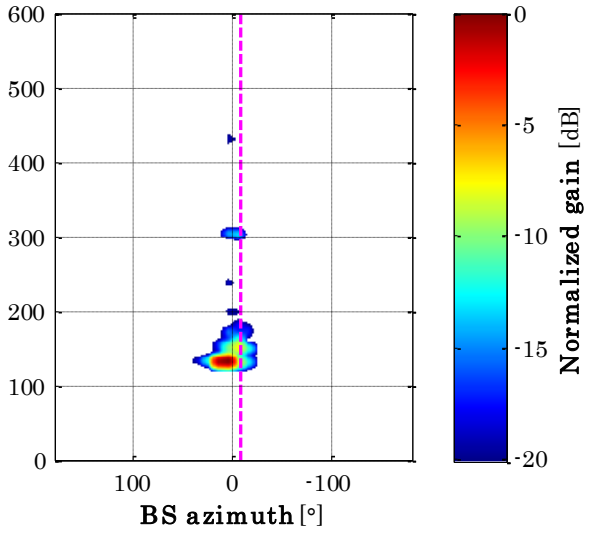
BS azimuth [°]
Normalized gain [dB]

S1

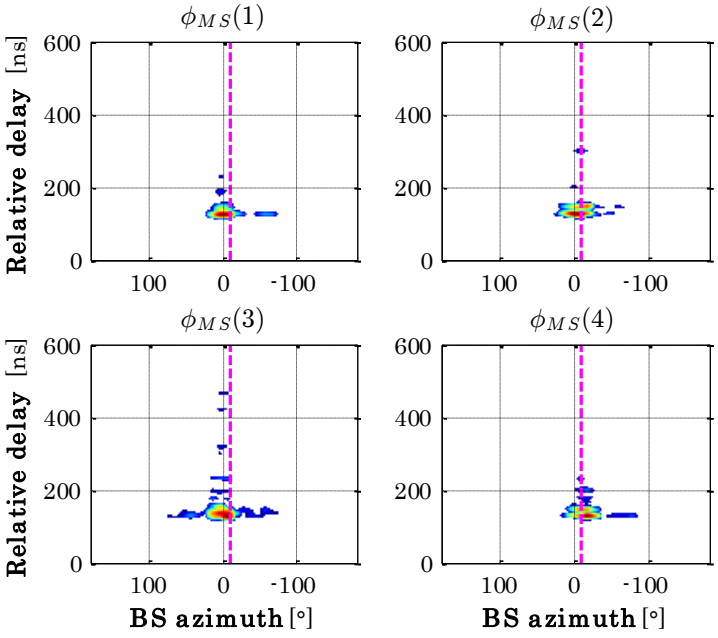
$\phi_{MS}(1)$
$\phi_{MS}(2)$
$\phi_{MS}(3)$
$\phi_{MS}(4)$
Relative delay [ns]
BS azimuth [°]

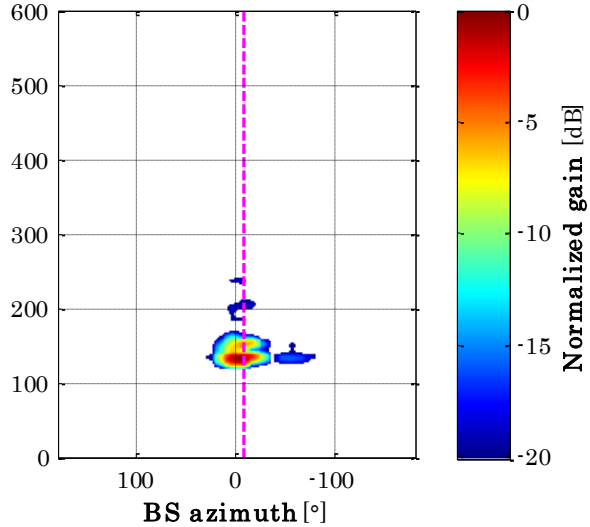
BS azimuth [°]
Normalized gain [dB]


17 GHz
TxC
C7

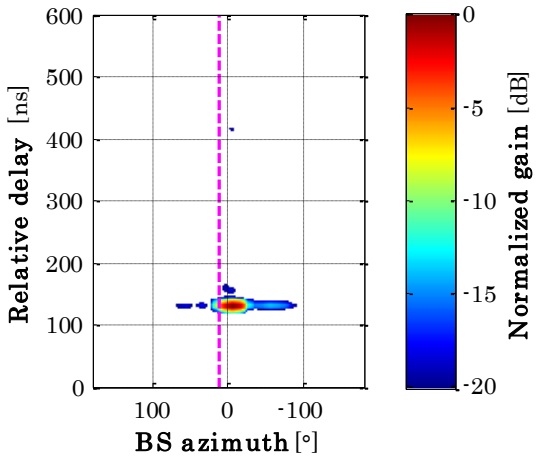
Relative delay [ns]
BS azimuth [°]
Normalized gain [dB]

S2

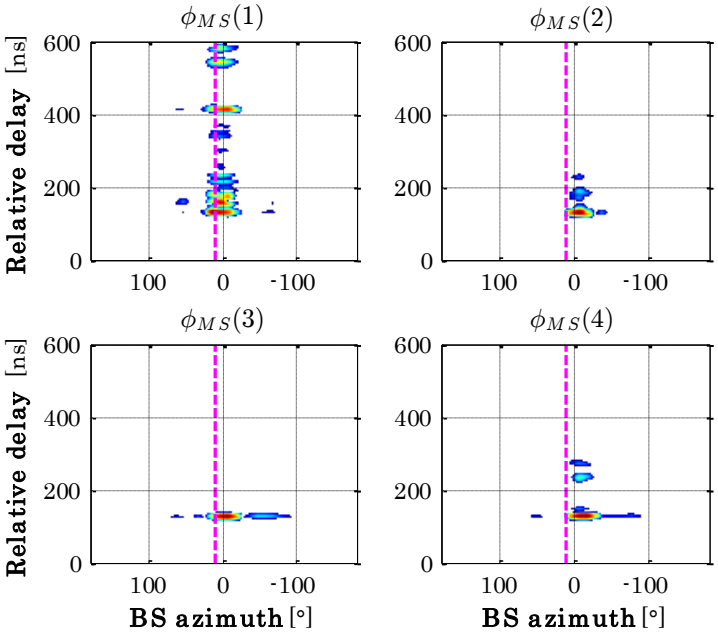
$\phi_{MS}(1)$
$\phi_{MS}(2)$
$\phi_{MS}(3)$
$\phi_{MS}(4)$
Relative delay [ns]
BS azimuth [°]

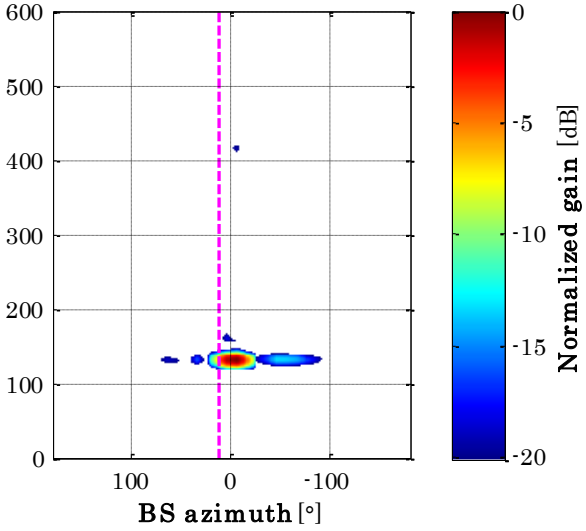
Relative delay [ns]
BS azimuth [°]
Normalized gain [dB]

S1

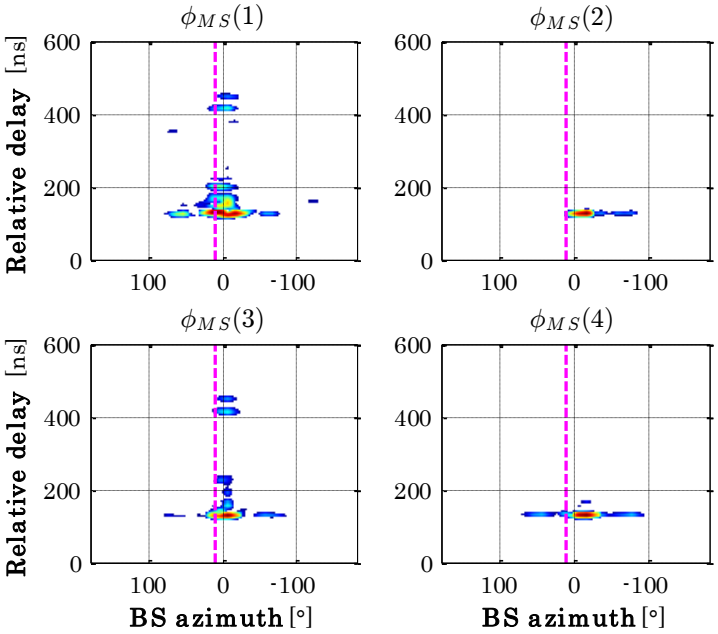
$\phi_{MS}(1)$
$\phi_{MS}(2)$
$\phi_{MS}(3)$
$\phi_{MS}(4)$
Relative delay [ns]
BS azimuth [°]

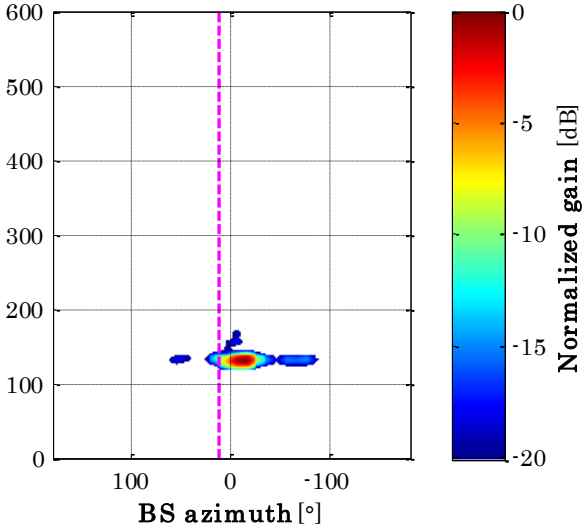
Relative delay [ns]
BS azimuth [°]
Normalized gain [dB]


17 GHz
TxC
C8

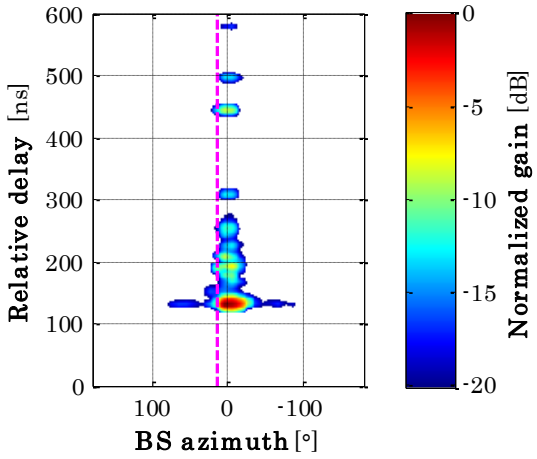
Relative delay [ns]
BS azimuth [°]
Normalized gain [dB]

S2

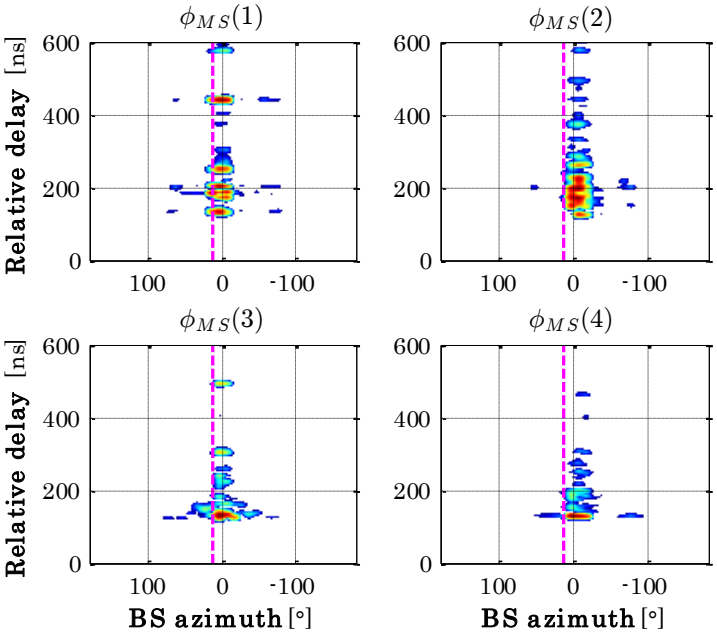
$\phi_{MS}(1)$
$\phi_{MS}(2)$
$\phi_{MS}(3)$
$\phi_{MS}(4)$
Relative delay [ns]
BS azimuth [°]

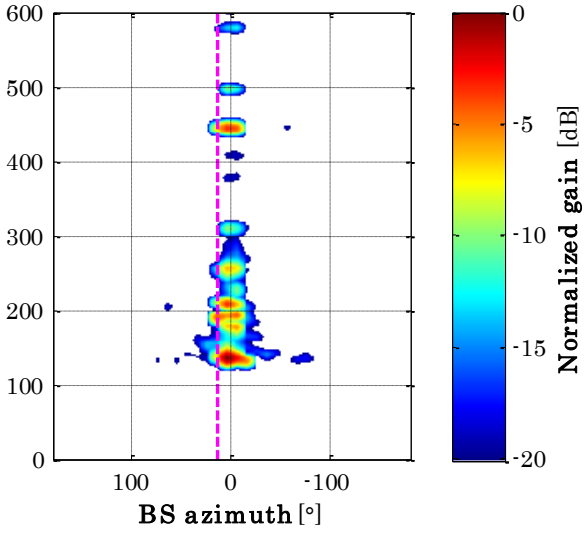
BS azimuth [°]
Normalized gain [dB]

S1

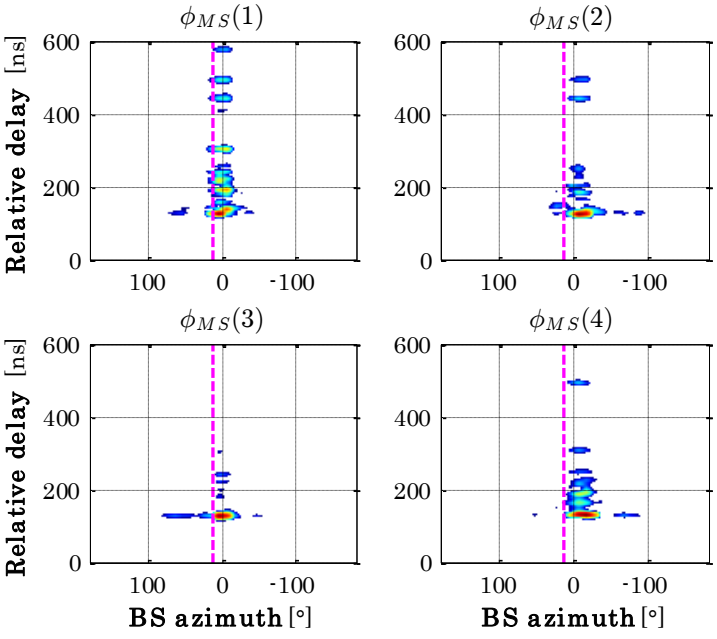
$\phi_{MS}(1)$
$\phi_{MS}(2)$
$\phi_{MS}(3)$
$\phi_{MS}(4)$
Relative delay [ns]
BS azimuth [°]

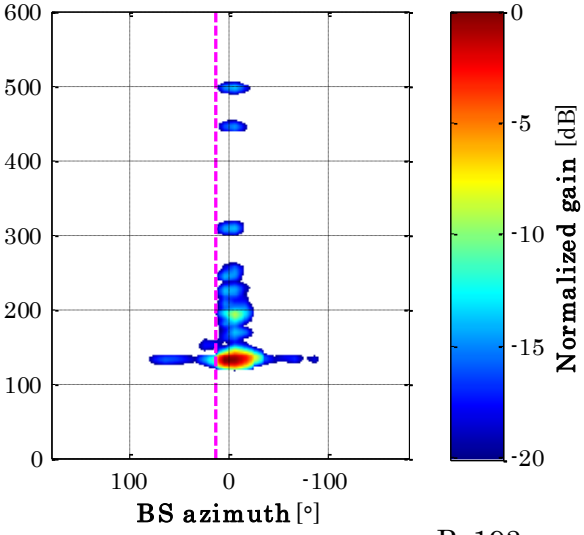
BS azimuth [°]
Normalized gain [dB]


60 GHz
TxA
A1

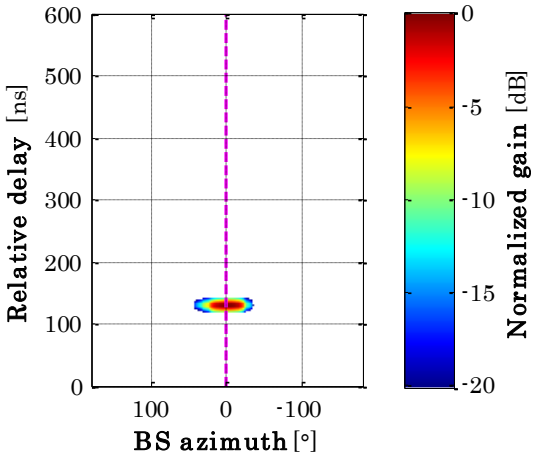
Relative delay [ns]
BS azimuth [°]
Normalized gain [dB]

S2

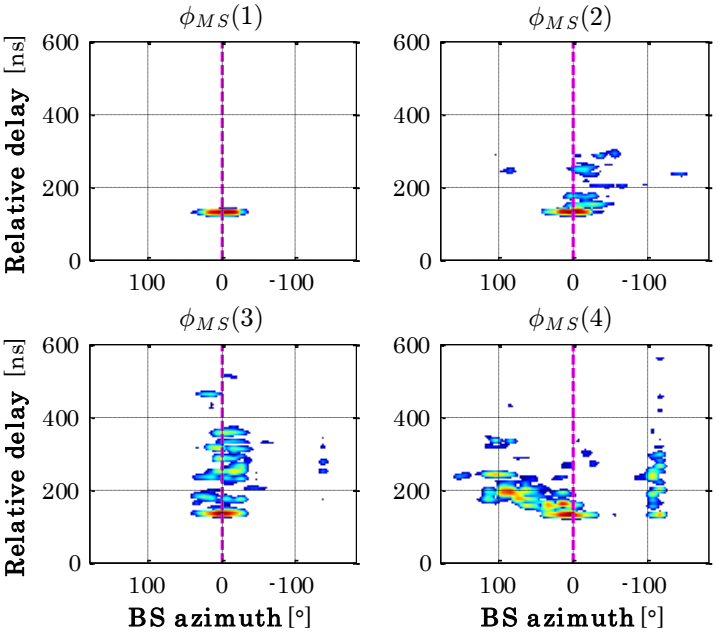
$\phi_{MS}(1)$
$\phi_{MS}(2)$
$\phi_{MS}(3)$
$\phi_{MS}(4)$
Relative delay [ns]
BS azimuth [°]

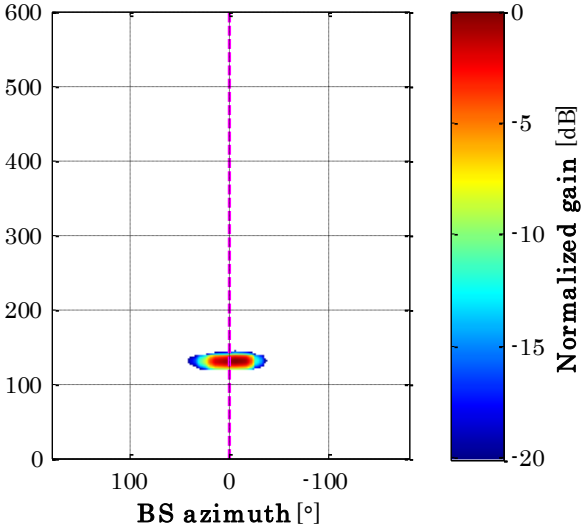
BS azimuth [°]
Normalized gain [dB]

S1

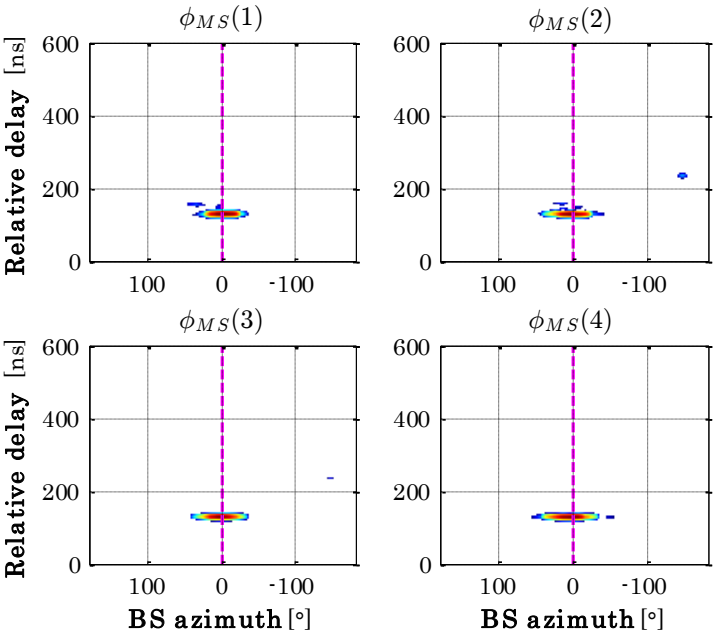
$\phi_{MS}(1)$
$\phi_{MS}(2)$
$\phi_{MS}(3)$
$\phi_{MS}(4)$
Relative delay [ns]
BS azimuth [°]

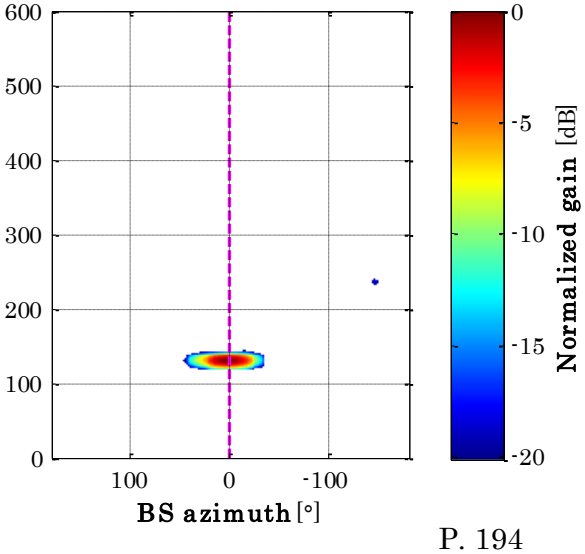
BS azimuth [°]
Normalized gain [dB]


60 GHz
TxA
A2

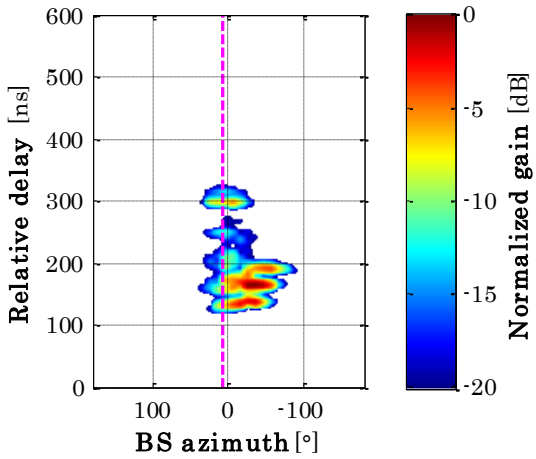
Relative delay [ns]
BS azimuth [°]
Normalized gain [dB]

S2

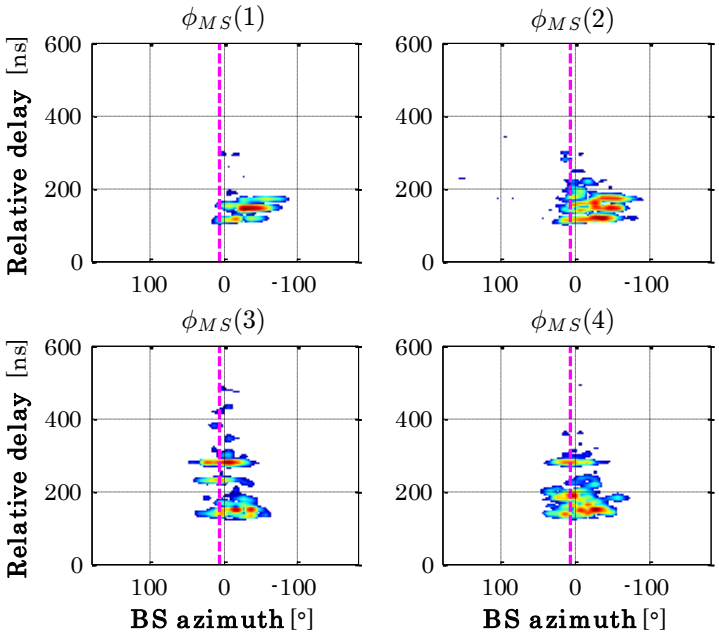
$\phi_{MS}(1)$
$\phi_{MS}(2)$
$\phi_{MS}(3)$
$\phi_{MS}(4)$
Relative delay [ns]
BS azimuth [°]

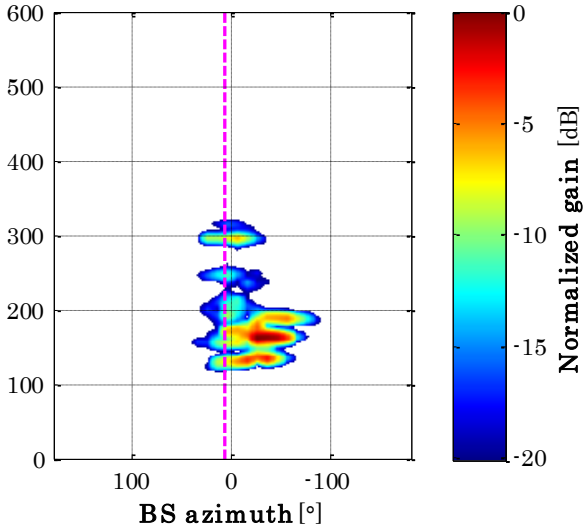
BS azimuth [°]
Normalized gain [dB]

S1

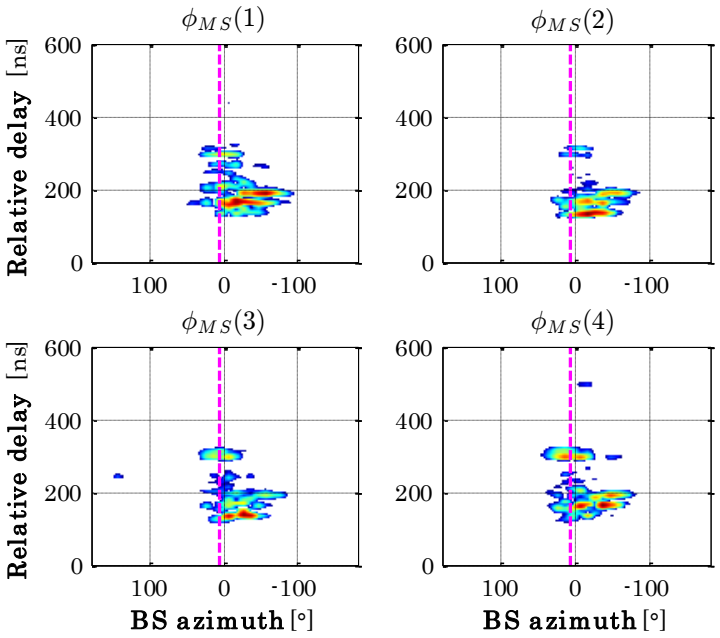
$\phi_{MS}(1)$
$\phi_{MS}(2)$
$\phi_{MS}(3)$
$\phi_{MS}(4)$
Relative delay [ns]
BS azimuth [°]

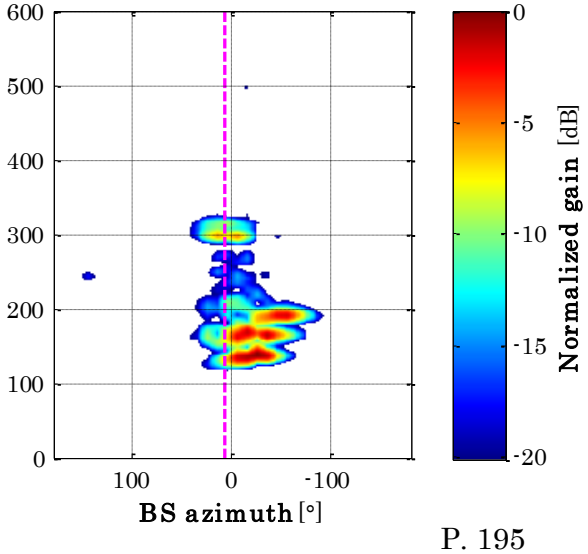
BS azimuth [°]
Normalized gain [dB]


60 GHz
TxA
A3

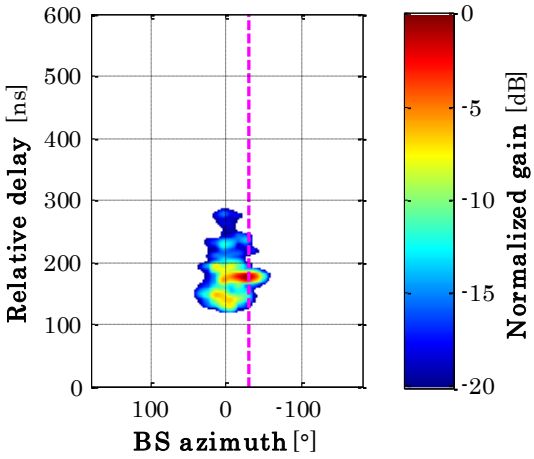
Relative delay [ns]
BS azimuth [°]
Normalized gain [dB]

S2

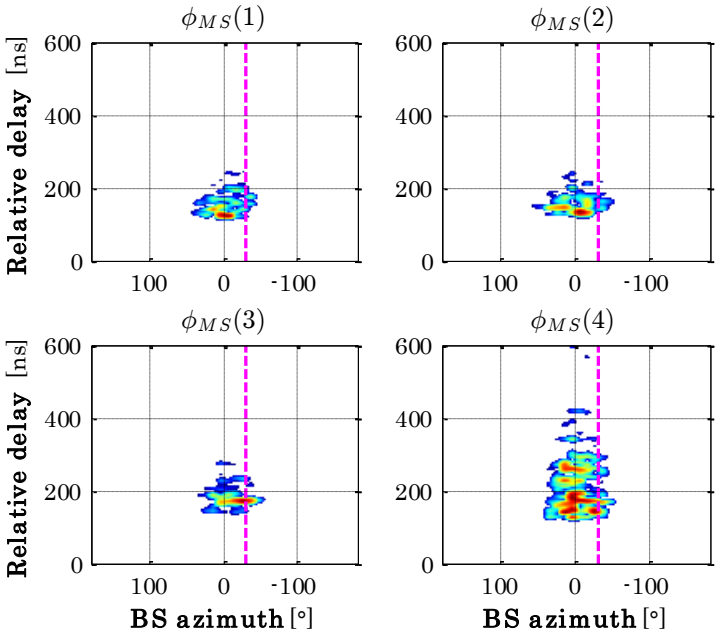
$\phi_{MS}(1)$
$\phi_{MS}(2)$
$\phi_{MS}(3)$
$\phi_{MS}(4)$
Relative delay [ns]
BS azimuth [°]

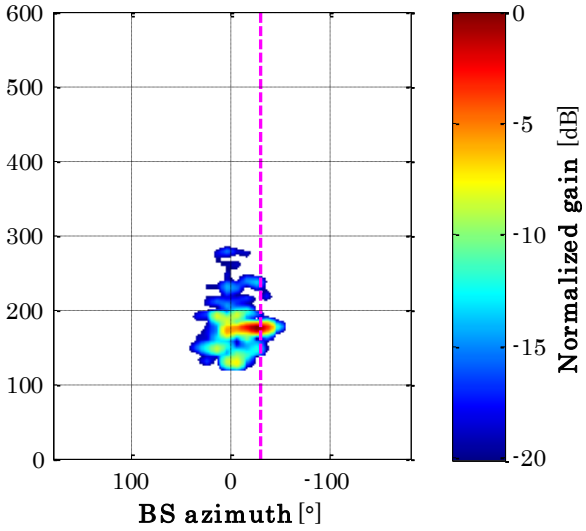
BS azimuth [°]
Normalized gain [dB]

S1

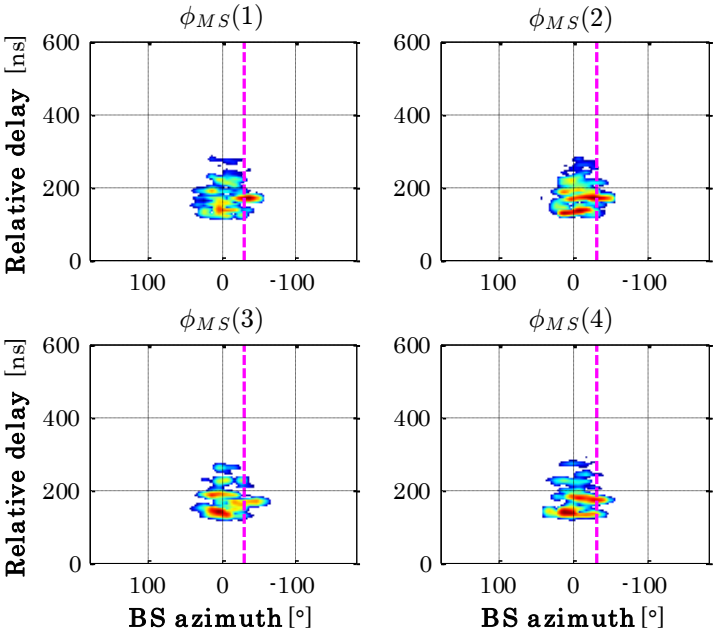
$\phi_{MS}(1)$
$\phi_{MS}(2)$
$\phi_{MS}(3)$
$\phi_{MS}(4)$
Relative delay [ns]
BS azimuth [°]

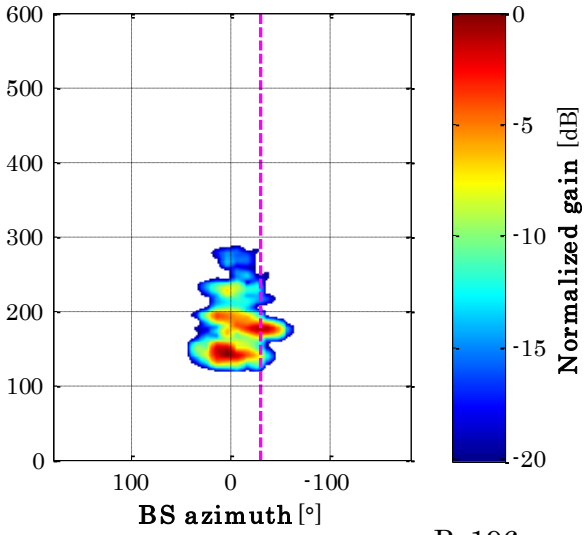
BS azimuth [°]
Normalized gain [dB]

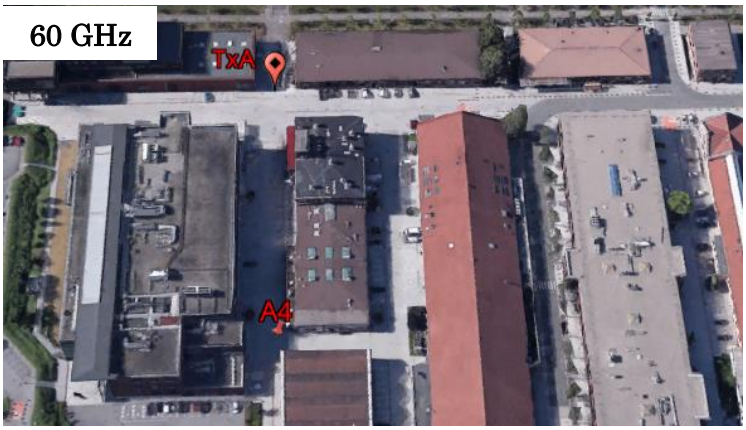
60 GHz
TxA
A4

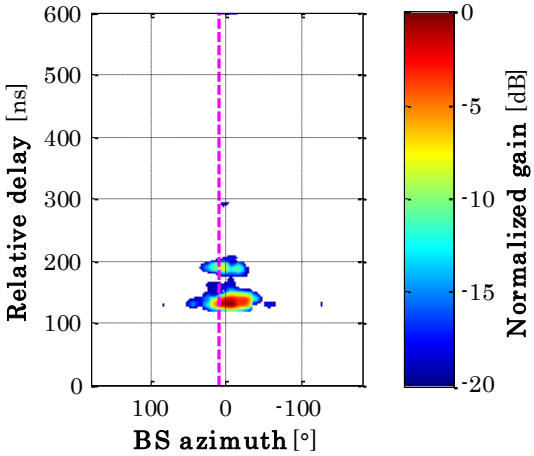
Relative delay [ns]
BS azimuth [°]
Normalized gain [dB]

S2

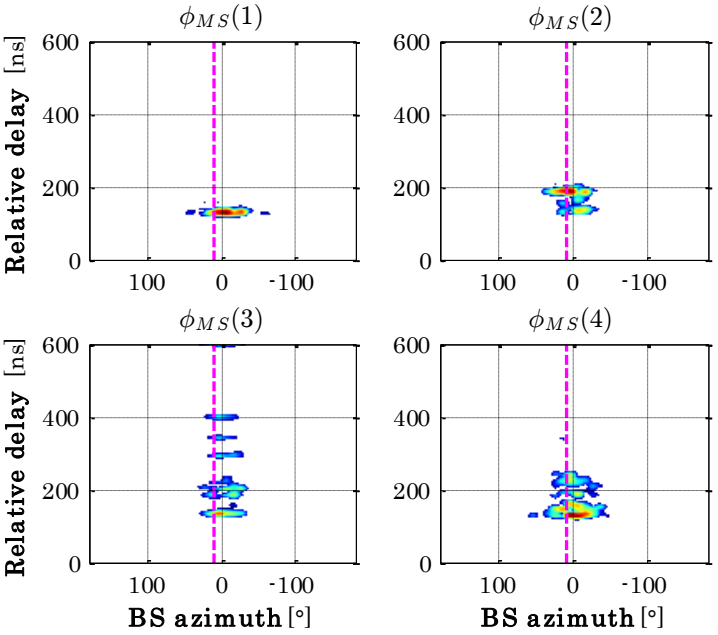
$\phi_{MS}(1)$
$\phi_{MS}(2)$
$\phi_{MS}(3)$
$\phi_{MS}(4)$
Relative delay [ns]
BS azimuth [°]

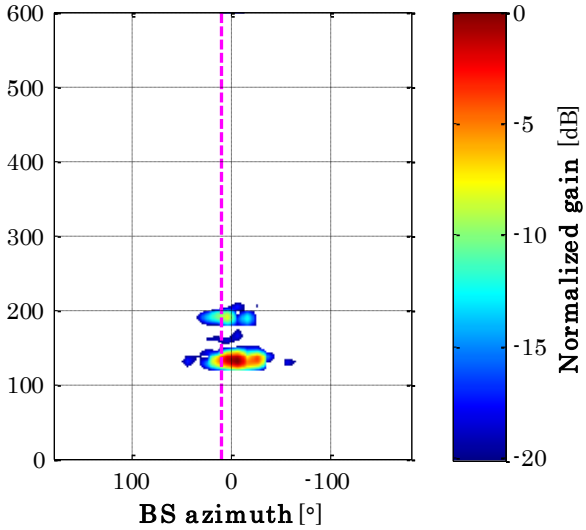
BS azimuth [°]
Normalized gain [dB]

S1

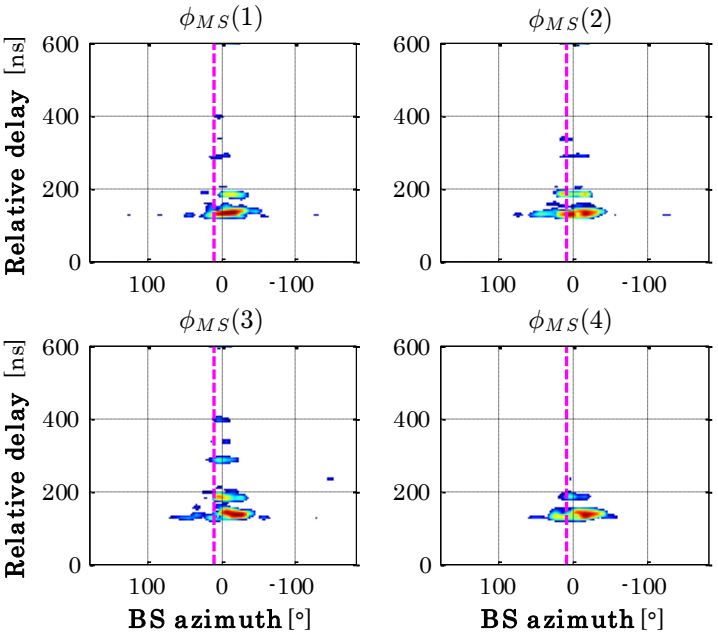
$\phi_{MS}(1)$
$\phi_{MS}(2)$
$\phi_{MS}(3)$
$\phi_{MS}(4)$
Relative delay [ns]
BS azimuth [°]

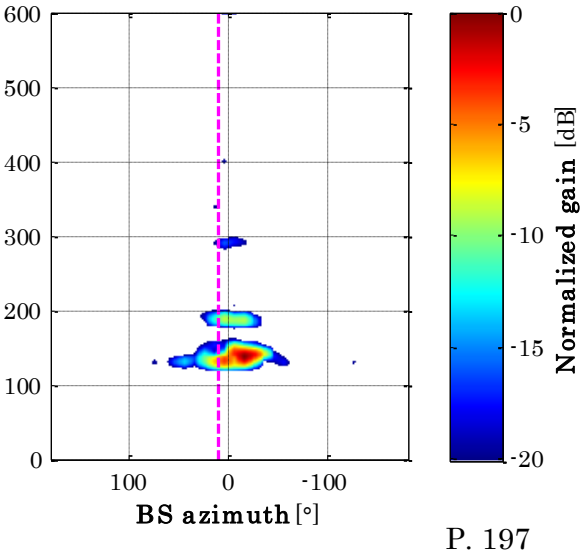
BS azimuth [°]
Normalized gain [dB]

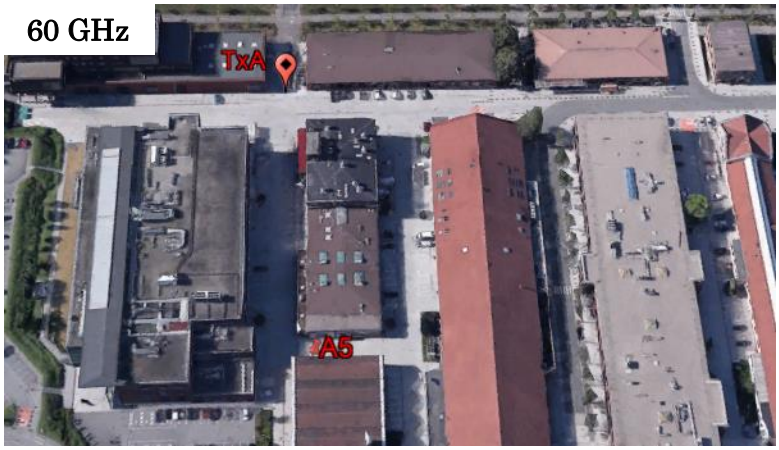
60 GHz
TxA
A5

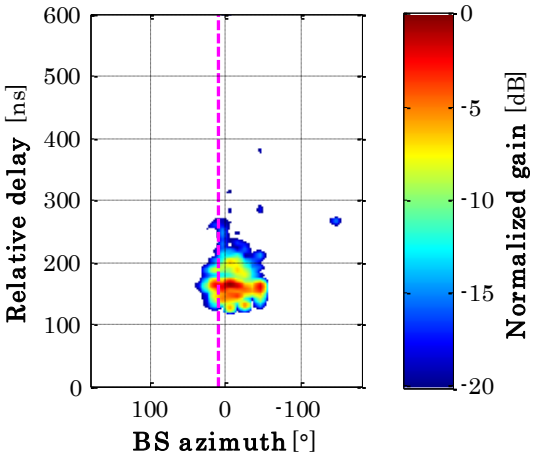
Relative delay [ns]
BS azimuth [°]
Normalized gain [dB]

S2

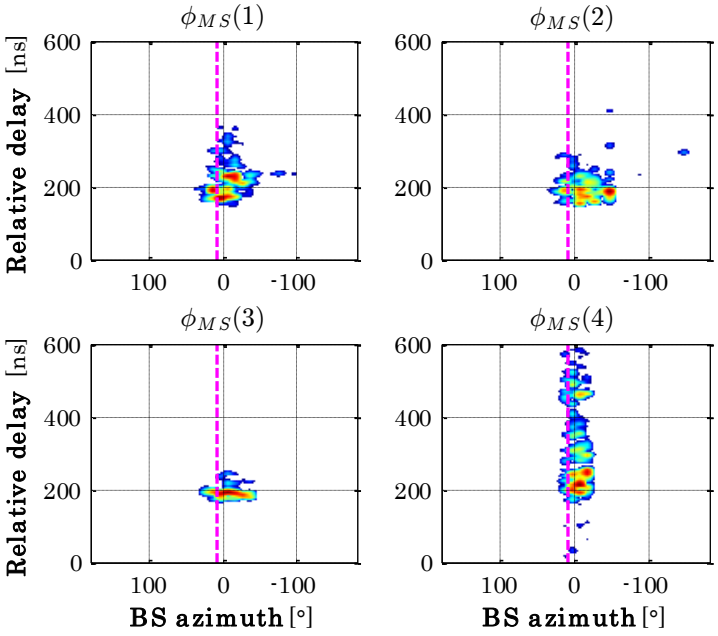
$\phi_{MS}(1)$
$\phi_{MS}(2)$
$\phi_{MS}(3)$
$\phi_{MS}(4)$
Relative delay [ns]
BS azimuth [°]

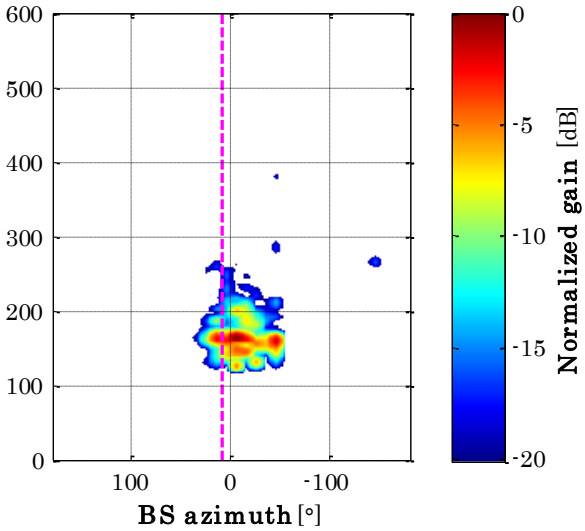
Relative delay [ns]
BS azimuth [°]
Normalized gain [dB]

S1

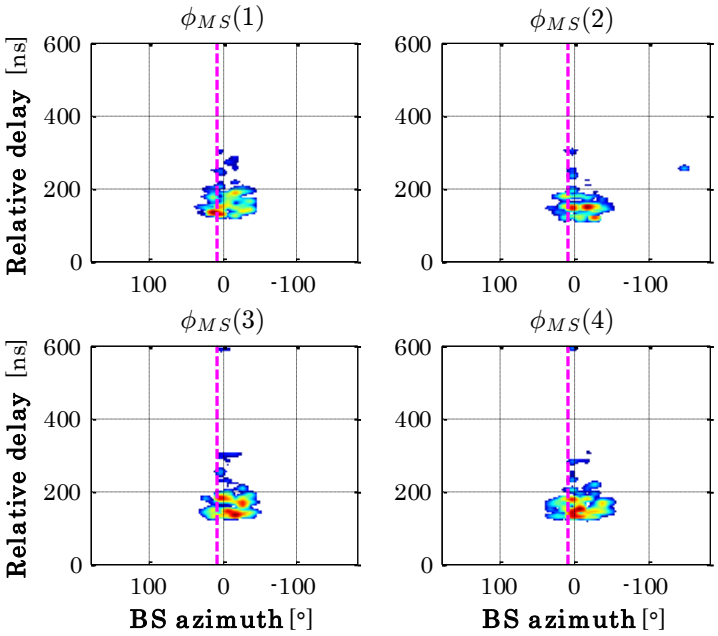
$\phi_{MS}(1)$
$\phi_{MS}(2)$
$\phi_{MS}(3)$
$\phi_{MS}(4)$
Relative delay [ns]
BS azimuth [°]

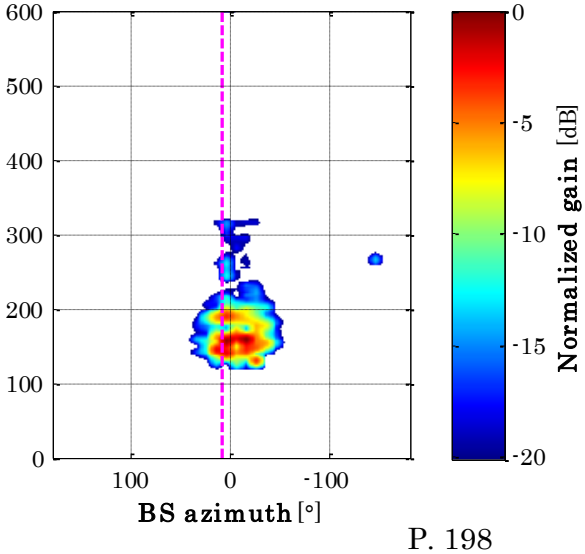
Relative delay [ns]
BS azimuth [°]
Normalized gain [dB]


60 GHz
TxA
A6

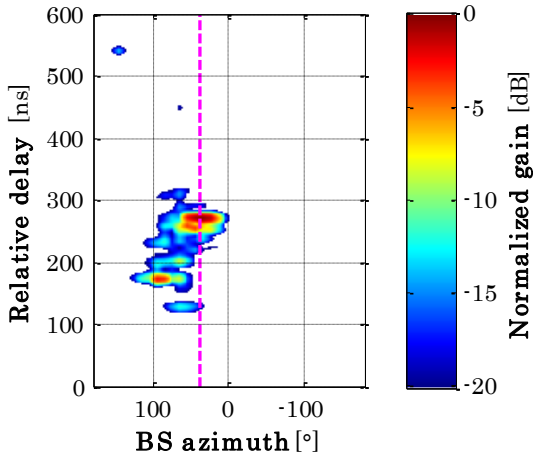
Relative delay [ns]
BS azimuth [°]
Normalized gain [dB]

S2

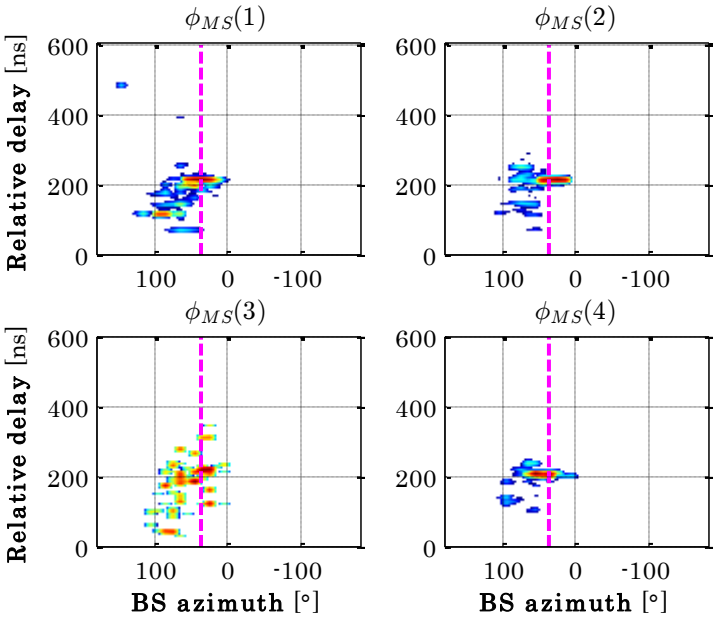
$\phi_{MS}(1)$
$\phi_{MS}(2)$
$\phi_{MS}(3)$
$\phi_{MS}(4)$
Relative delay [ns]
BS azimuth [°]

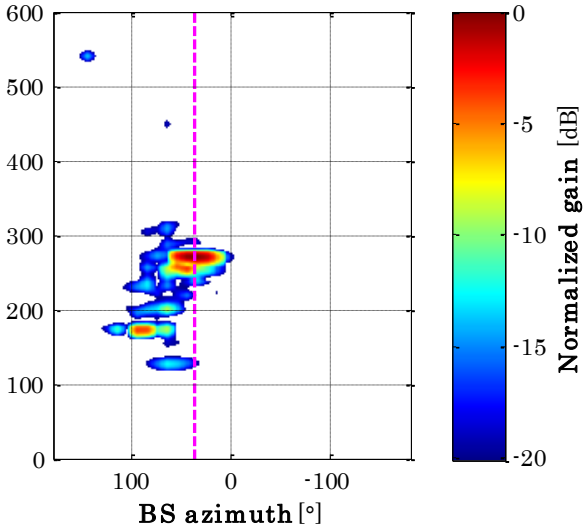
BS azimuth [°]
Normalized gain [dB]

S1

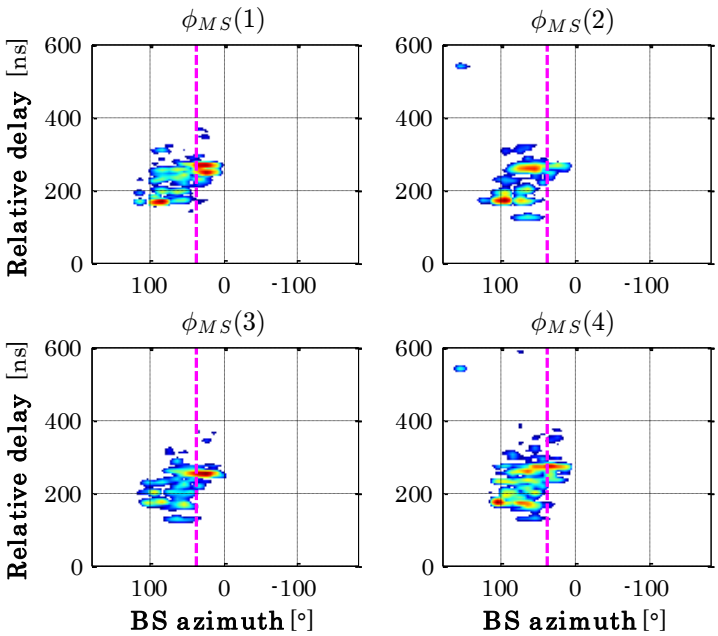
$\phi_{MS}(1)$
$\phi_{MS}(2)$
$\phi_{MS}(3)$
$\phi_{MS}(4)$
Relative delay [ns]
BS azimuth [°]

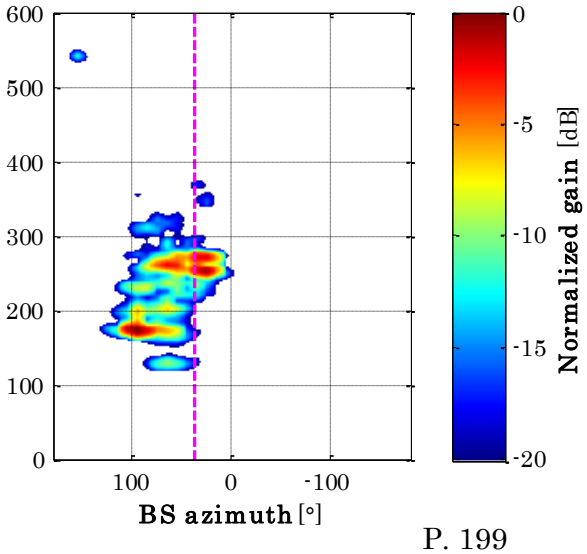
BS azimuth [°]
Normalized gain [dB]


60 GHz
TxA
A7

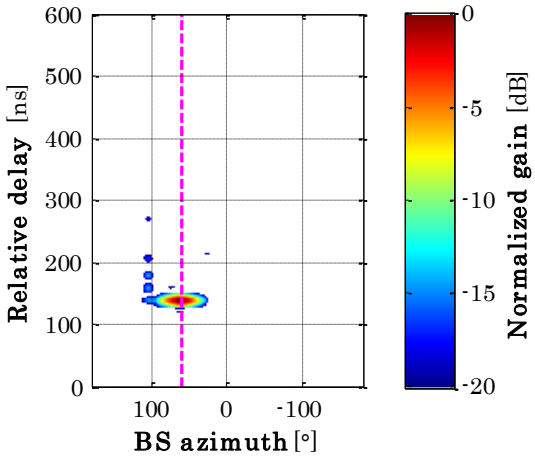
Relative delay [ns]
BS azimuth [°]
Normalized gain [dB]

S2

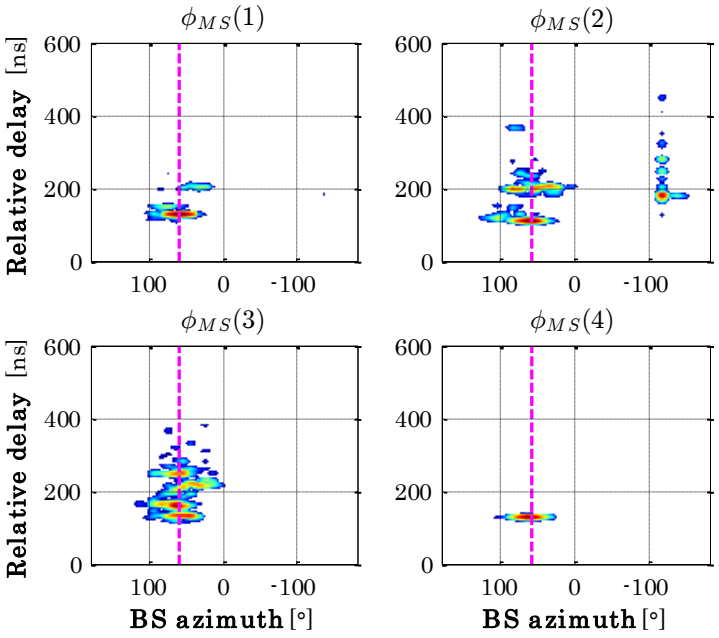
$\phi_{MS}(1)$
$\phi_{MS}(2)$
$\phi_{MS}(3)$
$\phi_{MS}(4)$
Relative delay [ns]
BS azimuth [°]

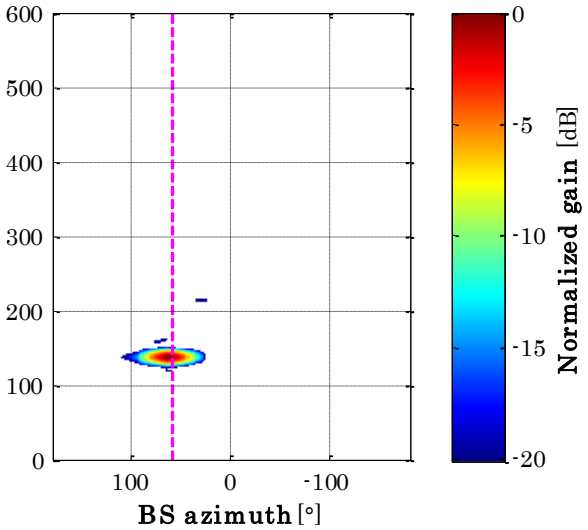
Relative delay [ns]
BS azimuth [°]
Normalized gain [dB]

S1

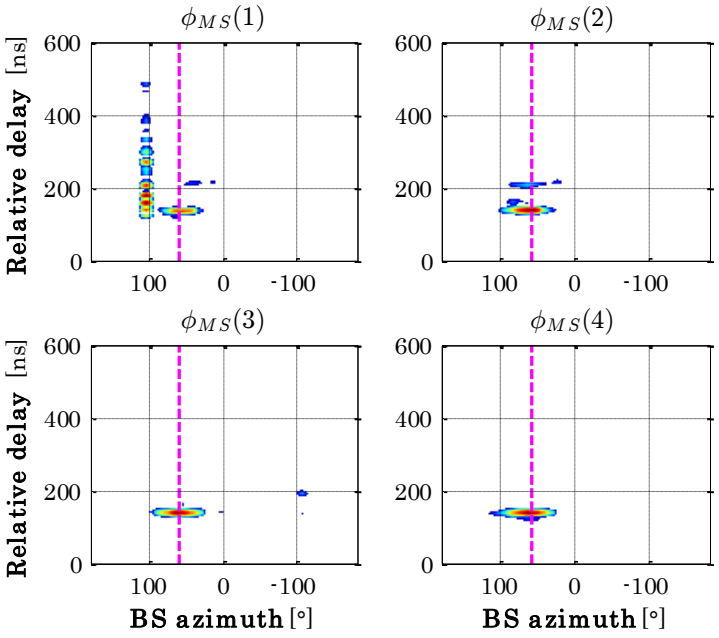
$\phi_{MS}(1)$
$\phi_{MS}(2)$
$\phi_{MS}(3)$
$\phi_{MS}(4)$
Relative delay [ns]
BS azimuth [°]

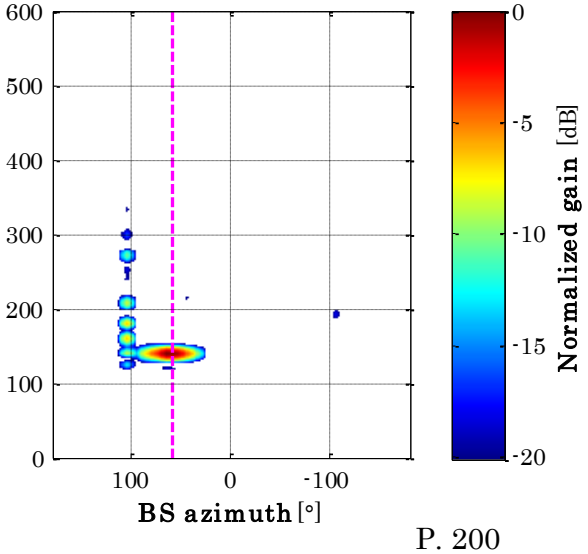
Relative delay [ns]
BS azimuth [°]
Normalized gain [dB]


60 GHz
TxA
A8

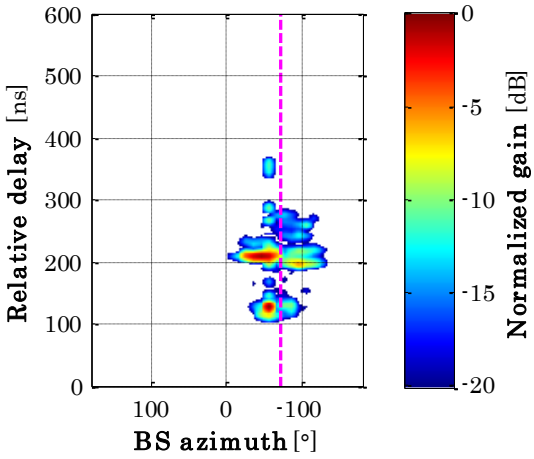
Relative delay [ns]
BS azimuth [°]
Normalized gain [dB]

S2

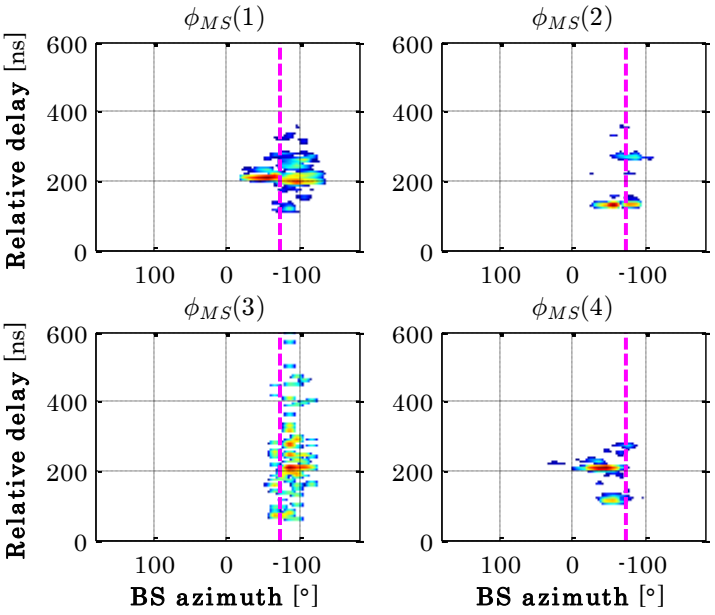
$\phi_{MS}(1)$
$\phi_{MS}(2)$
$\phi_{MS}(3)$
$\phi_{MS}(4)$
Relative delay [ns]
BS azimuth [°]

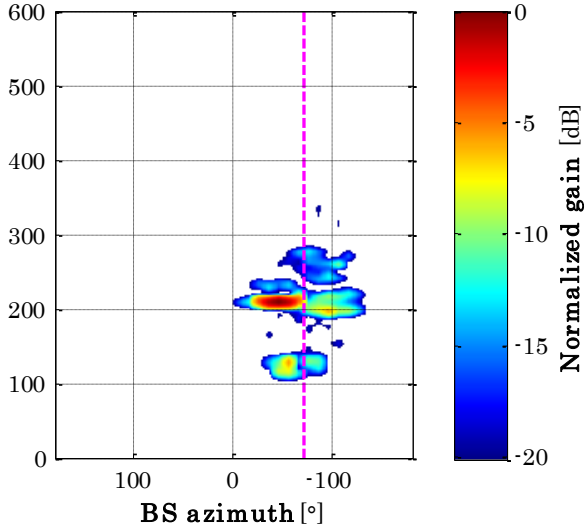
Relative delay [ns]
BS azimuth [°]
Normalized gain [dB]

S1

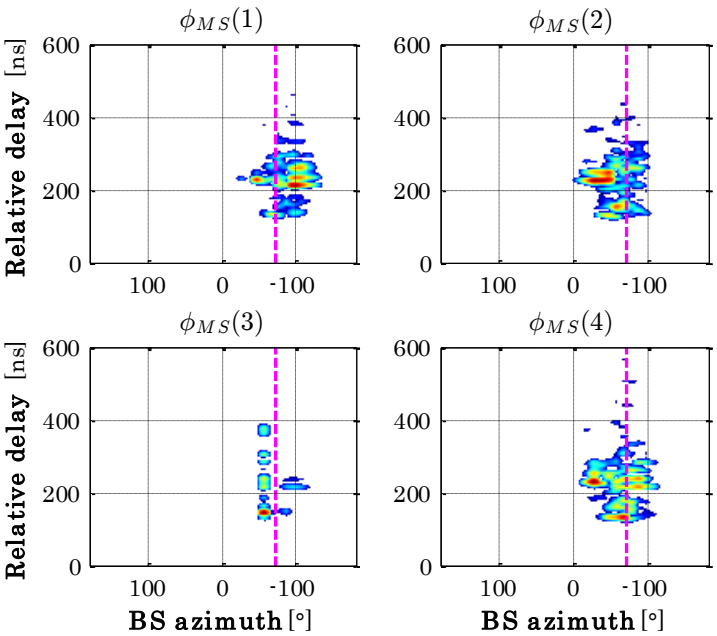
$\phi_{MS}(1)$
$\phi_{MS}(2)$
$\phi_{MS}(3)$
$\phi_{MS}(4)$
Relative delay [ns]
BS azimuth [°]

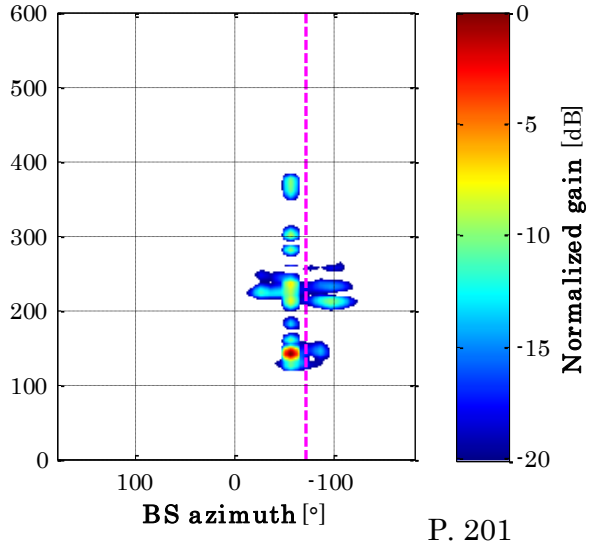
Relative delay [ns]
BS azimuth [°]
Normalized gain [dB]


60 GHz
TxA
A9

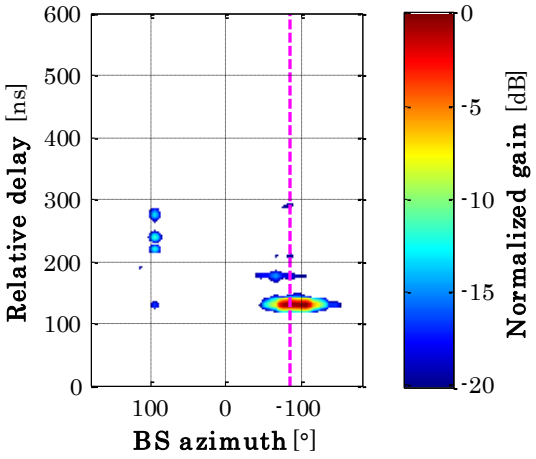
Relative delay [ns]
BS azimuth [°]
Normalized gain [dB]

S2

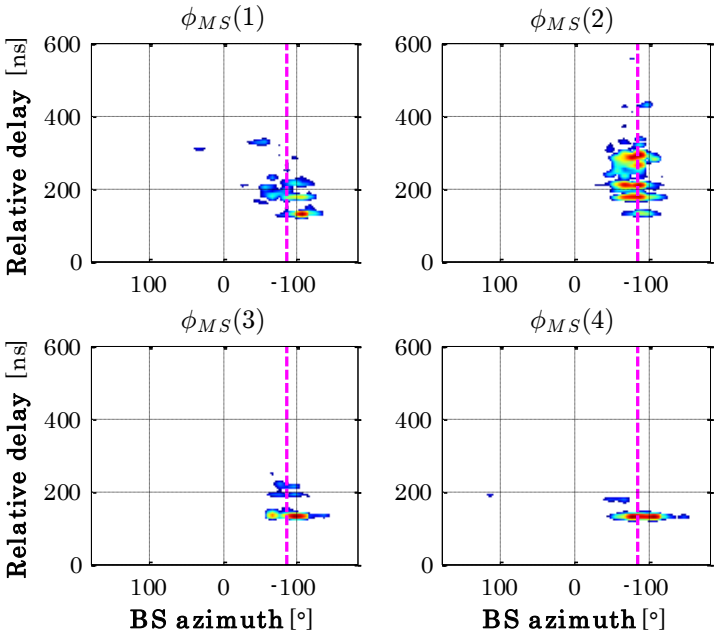
$\phi_{MS}(1)$
$\phi_{MS}(2)$
$\phi_{MS}(3)$
$\phi_{MS}(4)$
Relative delay [ns]
BS azimuth [°]

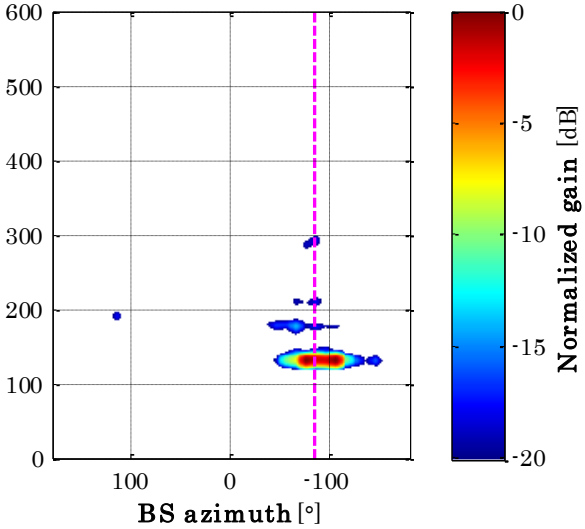
Relative delay [ns]
BS azimuth [°]
Normalized gain [dB]

S1

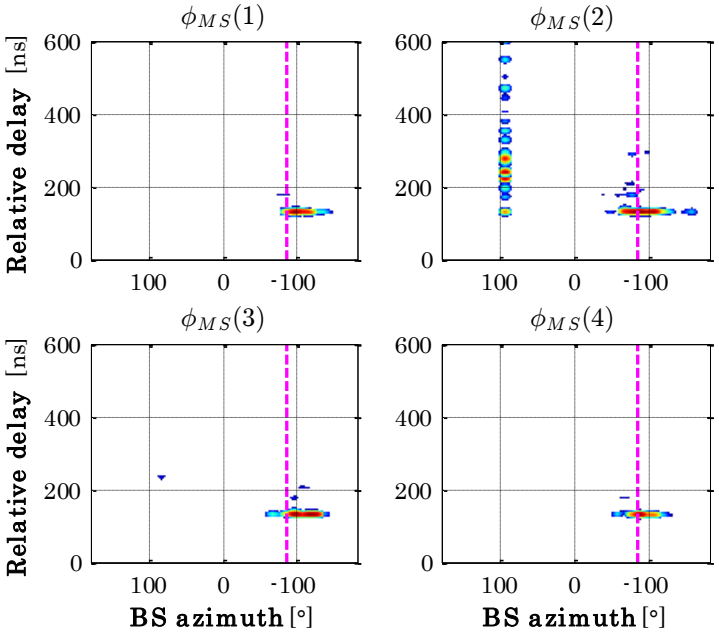
$\phi_{MS}(1)$
$\phi_{MS}(2)$
$\phi_{MS}(3)$
$\phi_{MS}(4)$
Relative delay [ns]
BS azimuth [°]

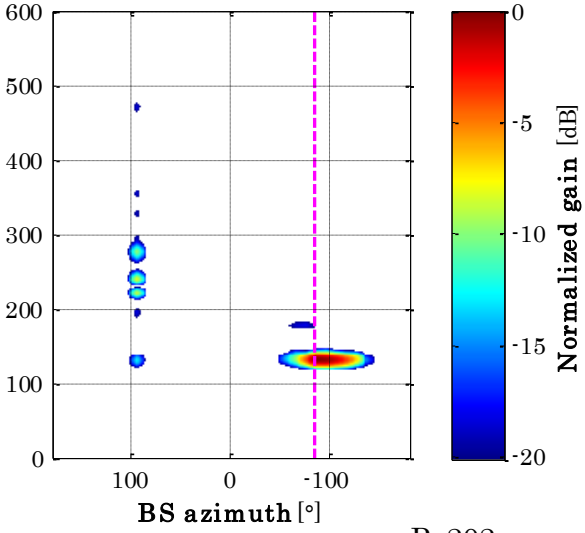
Relative delay [ns]
BS azimuth [°]
Normalized gain [dB]


60 GHz
TxA
A10

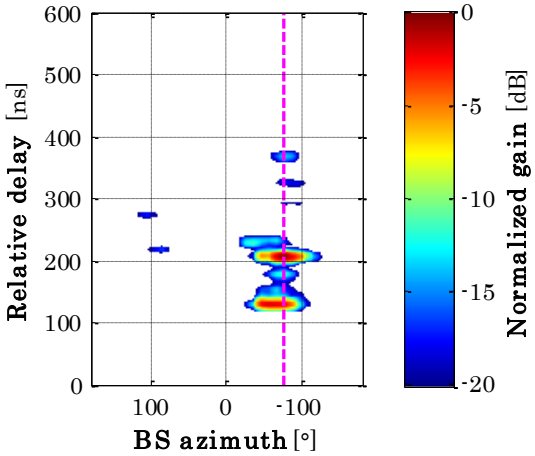
Relative delay [ns]
BS azimuth [°]
Normalized gain [dB]

S2

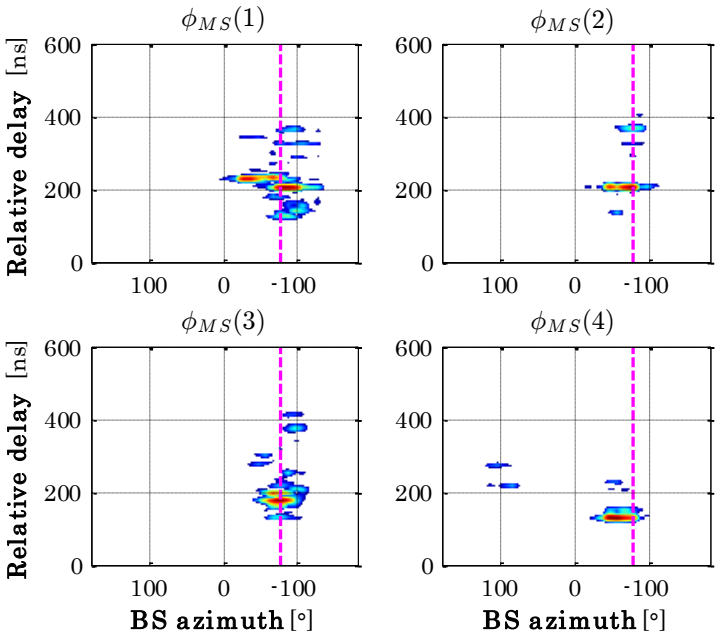
$\phi_{MS}(1)$
$\phi_{MS}(2)$
$\phi_{MS}(3)$
$\phi_{MS}(4)$
Relative delay [ns]
BS azimuth [°]

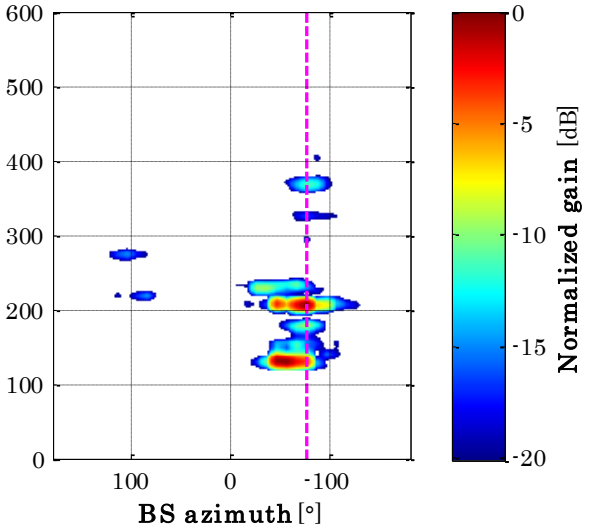
BS azimuth [°]
Normalized gain [dB]

S1

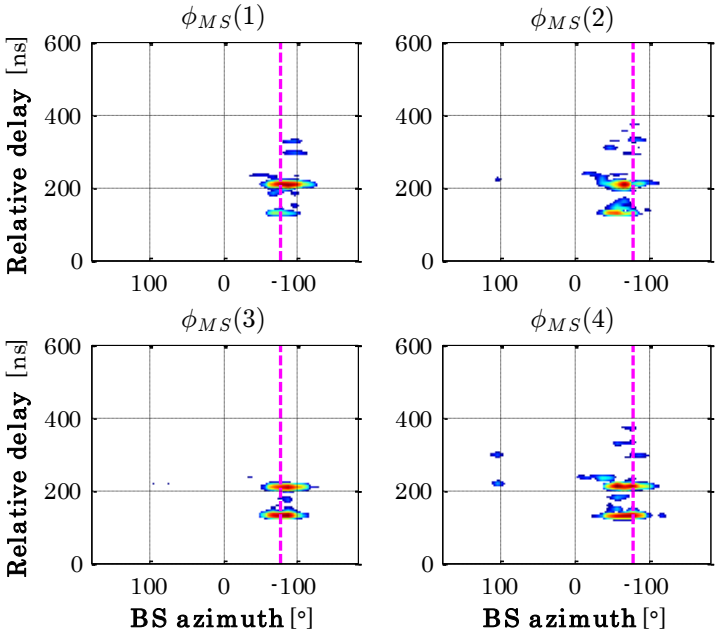
$\phi_{MS}(1)$
$\phi_{MS}(2)$
$\phi_{MS}(3)$
$\phi_{MS}(4)$
Relative delay [ns]
BS azimuth [°]

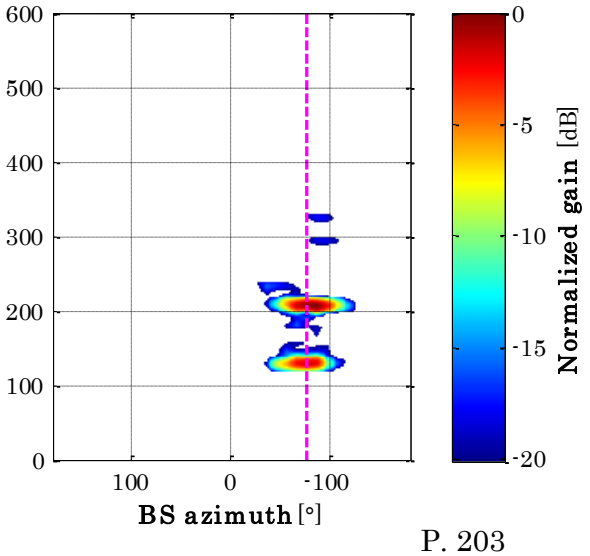
BS azimuth [°]
Normalized gain [dB]


60 GHz
TxA
A11

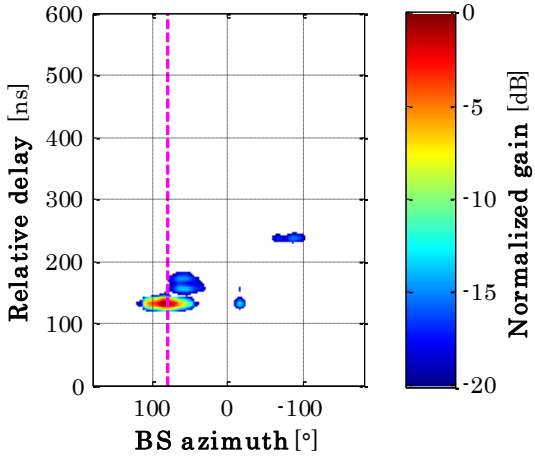
Relative delay [ns]
BS azimuth [°]
Normalized gain [dB]

S2

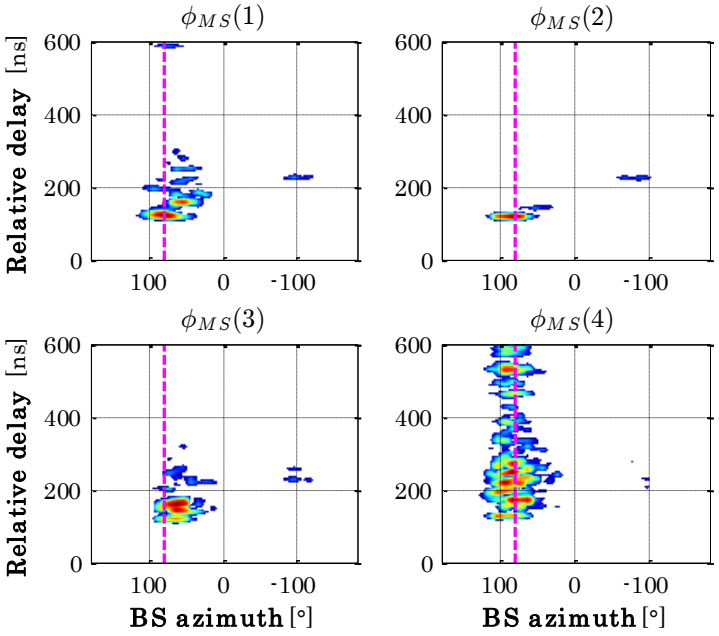
$\phi_{MS}(1)$
$\phi_{MS}(2)$
$\phi_{MS}(3)$
$\phi_{MS}(4)$
Relative delay [ns]
BS azimuth [°]

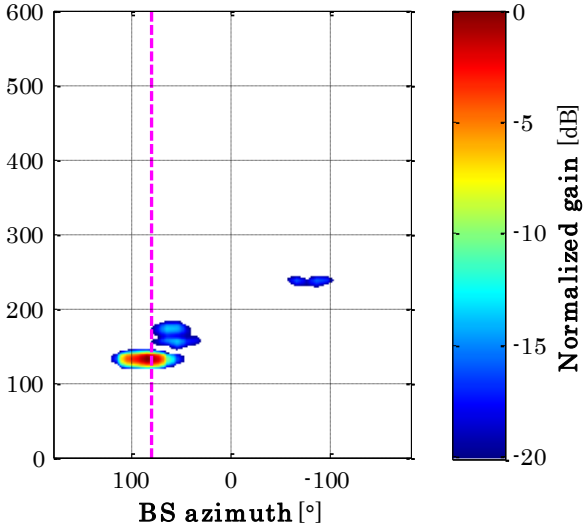
Relative delay [ns]
BS azimuth [°]
Normalized gain [dB]

S1

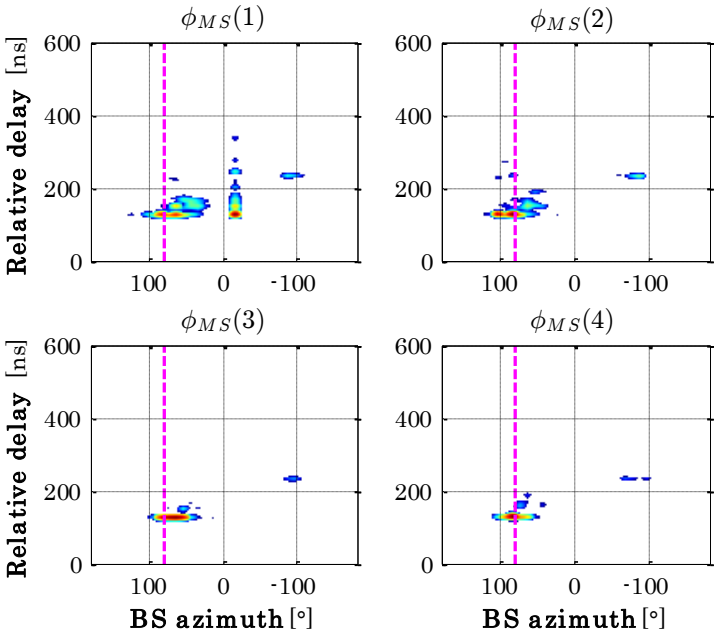
$\phi_{MS}(1)$
$\phi_{MS}(2)$
$\phi_{MS}(3)$
$\phi_{MS}(4)$
Relative delay [ns]
BS azimuth [°]

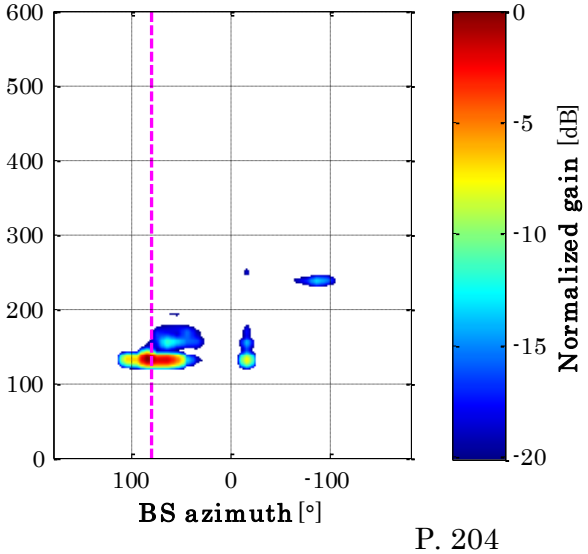
Relative delay [ns]
BS azimuth [°]
Normalized gain [dB]

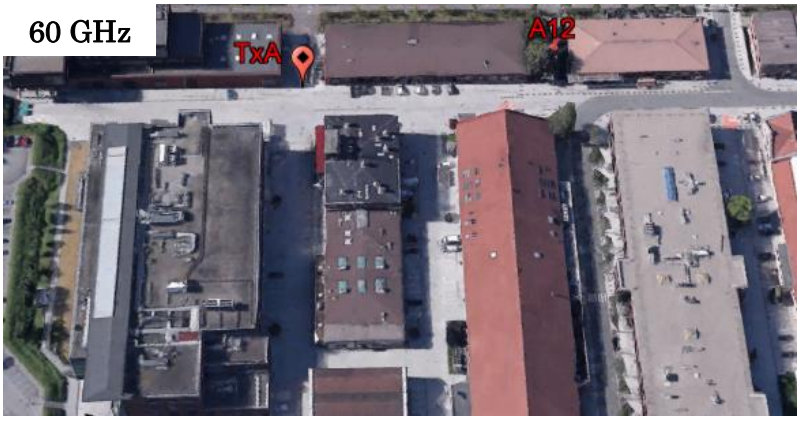
60 GHz
TxA
A12

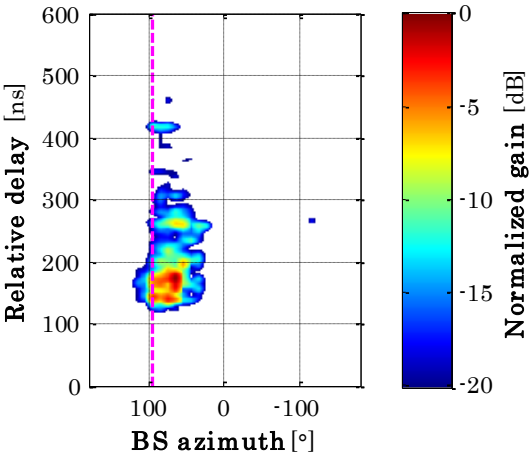
Relative delay [ns]
BS azimuth [°]
Normalized gain [dB]

S2

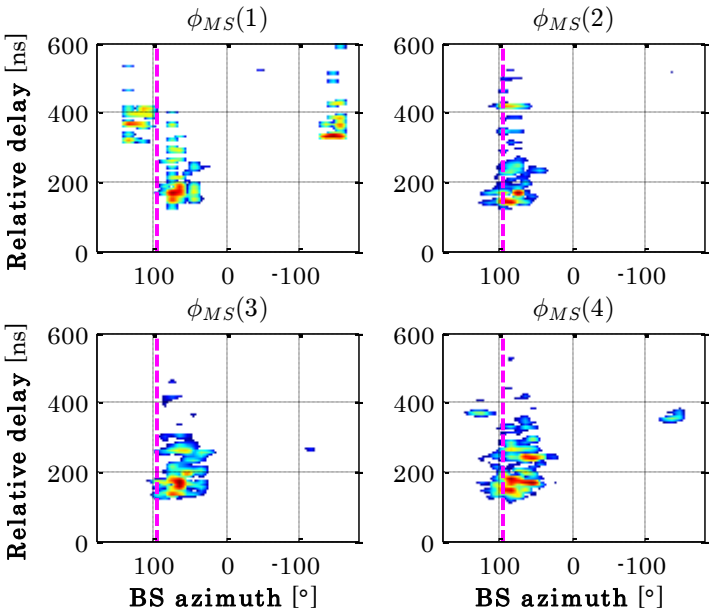
$\phi_{MS}(1)$
$\phi_{MS}(2)$
$\phi_{MS}(3)$
$\phi_{MS}(4)$
Relative delay [ns]
BS azimuth [°]

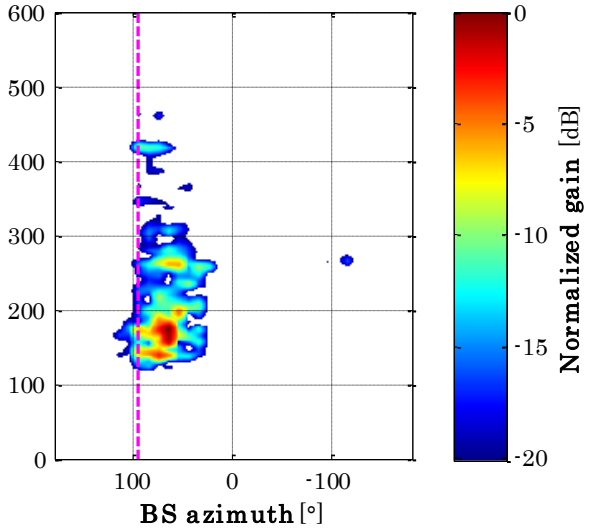
Relative delay [ns]
BS azimuth [°]
Normalized gain [dB]

S1

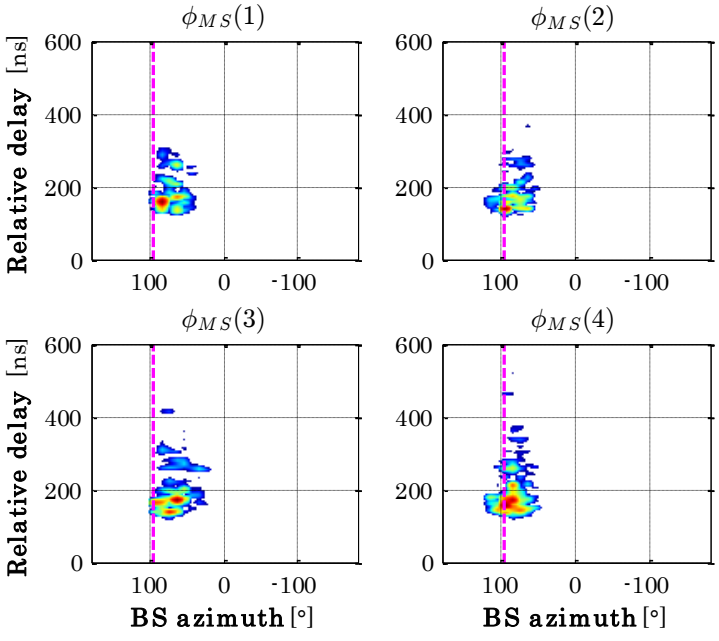
$\phi_{MS}(1)$
$\phi_{MS}(2)$
$\phi_{MS}(3)$
$\phi_{MS}(4)$
Relative delay [ns]
BS azimuth [°]

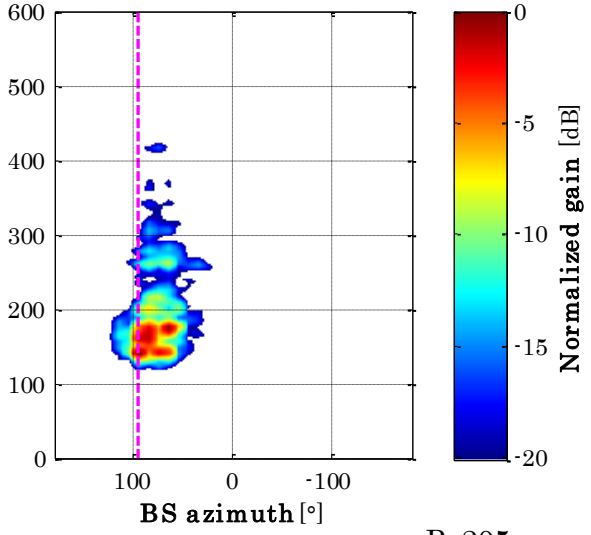
Relative delay [ns]
BS azimuth [°]
Normalized gain [dB]


60 GHz
TxA
A13

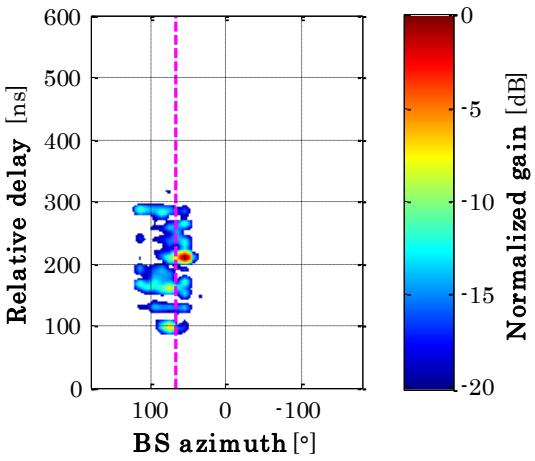
Relative delay [ns]
BS azimuth [°]
Normalized gain [dB]

S2

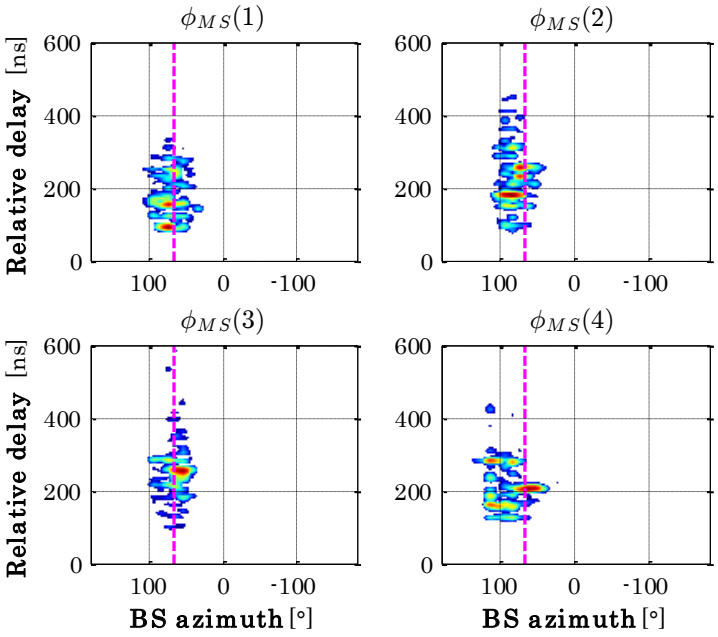
$\phi_{MS}(1)$
$\phi_{MS}(2)$
$\phi_{MS}(3)$
$\phi_{MS}(4)$
Relative delay [ns]
BS azimuth [°]

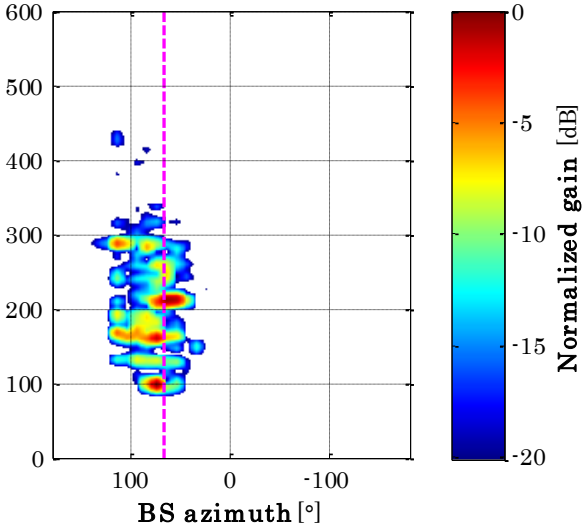
BS azimuth [°]
Normalized gain [dB]

S1

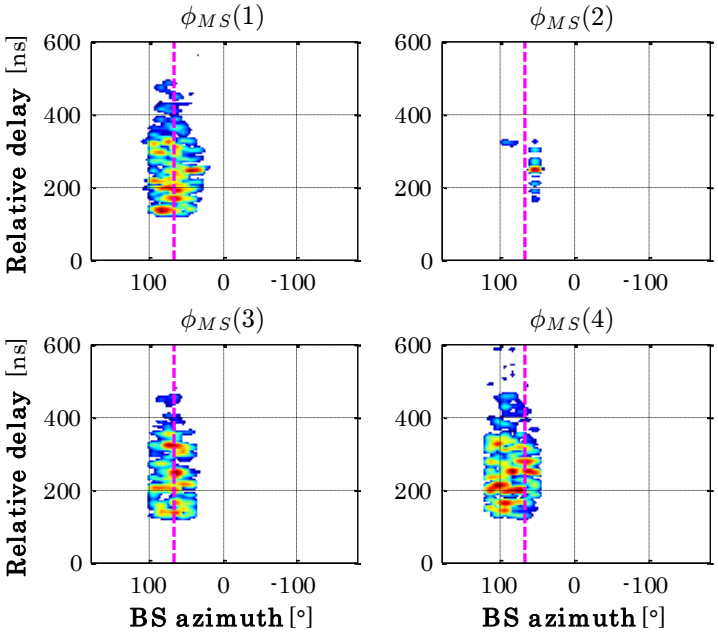
$\phi_{MS}(1)$
$\phi_{MS}(2)$
$\phi_{MS}(3)$
$\phi_{MS}(4)$
Relative delay [ns]
BS azimuth [°]

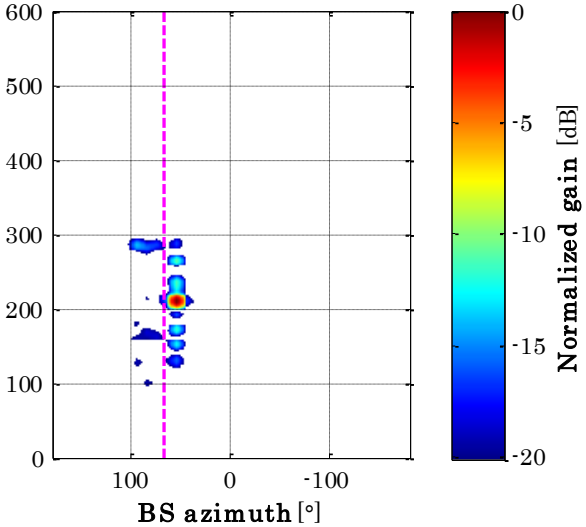
BS azimuth [°]
Normalized gain [dB]

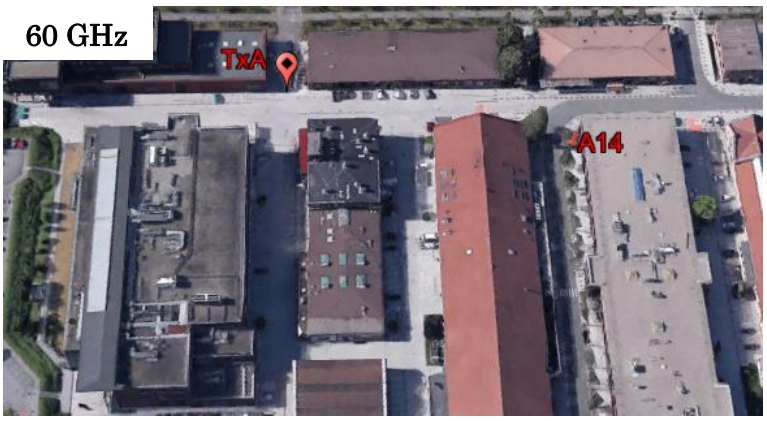
60 GHz
TxA
A14

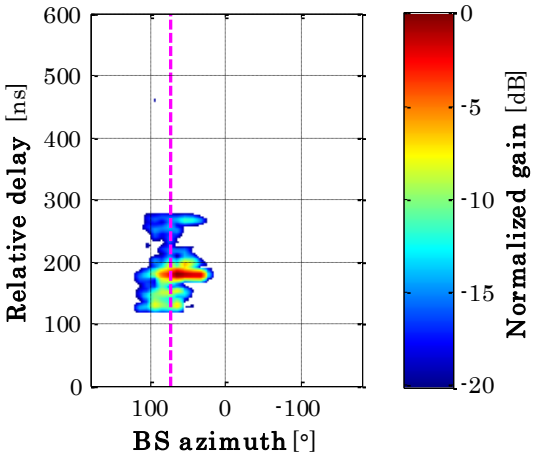
Relative delay [ns]
BS azimuth [°]
Normalized gain [dB]

S2

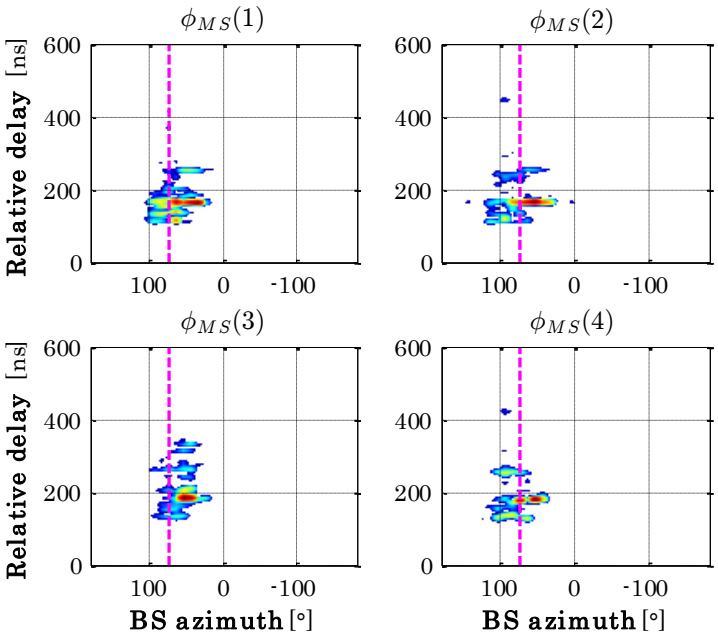
$\phi_{MS}(1)$
$\phi_{MS}(2)$
$\phi_{MS}(3)$
$\phi_{MS}(4)$
Relative delay [ns]
BS azimuth [°]

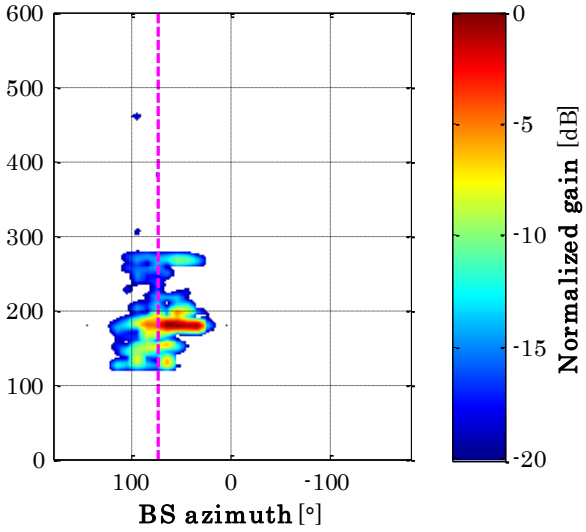
Relative delay [ns]
BS azimuth [°]
Normalized gain [dB]

S1

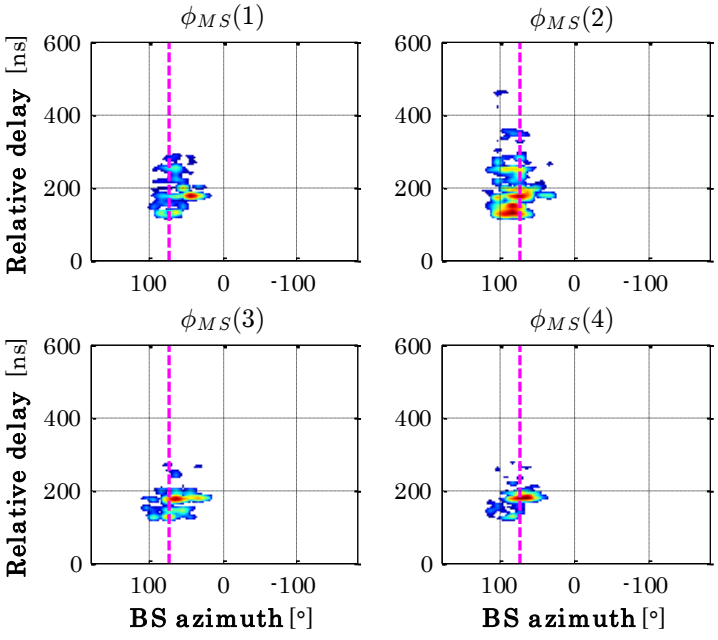
$\phi_{MS}(1)$
$\phi_{MS}(2)$
$\phi_{MS}(3)$
$\phi_{MS}(4)$
Relative delay [ns]
BS azimuth [°]

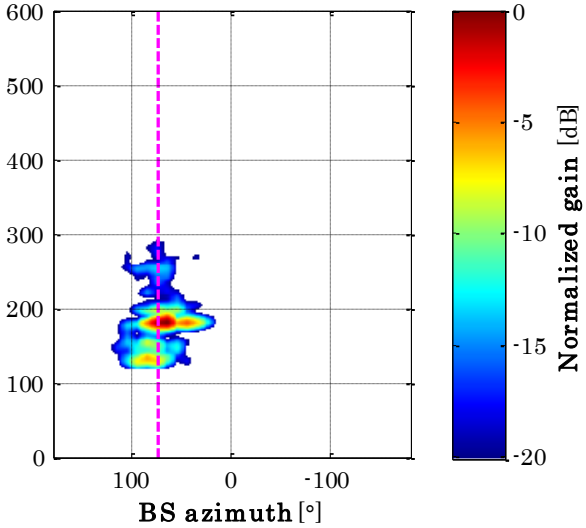
Relative delay [ns]
BS azimuth [°]
Normalized gain [dB]


60 GHz
TxA
A16

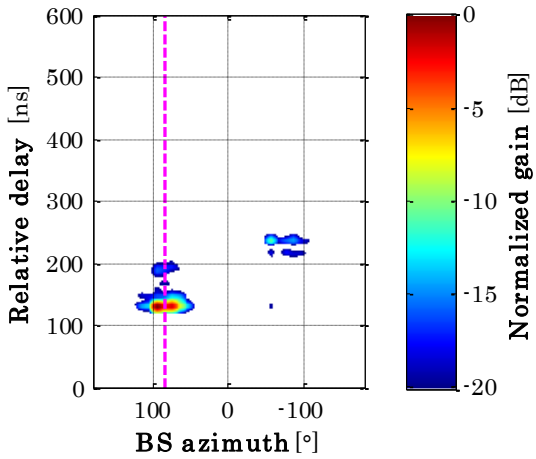
Relative delay [ns]
BS azimuth [°]
Normalized gain [dB]

S2

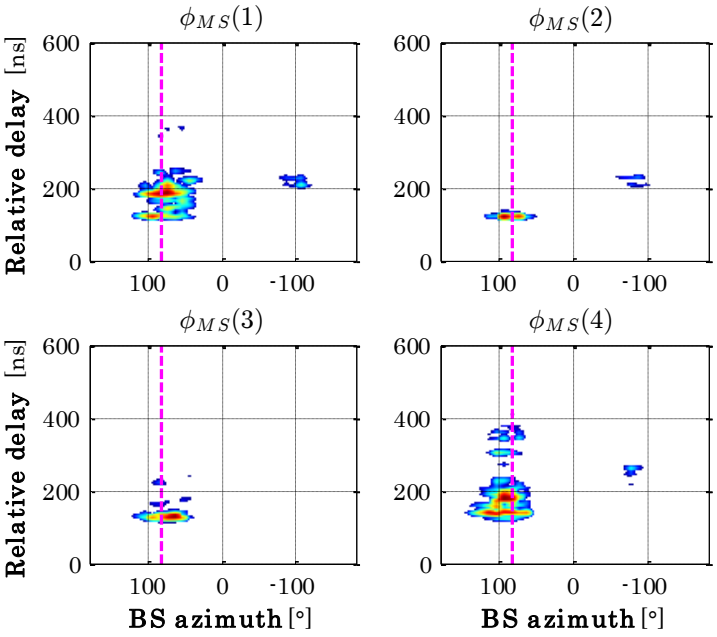
$\phi_{MS}(1)$
$\phi_{MS}(2)$
$\phi_{MS}(3)$
$\phi_{MS}(4)$
Relative delay [ns]
BS azimuth [°]

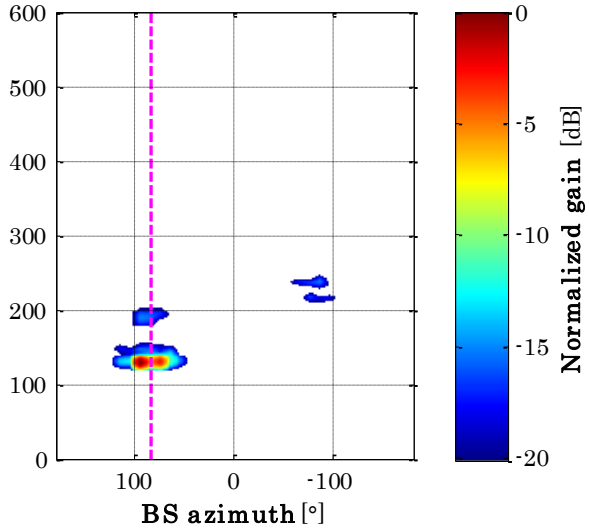
Relative delay [ns]
BS azimuth [°]
Normalized gain [dB]

S1

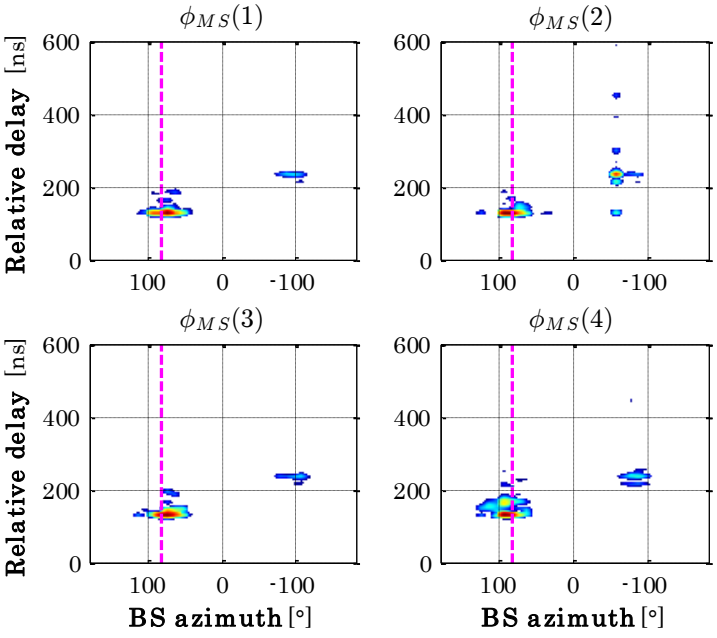
$\phi_{MS}(1)$
$\phi_{MS}(2)$
$\phi_{MS}(3)$
$\phi_{MS}(4)$
Relative delay [ns]
BS azimuth [°]

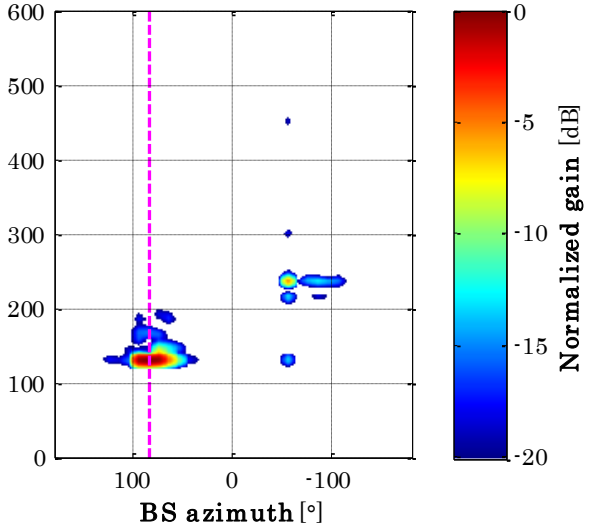
Relative delay [ns]
BS azimuth [°]
Normalized gain [dB]

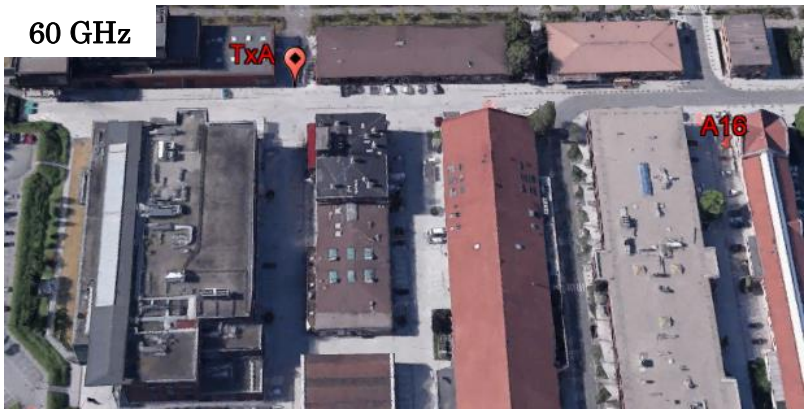
60 GHz
TxA
A16

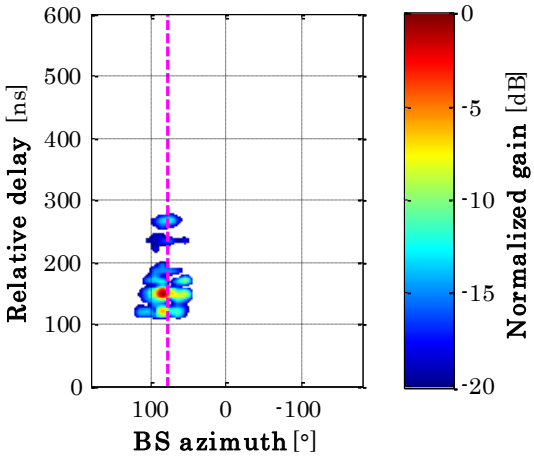
Relative delay [ns]
BS azimuth [°]
Normalized gain [dB]

S2

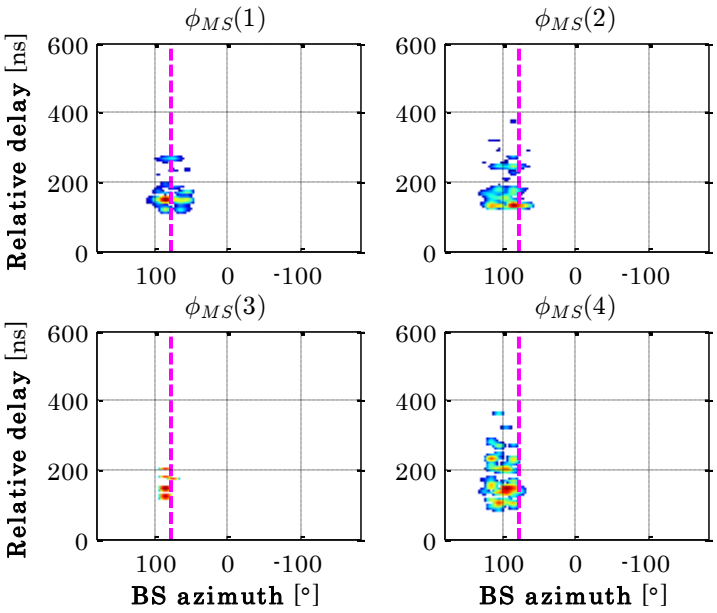
$\phi_{MS}(1)$
$\phi_{MS}(2)$
$\phi_{MS}(3)$
$\phi_{MS}(4)$
Relative delay [ns]
BS azimuth [°]

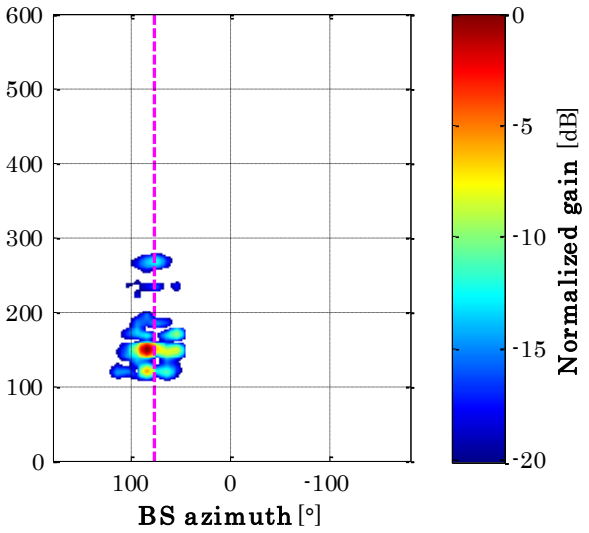
BS azimuth [°]
Normalized gain [dB]

S1

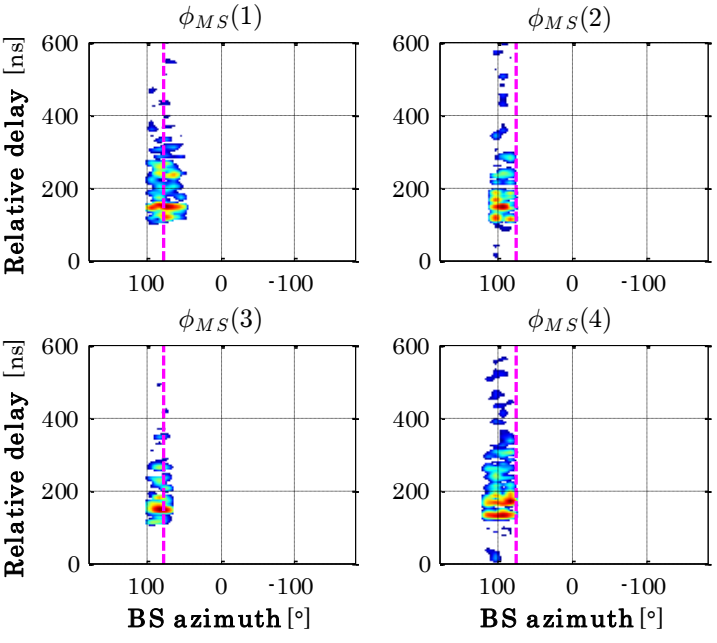
$\phi_{MS}(1)$
$\phi_{MS}(2)$
$\phi_{MS}(3)$
$\phi_{MS}(4)$
Relative delay [ns]
BS azimuth [°]

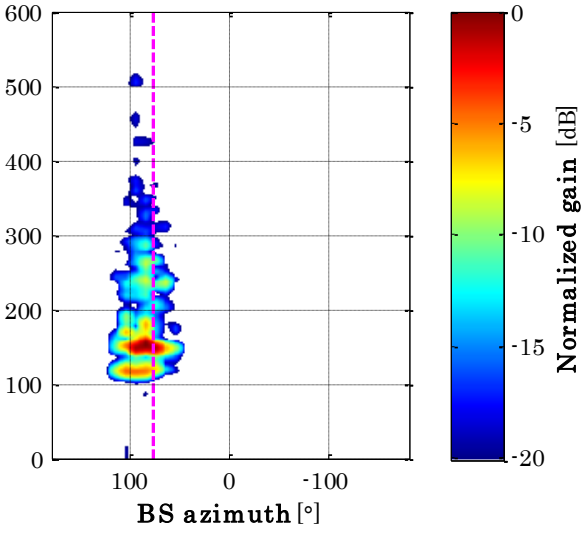
BS azimuth [°]
Normalized gain [dB]


60 GHz
TxB
B1

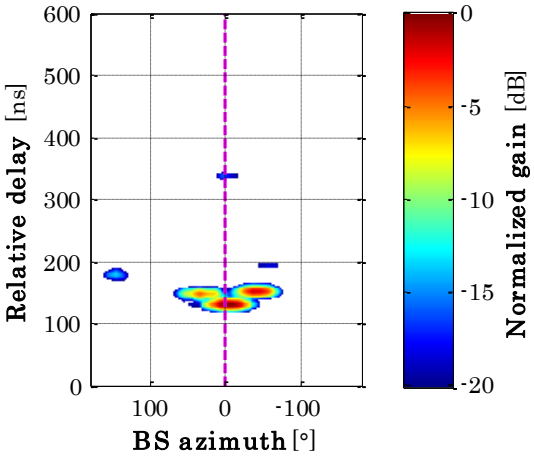
Relative delay [ns]
BS azimuth [°]
Normalized gain [dB]

S2

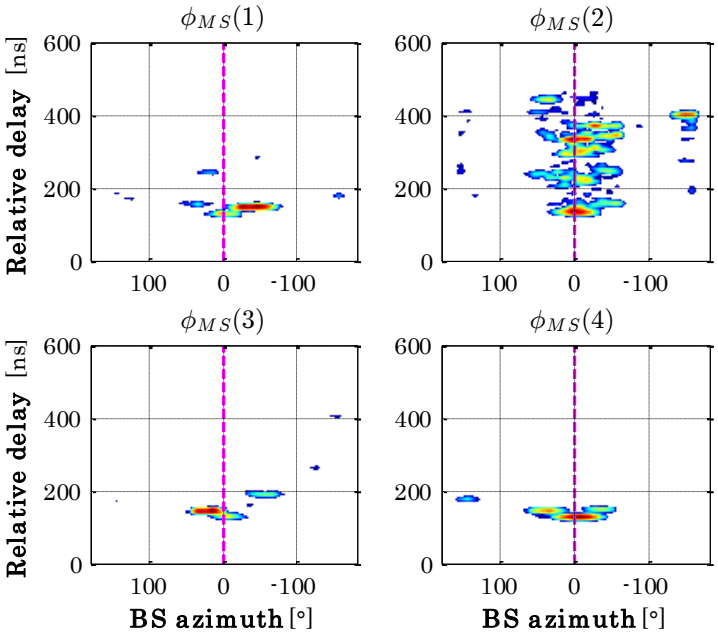
$\phi_{MS}(1)$
$\phi_{MS}(2)$
$\phi_{MS}(3)$
$\phi_{MS}(4)$
Relative delay [ns]
BS azimuth [°]

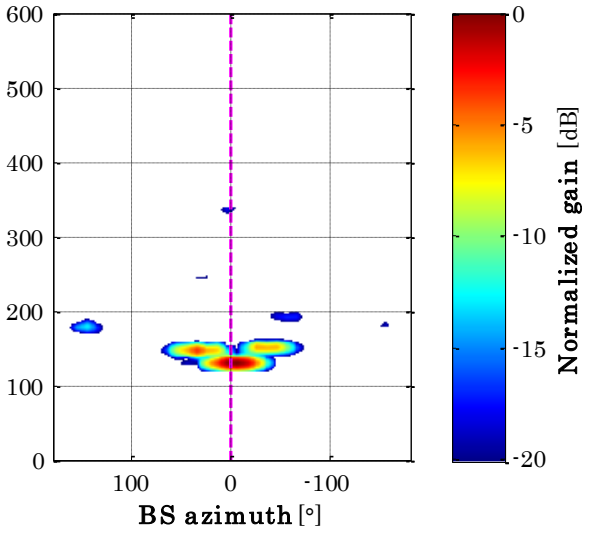
Relative delay [ns]
BS azimuth [°]
Normalized gain [dB]

S1

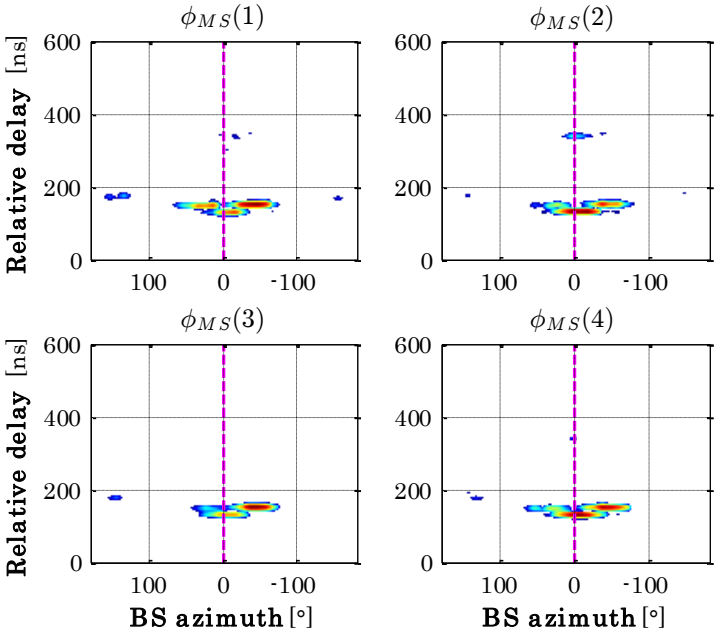
$\phi_{MS}(1)$
$\phi_{MS}(2)$
$\phi_{MS}(3)$
$\phi_{MS}(4)$
Relative delay [ns]
BS azimuth [°]

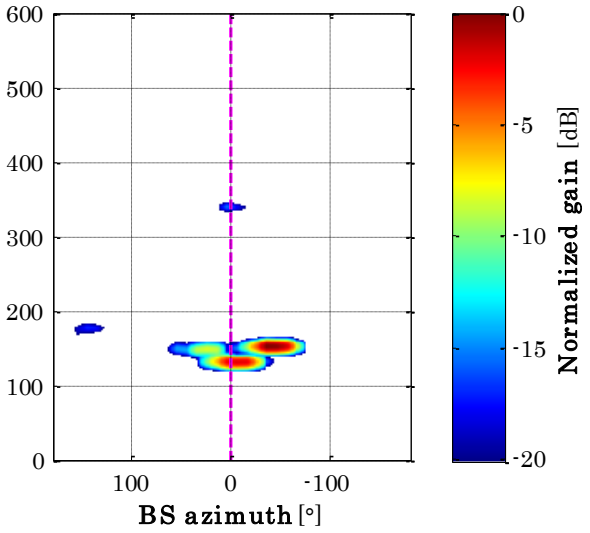
Relative delay [ns]
BS azimuth [°]
Normalized gain [dB]


60 GHz
TxB
B2

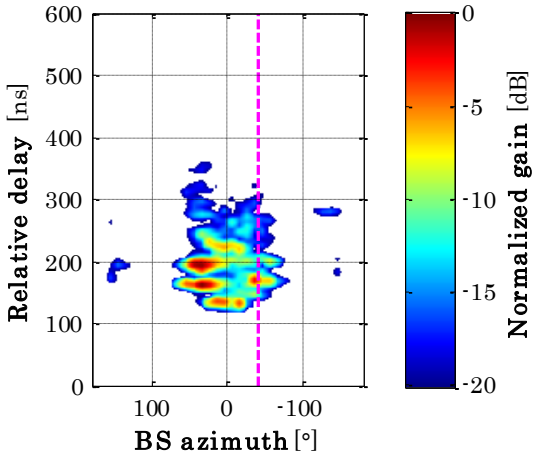
Relative delay [ns]
BS azimuth [°]
Normalized gain [dB]

S2

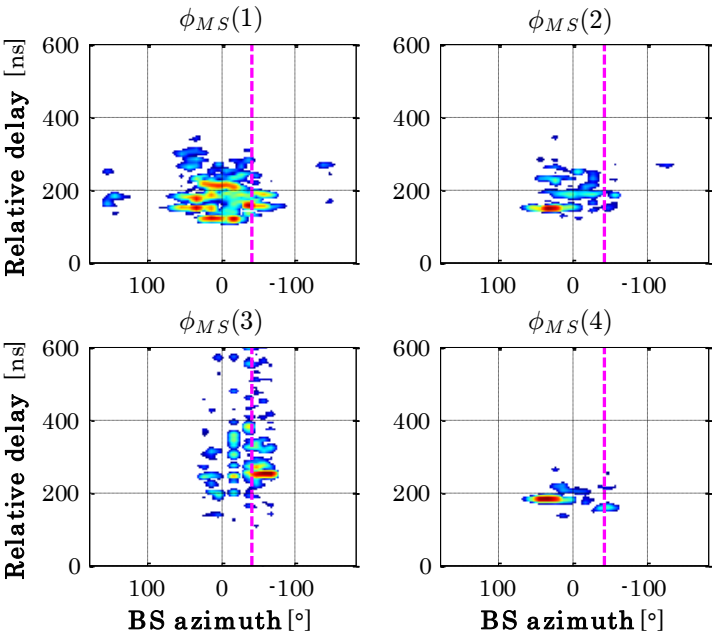
$\phi_{MS}(1)$
$\phi_{MS}(2)$
$\phi_{MS}(3)$
$\phi_{MS}(4)$
Relative delay [ns]
BS azimuth [°]

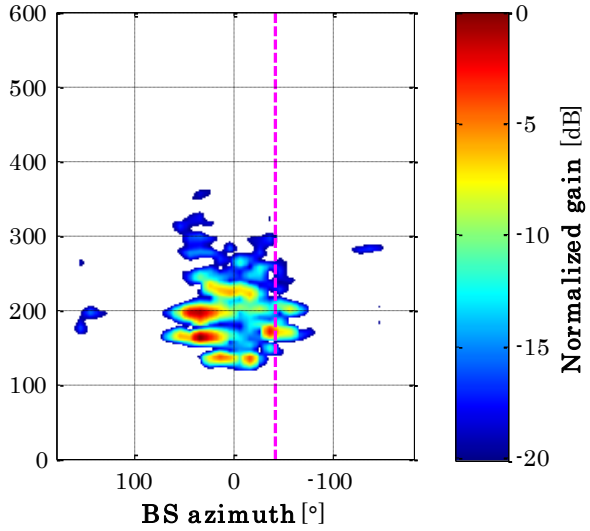
Relative delay [ns]
BS azimuth [°]
Normalized gain [dB]

S1

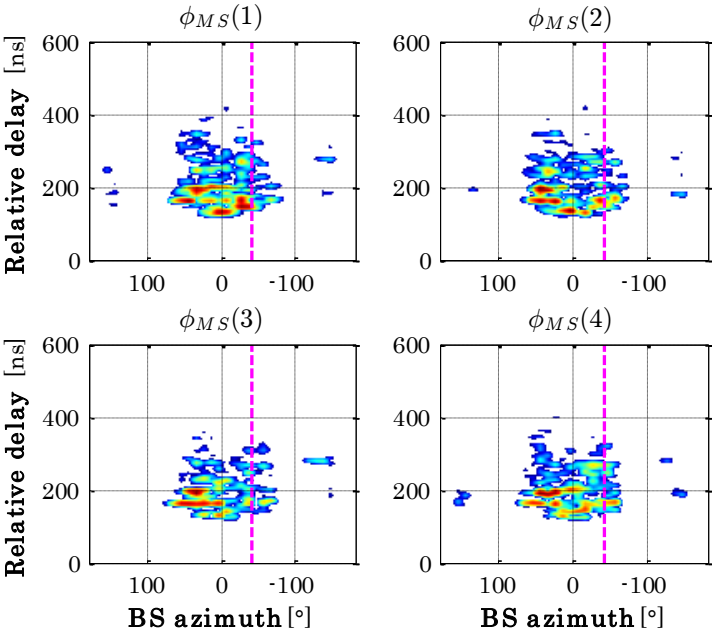
$\phi_{MS}(1)$
$\phi_{MS}(2)$
$\phi_{MS}(3)$
$\phi_{MS}(4)$
Relative delay [ns]
BS azimuth [°]

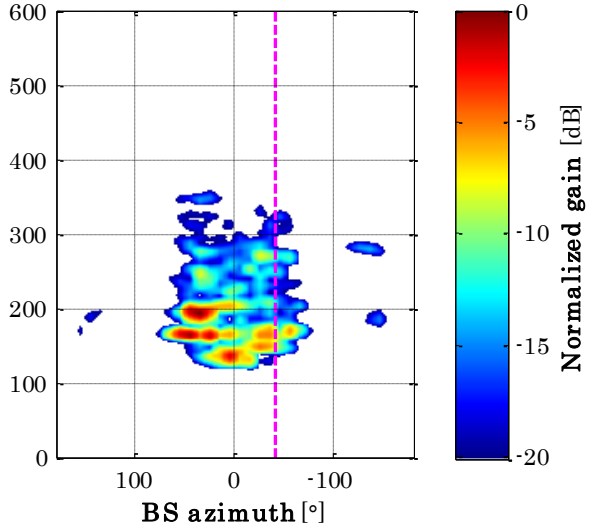
Relative delay [ns]
BS azimuth [°]
Normalized gain [dB]

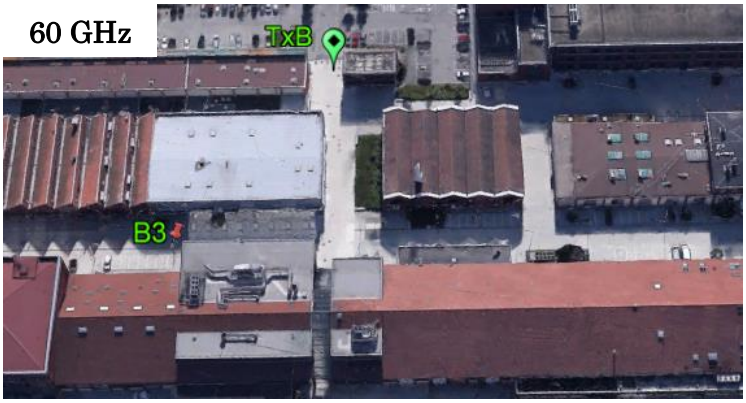
60 GHz
TxB
B3

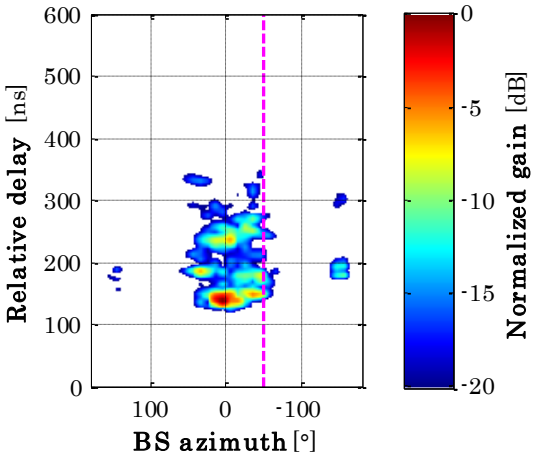
Relative delay [ns]
BS azimuth [°]
Normalized gain [dB]

S2

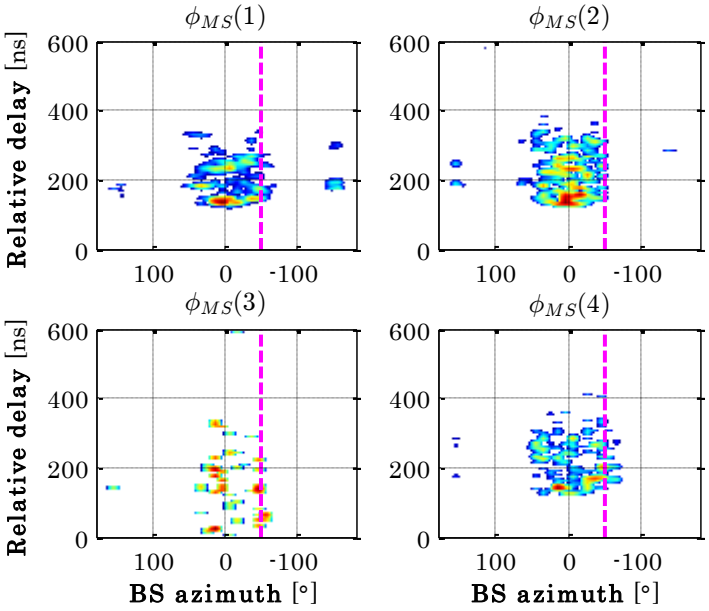
$\phi_{MS}(1)$
$\phi_{MS}(2)$
$\phi_{MS}(3)$
$\phi_{MS}(4)$
Relative delay [ns]
BS azimuth [°]

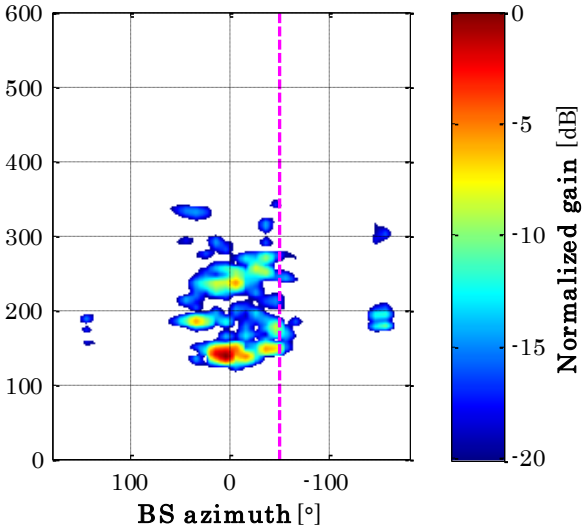
BS azimuth [°]
Normalized gain [dB]

S1

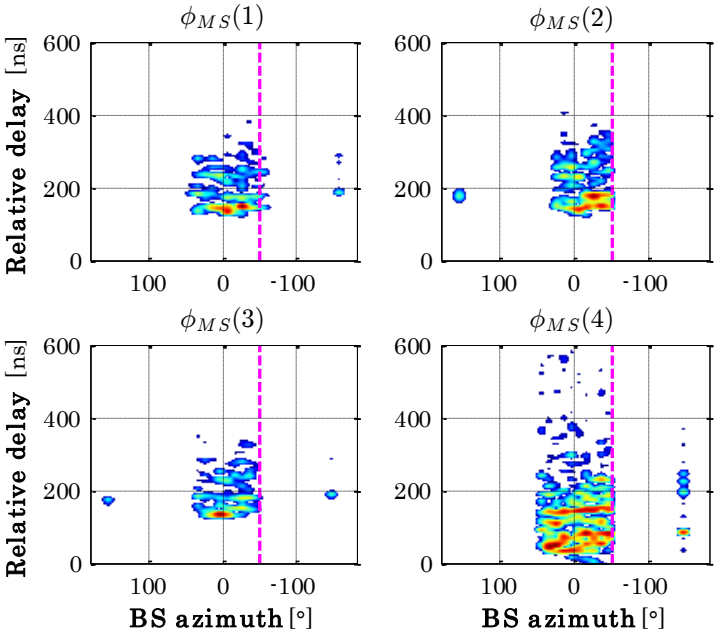
$\phi_{MS}(1)$
$\phi_{MS}(2)$
$\phi_{MS}(3)$
$\phi_{MS}(4)$
Relative delay [ns]
BS azimuth [°]

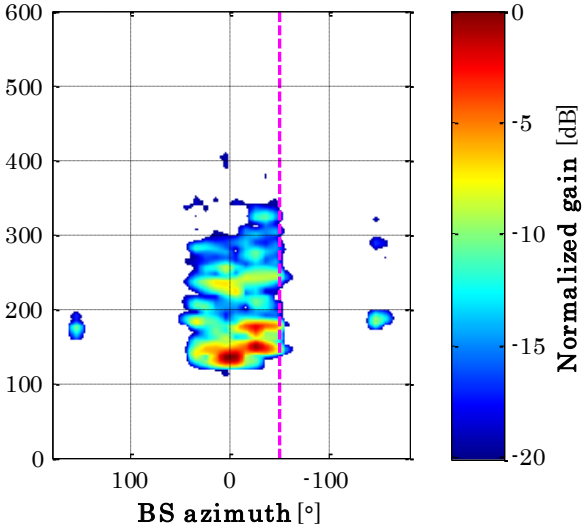
BS azimuth [°]
Normalized gain [dB]


60 GHz
TxB
B4

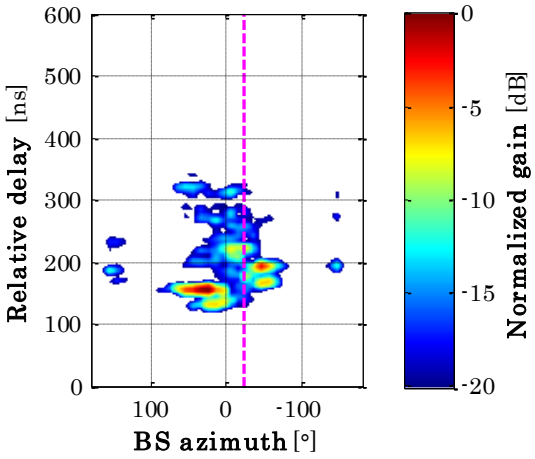
Relative delay [ns]
BS azimuth [°]
Normalized gain [dB]

S2

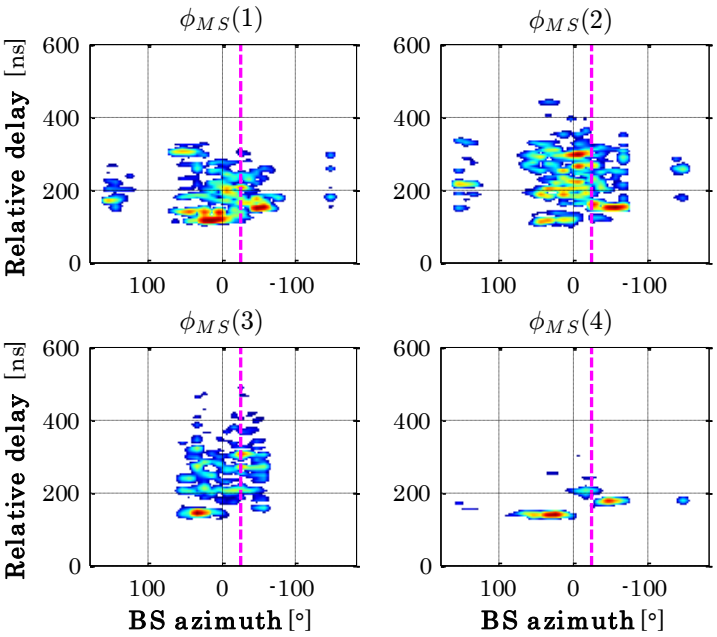
$\phi_{MS}(1)$
$\phi_{MS}(2)$
$\phi_{MS}(3)$
$\phi_{MS}(4)$
Relative delay [ns]
BS azimuth [°]

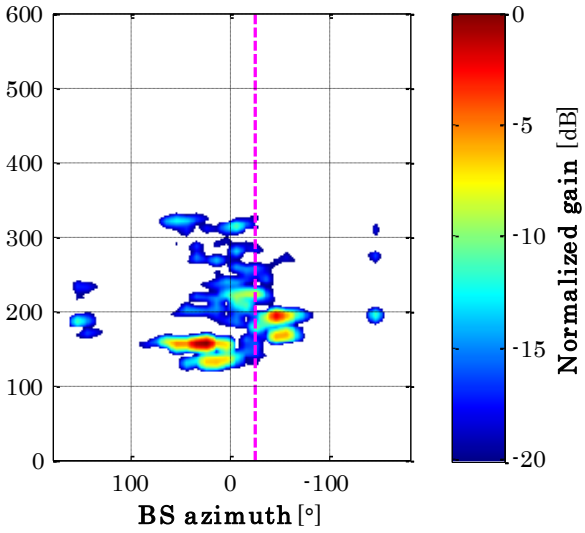
Relative delay [ns]
BS azimuth [°]
Normalized gain [dB]

S1

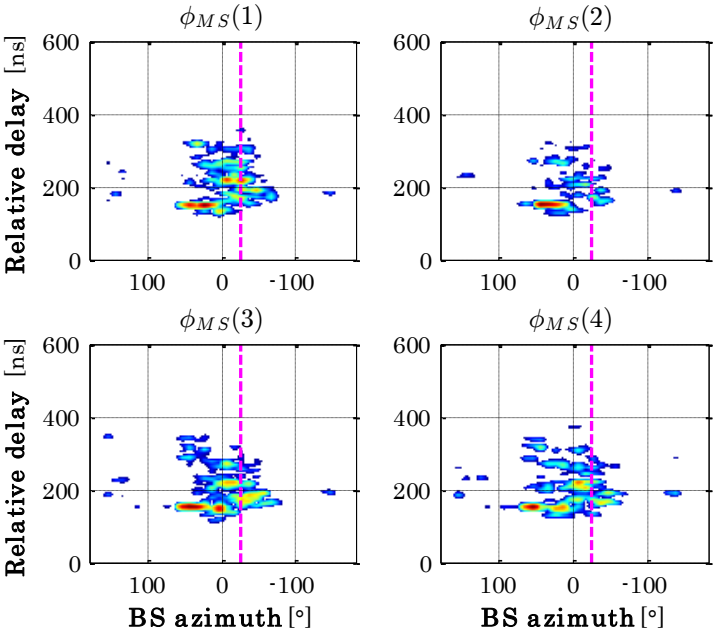
$\phi_{MS}(1)$
$\phi_{MS}(2)$
$\phi_{MS}(3)$
$\phi_{MS}(4)$
Relative delay [ns]
BS azimuth [°]

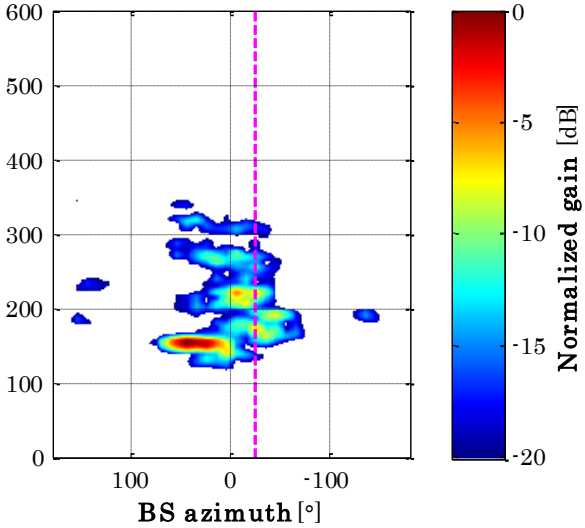
Relative delay [ns]
BS azimuth [°]
Normalized gain [dB]


60 GHz
TxB
B5

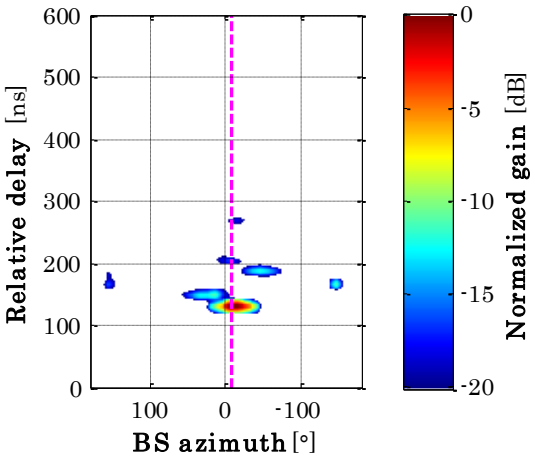
Relative delay [ns]
BS azimuth [°]
Normalized gain [dB]

S2

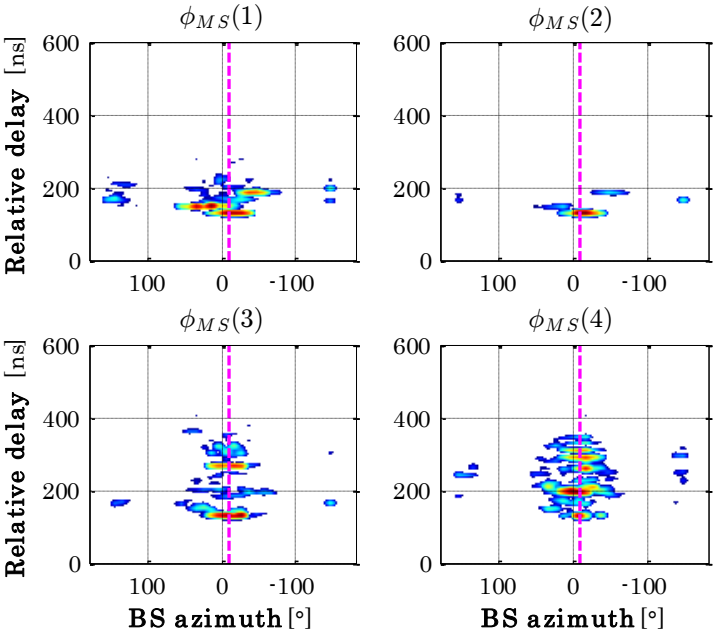
$\phi_{MS}(1)$
$\phi_{MS}(2)$
$\phi_{MS}(3)$
$\phi_{MS}(4)$
Relative delay [ns]
BS azimuth [°]

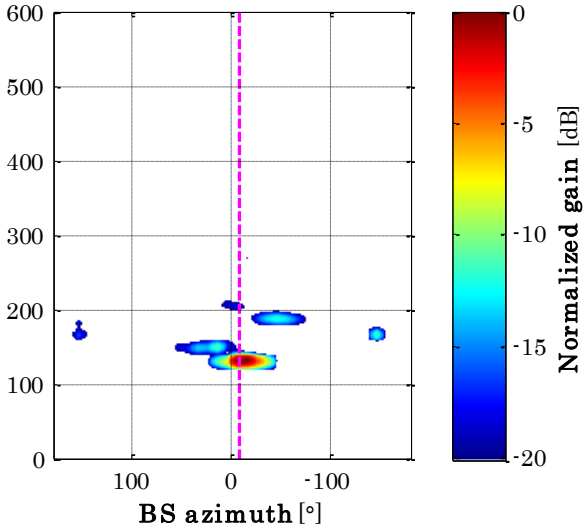
Relative delay [ns]
BS azimuth [°]
Normalized gain [dB]

S1

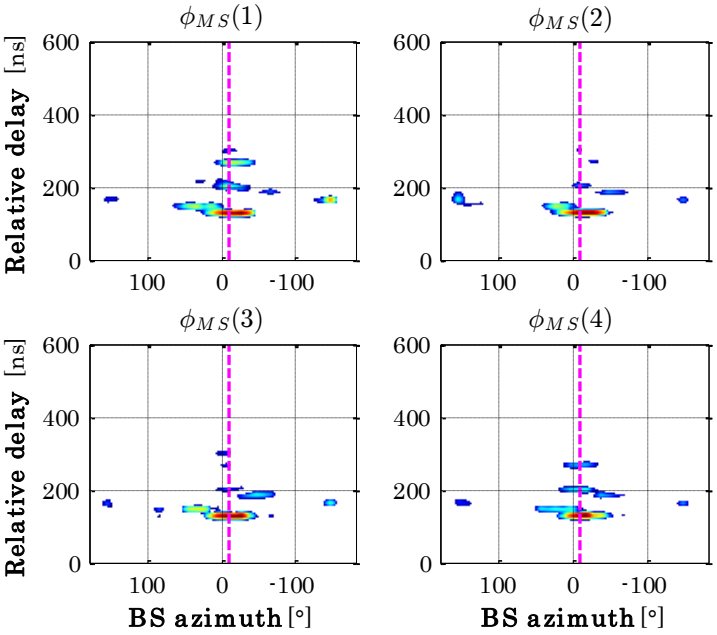
$\phi_{MS}(1)$
$\phi_{MS}(2)$
$\phi_{MS}(3)$
$\phi_{MS}(4)$
Relative delay [ns]
BS azimuth [°]

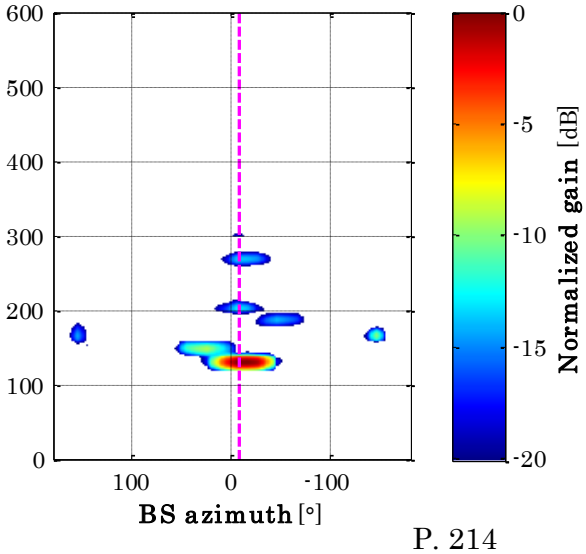
Relative delay [ns]
BS azimuth [°]
Normalized gain [dB]


60 GHz
TxB
B6

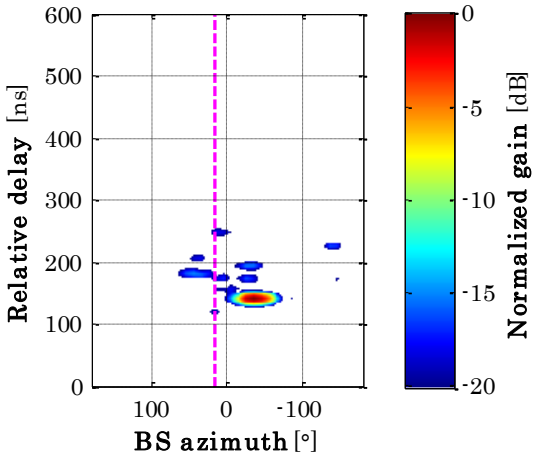
Relative delay [ns]
BS azimuth [°]
Normalized gain [dB]

S2

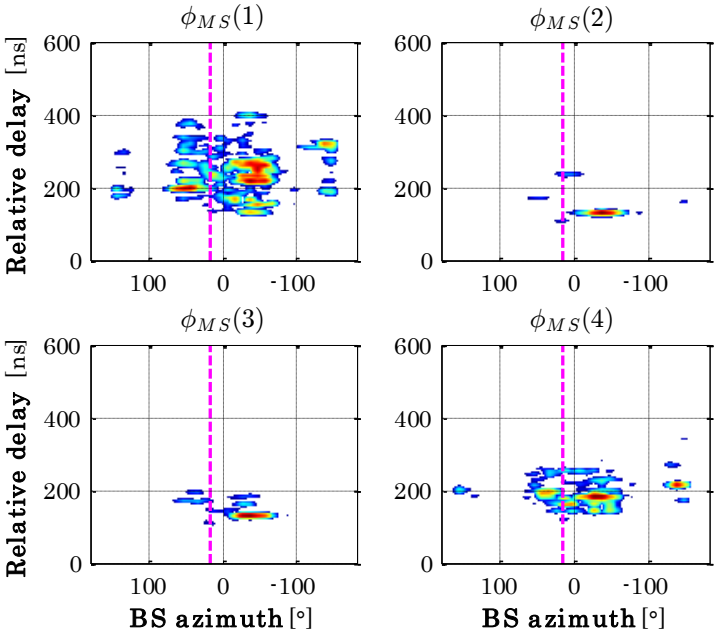
$\phi_{MS}(1)$
$\phi_{MS}(2)$
$\phi_{MS}(3)$
$\phi_{MS}(4)$
Relative delay [ns]
BS azimuth [°]

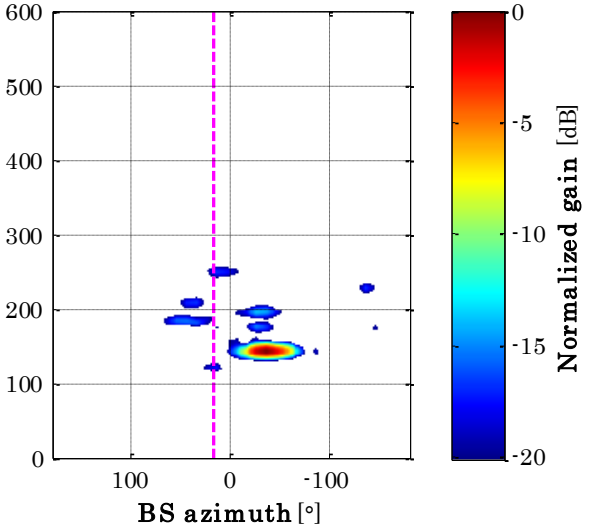
BS azimuth [°]
Normalized gain [dB]

S1

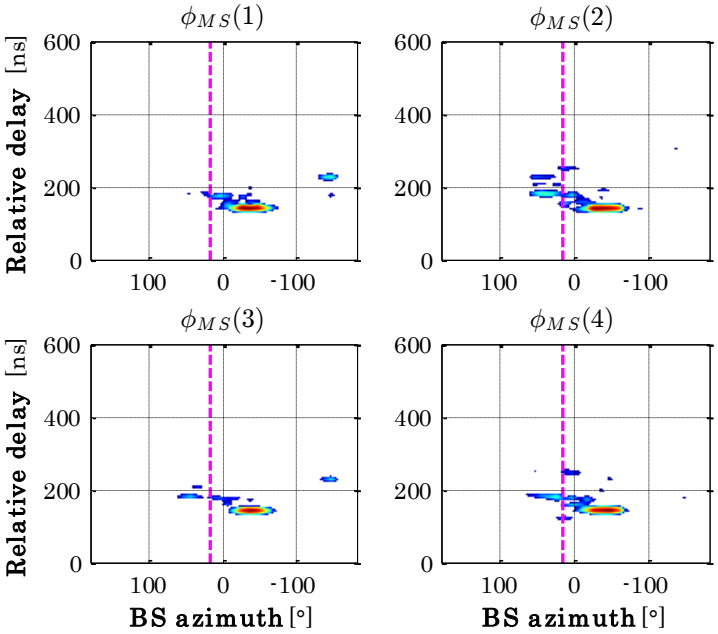
$\phi_{MS}(1)$
$\phi_{MS}(2)$
$\phi_{MS}(3)$
$\phi_{MS}(4)$
Relative delay [ns]
BS azimuth [°]

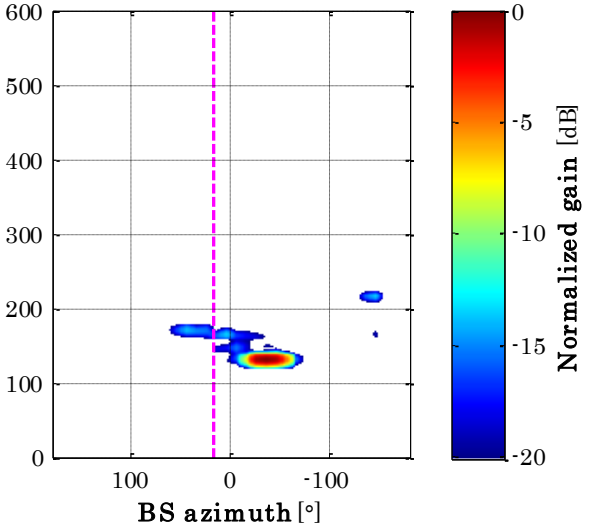
BS azimuth [°]
Normalized gain [dB]


60 GHz
TxB
B7

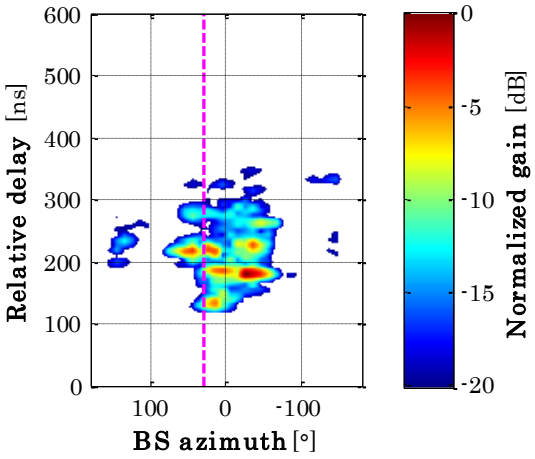
Relative delay [ns]
BS azimuth [°]
Normalized gain [dB]

S2

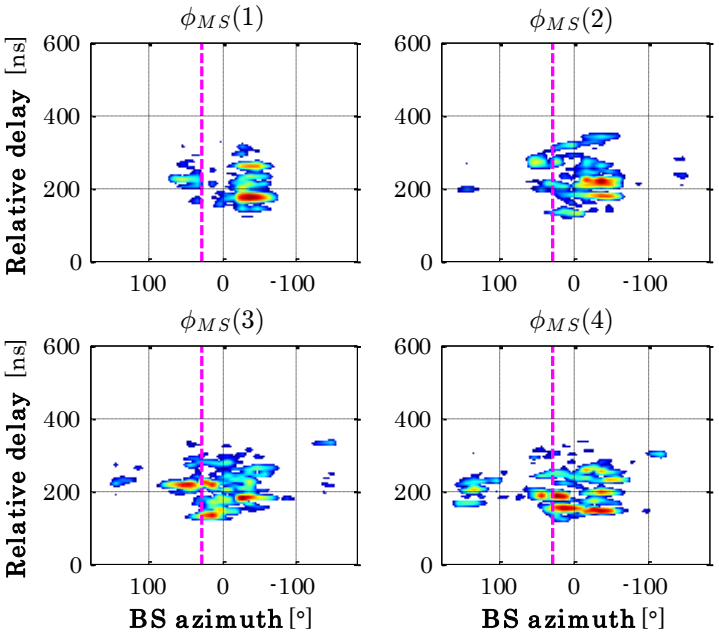
$\phi_{MS}(1)$
$\phi_{MS}(2)$
$\phi_{MS}(3)$
$\phi_{MS}(4)$
Relative delay [ns]
BS azimuth [°]

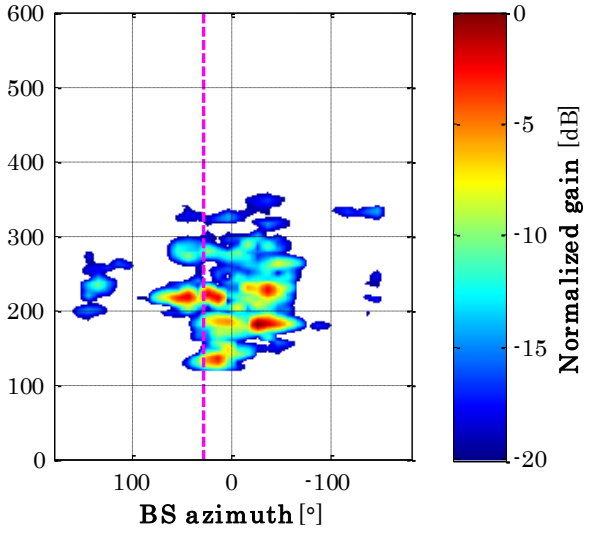
Relative delay [ns]
BS azimuth [°]
Normalized gain [dB]

S1

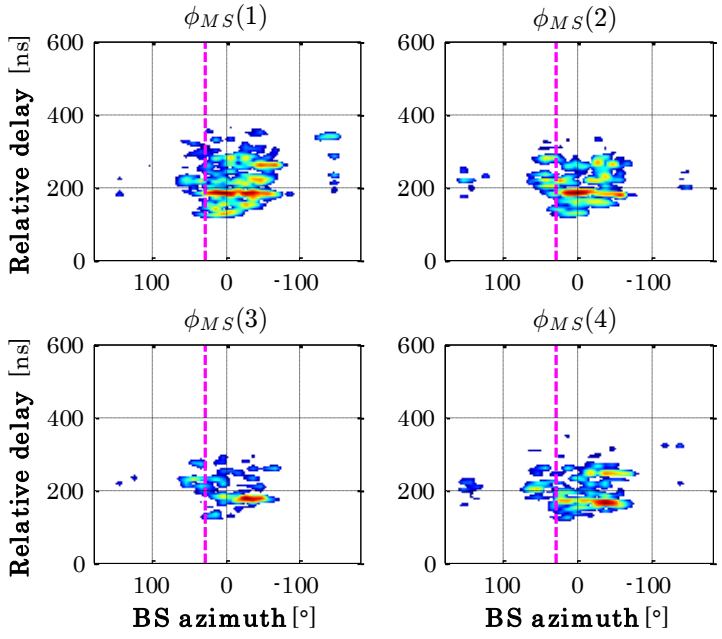
$\phi_{MS}(1)$
$\phi_{MS}(2)$
$\phi_{MS}(3)$
$\phi_{MS}(4)$
Relative delay [ns]
BS azimuth [°]

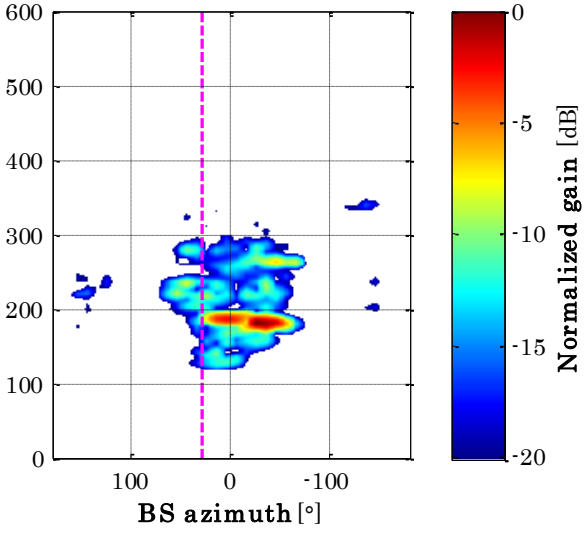
Relative delay [ns]
BS azimuth [°]
Normalized gain [dB]


60 GHz
TxB
B8

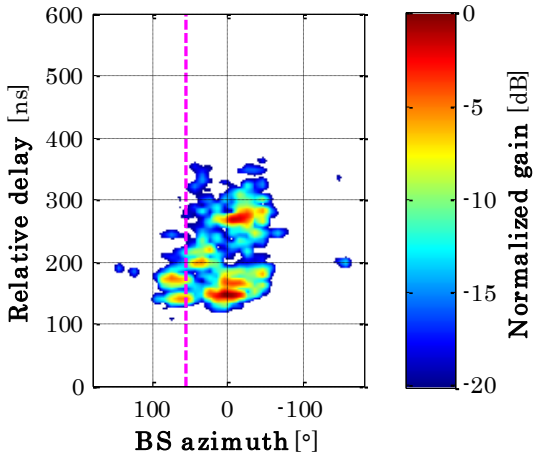
Relative delay [ns]
BS azimuth [°]
Normalized gain [dB]

S2

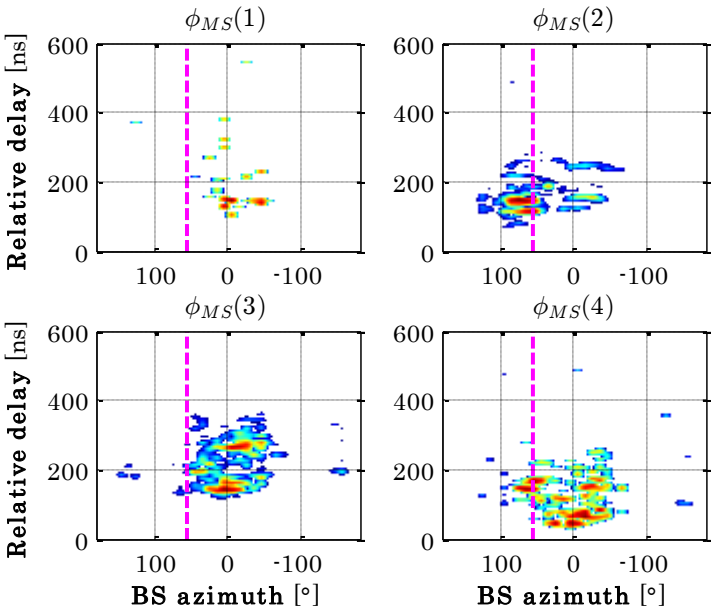
$\phi_{MS}(1)$
$\phi_{MS}(2)$
$\phi_{MS}(3)$
$\phi_{MS}(4)$
Relative delay [ns]
BS azimuth [°]

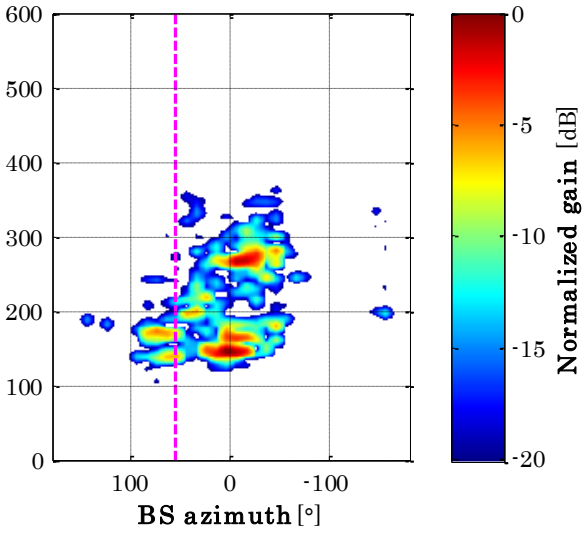
Relative delay [ns]
BS azimuth [°]
Normalized gain [dB]

S1

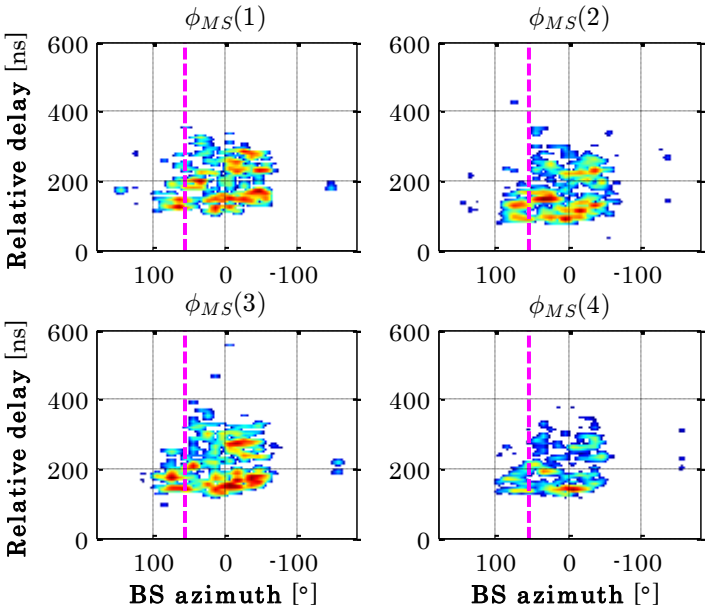
$\phi_{MS}(1)$
$\phi_{MS}(2)$
$\phi_{MS}(3)$
$\phi_{MS}(4)$
Relative delay [ns]
BS azimuth [°]

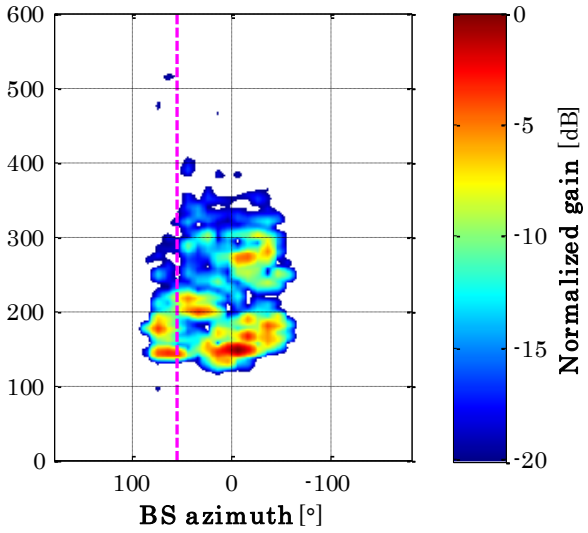
Relative delay [ns]
BS azimuth [°]
Normalized gain [dB]


60 GHz
TxB
B9

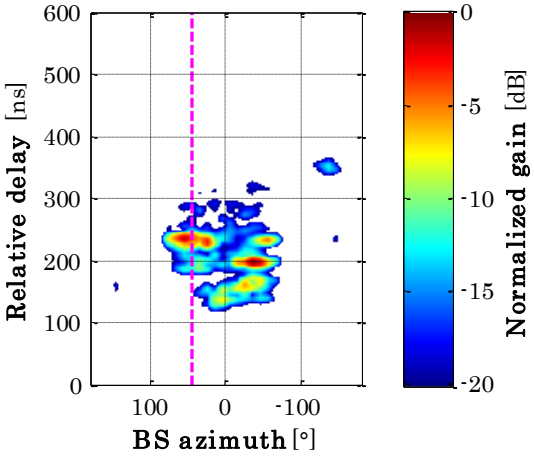
Relative delay [ns]
BS azimuth [°]
Normalized gain [dB]

S2

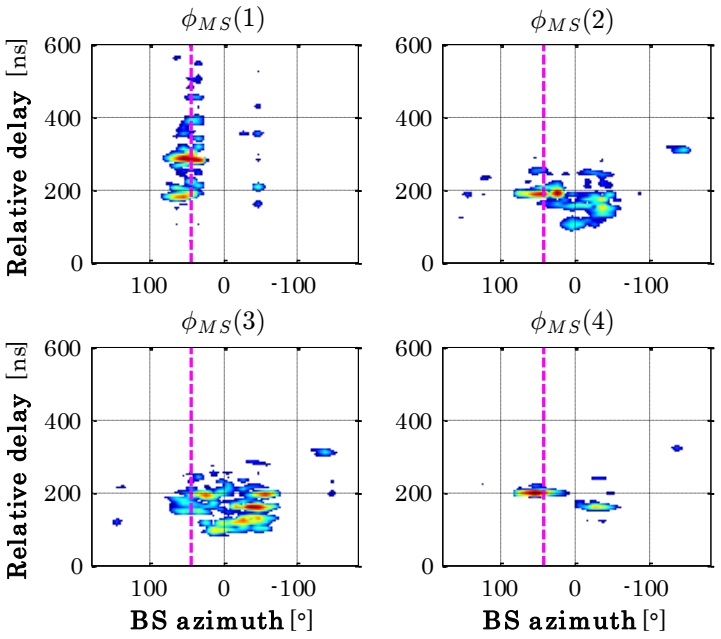
$\phi_{MS}(1)$
$\phi_{MS}(2)$
$\phi_{MS}(3)$
$\phi_{MS}(4)$
Relative delay [ns]
BS azimuth [°]

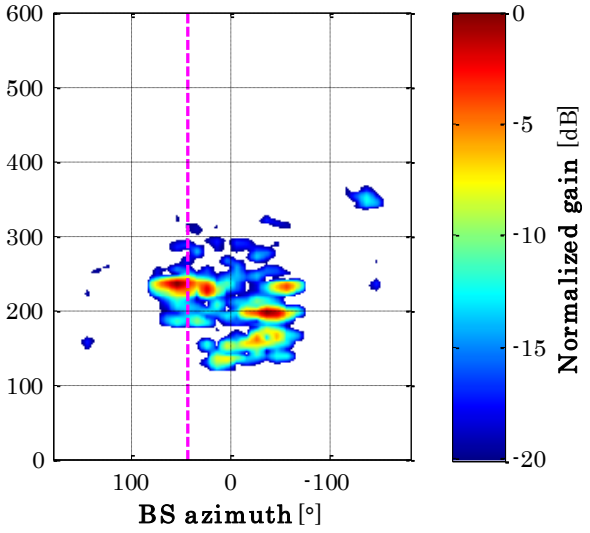
Relative delay [ns]
BS azimuth [°]
Normalized gain [dB]

S1

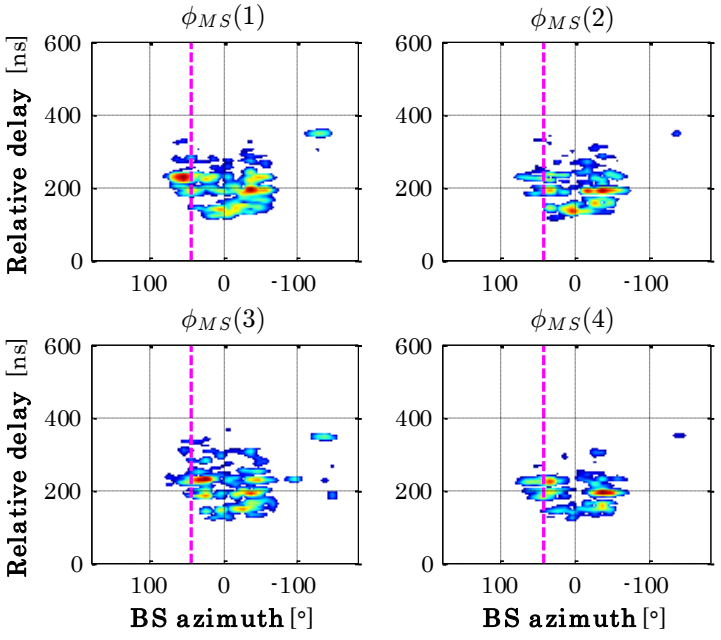
$\phi_{MS}(1)$
$\phi_{MS}(2)$
$\phi_{MS}(3)$
$\phi_{MS}(4)$
Relative delay [ns]
BS azimuth [°]

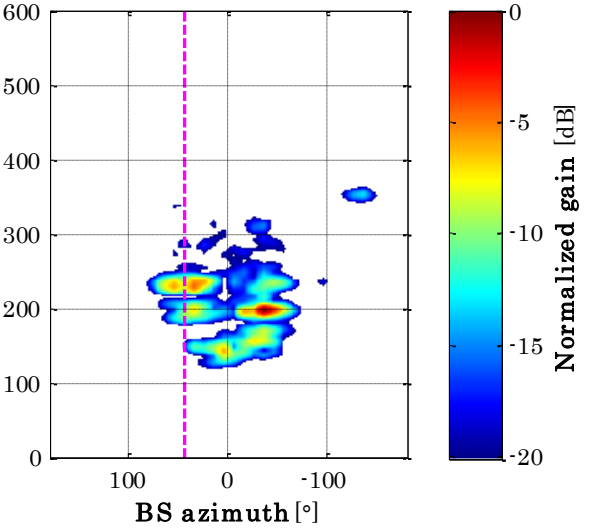
Relative delay [ns]
BS azimuth [°]
Normalized gain [dB]


60 GHz
TxB
B10

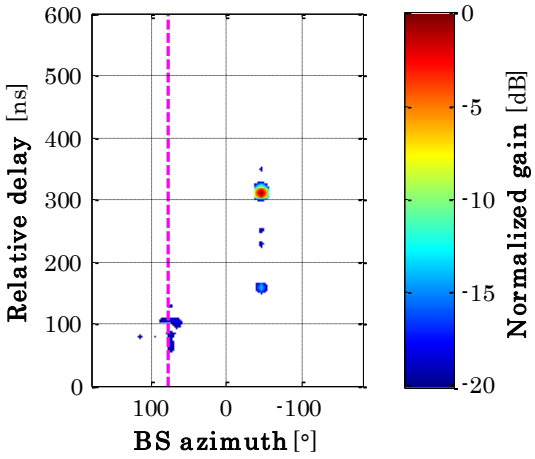
Relative delay [ns]
BS azimuth [°]
Normalized gain [dB]

S2

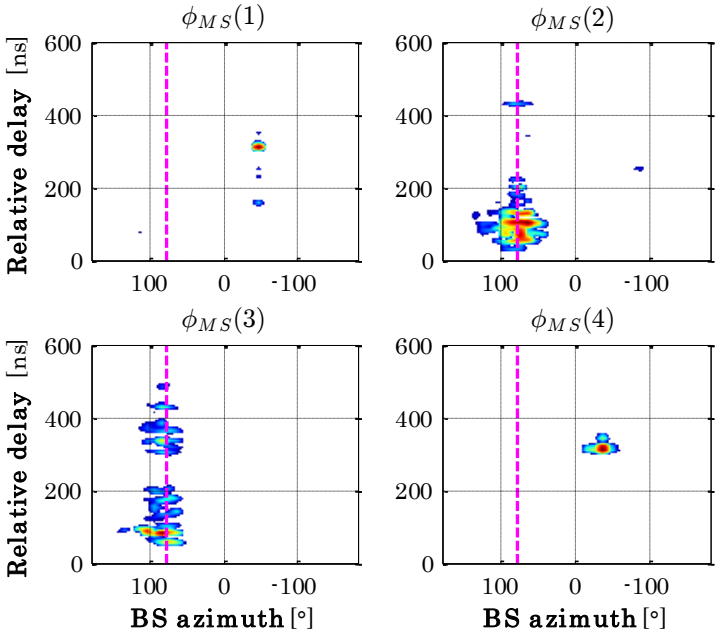
$\phi_{MS}(1)$
$\phi_{MS}(2)$
$\phi_{MS}(3)$
$\phi_{MS}(4)$
Relative delay [ns]
BS azimuth [°]

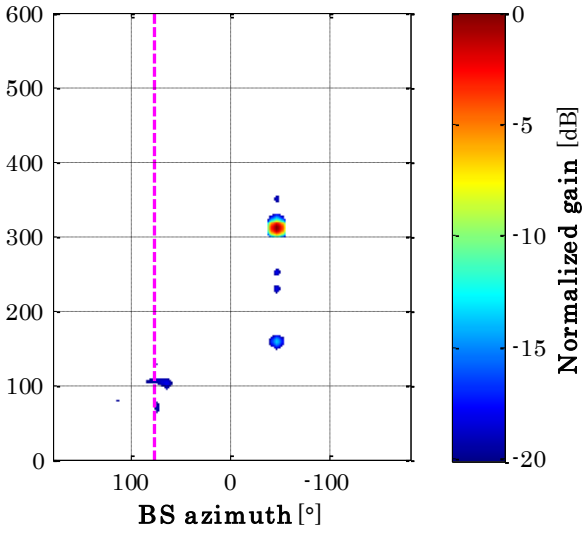
Relative delay [ns]
BS azimuth [°]
Normalized gain [dB]

S1

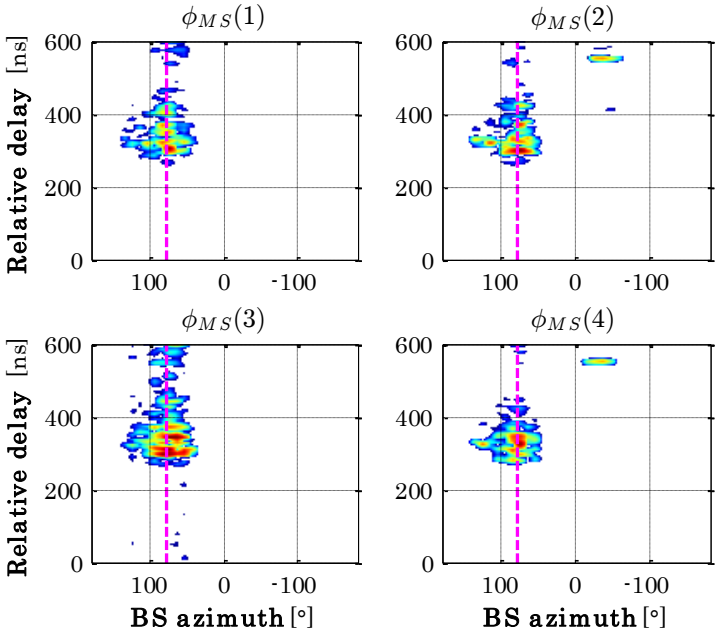
$\phi_{MS}(1)$
$\phi_{MS}(2)$
$\phi_{MS}(3)$
$\phi_{MS}(4)$
Relative delay [ns]
BS azimuth [°]

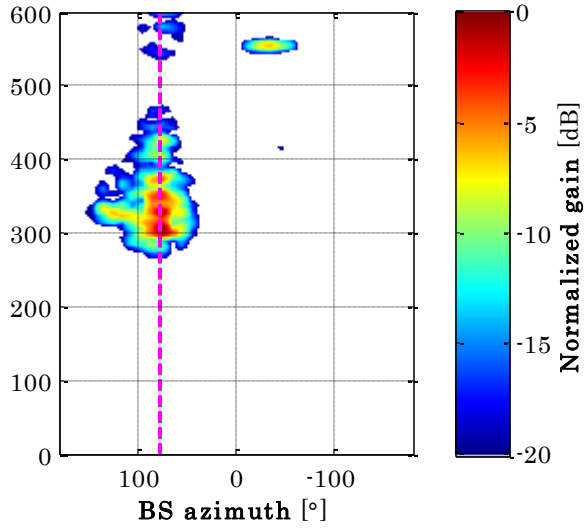
Relative delay [ns]
BS azimuth [°]
Normalized gain [dB]


60 GHz
TxB
B11

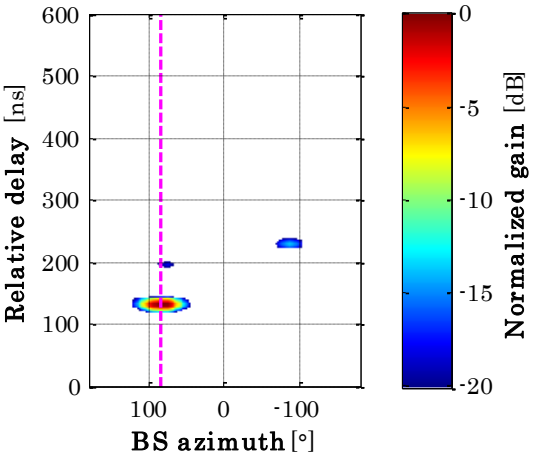
Relative delay [ns]
BS azimuth [°]
Normalized gain [dB]

S2

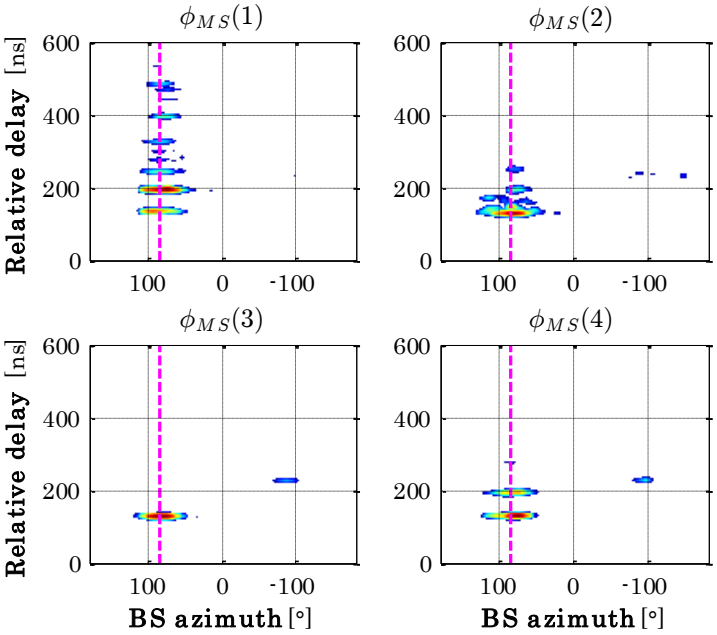
$\phi_{MS}(1)$
$\phi_{MS}(2)$
$\phi_{MS}(3)$
$\phi_{MS}(4)$
Relative delay [ns]
BS azimuth [°]

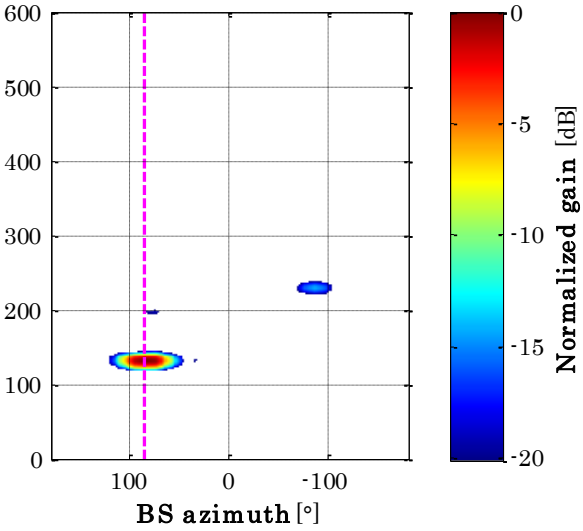
Relative delay [ns]
BS azimuth [°]
Normalized gain [dB]

S1

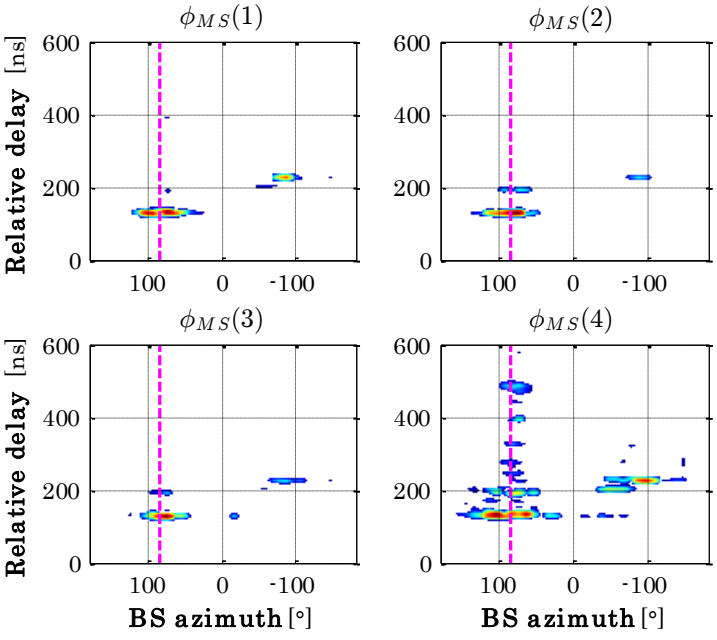
$\phi_{MS}(1)$
$\phi_{MS}(2)$
$\phi_{MS}(3)$
$\phi_{MS}(4)$
Relative delay [ns]
BS azimuth [°]

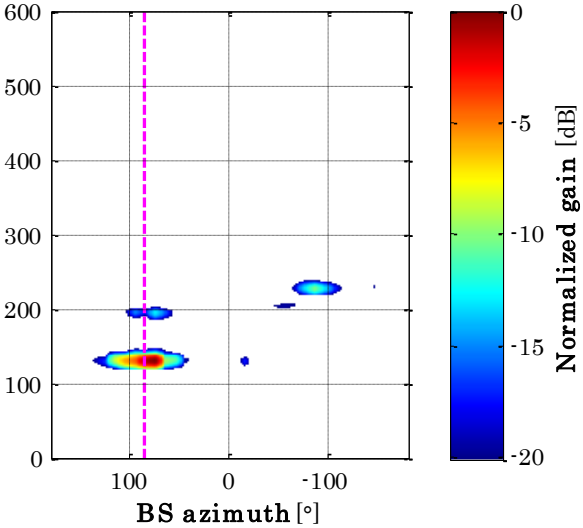
Relative delay [ns]
BS azimuth [°]
Normalized gain [dB]


60 GHz
TxC
C1

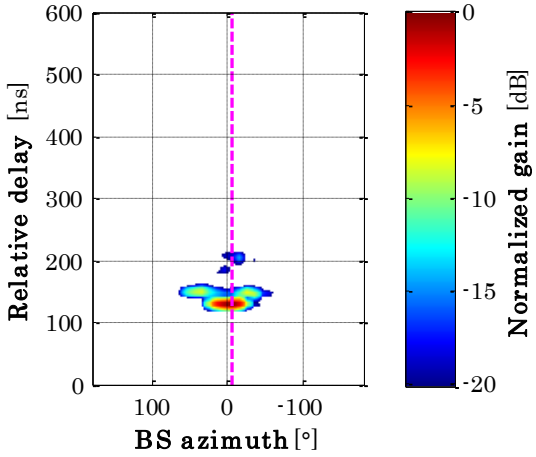
Relative delay [ns]
BS azimuth [°]
Normalized gain [dB]

S2

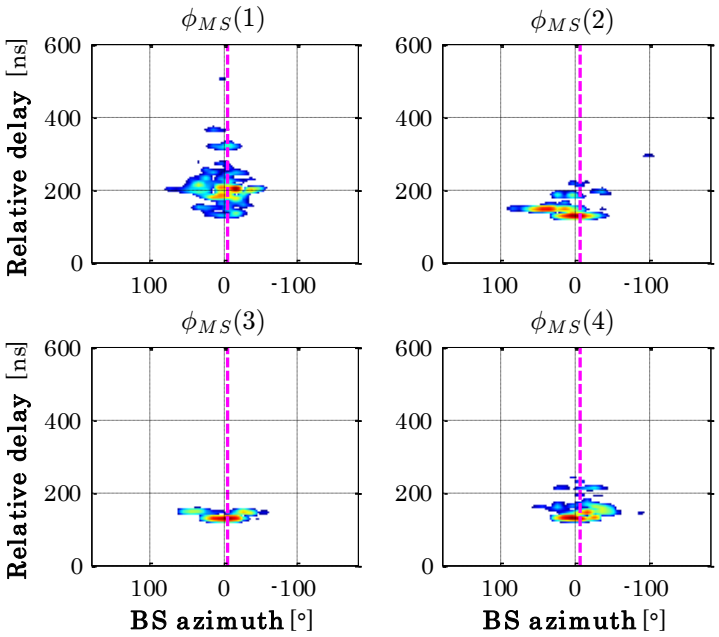
$\phi_{MS}(1)$
$\phi_{MS}(2)$
$\phi_{MS}(3)$
$\phi_{MS}(4)$
Relative delay [ns]
BS azimuth [°]

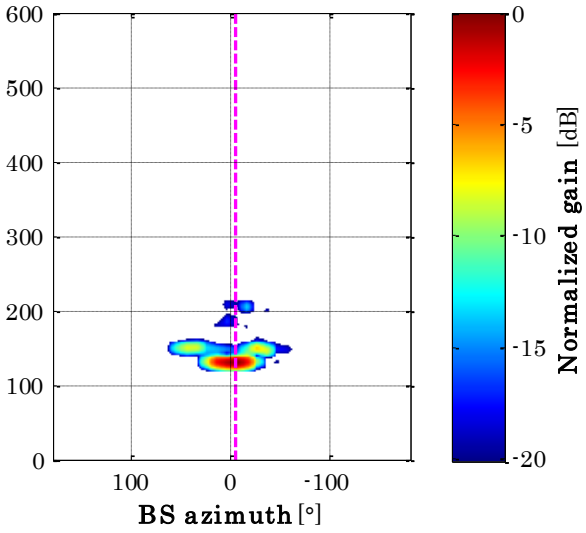
BS azimuth [°]
Normalized gain [dB]

S1

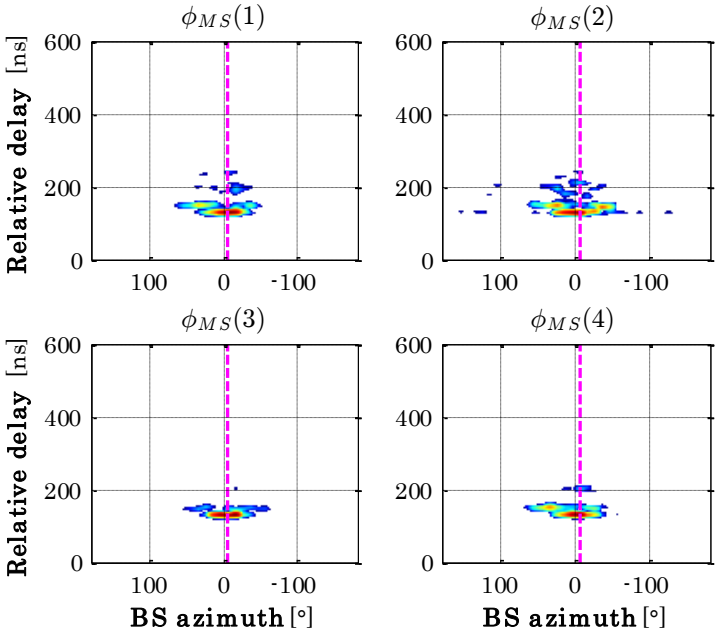
$\phi_{MS}(1)$
$\phi_{MS}(2)$
$\phi_{MS}(3)$
$\phi_{MS}(4)$
Relative delay [ns]
BS azimuth [°]

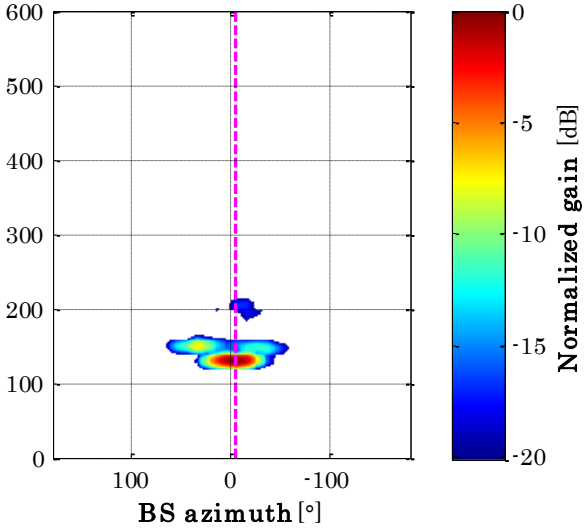
BS azimuth [°]
Normalized gain [dB]


60 GHz
TxC
C2

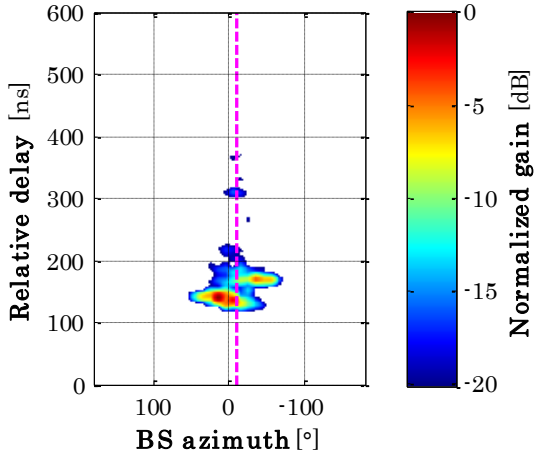
Relative delay [ns]
BS azimuth [°]
Normalized gain [dB]

S2

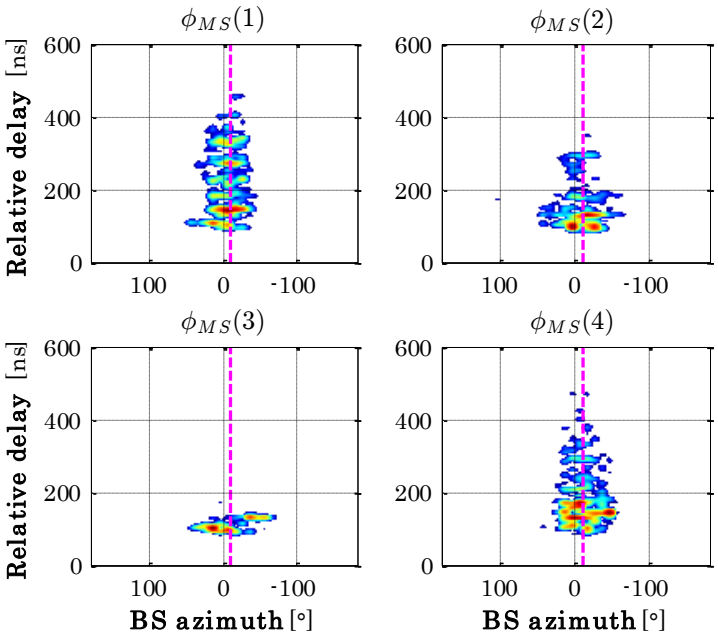
$\phi_{MS}(1)$
$\phi_{MS}(2)$
$\phi_{MS}(3)$
$\phi_{MS}(4)$
Relative delay [ns]
BS azimuth [°]

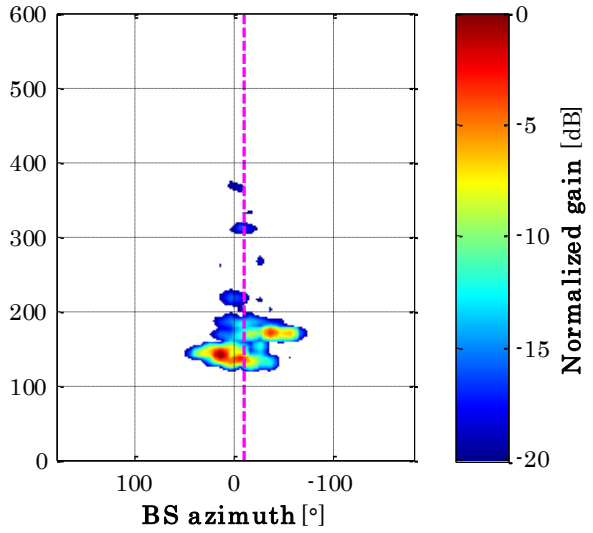
Relative delay [ns]
BS azimuth [°]
Normalized gain [dB]

S1

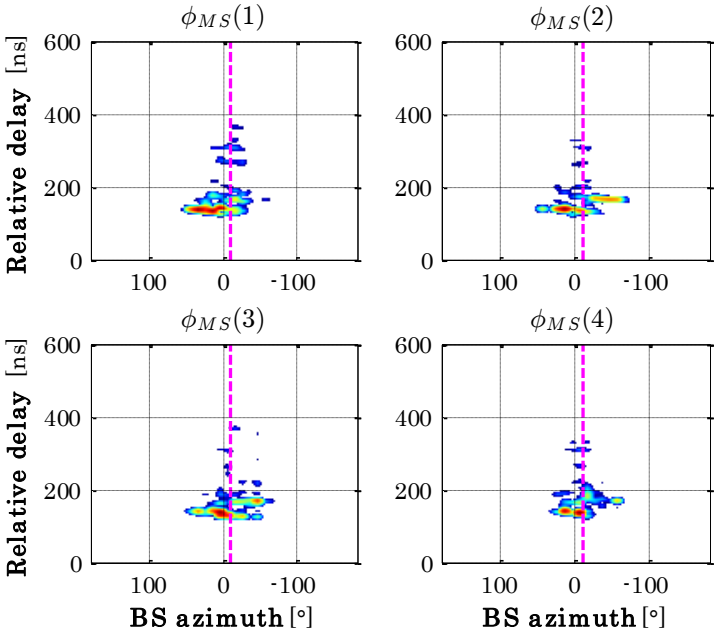
$\phi_{MS}(1)$
$\phi_{MS}(2)$
$\phi_{MS}(3)$
$\phi_{MS}(4)$
Relative delay [ns]
BS azimuth [°]

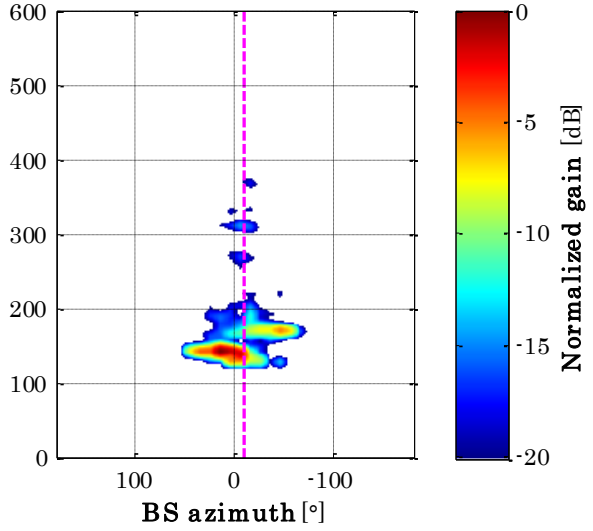
Relative delay [ns]
BS azimuth [°]
Normalized gain [dB]


60 GHz
TxC
C3

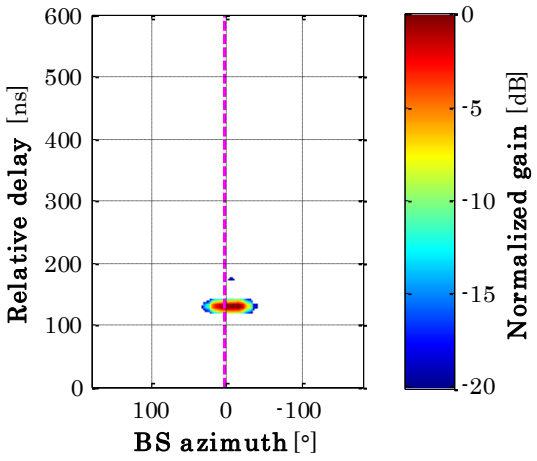
Relative delay [ns]
BS azimuth [°]
Normalized gain [dB]

S2

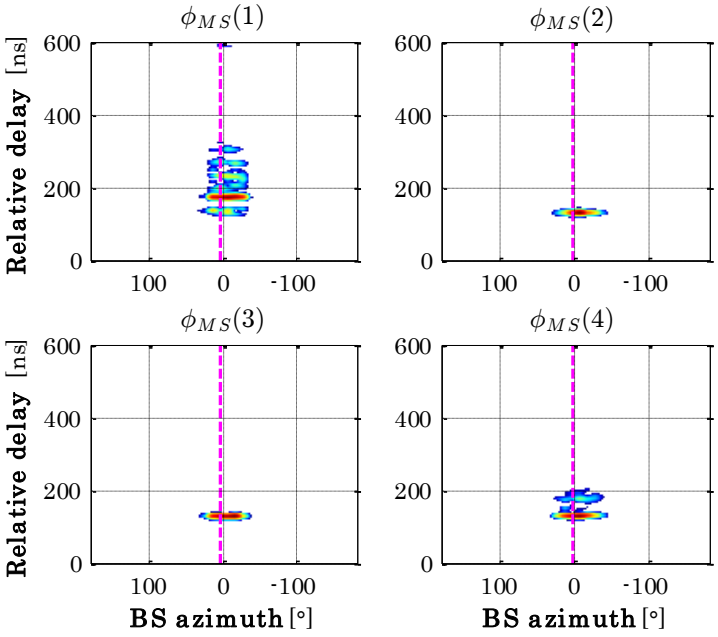
$\phi_{MS}(1)$
$\phi_{MS}(2)$
$\phi_{MS}(3)$
$\phi_{MS}(4)$
Relative delay [ns]
BS azimuth [°]

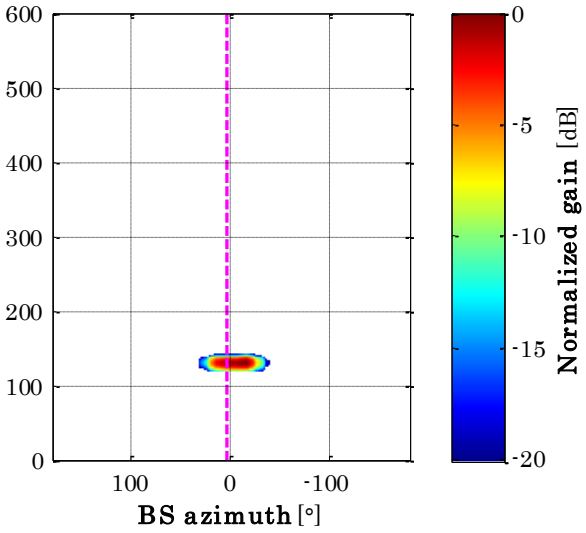
Relative delay [ns]
BS azimuth [°]
Normalized gain [dB]

S1

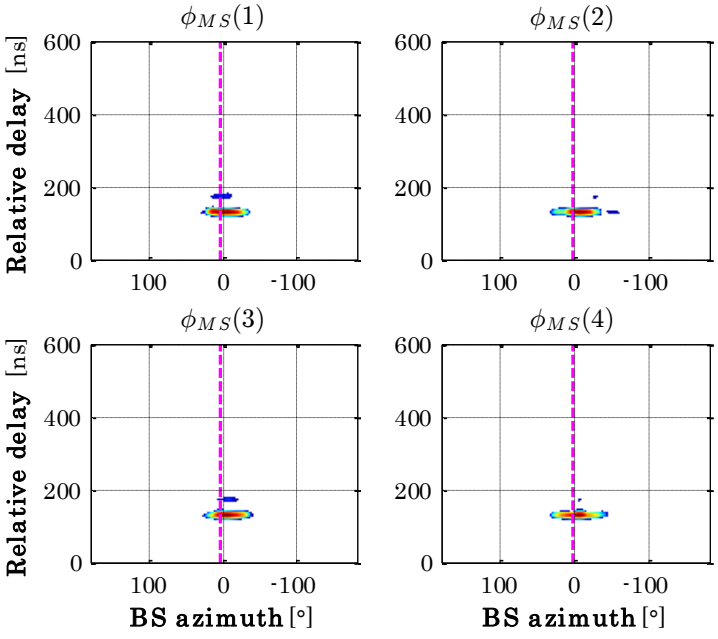
$\phi_{MS}(1)$
$\phi_{MS}(2)$
$\phi_{MS}(3)$
$\phi_{MS}(4)$
Relative delay [ns]
BS azimuth [°]

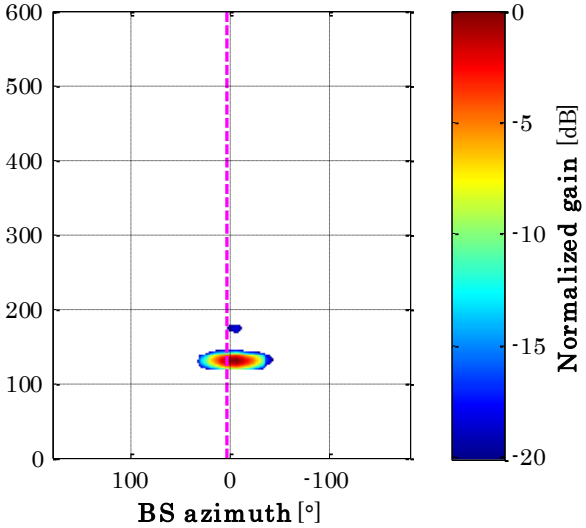
Relative delay [ns]
BS azimuth [°]
Normalized gain [dB]


60 GHz
TxC
C4

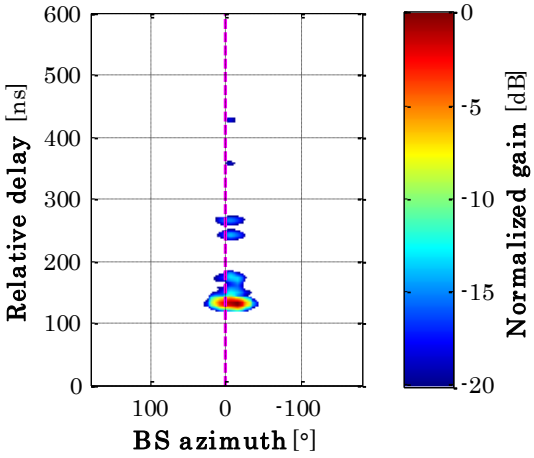
Relative delay [ns]
BS azimuth [°]
Normalized gain [dB]

S2

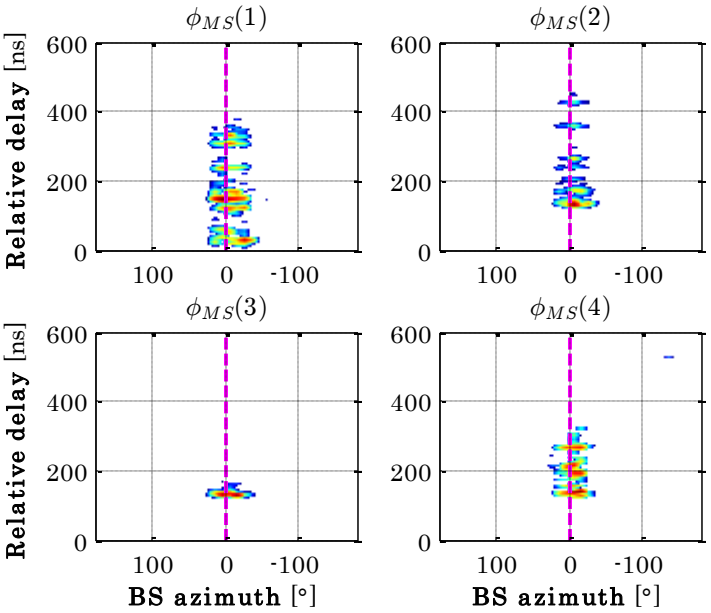
$\phi_{MS}(1)$
$\phi_{MS}(2)$
$\phi_{MS}(3)$
$\phi_{MS}(4)$
Relative delay [ns]
BS azimuth [°]

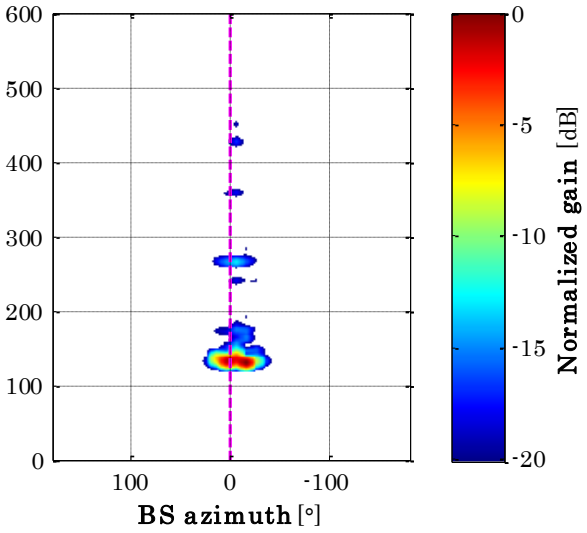
Relative delay [ns]
BS azimuth [°]
Normalized gain [dB]

S1

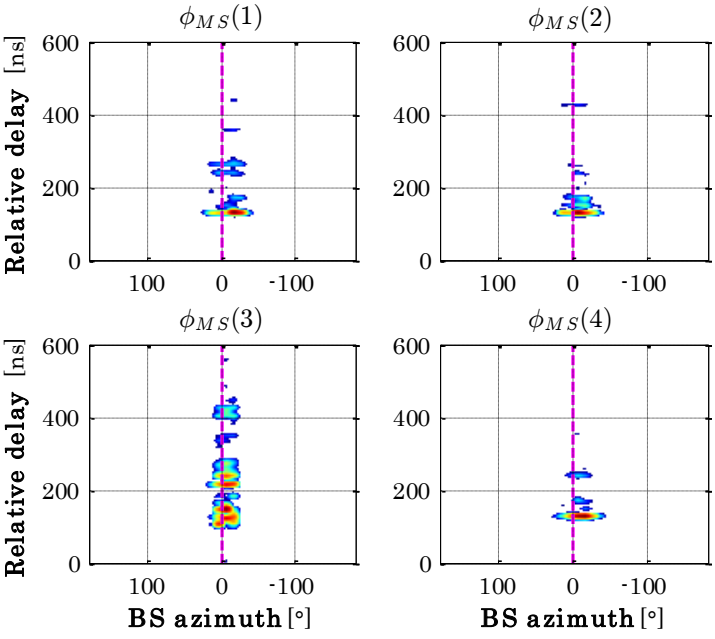
$\phi_{MS}(1)$
$\phi_{MS}(2)$
$\phi_{MS}(3)$
$\phi_{MS}(4)$
Relative delay [ns]
BS azimuth [°]

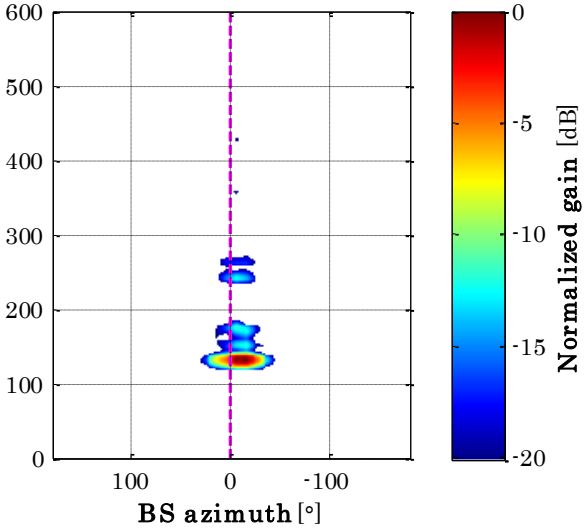
Relative delay [ns]
BS azimuth [°]
Normalized gain [dB]

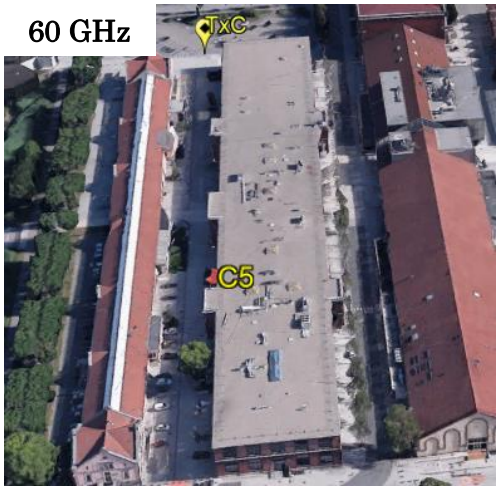
60 GHz
TxC
C5

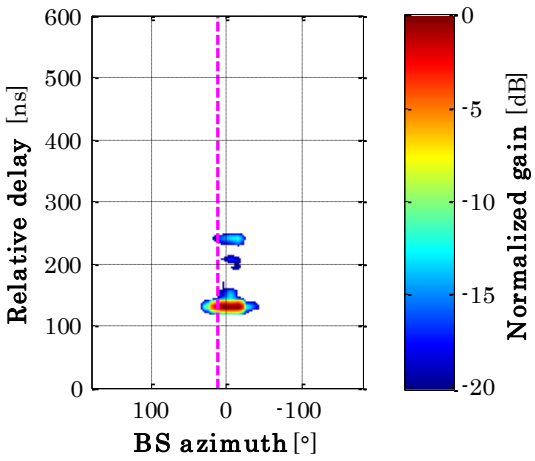
Relative delay [ns]
BS azimuth [°]
Normalized gain [dB]

S2

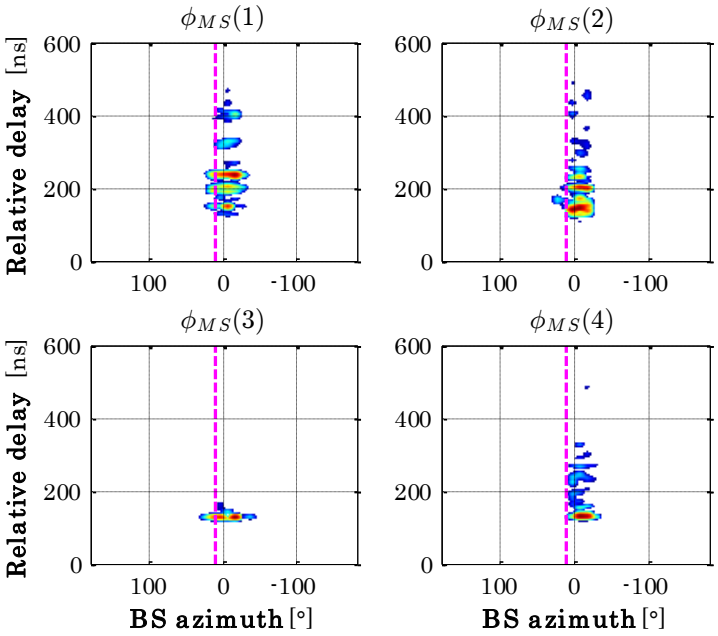
$\phi_{MS}(1)$
$\phi_{MS}(2)$
$\phi_{MS}(3)$
$\phi_{MS}(4)$
Relative delay [ns]
BS azimuth [°]

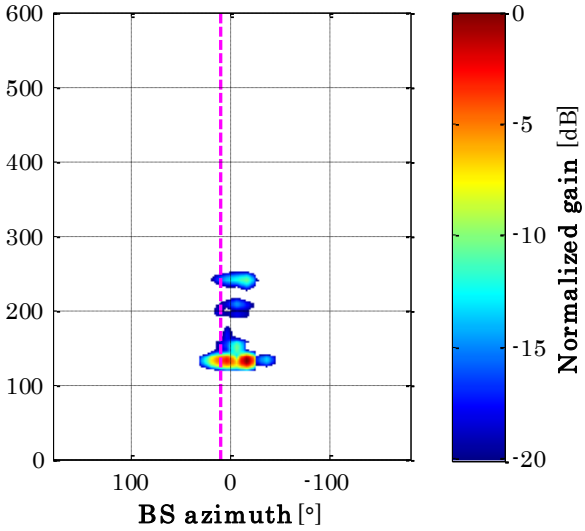
Relative delay [ns]
BS azimuth [°]
Normalized gain [dB]

S1

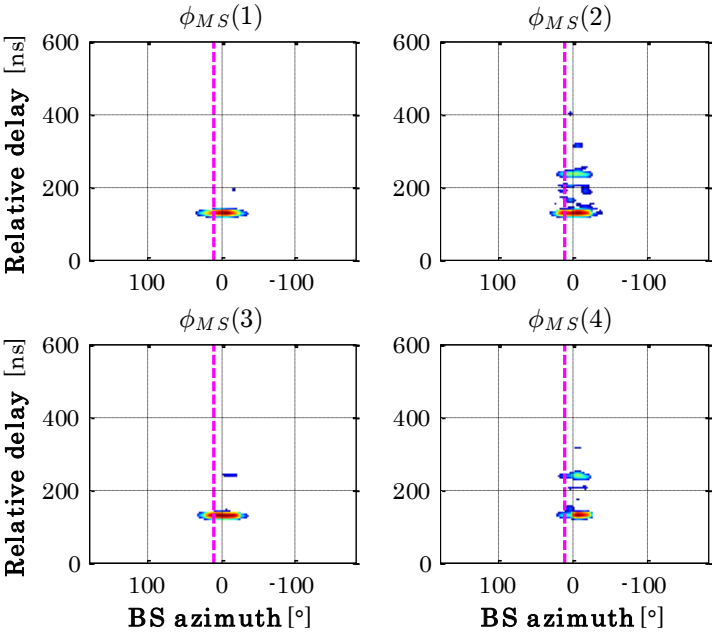
$\phi_{MS}(1)$
$\phi_{MS}(2)$
$\phi_{MS}(3)$
$\phi_{MS}(4)$
Relative delay [ns]
BS azimuth [°]

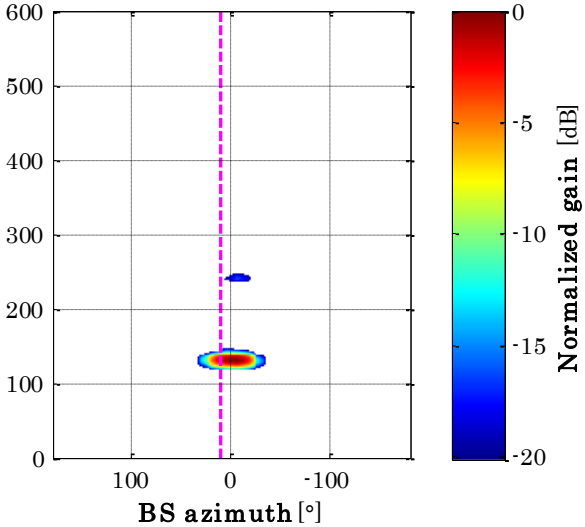
Relative delay [ns]
BS azimuth [°]
Normalized gain [dB]


60 GHz
TxC
C6

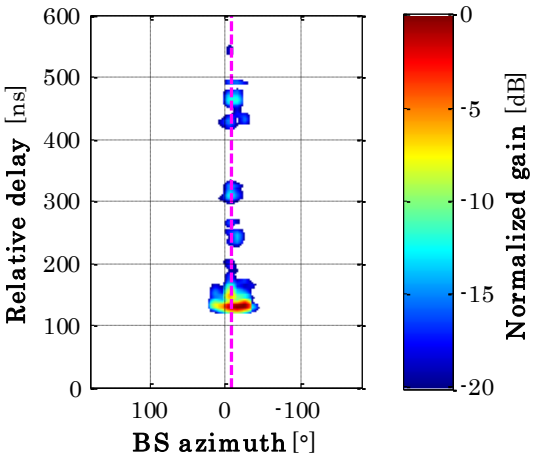
Relative delay [ns]
BS azimuth [°]
Normalized gain [dB]

S2

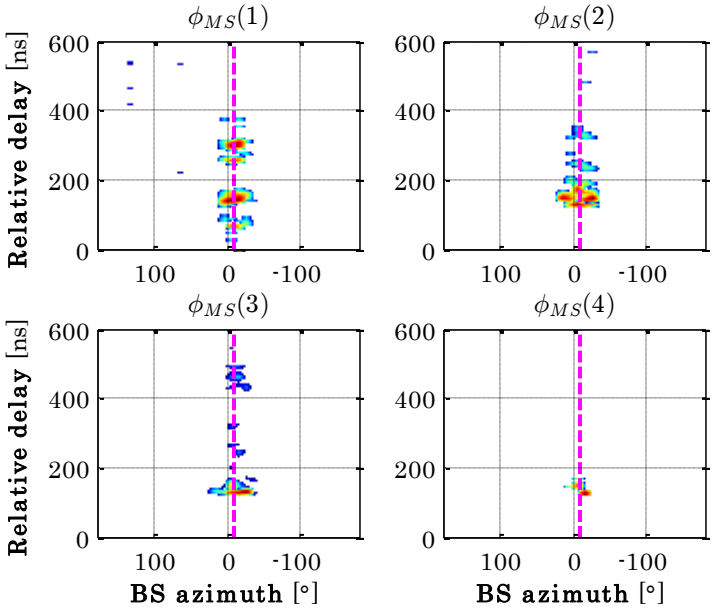
$\phi_{MS}(1)$
$\phi_{MS}(2)$
$\phi_{MS}(3)$
$\phi_{MS}(4)$
Relative delay [ns]
BS azimuth [°]

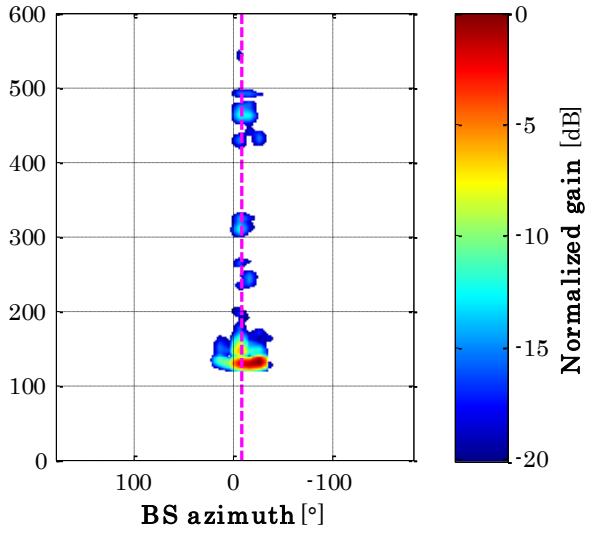
Relative delay [ns]
BS azimuth [°]
Normalized gain [dB]

S1

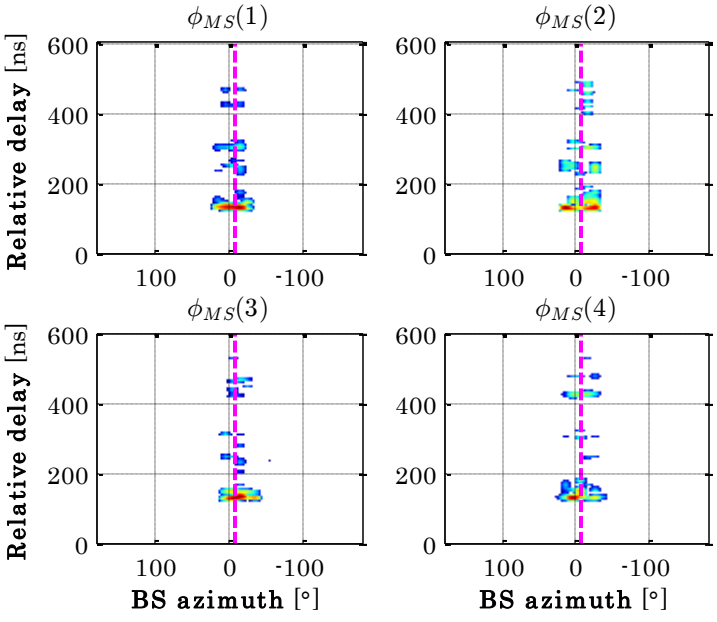
$\phi_{MS}(1)$
$\phi_{MS}(2)$
$\phi_{MS}(3)$
$\phi_{MS}(4)$
Relative delay [ns]
BS azimuth [°]

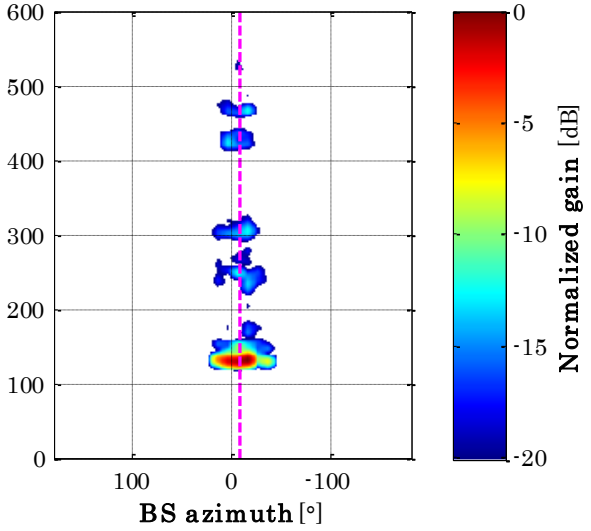
Relative delay [ns]
BS azimuth [°]
Normalized gain [dB]


60 GHz
TxC
C7

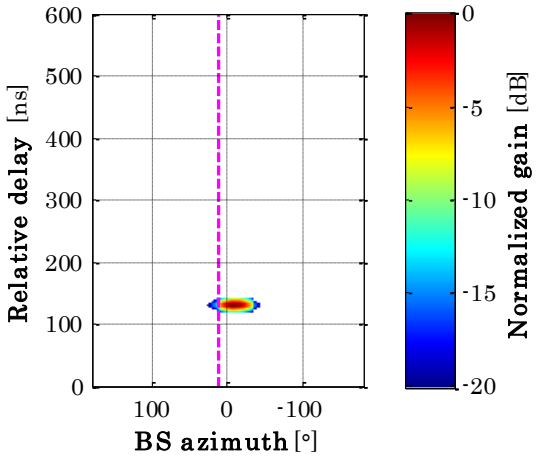
Relative delay [ns]
BS azimuth [°]
Normalized gain [dB]

S2

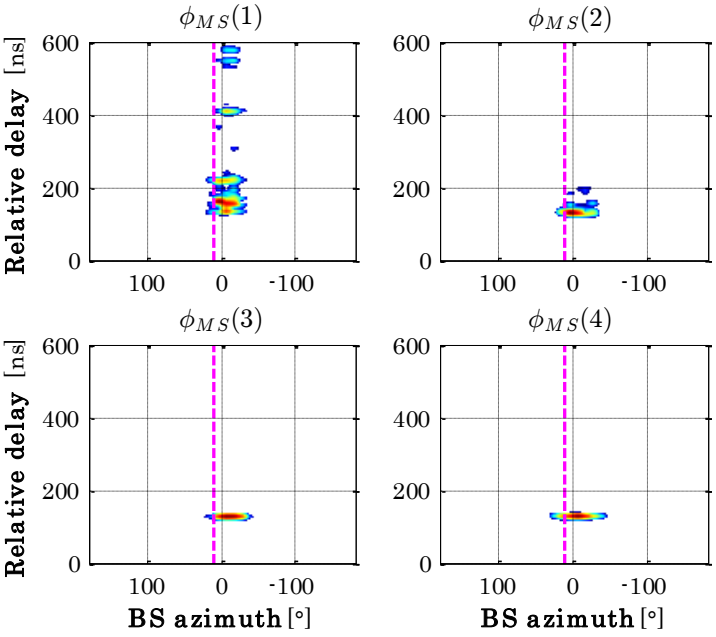
$\phi_{MS}(1)$
$\phi_{MS}(2)$
$\phi_{MS}(3)$
$\phi_{MS}(4)$
Relative delay [ns]
BS azimuth [°]

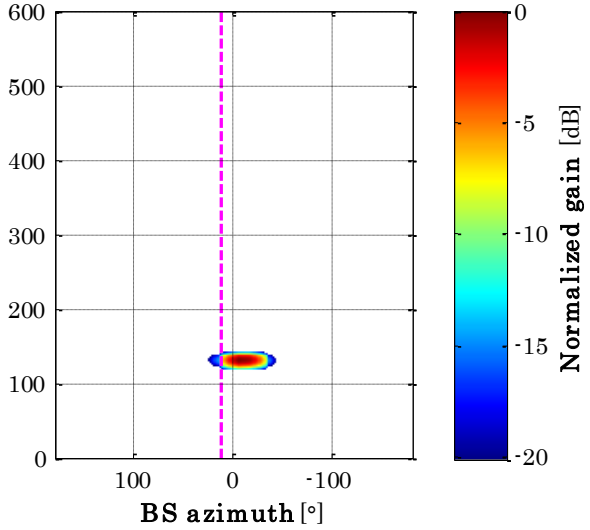
BS azimuth [°]
Normalized gain [dB]

S1

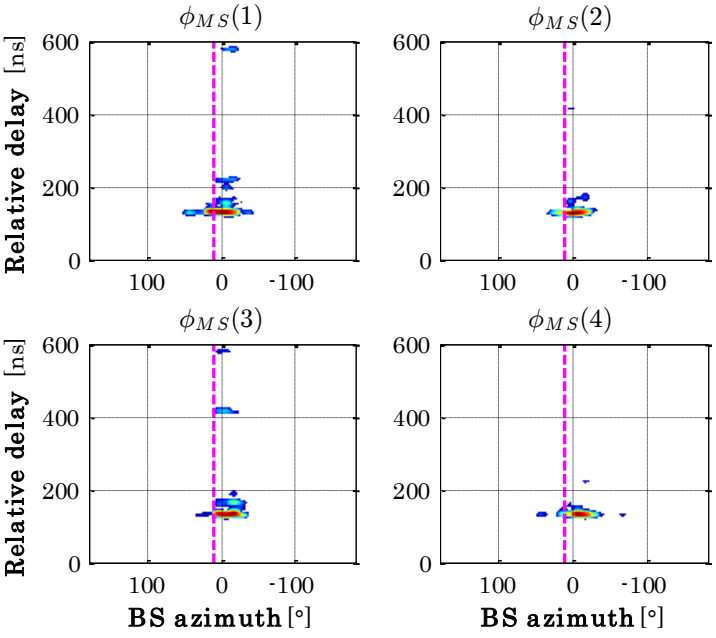
$\phi_{MS}(1)$
$\phi_{MS}(2)$
$\phi_{MS}(3)$
$\phi_{MS}(4)$
Relative delay [ns]
BS azimuth [°]

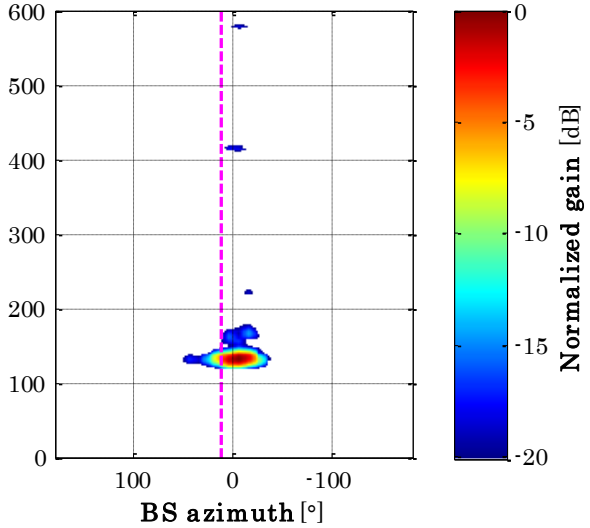
BS azimuth [°]
Normalized gain [dB]


60 GHz
TxC
C8

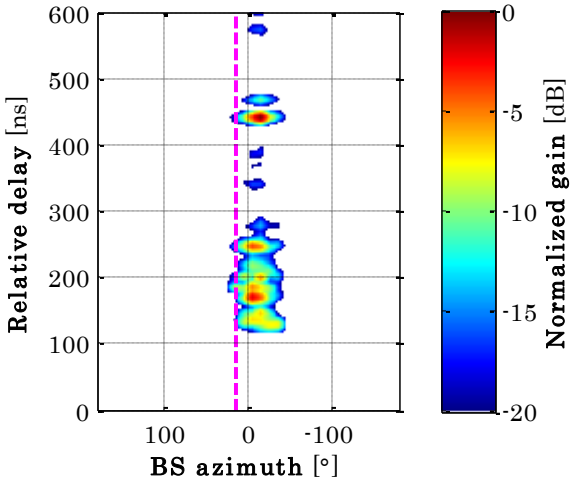
Relative delay [ns]
BS azimuth [°]
Normalized gain [dB]

S2

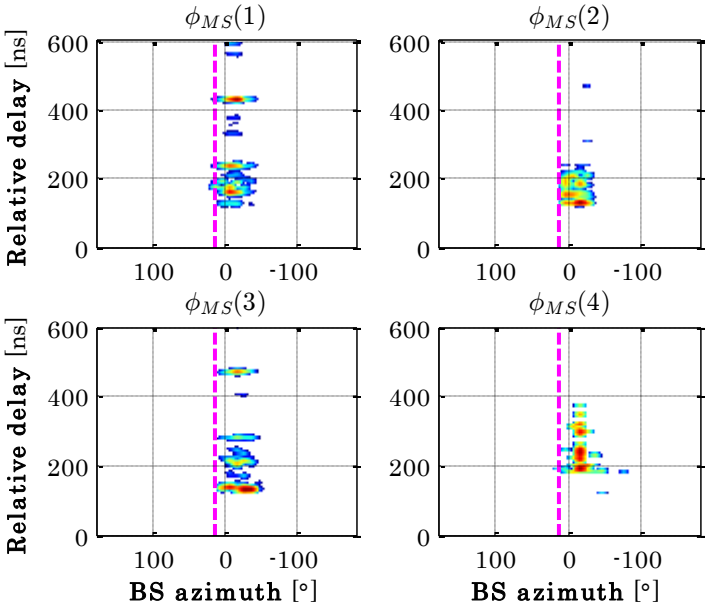
$\phi_{MS}(1)$
$\phi_{MS}(2)$
$\phi_{MS}(3)$
$\phi_{MS}(4)$
Relative delay [ns]
BS azimuth [°]

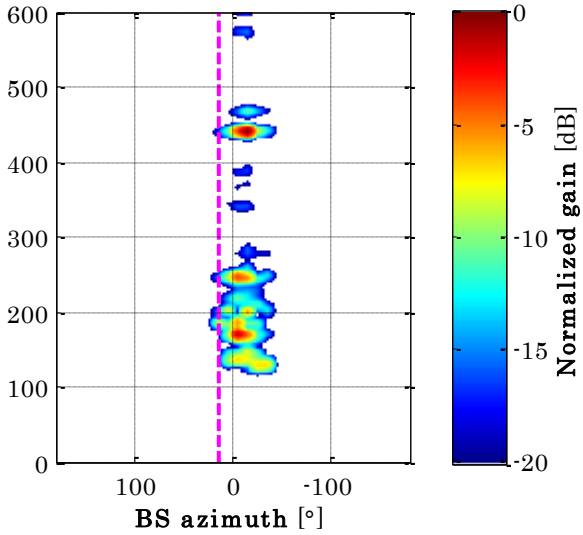
Relative delay [ns]
BS azimuth [°]
Normalized gain [dB]

S1

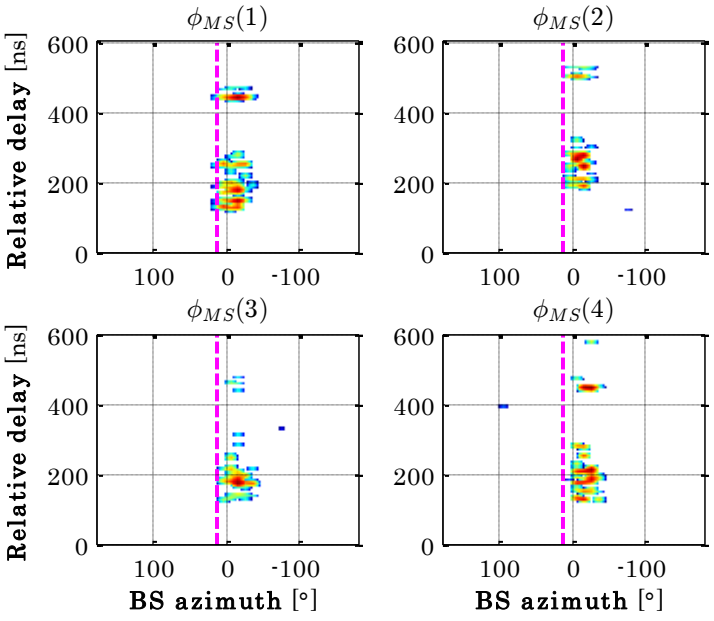
$\phi_{MS}(1)$
$\phi_{MS}(2)$
$\phi_{MS}(3)$
$\phi_{MS}(4)$
Relative delay [ns]
BS azimuth [°]

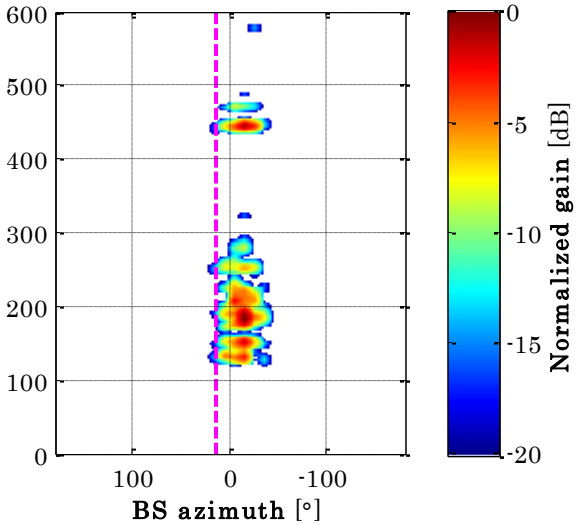
Relative delay [ns]
BS azimuth [°]
Normalized gain [dB]

Publications

- C. A. L. Diakhate, J. Conrat, J. Cousin and A. Sibille, "Frequency–dependence of channel delay spread in an outdoor environment," *2017 IEEE 28th Annual International Symposium on Personal, Indoor, and Mobile Radio Communications (PIMRC)*, Montreal, QC, 2017, pp. 1–5.
- C. A. L. Diakhate, J. Conrat, J. Cousin and A. Sibille, "Antenna aperture impact on channel delay spread in an urban outdoor scenario at 17 and 60 GHz," *12th European Conference on Antennas and Propagation (EuCAP 2018)*, London, 2018, pp. 1–5.
- C. A. L. Diakhate, J. Conrat, J. Cousin and A. Sibille, "Millimeter–wave outdoor–to–indoor channel measurements at 3, 10, 17 and 60 GHz," *2017 11th European Conference on Antennas and Propagation (EUCAP)*, Paris, 2017, pp. 1798–1802.

References

[1] ITU-R, "IMT Vision – Framework and overall objectives of the future development of IMT for 2020 and beyond," September, 2015.

[2] Ericsson, "Ericsson Mobility Report," June, 2018.

[3] Ericsson. (2018). *Ericsson Mobility Visualizer*. Available: https://www.ericsson.com/en/mobility-report/mobility-visualizer?f=1&ft=1&r=2,3,4,5,6,7,8,9&t=8&s=1,2,3&u=1&y=2017,2023&c=1

[4] CISCO, "Cisco Visual Networking Index: Global Mobile Data Traffic Forecast Update, 2016–2021," 2017.

[5] Huawei, "5G: A Technology Vision," 2013.

[6] J. G. Andrews, S. Buzzi, W. Choi, S. V. Hanly, A. Lozano, A. C. K. Soong, and J. C. Zhang, "What Will 5G Be?," *IEEE Journal on Selected Areas in Communications,* vol. 32, pp. 1065-1082, 2014.

[7] N. DOCOMO, "5G Radio Access: Requirements, Concept and Technologies," 2014.

[8] Ericsson, "5G Radio Access Technology and Capabilities," February, 2015.

[9] Nokia, "Looking Ahead to 5G," 2014.

[10] Orange, "Orange 5G Vision," September, 2016.

[11] S. M. Alamouti, "A simple transmit diversity technique for wireless communications," *IEEE Journal on Selected Areas in Communications,* vol. 16, pp. 1451-1458, 1998.

[12] P. W. Wolniansky, G. J. Foschini, G. D. Golden, and R. A. Valenzuela, "V-BLAST: an architecture for realizing very high data rates over the rich-scattering wireless channel," in *1998 URSI International Symposium on Signals, Systems, and Electronics. Conference Proceedings (Cat. No.98EX167)*, 1998, pp. 295-300.

[13] B. N. Getu and J. B. Andersen, "BER and spectral efficiency of a MIMO system," in *The 5th International Symposium on Wireless Personal Multimedia Communications*, 2002, pp. 397-401 vol.2.

[14] F. Rusek, D. Persson, B. K. Lau, E. G. Larsson, T. L. Marzetta, O. Edfors, and F. Tufvesson, "Scaling Up MIMO: Opportunities and Challenges with Very Large Arrays," *IEEE Signal Processing Magazine,* vol. 30, pp. 40-60, 2013.

[15] E. G. Larsson, O. Edfors, F. Tufvesson, and T. L. Marzetta, "Massive MIMO for next generation wireless systems," *IEEE Communications Magazine,* vol. 52, pp. 186-195, 2014.

[16] T. L. Marzetta, "Massive MIMO: An Introduction," *Bell Labs Technical Journal,* vol. 20, pp. 11-22, 2015.

[17] O. Elijah, C. Y. Leow, T. A. Rahman, S. Nunoo, and S. Z. Iliya, "A Comprehensive Survey of Pilot Contamination in Massive MIMO—5G System," *IEEE Communications Surveys & Tutorials,* vol. 18, pp. 905-923, 2016.

[18] Z. Gong, C. Li, and F. Jiang, "Pilot contamination mitigation strategies in massive MIMO systems," *IET Communications,* vol. 11, pp. 2403-2409, 2017.

[19] U. Gustavsson, C. Sanchéz-Perez, T. Eriksson, F. Athley, G. Durisi, P. Landin, K. Hausmair, C. Fager, and L. Svensson, "On the impact of hardware impairments on

massive MIMO," in *2014 IEEE Globecom Workshops (GC Wkshps)*, 2014, pp. 294-300.

[20] ITU-R, "Future spectrum requirements estimate for terrestrial IMT," December, 2013.

[21] A. K. Sen, "Sir J.C. Bose and millimeter waves," in *Proceedings of IEEE TENCON '98. IEEE Region 10 International Conference on Global Connectivity in Energy, Computer, Communication and Control (Cat. No.98CH36229)*, 1998, pp. 288-290 vol.2.

[22] D. T. Jangam, "Mm Waves Role in Satellite Communication," *IOSR Journal of Electronics and Communication Engineering (IOSR-JECE),* vol. 4, pp. 01-04, Jan. - Feb. 2013.

[23] N. P. Narekar and D. M. Bhalerao, "A survey on obstacles for 5G communication," in *2015 International Conference on Communications and Signal Processing (ICCSP)*, 2015, pp. 0831-0835.

[24] P. Nagaraj, "Impact of atmospheric impairments on mmWave based outdoor communication," 13 June, 2018.

[25] H. M. Rahim, C. Y. Leow, and T. A. Rahman, "Millimeter wave propagation through foliage: Comparison of models," in *2015 IEEE 12th Malaysia International Conference on Communications (MICC)*, 2015, pp. 236-240.

[26] J. L. Langston, "Local Multipoint Distribution Services (LMDS) system concepts and implementation," in *1997 IEEE MTT-S Symposium on Technologies for Wireless Applications Digest*, 1997, pp. 12-15.

[27] C. J. Hansen, "WiGiG: Multi-gigabit wireless communications in the 60 GHz band," *IEEE Wireless Communications,* vol. 18, pp. 6-7, 2011.

[28] T. S. Rappaport, S. Sun, R. Mayzus, H. Zhao, Y. Azar, K. Wang, G. N. Wong, J. K. Schulz, M. Samimi, and F. Gutierrez, "Millimeter Wave Mobile Communications for 5G Cellular: It Will Work!," *IEEE Access,* vol. 1, pp. 335-349, 2013.

[29] S. Rangan, T. S. Rappaport, and E. Erkip, "Millimeter-Wave Cellular Wireless Networks: Potentials and Challenges," *Proceedings of the IEEE,* vol. 102, pp. 366-385, 2014.

[30] T. E. Bogale and L. B. Le, "Massive MIMO and mmWave for 5G Wireless HetNet: Potential Benefits and Challenges," *IEEE Vehicular Technology Magazine,* vol. 11, pp. 64-75, 2016.

[31] M. Mantash and T. A. Denidni, "Millimeter-wave beam-steering antenna array for 5G applications," in *2017 IEEE 28th Annual International Symposium on Personal, Indoor, and Mobile Radio Communications (PIMRC)*, 2017, pp. 1-3.

[32] B. Romanous, N. Bitar, A. Imran, and H. Refai, "Network densification: Challenges and opportunities in enabling 5G," in *2015 IEEE 20th International Workshop on Computer Aided Modelling and Design of Communication Links and Networks (CAMAD)*, 2015, pp. 129-134.

[33] V. Chandrasekhar, J. G. Andrews, and A. Gatherer, "Femtocell networks: a survey," *IEEE Communications Magazine,* vol. 46, pp. 59-67, 2008.

[34] I. Petrut, M. Otesteanu, C. Balint, and G. Budura, "Improved LTE macro layer indoor coverage using small cell technologies," in *2014 11th International Symposium on Electronics and Telecommunications (ISETC)*, 2014, pp. 1-4.

[35] E. Hossain and M. Hasan, "5G cellular: key enabling technologies and research challenges," *IEEE Instrumentation & Measurement Magazine,* vol. 18, pp. 11-21, 2015.

[36] K. S. R. S. Jyothsna, "Enhanced CoMP technique for interference cancellation in HETNets of LTE," *International Journal of Scientific & Engineering Research,* vol. 7, February, 2016.
[37] A. M. Sadekar and R. H. Hafez, "LTE-A enhanced Inter-cell Interference Coordination (eICIC) with Pico cell adaptive antenna," in *2015 6th International Conference on the Network of the Future (NOF)*, 2015, pp. 1-6.
[38] 3GPP.TR36.839, "3rd Generation Partnership Project; Technical Specification Group Radio Access Network; Evolved Universal Terrestrial Radio Access (E-UTRA); Mobility Enhancements in Heterogeneous Networks (Release 11)," Technical Report, V0.6.0, May, 2015.
[39] A. Mahbas, H. Zhu, and J. Wang, "Mobility Management in Small Cell Networks," in *GLOBECOM 2017 - 2017 IEEE Global Communications Conference*, 2017, pp. 1-6.
[40] M. T. Nguyen, S. Kwon, and H. Kim, "Mobility Robustness Optimization for Handover Failure Reduction in LTE Small-Cell Networks," *IEEE Transactions on Vehicular Technology,* vol. 67, pp. 4672-4676, 2018.
[41] T. M. Nguyen, W. Ajib, and C. Assi, "A Novel Cooperative Non-Orthogonal Multiple Access (NOMA) in Wireless Backhaul Two-Tier HetNets," *IEEE Transactions on Wireless Communications,* vol. 17, pp. 4873-4887, 2018.
[42] Telefonica, "Cloud RAN Architecture for 5G," 2016.
[43] C. M. R. Institute, "C-RAN The Road Towards Green RAN," Version 2.5, October, 2011.
[44] ETSI, "Network Functions Virtualisation (NFV); Architectural Framework," October, 2013.
[45] 5GAmericas, "Network Slicing for 5G Networks & Services," November, 2016.
[46] S. Abdelwahab, "Network Function Virtualization in 5G," *IEEE Communications Magazine,* April, 2016.
[47] B. Chatras, U. S. T. Kwong, and N. Bihannic, "NFV enabling network slicing for 5G," in *2017 20th Conference on Innovations in Clouds, Internet and Networks (ICIN)*, 2017, pp. 219-225.
[48] 3GPP.TR22.891, "3rd Generation Partnership Project; Technical Specification Group Services and System Aspects; Feasibility Study on New Services and Markets Technology Enablers; Stage 1 (Release 14)," Technical Report V14.2.0, September, 2016.
[49] J. I. Choi, "Achieving Single Channel, Full Duplex Wireless Communication," *MobiCom'10,* September 20–24 2010.
[50] N. H. Mahmood, M. G. Sarret, G. Berardinelli, and P. Mogensen, "Full duplex communications in 5G small cells," in *2017 13th International Wireless Communications and Mobile Computing Conference (IWCMC)*, 2017, pp. 1665-1670.
[51] M. G. Sarret, M. Fleischer, G. Berardinelli, N. H. Mahmood, P. Mogensen, and H. Heinz, "On the potential of full duplex performance in 5G ultra-dense small cell networks," in *2016 24th European Signal Processing Conference (EUSIPCO)*, 2016, pp. 764-768.
[52] J. M. B. d. Silva, Y. Xu, G. Fodor, and C. Fischione, "Distributed spectral efficiency maximization in full-duplex cellular networks," in *2016 IEEE International Conference on Communications Workshops (ICC)*, 2016, pp. 80-86.
[53] J. M. B. d. Silva, G. Fodor, and C. Fischione, "On the spectral efficiency and fairness in full-duplex cellular networks," in *2017 IEEE International Conference on Communications (ICC)*, 2017, pp. 1-6.

[54] P. K. Barik, C. Singhal, and R. Datta, "Throughput enhancement using D2D based relay-assisted communication in cellular networks," in *2017 IEEE 28th Annual International Symposium on Personal, Indoor, and Mobile Radio Communications (PIMRC)*, 2017, pp. 1-6.
[55] Y. Hassan, F. Hussain, S. Hossen, S. Choudhury, and M. M. Alam, "Interference Minimization in D2D Communication Underlaying Cellular Networks," *IEEE Access,* vol. 5, pp. 22471-22484, 2017.
[56] M. N. Tehrani, M. Uysal, and H. Yanikomeroglu, "Device-to-device communication in 5G cellular networks: challenges, solutions, and future directions," *IEEE Communications Magazine,* vol. 52, pp. 86-92, 2014.
[57] 3GPP.TR25.996, "3rd Generation Partnership Project; Technical Specification Group Radio Access Network; Spatial channel model for Multiple Input Multiple Output (MIMO) simulations (Release 6)," Technical Report, V6.1.0, September, 2003.
[58] D. S. Baum, J. Hansen, J. Salo, G. D. Galdo, M. Milojevic, P. Ky, xF, and sti, "An interim channel model for beyond-3G systems: extending the 3GPP spatial channel model (SCM)," in *2005 IEEE 61st Vehicular Technology Conference*, 2005, pp. 3132-3136 Vol. 5.
[59] WINNER, "Final Report on Link Level and System Level Channel Models," D5.4 v. 1.4, Nov. 18th, 2005.
[60] WINNER, "WINNER II Channel Models," D1.1.2 V1.2, November, 2007.
[61] L. Liu, C. Oestges, J. Poutanen, K. Haneda, P. Vainikainen, F. Quitin, F. Tufvesson, and P. D. Doncker, "The COST 2100 MIMO channel model," *IEEE Wireless Communications,* vol. 19, pp. 92-99, 2012.
[62] ITU-R, "Guidelines for evaluation of radio interface technologies for IMT-Advanced," Rep. ITU-R M.2135-1, December, 2009.
[63] WINNER, "WINNER+ Final Channel Models," D5.3 V1.0 June 30th, 2010.
[64] 3GPP.TR36.873, "3rd Generation Partnership Project; Technical Specification Group Radio Access Network; Study on 3D channel model for LTE (Release 12)," Technical Report V12.2.0, June, 2015.
[65] L. M. Correia, *Mobile Broadband Multimedia Networks* Academic Press, 2006.
[66] IEEE, "Channel Models for 60 GHz WLAN Systems," IEEE P802.11 - Wireless LANs,May 20th, 2010.
[67] METIS, "METIS Channel Models," ICT-317669-METIS/D1.4, July, 2015.
[68] MiWEBA, "Channel Modeling and Characterization," ICT 368721/D5.1, June, 2014.
[69] mmMAGIC, "Measurement Results and Final mmMAGIC Channel Models," 2017.
[70] 3GPP.TR38.900, "3rd Generation Partnership Project; Technical Specification Group Radio Access Network; Study on channel model for frequency spectrum above 6 GHz (Release 14)," Technical Report, V14.0.0, June, 2016.
[71] 3GPP.TR38.901, "3rd Generation Partnership Project; Technical Specification Group Radio Access Network; Study on channel model for frequencies from 0.5 to 100 GHz (Release 14)," Technical Report, V14.0.0, March, 2017.
[72] S. Jaeckel, L. Raschkowski, K. Börner, and L. Thiele, "QuaDRiGa: A 3-D Multi-Cell Channel Model With Time Evolution for Enabling Virtual Field Trials," *IEEE Transactions on Antennas and Propagation,* vol. 62, pp. 3242-3256, 2014.
[73] T. S. Rappaport, G. R. MacCartney, M. K. Samimi, and S. Sun, "Wideband Millimeter-Wave Propagation Measurements and Channel Models for Future Wireless Communication System Design," *IEEE Transactions on Communications,* vol. 63, pp. 3029-3056, 2015.

[74] P. Bello, "Characterization of Randomly Time-Variant Linear Channels," *IEEE Transactions on Communications Systems,* vol. 11, pp. 360-393, 1963.

[75] H. Zhao, R. Mayzus, S. Sun, M. Samimi, J. K. Schulz, Y. Azar, K. Wang, G. N. Wong, F. Gutierrez, and T. S. Rappaport, "28 GHz millimeter wave cellular communication measurements for reflection and penetration loss in and around buildings in New York city," in *2013 IEEE International Conference on Communications (ICC)*, 2013, pp. 5163-5167.

[76] P. Ökvist, H. Asplund, A. Simonsson, B. Halvarsson, J. Medbo, and N. Seifi, "15 GHz propagation properties assessed with 5G radio access prototype," in *2015 IEEE 26th Annual International Symposium on Personal, Indoor, and Mobile Radio Communications (PIMRC)*, 2015, pp. 2220-2224.

[77] I. Rodriguez, H. C. Nguyen, N. T. K. Jorgensen, T. B. Sorensen, and P. Mogensen, "Radio Propagation into Modern Buildings: Attenuation Measurements in the Range from 800 MHz to 18 GHz," in *2014 IEEE 80th Vehicular Technology Conference (VTC2014-Fall)*, 2014, pp. 1-5.

[78] C. Larsson, F. Harrysson, B. Olsson, and J. Berg, "An outdoor-to-indoor propagation scenario at 28 GHz," in *The 8th European Conference on Antennas and Propagation (EuCAP 2014)*, 2014, pp. 3301-3304.

[79] A. Roivainen, V. Hovinen, N. Tervo, and M. Latva-aho, "Outdoor-to-indoor path loss modeling at 10.1 GHz," in *2016 10th European Conference on Antennas and Propagation (EuCAP)*, 2016, pp. 1-4.

[80] T. Imai, K. Kitao, N. Tran, N. Omaki, Y. Okumura, and K. Nishimori, "Outdoor-to-Indoor path loss modeling for 0.8 to 37 GHz band," in *2016 10th European Conference on Antennas and Propagation (EuCAP)*, 2016, pp. 1-4.

[81] I. Rodriguez, H. C. Nguyen, T. B. Sorensen, J. Elling, J. A. Holm, P. Mogensen, and B. Vejlgaard, "Analysis of 38 GHz mmWave Propagation Characteristics of Urban Scenarios," in *Proceedings of European Wireless 2015; 21th European Wireless Conference*, 2015, pp. 1-8.

[82] E. J. Violette, R. H. Espeland, R. O. DeBolt, and F. K. Schwering, "Millimeter-wave propagation at street level in an urban environment," *IEEE Transactions on Geoscience and Remote Sensing,* vol. 26, pp. 368-380, 1988.

[83] J. Ryan, G. R. MacCartney, and T. S. Rappaport, "Indoor office wideband penetration loss measurements at 73 GHz," in *2017 IEEE International Conference on Communications Workshops (ICC Workshops)*, 2017, pp. 228-233.

[84] S. Rajagopal, S. Abu-Surra, and M. Malmirchegini, "Channel Feasibility for Outdoor Non-Line-of-Sight mmWave Mobile Communication," in *2012 IEEE Vehicular Technology Conference (VTC Fall)*, 2012, pp. 1-6.

[85] J. Conrat, H. Dekov, A. Nasr, and M. Lienard, "Analysis of the Space-Time Channel Behavior in Outdoor-to-Indoor Environment," in *VTC Spring 2009 - IEEE 69th Vehicular Technology Conference*, 2009, pp. 1-5.

[86] Q. Zheng, J. Zhang, H. Yu, Y. Zhang, and L. Tian, "Propagation statistic characteristic of 3D MIMO channel in outdoor-to-indoor scenario with different antenna heights," in *2016 19th International Symposium on Wireless Personal Multimedia Communications (WPMC)*, 2016, pp. 411-416.

[87] M. Kyro, V. Kolmonen, and P. Vainikainen, "Experimental Propagation Channel Characterization of mm-Wave Radio Links in Urban Scenarios," *IEEE Antennas and Wireless Propagation Letters,* vol. 11, pp. 865-868, 2012.

[88] G. Lovnes, J. J. Reis, and R. H. Raekken, "Channel sounding measurements at 59 GHz in city streets," in *5th IEEE International Symposium on Personal, Indoor and Mobile Radio Communications, Wireless Networks - Catching the Mobile Future.*, 1994, pp. 496-500 vol.2.

[89] P. F. M. Smulders and L. M. Correia, "Characterisation of propagation in 60 GHz radio channels," *Electronics & Communication Engineering Journal,* vol. 9, pp. 73-80, 1997.

[90] R. J. Weiler, M. Peter, T. Kühne, M. Wisotzki, and W. Keusgen, "Simultaneous millimeter-wave multi-band channel sounding in an urban access scenario," in *2015 9th European Conference on Antennas and Propagation (EuCAP)*, 2015, pp. 1-5.

[91] J. Park, J. Liang, J. Lee, H. Kwon, M. Kim, and B. Park, "Millimeter-wave channel model parameters for urban microcellular environment based on 28 and 38 GHz measurements," in *2016 IEEE 27th Annual International Symposium on Personal, Indoor, and Mobile Radio Communications (PIMRC)*, 2016, pp. 1-5.

[92] R. Naderpour, J. Vehmas, S. Nguyen, J. Järveläinen, and K. Haneda, "Spatio-temporal channel sounding in a street canyon at 15, 28 and 60 GHz," in *2016 IEEE 27th Annual International Symposium on Personal, Indoor, and Mobile Radio Communications (PIMRC)*, 2016, pp. 1-6.

[93] E. L. Cid, M. P. Táboas, M. G. Sánchez, and A. V. Alejos, "Microcellular Radio Channel Characterization at 60 GHz for 5G Communications," *IEEE Antennas and Wireless Propagation Letters,* vol. 16, pp. 1476-1479, 2016.

[94] S. Hur, Y. Cho, K. Taehwan, J. Park, A. F. Molisch, K. Haneda, and M. Peter, "Wideband spatial channel model in an urban cellular environments at 28 GHz," in *2015 9th European Conference on Antennas and Propagation (EuCAP)*, 2015, pp. 1-5.

[95] M. Kim, J. Takada, Y. Chang, J. Shen, and Y. Oda, "Large scale characteristics of urban cellular wideband channels at 11 GHz," in *2015 9th European Conference on Antennas and Propagation (EuCAP)*, 2015, pp. 1-4.

[96] V. Kristem, C. U. Bas, R. Wang, and A. F. Molisch, "Outdoor Wideband Channel Measurements and Modeling in the 3–18 GHz Band," *IEEE Transactions on Wireless Communications,* vol. 17, pp. 4620-4633, 2018.

[97] J. Ko, Y. Cho, S. Hur, T. Kim, J. Park, A. F. Molisch, K. Haneda, M. Peter, D. Park, and D. Cho, "Millimeter-Wave Channel Measurements and Analysis for Statistical Spatial Channel Model in In-Building and Urban Environments at 28 GHz," *IEEE Transactions on Wireless Communications,* vol. 16, pp. 5853-5868, 2017.

[98] P. Tang, L. Tian, and J. Zhang, "Analysis of the millimeter wave channel characteristics for urban micro-cell mobile communication scenario," in *2017 11th European Conference on Antennas and Propagation (EUCAP)*, 2017, pp. 2880-2884.

[99] M. Ghoraishi, S. Salous, Y. Gao, and R. Tafazolli, "Millimeter wave spread in delay and azimuth for small cell propagation channel at 60 GHz," in *2017 XXXIInd General Assembly and Scientific Symposium of the International Union of Radio Science (URSI GASS)*, 2017, pp. 1-4.

[100] S. L. H. Nguyen, J. Medbo, M. Peter, A. Karttunen, K. Haneda, A. Bamba, R. D. Errico, N. Iqbal, C. Diakhate, and J. Conrat, "On the frequency dependency of radio channel's delay spread: Analyses and findings from mmMAGIC multi-frequency channel sounding," in *12th European Conference on Antennas and Propagation (EuCAP 2018)*, 2018, pp. 1-5.

[101] W. Keusgen, R. J. Weiler, M. Peter, M. Wisotzki, and B. Göktepe, "Propagation measurements and simulations for millimeter-wave mobile access in a busy urban environment," in *2014 39th International Conference on Infrared, Millimeter, and Terahertz waves (IRMMW-THz)*, 2014, pp. 1-3.

[102] M. Kim, J. Liang, Y. K. Yoon, and J. H. Kim, "28GHz path loss measurements in urban environments using wideband channel sounder," in *2015 IEEE International Symposium on Antennas and Propagation & USNC/URSI National Radio Science Meeting*, 2015, pp. 1798-1799.

[103] Z. Zhong, C. Li, J. Zhao, and X. Zhang, "Height-dependent path loss model and large-scale characteristics analysis of 28 GHz and 38.6 GHz in urban micro scenarios," in *2017 11th European Conference on Antennas and Propagation (EUCAP)*, 2017, pp. 1818-1822.

[104] H. C. Nguyen, I. Rodriguez, T. B. Sorensen, L. L. Sanchez, I. Kovacs, and P. Mogensen, "An Empirical Study of Urban Macro Propagation at 10, 18 and 28 GHz," in *2016 IEEE 83rd Vehicular Technology Conference (VTC Spring)*, 2016, pp. 1-5.

[105] T. Jiang, L. Tian, P. Tang, Z. Hu, and J. Zhang, "Basestation 3-dimensional spatial propagation characteristics in urban microcell at 28 GHz," in *2017 11th European Conference on Antennas and Propagation (EUCAP)*, 2017, pp. 3167-3171.

[106] Y. Han, L. Tian, X. Zhang, P. Tang, Z. Hu, and J. Zhang, "Spatial Propagation Characteristics of 28 GHz Frequency Band in UMi Scenario," in *2017 IEEE 86th Vehicular Technology Conference (VTC-Fall)*, 2017, pp. 1-6.

[107] J. A. Kong, *Electromagnetic Wave Theory*. Cambridge, Massachusetts: John Wiley & Sons, Inc, 1990.

[108] ITU-R, "Effects of building materials and structures on radiowave propagation above about 100 MHz," Recommendation ITU-R P.2040-1, July, 2015.

[109] S. Gobain. Available: https://glassolutions.fr/fr/naviglass

[110] S. Dwivedi, "Window loss measurements and Model Validation," *European Cooperation in Science and Technology (EURO-COST),* vol. CA15104, May 30 - June 1, 2018.

[111] D. A. McNamara, *ITRODUCTION TO The Uniform Geometrical Theory of Diffraction*. Boston, London: Artech House, 1990.

[112] J. Conrat, P. Pajusco, and J. Thiriet, "A Multibands Wideband Propagation Channel Sounder from 2 to 60 GHz," in *2006 IEEE Instrumentation and Measurement Technology Conference Proceedings*, 2006, pp. 590-595.

[113] S. Sun, G. R. MacCartney, M. K. Samimi, and T. S. Rappaport, "Synthesizing Omnidirectional Antenna Patterns, Received Power and Path Loss from Directional Antennas for 5G Millimeter-Wave Communications," in *2015 IEEE Global Communications Conference (GLOBECOM)*, 2015, pp. 1-7.